The atmospheric general circulation model ECHAM6

Model description

**M. Esch, S. Rast[1], R. Brokopf, K.–H. Wieners, J. Bader,
T. Crueger, M.A. Giorgetta, C. Hohenegger, S. Kinne,
L. Kornblueh, T. Krismer, E. Manzini, T. Mauritsen, B. Möbis,
R. Pincus, E. Roeckner, H. Schmidt, B. Stevens**

Max Planck Institute for Meteorology, Hamburg, Germany

September 25, 2014

[1]sebastian.rast@mpimet.mpg.de

Contents

List of Tables

List of Figures

1. Introduction

The new MPI Earth System Model (`MPIESM`) consists of the atmospheric general circulation model (GCM) `ECHAM6`, the land vegetation model `JSBACH`, the ocean GCM `MPIOM` and the ocean biogeochemistry model `HAMOCC`. The `OASIS` coupler is used to exchange state information and fluxes between the atmosphere and the ocean. This document describes the formulation of `ECHAM6` and the data sets providing initial and boundary conditions.

`ECHAM6` is a new major version of the ECHAM series of atmospheric general circulation models, which has been developed on the basis of ECHAM5 (Roeckner et al. (2003) and Roeckner et al. (2006)). Significant differences between ECHAM5 and `ECHAM6` concern the land processes, the radiation schemes, the computation of the surface albedo, and the triggering condition for convection. The technical infrastructure has been significantly modified to optimize the computational performance on the current DKRZ high performance computer.

For land processes the `JSBACH` land vegetation model has been integrated in `ECHAM6`. `JSBACH` includes parameterizations for the physical aspects, i.e. the heat and water storage and exchange with the atmosphere, as in ECHAM5, and in addition parameterizations describing the photosynthetic activity of plants, carbon allocation and storage in plants and soils, and soil respiration. `JSBACH` also includes a hydrological discharge model providing river runoff to the oceans. These features were already developed in the JSBACH version coupled to ECHAM5 (Raddatz et al. (2007)), as used for example in Roeckner et al. (2011)). New extensions of JSBACH, developed for the current CMIP5 simulations, allow to compute also the dynamics of natural vegetation and to account for externally specified, anthropogenic land cover change in the carbon cycle. JSBACH thus describes the land-based processes for the carbon cycle.

The radiative forcing in `ECHAM6` is modified in several aspects compared to ECHAM5. The SW and LW schemes have been replaced and updated, respectively. The newly implemented RRTMG-SW scheme is based on the correlated-k method, like the corresponding RRTMG-LW scheme (Iacono et al. (2008)), and uses 112 g-points in 14 bands. The surface albedo scheme has been improved for sea, sea ice - where melt ponds are now considered - and snow covered land. Further, external data sets describing the climatological spatial and temporal distribution of aerosol and ozone have been replaced by transient, observation-based data sets extended backward to 1850, and forward to 2100 based on the Representative Concentration Pathway scenarios developed for the 5th Assessment Report of IPCC. The new tropospheric aerosol data developed for `ECHAM6` (Kinne, 2011, in prep.) are based on the AEROCOM median model for the year 2000 and observations from the AERONET global sun photometer network. The fine mode aerosol is scaled by anthropogenic sulfur emissions (SO_2), as described by past emissions and by RCP scenarios for the future until 2100. The scaling of the `ECHAM6` aerosol data is based on ECHAM5-HAM simulations forced by sulfur emissions in 5 major regions differentiated in the RCP scenarios.

Minor changes in `ECHAM6` compared to ECHAM5 exist at the level of tuning parameters for moist convection, cloud optical properties, sub-grid scale orographic drag and atmospheric gravity wave drag. The spectral transform dynamical core and the flux form semi-Lagrangian

transport scheme remain essentially unchanged.

ECHAM6 can be used with prescribed lower oceanic boundary conditions or as atmospheric and terrestrial component of the MPIESM. ECHAM6 has been developed for the resolutions T63L47, T63L95 and T127L95. The T63 and T127 spectral representations are associated with Gaussian grids of approximately 1.9 deg and 0.95 deg resolution, respectively. Both vertical grids resolve the atmosphere up to 0.01 hPa, thus resolve the troposphere and the stratosphere.

The accompanying Users Manual for ECHAM6 explains the practical usage of the model concerning compiling, model configuration by Fortran namelists, input data, output data and variables, run scripts, and postprocessing. Further the manual provides technical documentation for model developers concerning parallelization, data structures and memory use, date and time variables, and the submodel interface.

2. Atmosphere

2.1. Dynamical Core

In this section we describe the dynamical core of ECHAM. The first two sections present the governing equations, the coordinates and the discretization schemes used. Attention is concentrated on the representation of the explicitly resolved adiabatic processes. A derivation of the equations including terms requiring parameterization is included in Appendix A.

The dynamical part of ECHAM is formulated in spherical harmonics. After the inter-model comparisons by Jarraud et al. (1981) and Girard and Jarraud (1982) truncated expansions in terms of spherical harmonics were adopted for the representation of dynamical fields. The transform technique developed by Eliasen et al. (1970), Orszag (1970), and Machenhauer and Rasmussen (1972) is used such that non-linear terms, including parameterizations, are evaluated at a set of almost regularly distributed grid points - the Gaussian grid.

In the vertical, a flexible coordinate is used, enabling the model to use either the usual terrain-following sigma coordinate (Phillips, 1957), or a hybrid coordinate for which upper-level model surfaces flatten over steep terrain, becoming surfaces of constant pressure in the stratosphere (Simmons and Burridge (1981) and Simmons and Strüfing (1981)). Moist processes are treated in a different way using a mass conserving algorithm for the transport (Lin and Rood, 1996) of the different water species and potential chemical tracers. The transport is determined on the Gaussian grid.

First, in section 2.1.1 the continuous form of the governing equations is presented. Sections 2.1.2 and 2.1.3 give details of the spectral representation and of the vertical coordinate and its associated vertical finite difference scheme. The temporal finite-difference scheme, which includes not only a conventional semi-implicit treatment of gravity-wave terms (Robert et al., 1972), but also a semi-implicit treatment of the advection of vorticity (Jarraud et al., 1982), is described in section 2.1.4.

2.1.1. The continuous equations

Although the model has been implemented for one particular form of a vertical coordinate, which is introduced in section 2.1.3, it is convenient to introduce the equations and their spectral representation for a general pressure-based terrain-following vertical coordinate $\eta(p, p_s)$, which must be a monotonic function of pressure p, and depends as well on the surface pressure p_s, in such a way that

$$\eta(0, p_s) = 0 \qquad \text{and} \qquad \eta(p_s, p_s) = 1$$

For such a coordinate, the continuous formulation of the primitive equations for a dry atmosphere may be directly derived from their basic height coordinate forms following Kasahara (1974).

During the design of the model, a detailed derivation of the corresponding equations for a moist atmosphere, including a separation into terms to be represented explicitly in the subsequent discretized form of the equations and terms to be parameterized, was carried out. It is shown in Appendix A that under certain approximations, the momentum, thermodynamic and moisture equations may be written:

$$\frac{\partial U}{\partial t} - (f + \xi)V + \dot{\eta}\frac{\partial U}{\partial \eta} + \frac{R_d T_v}{a}\frac{\partial \ln p}{\partial \lambda} + \frac{1}{a}\frac{\partial(\phi + E)}{\partial \lambda} \quad = \quad P_U + K_U \quad (2.1)$$

$$\frac{\partial V}{\partial t} + (f + \xi)U + \dot{\eta}\frac{\partial V}{\partial \eta} + \frac{R_d T_v}{a}(1 - \mu^2)\frac{\partial \ln p}{\partial \mu} + \frac{(1 - \mu^2)}{a}\frac{\partial(\phi + E)}{\partial \mu} \quad = \quad P_V + K_V \quad (2.2)$$

$$\frac{\partial T}{\partial t} + \frac{U}{a(1 - \mu^2)}\frac{\partial T}{\partial \lambda} + \frac{V}{a}\frac{\partial T}{\partial \mu} + \dot{\eta}\frac{\partial T}{\partial \eta} - \frac{\kappa T_v \omega}{(1 + (\delta - 1)q_v)p} \quad = \quad P_T + K_T \quad (2.3)$$

$$\frac{\partial q_i}{\partial t} + \frac{U}{a(1 - \mu^2)}\frac{\partial q_i}{\partial \lambda} + \frac{V}{a}\frac{\partial q_i}{\partial \mu} + \dot{\eta}\frac{\partial q_i}{\partial \eta} \quad = \quad P_{q_i} \quad (2.4)$$

where q_i are the mixing ratios of the different water species.

The continuity equation is

$$\frac{\partial}{\partial \eta}\left(\frac{\partial p}{\partial t}\right) + \nabla \cdot \left(\vec{v}_h \frac{\partial p}{\partial \eta}\right) + \frac{\partial}{\partial \eta}\left(\dot{\eta}\frac{\partial p}{\partial \eta}\right) = 0 \tag{2.5}$$

and the hydrostatic equation takes the form

$$\frac{\partial \phi}{\partial \eta} = -\frac{R_d T_v}{p}\frac{\partial p}{\partial \eta} \tag{2.6}$$

The pressure coordinate vertical velocity is given by

$$\omega = \vec{v}_h \nabla p - \int_0^\eta \nabla \cdot \left(\vec{v}_h \frac{\partial p}{\partial \eta}\right) d\eta \tag{2.7}$$

and explicit expressions for the rate of change of surface pressure, and for $\dot{\eta}$, are obtained by integrating equation 2.5, using the boundary conditions $\dot{\eta} = 0$ at $\eta = 0$ and $\eta = 1$:

$$\frac{\partial p_s}{\partial t} = -\int_0^1 \nabla \cdot \left(\vec{v}_h \frac{\partial p}{\partial \eta}\right) d\eta \tag{2.8}$$

and

$$\dot{\eta}\frac{\partial p}{\partial \eta} = -\frac{\partial p}{\partial t} - \int_0^\eta \nabla \cdot \left(\vec{v}_h \frac{\partial p}{\partial \eta}\right) d\eta \tag{2.9}$$

equation 2.8 may also be written

$$\frac{\partial \ln p_s}{\partial t} = -\frac{1}{p_s}\int_0^1 \nabla \cdot \left(\vec{v}_h \frac{\partial p}{\partial \eta}\right) d\eta \tag{2.10}$$

Following the derivation given in Appendix A, the terms P_U, P_V, P_T, and P_{q_i} are written:

$$P_U = -g\cos\theta\left(\frac{\partial p}{\partial \eta}\right)^{-1}\frac{\partial J_U}{\partial \eta} \tag{2.11}$$

$$P_V = -g\cos\theta\left(\frac{\partial p}{\partial \eta}\right)^{-1}\frac{\partial J_V}{\partial \eta} \tag{2.12}$$

$$P_T = \frac{1}{c_p}\left[Q_R + Q_L + Q_D - g\left(\frac{\partial p}{\partial \eta}\right)^{-1}\left(\frac{\partial J_S}{\partial \eta} - c_{pd}T(\delta-1)\frac{\partial J_{q_v}}{\partial \eta}\right)\right] \tag{2.13}$$

$$P_{q_i} = S_{q_i} - g\left(\frac{\partial p}{\partial \eta}\right)^{-1}\frac{\partial J_{q_i}}{\partial \eta} \tag{2.14}$$

where

$$c_p = c_{pd}(1 + (\delta-1)q_v)$$

In equations 2.11 - 2.14, J_U, J_V, J_S, and J_{q_i} represent net parameterized vertical fluxes of momentum, dry static energy ($c_p T + \phi$), moisture and cloud species. They include fluxes due to convection and boundary-layer turbulence. Q_R, Q_L, and Q_D represent heating due to radiation, phase changes and to internal dissipation of kinetic energy associated with the P_U and P_V terms, respectively. S_{q_i} denotes the rates of change of q_i due to phase changes and precipitation formation. Details of the calculation of these terms are given in section 2.7.

The K terms in equations 2.1 - 2.4 represent the influence of unresolved horizontal scales. Their treatment differs from that of the P terms in that it does not involve a physical model of sub-grid scale processes, but rather a numerically convenient form of scale selective diffusion of a magnitude determined empirically to ensure a realistic behaviour of resolved scales.

In order to apply the spectral method, equations 2.1 and 2.2 are written in vorticity and divergence form following Bourke (1972). They become

$$\frac{\partial \xi}{\partial t} = \frac{1}{a(1-\mu^2)}\frac{\partial(F_V + P_V)}{\partial \lambda} - \frac{1}{a}\frac{\partial(F_U + P_U)}{\partial \mu} + K_\xi \tag{2.15}$$

$$\frac{\partial D}{\partial t} = \frac{1}{a(1-\mu^2)}\frac{\partial(F_U + P_U)}{\partial \lambda} + \frac{1}{a}\frac{\partial(F_V + P_V)}{\partial \mu} - \nabla^2 G + K_D \tag{2.16}$$

where

$$F_U = (f+\xi)V - \dot{\eta}\frac{\partial U}{\partial \eta} - \frac{R_d T_v}{a}\frac{\partial \ln p}{\partial \lambda} \tag{2.17}$$

$$F_V = -(f+\xi)U - \dot{\eta}\frac{\partial V}{\partial \eta} - \frac{R_d T_v}{a}(1-\mu^2)\frac{\partial \ln p}{\partial \lambda} \tag{2.18}$$

and

$$G = \phi + E \tag{2.19}$$

14

We also note that a streamfunction ψ and velocity potential χ may be introduced such that

$$
\begin{aligned}
U &= \frac{1}{a}\left[-(1-\mu^2)\frac{\partial\psi}{\partial\mu} + \frac{\partial\chi}{\partial\lambda}\right] \\
V &= \frac{1}{a}\left[\frac{\partial\psi}{\partial\lambda} + (1-\mu^2)\frac{\partial\chi}{\partial\mu}\right]
\end{aligned}
\tag{2.20}
$$

and

$$
\begin{aligned}
\xi &= \nabla^2\psi \\
D &= \nabla^2\chi
\end{aligned}
\tag{2.21}
$$

2.1.2. Horizontal discretization

Spectral representation

The basic prognostic variables of the model are ξ, D, T, q_i, and $\ln p_s$. While q_i are represented in grid point space, the other variables, and the surface geopotential ϕ_s, are represented in the horizontal by truncated series of spherical harmonics:

$$
X(\lambda,\mu,\eta,t) = \sum_{m=-M}^{M}\sum_{n=m}^{N(M)} X_n^m(\eta,t)P_n^m(\mu)\,\mathrm{e}^{im\lambda}
\tag{2.22}
$$

where X is any variable, m is the zonal wave number and n is the meridional index. The P_n^m are the Associated Legendre Functions of the first kind, defined here by

$$
P_n^m(\mu) = \sqrt{(2n+1)\frac{(n-m)!}{(n+m)!}}\,\frac{1}{2^n n!}(1-\mu^2)^{\frac{m}{2}}\frac{d^{(n+m)}}{d\mu^{(n+m)}}(\mu^2-1)^n, \quad (m \geq 0)
\tag{2.23}
$$

and

$$
P_n^{-m}(\mu) = P_n^m(\mu)
$$

This definition is such that

$$
\frac{1}{2}\int_{-1}^{1} P_n^m(\mu)P_s^m(\mu)d\mu = \delta_{ns}
\tag{2.24}
$$

where δ_{ns} is the Kronecker delta function. The X_n^m are the complex-valued spectral coefficients of the field X and given by

$$
X_n^m(\eta,t) = \frac{1}{4\pi}\int_{-1}^{1}\int_{0}^{2\pi} X(\lambda,\mu,\eta,t)P_n^m(\mu)\,\mathrm{e}^{-im\lambda}d\lambda d\mu
\tag{2.25}
$$

Since X is real

$$X_n^{-m} = (X_n^m)^*$$ (2.26)

is valid, where ( )* denotes the complex conjugate. The model thus deals explicitly only with the X_n^m for $m \geq 0$.

The Fourier coefficients of X, $X_m(\mu, \eta, t)$ are defined by

$$X_m(\mu, \eta, t) = \frac{1}{2\pi} \int\limits_0^{2\pi} X(\lambda, \mu, \eta, t) \, \mathrm{e}^{-im\lambda} d\lambda$$ (2.27)

or, using equation 2.22, by

$$X_m(\mu, \eta, t) = \sum_{n=m}^{N(m)} X_n^m(\eta, t) P_n^m(\mu)$$ (2.28)

with

$$X(\lambda, \mu, \eta, t) = \sum_{m=-M}^{M} X_m(\mu, \eta, t) \, \mathrm{e}^{im\lambda}$$ (2.29)

Horizontal derivatives are given analytically by

$$\left(\frac{\partial X}{\partial \lambda}\right)_m = imX_m \quad \text{and} \quad \left(\frac{\partial X}{\partial \mu}\right)_m = \sum_{n=m}^{N(m)} X_n^m \frac{dP_n^m}{d\mu}$$ (2.30)

where the derivative of the Legendre Function is given by the recurrence relation:

$$(1-\mu^2)\frac{dP_n^m}{d\mu} = -n\varepsilon_{n+1}^m P_{n+1}^m + (n+1)\varepsilon_n^m P_{n-1}^m \quad \text{with} \quad \varepsilon_n^m = \sqrt{\frac{n^2 - m^2}{4n^2 - 1}}$$ (2.31)

An important property of the spherical harmonics is the algebraic form of the Laplacian:

$$\nabla^2(P_n^m(\mu) \, \mathrm{e}^{im\lambda}) = -\frac{n(n+1)}{a^2} P_n^m(\mu) \, \mathrm{e}^{im\lambda}$$ (2.32)

Relationships 2.20 and 2.21 may thus be used to derive expressions for the Fourier velocity coefficients, U_m and V_m in terms of the spectral coefficients ξ_n^m and D_n^m. It is convenient for later reference to write these expressions in the form

$$U_m = U_{\xi m} + U_{Dm} \quad \text{and} \quad V_m = V_{\xi m} + V_{Dm}$$ (2.33)

16

where

$$U_{\xi m} = -a \sum_{n=m}^{N(m)} \frac{1}{n(n+1)} \xi_n^m H_n^m(\mu) \qquad (2.34)$$

$$U_{Dm} = -a \sum_{n=m}^{N(m)} \frac{im}{n(n+1)} D_n^m P_n^m(\mu) \qquad (2.35)$$

$$V_{\xi m} = -a \sum_{n=m}^{N(m)} \frac{im}{n(n+1)} \xi_n^m P_n^m(\mu) \qquad (2.36)$$

$$V_{Dm} = -a \sum_{n=m}^{N(m)} \frac{1}{n(n+1)} D_n^m H_n^m(\mu) \qquad (2.37)$$

with

$$H_n^m(\mu) = -(1 - \mu^2) \frac{dP_n^m}{d\mu} \qquad (2.38)$$

The H_n^m can be computed from the recurrence relation 2.31. In `ECHAM6` only triangular truncations can be used which is the preferred type of truncations for resolutions larger than T31. This restriction is implied by the parallelization of the spectral part of the model. The triangular truncation is completely defined by the three parameters illustrated in figure 2.1.
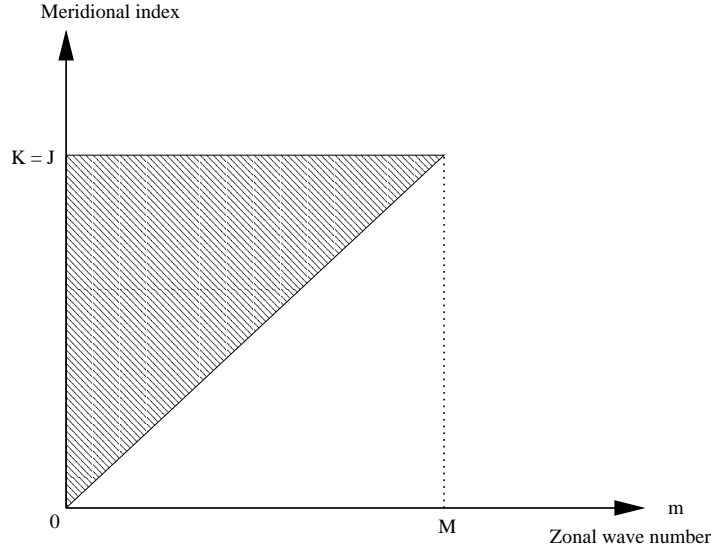
Figure 2.1.: Triangular truncation

The triangular truncations are special cases of the pentagonal one in which $M = J = K$.

The summation limit, $N(m)$ is given by

$$N = J + |m| \qquad \text{if} \qquad J + |m| \le K \qquad \text{and} \qquad N = K \qquad \text{if} \qquad J + |m| > K$$

The standard truncations used in `ECHAM6` are at wave numbers 31, 63, 127 or 255.

Spectral/grid-point transforms, and the evaluation of spectral tendencies

The general form of the equations follow that of the early multi-level spectral models described by Bourke (1974) and Hoskins and Simmons (1975), although the present model differs in its use of an advective form for the equations 2.15, 2.16, 2.3, and 2.10. Equations for the corresponding spectral coefficients are obtained by multiplying each side of these equations by $P_n^m(\mu)\,\mathrm{e}^{-im\lambda}$ and integrating over the sphere. This yields, from 2.25,

$$
\frac{\partial \xi_n^m}{\partial t} = \frac{1}{4\pi a}\int_{-1}^{1}\int_{0}^{2\pi}\left(\frac{1}{1-\mu^2}\frac{\partial(F_V+P_V)}{\partial\lambda} - \frac{\partial(F_U+P_U)}{\partial\mu}\right)P_n^m(\mu)\,\mathrm{e}^{-im\lambda}d\lambda d\mu
$$
$$
+(K_\xi)_n^m \tag{2.39}
$$

$$
\frac{\partial D_n^m}{\partial t} = \frac{1}{4\pi a}\int_{-1}^{1}\int_{0}^{2\pi}\left(\frac{1}{1-\mu^2}\frac{\partial(F_U+P_U)}{\partial\lambda} + \frac{\partial(F_V+P_V)}{\partial\mu}\right)P_n^m(\mu)\,\mathrm{e}^{-im\lambda}d\lambda d\mu
$$
$$
-\frac{1}{4\pi}\int_{-1}^{1}\int_{0}^{2\pi}(\nabla^2 G)P_n^m(\mu)\,\mathrm{e}^{-im\lambda}d\lambda d\mu + (K_D)_n^m \tag{2.40}
$$

$$
\frac{\partial T_n^m}{\partial t} = \frac{1}{4\pi}\int_{-1}^{1}\int_{0}^{2\pi}(F_T+P_T)P_n^m(\mu)\,\mathrm{e}^{-im\lambda}d\lambda d\mu + (K_T)_n^m \tag{2.41}
$$

$$
\frac{\partial(\ln p_s)_n^m}{\partial t} = \frac{1}{4\pi}\int_{-1}^{1}\int_{0}^{2\pi}F_P P_n^m(\mu)\,\mathrm{e}^{-im\lambda}d\lambda d\mu \tag{2.42}
$$

where F_U, F_V and G are given by 2.17 - 2.19, and

$$
F_T = -\frac{U}{a(1-\mu^2)}\frac{\partial T}{\partial\lambda} - \frac{V}{a}\frac{\partial T}{\partial\mu} - \dot\eta\frac{\partial T}{\partial\eta} + \frac{\kappa T_\nu\omega}{(1+(\delta-1)q_v)p} \tag{2.43}
$$

$$
F_P = -\frac{1}{p_s}\int_{0}^{1}\nabla\cdot(\vec{v}_h\frac{\partial p}{\partial\eta})d\eta \tag{2.44}
$$

Equations 2.41 - 2.42 are in the form used in the model. The corresponding forms for the vorticity and divergence equations are obtained from 2.39 and 2.40 by integration by parts and use of 2.32:

$$\frac{\partial \xi_n^m}{\partial t} = \frac{1}{4\pi a} \int\limits_{-1}^{1} \int\limits_{0}^{2\pi} \frac{1}{1-\mu^2} [im(F_V + P_V)P_n^m(\mu) - (F_U + P_U)H_n^m(\mu)] \, \mathrm{e}^{-im\lambda} d\lambda d\mu$$
$$+ (K_\xi)_n^m \tag{2.45}$$

$$\frac{\partial D_n^m}{\partial t} = \frac{1}{4\pi a} \int\limits_{-1}^{1} \int\limits_{0}^{2\pi} \frac{1}{1-\mu^2} [im(F_U + P_U)P_n^m(\mu) + (F_V + P_V)H_n^m(\mu)] \, \mathrm{e}^{-im\lambda} d\lambda d\mu$$
$$+ \frac{n(n+1)}{4\pi a^2} \int\limits_{0}^{1} \int\limits_{0}^{2\pi} G P_n^m(\mu) \, \mathrm{e}^{-im\lambda} d\lambda d\mu + (K_D)_n^m \tag{2.46}$$

where $H_n^m(\mu)$ is given by 2.38.

An outline of the model's computation of spectral tendencies may now be given. First, a grid of points covering the sphere is defined. Using the basic definition of the spectral expansions 2.22 and equations 2.33 - 2.37, values of ξ, D, U, V, T, and $\ln p_s$ are calculated at the gridpoints, as are the derivatives

$$\frac{\partial T}{\partial \lambda}, \frac{\partial T}{\partial \mu}, \frac{\partial \ln p_s}{\partial \lambda} \text{and} \frac{\partial \ln p_s}{\partial \mu}$$

using 2.30. The resulting gridpoint values are sufficient to calculate gridpoint values of F_U, F_V, F_T, F_p and G, together with the parameterized tendencies P_U, P_V, and P_T, since prognostic surface fields associated with the parameterization are defined and updated on the same grid. The integrands of the prognostic equations 2.45, 2.46, 2.41 - 2.42 are thus known at each gridpoint, and spectral tendencies are calculated by numerical quadrature.

The grid on which the calculations are performed is chosen to give an exact (given the spectral truncation of the fields, and within round-off error) contribution to spectral tendencies from quadratic non-linear terms. The integrals with respect to λ involve the product of three trigonometric functions, and as shown by Machenhauer and Rasmussen (1972) they may be evaluated exactly using a regularly-spaced grid of at least $3 \cdot M + 1$ points. For the latitudinal integrals, Eliasen et al. (1970) showed that quadratic nonlinear terms lead to integrands which are polynomials in μ of a certain order.

They may thus be computed exactly using Gaussian quadrature (e.g. Krylov (1962), with points located at the (approximately equally-spaced) latitudes which satisfy $P_{N_G}^0(\mu) = 0$, for sufficiently large integer N_G. These latitudes form what are referred to as the Gaussian latitudes.

In order to find the necessary number of Gaussian latitudes for the triangular truncation, and from the exactness condition for the Gaussian integration it may be shown that the number of Gaussian latitudes N_G must fulfil the following condition:

$$N_G \geq \frac{3 \cdot K + 1}{2}$$

The associated number of Gaussian latitudes with respect to the given spectral resolution in `ECHAM6` is given in table 2.1.

Truncation	No. of Longitudes	No. of Latitudes
T31	96	48
T63	192	96
T127	384	192
T255	768	384

Table 2.1.: Truncation and associated number of Gaussian latitudes (and longitudinal number of gridpoints).

An asymptotic property of the Legendre Functions which may be derived directly from the definition 2.23 is

$$P_n^m(\mu) \sim (1 - \mu^2)^{m/2} \text{ as } (\mu \to \pm 1).$$

Thus for large m the functions become vanishingly small as the poles are approached, and the contributions to the integrals 2.39 - 2.42 from polar regions become less than the unavoidable round-off error for sufficiently large zonal wavenumbers.

2.1.3. Vertical discretization

The hybrid vertical representation

To represent the vertical variation of the dependent variables ξ, D, and T the atmosphere is divided into layers as illustrated in table 2.2. These layers are defined by the pressures of the interfaces between them (the "half levels"), and these pressures are given by

$$p_{k+1/2} = A_{k+1/2} + B_{k+1/2} \ p_s \tag{2.47}$$

for $k = 0, 1, 2 \ldots NLEV$. The $A_{k+1/2}$ and $B_{k+1/2}$ are constants whose values effectively define the vertical coordinate. Necessary values are

$$A_{1/2} = B_{1/2} = A_{NLEV+1/2} = 0 \ \text{ and } \ B_{NLEV+1/2} = 1 \tag{2.48}$$

The usual sigma coordinate is obtained as the special case

$$A_{k+1/2} = 0 \ , \ k = 0, 1, \ldots, NLEV \tag{2.49}$$

This form of hybrid coordinate has been chosen because it is particularly efficient from a computational viewpoint. It also allows a simple direct control over the "flattening" of coordinate surfaces as pressure decreases, since the $A's$ and $B's$ may be determined by specifying the distribution of half-level pressures for a typical sea-level surface pressure and for a surface pressure typical of the lowest expected to be attained in the model. Coordinate surfaces are surfaces of constant pressure at levels where $B_{k+1/2} = 0$.

The prognostic variables ξ, D, T and q_i are represented by their values at intermediate (full-level) pressures, p_k. Values for p_k are not explicitly required by the model's vertical finite-difference scheme, which is described in the following section, but they are required by parameterization schemes, in the creation of initial data, and in the interpolation to pressure levels that forms part of the post-processing. Alternative forms for p_k have been discussed by Simmons and Burridge (1981) and Simmons and Strüfing (1981). Little sensitivity has been found, and the simple form

$$p_k = \frac{1}{2}(p_{k+1/2} + p_{k-1/2}) \tag{2.50}$$

has been adopted, where half-level values are as given by 2.47. The explicit relationship between p and p_s defined for model half levels implicitly determines a vertical coordinate η. The model formulation is in fact such that this coordinate need not be known explicitly, as demonstrated in the following section. However, it is computationally convenient to define η for the radiative parameterization and for the vertical interpolation used in the post-processing. The half-level values are given by

$$\eta_{k+1/2} = \frac{A_{k+1/2}}{p_0} + B_{k+1/2} \tag{2.51}$$

where p_0 is constant pressure. From 2.47 it is seen that this coordinate is identical to the usual σ when $A_{k+1/2} = 0$, and in general equals σ when $p_0 = p_s \cdot \eta = p/p_0$ at levels where coordinate surfaces are surfaces of constant pressure. Values of η between half-levels are given by linear interpolation :

$$\eta = \eta_{k+1/2} + \frac{(p - p_{k+1/2})(\eta_{k+1/2} - \eta_{k-1/2})}{(p_{k+1/2} - p_{k-1/2})} \quad \text{for} \quad p_{k-1/2} \leq p \leq p_{k+1/2} \tag{2.52}$$

`ECHAM6` is used with 47 and 95 levels. Both vertical grids share the lowermost 12 layers as well as the uppermost layer centered at 1 Pa. The top-of-the-model pressure is 0 Pa, thus the whole atmospheric mass is in the model domain. The value of p_0 used for the definition of η is the reference sea-level pressure of 101325 Pa.

k	$A_{k+\frac{1}{2}}$ [Pa]	$B_{k+\frac{1}{2}}$	$A_{k+\frac{1}{2}}$ [Pa]	$B_{k+\frac{1}{2}}$
0	0.000000	0.0000000000	0.00000000	0.00000000
1	1.989185	0.0000000000	1.98918247	0.00000000
2	6.572090	0.0000000000	2.69261074	0.00000000
3	15.673903	0.0000000000	3.54616451	0.00000000
4	30.624279	0.0000000000	4.57676125	0.00000000
5	54.545720	0.0000000000	5.81494045	0.00000000
6	92.558830	0.0000000000	7.29508114	0.00000000
7	150.504697	0.0000000000	9.05558681	0.00000000
8	235.327458	0.0000000000	11.13899899	0.00000000
9	356.100259	0.0000000000	13.59204197	0.00000000
10	523.919524	0.0000000000	16.46557617	0.00000000
11	751.042942	0.0000000000	19.81443787	0.00000000
12	1051.137225	0.0000000000	23.69715881	0.00000000
13	1438.988411	0.0000000000	28.17553710	0.00000000
14	1930.177360	0.0000000000	33.31410217	0.00000000
15	2540.697000	0.0000000000	39.17933655	0.00000000
16	3286.553000	0.0000000000	45.83877563	0.00000000
17	4199.574000	0.0000000000	53.36004639	0.00000000
18	5303.957000	0.0000000000	61.84652710	0.00000000
19	6624.704000	0.0000000000	71.41293335	0.00000000
20	8187.185000	0.0000000000	82.18634033	0.00000000
21	9976.137000	0.0004000000	94.30740356	0.00000000
22	11820.540000	0.0029000000	107.93159485	0.00000000
23	13431.390000	0.0092000000	123.23060608	0.00000000
24	14736.360000	0.0203000000	140.39379883	0.00000000
25	15689.210000	0.0370000000	159.62977600	0.00000000
26	16266.610000	0.0595000000	181.16809082	0.00000000
27	16465.000000	0.0879000000	205.26101685	0.00000000
28	16297.620000	0.1220000000	232.18553162	0.00000000
29	15791.600000	0.1614000000	262.24536133	0.00000000
30	14985.270000	0.2057000000	295.77294922	0.00000000
31	13925.520000	0.2542000000	333.13256836	0.00000000

table to be continued . . .

k	$A_{k+\frac{1}{2}}$ $[Pa]$	$B_{k+\frac{1}{2}}$	$A_{k+\frac{1}{2}}$ $[Pa]$	$B_{k+\frac{1}{2}}$
32	12665.290000	0.3062000000	374.72143555	0.00000000
33	11261.230000	0.3611000000	420.97338867	0.00000000
34	9771.406000	0.4182000000	472.36132813	0.00000000
35	8253.211000	0.4767000000	529.40039063	0.00000000
36	6761.340000	0.5359000000	592.64990234	0.00000000
37	5345.914000	0.5951000000	662.71801758	0.00000000
38	4050.718000	0.6536000000	740.26416016	0.00000000
39	2911.569000	0.7106000000	826.00268555	0.00000000
40	1954.805000	0.7654000000	920.70605468	0.00000000
41	1195.890000	0.8172000000	1025.20947265	0.00000000
42	638.148900	0.8650000000	1140.41430664	0.00000000
43	271.626500	0.9077000000	1267.29199218	0.00000000
44	72.063600	0.9442000000	1406.88818359	0.00000000
45	0.000000	0.9730000000	1560.32666016	0.00000000
46	0.000000	0.9923000000	1728.81445313	0.00000000
47	0.000000	1.0000000000	1913.64550781	0.00000000
48			2116.40527343	0.00000000
49			2338.83251953	0.00000000
50			2582.83544922	0.00000000
51			2850.50659180	0.00000000
52			3144.14184570	0.00000000
53			3466.25976563	0.00000000
54			3819.62304688	0.00000000
55			4207.26171875	0.00000000
56			4632.50390625	0.00000000
57			5098.99218750	0.00000000
58			5610.73046875	0.00000000
59			6172.44531250	0.00000000
60			6789.26171875	0.00000000
61			7464.85546875	0.00000000
62			8205.07421875	0.00000000
63			9013.73437500	0.00004644
64			9876.25000000	0.00034244

table 2.2 to be continued . . .

k	$A_{k+\frac{1}{2}}$ [Pa]	$B_{k+\frac{1}{2}}$	$A_{k+\frac{1}{2}}$ [Pa]	$B_{k+\frac{1}{2}}$
65			10779.67968750	0.00110447
66			11698.04296875	0.00262147
67			12606.03906250	0.00530741
68			13479.76171875	0.00948636
69			14289.19140625	0.01555587
70			15005.62109375	0.02390020
71			15604.63671875	0.03493614
72			16062.08593750	0.04900495
73			16355.96484375	0.06649876
74			16464.95703125	0.08780068
75			16370.24609375	0.11324221
76			16058.29296875	0.14307529
77			15520.17968750	0.17757314
78			14753.79296875	0.21690041
79			13765.30859375	0.26105165
80			12573.00000000	0.30987769
81			11218.07421875	0.36276281
82			9756.42187500	0.41877347
83			8253.21093750	0.47670001
84			6761.33984375	0.53590000
85			5345.91406250	0.59509999
86			4050.71801758	0.65359998
87			2911.56909180	0.71060002
88			1954.80493164	0.76539999
89			1195.88989258	0.81720001
90			638.14892578	0.86500001
91			271.62646484	0.90770000
92			72.06359863	0.94419998
93			0.00000000	0.97299999
94			0.00000000	0.99229997
95			0.00000000	1.00000000

Table 2.2.: Vertical-coordinate parameters of the 47- and 95-layer `ECHAM6` model

The vertical finite-difference scheme

The vertical finite-difference scheme is a generalization to the hybrid coordinate with form 2.47 of the scheme adopted in the first operational ECMWF model (Burridge and Haseler, 1977), apart from a small modification concerned with the conservation of angular momentum. The generalized scheme has been discussed by Simmons and Burridge (1981) and Simmons and Strüfing (1981), and the presentation here is restricted to a prescription of the finite-difference forms of the various terms of the continuous equations that involve η.

The surface-pressure tendency

The finite-difference analogue of 2.10 is

$$\frac{\partial \ln p_s}{\partial t} = -\frac{1}{p_s} \sum_{k=1}^{NLEV} \nabla \cdot (\vec{v}_k \Delta p_k) \tag{2.53}$$

where the subscript k denotes a value for the k-th layer, and

$$\Delta p_k = p_{k+1/2} - p_{k-1/2} \tag{2.54}$$

From 2.47 we obtain

$$\frac{\partial \ln p_s}{\partial t} = -\sum_{k=1}^{NLEV} \left\{ \frac{1}{p_s} D_k \Delta p_k + (\vec{v}_k \cdot \nabla \ln p_s) \Delta B_k \right\} \tag{2.55}$$

where

$$\Delta B_k = B_{k+1/2} - B_{k-1/2} \tag{2.56}$$

The continuity equation

Equation 2.9 gives

$$\left(\dot{\eta} \frac{\partial p}{\partial \eta} \right)_{k+1/2} = -\frac{\partial p_{k+1/2}}{\partial t} - \sum_{j=1}^{k} \nabla \cdot (\vec{v}_j \Delta p_j) \tag{2.57}$$

and from 2.47

$$\left(\dot{\eta} \frac{\partial p}{\partial \eta} \right)_{k+1/2} = -p_s \left[B_{k+1/2} \frac{\partial \ln p_s}{\partial t} + \sum_{j=1}^{k} \left\{ \frac{1}{p_s} D_j \Delta p_j + (\vec{v}_j \cdot \nabla \ln p_s) \Delta B_j \right\} \right] \tag{2.58}$$

where $\frac{\partial \ln p_s}{\partial t}$ is given by 2.55.

Vertical advection

Given $\left(\dot{\eta}\frac{\partial p}{\partial \eta}\right)_{k+1/2}$ computed from 2.58, vertical advection of a variable is given by

$$\left(\dot{\eta}\frac{\partial X}{\partial \eta}\right)_k = \frac{1}{2\Delta p_k}\left\{\left(\dot{\eta}\frac{\partial p}{\partial \eta}\right)_{k+1/2}(X_{k+1} - X_k) + \left(\dot{\eta}\frac{\partial X}{\partial \eta}\right)_{k-1/2}\cdot(X_k - X_{k-1})\right\} \qquad (2.59)$$

This form ensures that there is no spurious source or sink of kinetic and potential energy due to the finite-difference representation of vertical advection.

The hydrostatic equation

The form chosen for the finite-difference analogue of 2.6 is

$$\Phi_{k+1/2} - \Phi_{k-1/2} = -R_d \cdot (T_v)_k \cdot \ln\left(\frac{p_{k+1/2}}{p_{k-1/2}}\right) \qquad (2.60)$$

which gives

$$\Phi_{k+1/2} = \Phi_S + \sum_{j=k+1}^{NLEV} R_d \cdot (T_v)_j \cdot \ln\left(\frac{p_{j+1/2}}{p_{j-1/2}}\right) \qquad (2.61)$$

Full level values of geopotential are given by

$$\Phi_k = \Phi_{k+1/2} + \alpha_k \cdot R_d \cdot (T_v)_k \;, \qquad (2.62)$$

where

$$\alpha_1 = \ln 2 \qquad (2.63)$$

and, for $k > 1$,

$$\alpha_k = 1 - \frac{p_{k-1/2}}{\Delta p_k}\cdot\ln\left(\frac{p_{k+1/2}}{p_{k-1/2}}\right) \qquad (2.64)$$

Reasons for this particular choice of the α_k are given below.

The pressure gradient term

It is shown by Simmons and Strüfing (1981) that if the geopotential is given by 2.62, the form

$$R_d \cdot (T_v \cdot \nabla \ln p)_k = \frac{R_d \cdot (T_v)_k}{\Delta p_k}\left\{\left(\ln\frac{p_{k+1/2}}{p_{k-1/2}}\right)\cdot\nabla p_{k-1/2} + \alpha_k \cdot \nabla(\Delta p_k)\right\} \qquad (2.65)$$

for the pressure-gradient term ensures no spurious source or sink of angular momentum due to vertical differencing. This expression is adopted in the model, but with the α_k given by 2.64 for all k. This ensures that the pressure-gradient term reduces to the familiar form $R_d(T_v)_k \nabla \ln p_s$ in the case of sigma coordinates, and the angular momentum conserving property of the scheme still holds in the case in which the first half-level below $p = 0$ is a surface of constant pressure. The choice $\alpha_1 = 1$ in the hydrostatic equation would have given angular momentum conservation in general, but a geopotential Φ_1 inappropriate to the pressure-level $p = p_1 = \Delta p/2$. If, alternatively, Φ_1 were to be interpreted not as a value for a particular level, but rather the mass-weighted layer-mean value, then the choice α_1 would be appropriate.

It is shown by Simmons and Chen (1991) that the form 2.65 can be significantly improved, with benefit particularly in regions of steep terrain, if T_v is replaced by its deviation from a reference state,

$$\tilde{T}_v = T_v - T_0 \left(\frac{p}{p_0} \right)^{\beta} \tag{2.66}$$

where $\beta = \gamma \cdot \frac{R_d}{g}$, $p_0 = 1013.25$ hPa, $T_0 = 288$ K and $\gamma = 6.5$ K/km. The reference temperature 2.66 is based on the tropospheric part of the ICAO (1964) standard atmosphere with a uniform lapse rate γ.

Using the form 2.47 for the half-level pressures 2.65 may be written

$$R_d \cdot (\tilde{T}_v \cdot \nabla \ln p)_k = \frac{R_d \cdot (\tilde{T}_v)_k}{\Delta p_k} \left\{ \Delta B_k + C_k \cdot \frac{1}{\Delta p_k} \cdot \left(\ln \frac{p_{k+1/2}}{p_{k-1/2}} \right) \right\} \nabla p_s \tag{2.67}$$

where

$$C_k = A_{k+1/2} \cdot B_{k-1/2} - A_{k-1/2} \cdot B_{k+1/2} \tag{2.68}$$

The modified form 2.67 finally requires a reformulation of the surface geopotential according to

$$\Phi_S = g \cdot z_S + \frac{R_d \cdot T_0}{\beta} \cdot \left(\frac{p_s}{p_0} \right)^{\beta} \tag{2.69}$$

Energy-conversion term

To obtain a form for the term $\kappa \cdot T_v \cdot \omega / (1 + (\delta - 1)q_v)$ in 2.3 we use 2.7 to write

$$\left(\frac{\kappa \cdot T_v \cdot \omega}{(1 + (\delta - 1)q_v)p} \right)_k = \frac{\kappa \cdot (T_v)_k}{1 + (\delta - 1)(q_v)_k} \left(\frac{\omega}{p} \right)_k \tag{2.70}$$

where

$$\left(\frac{\omega}{p} \right)_k = -\frac{1}{p} \int_0^{\eta_k} \nabla \cdot \left(\vec{v} \cdot \frac{\partial p}{\partial \eta} \right) d\eta + (\vec{v} \cdot \nabla \ln p)_k \tag{2.71}$$

An expression for $\left(\frac{\omega}{p}\right)_k$ is then determined by the requirement that the difference scheme conserves the total energy of the model atmosphere for adiabatic, frictionless motion. This is achieved by

- evaluating the first term on the right-hand side of 2.71 by

$$-\frac{1}{\Delta p_k}\left\{\left(\ln\frac{p_{k+1/2}}{p_{k-1/2}}\right)\cdot\sum_{k=1}^{k-1}\nabla\cdot(\vec{v}_j\cdot\Delta p_j)+\alpha_k\nabla\cdot(\vec{v}_k\cdot\Delta p_k)\right\} \qquad (2.72)$$

where the α_k are as given by 2.63 and 2.64, and as in 2.55 and 2.57

$$\nabla\cdot(\vec{v}_k\cdot\Delta p_k)=D_k\cdot\Delta p_k+p_s\cdot(\vec{v}_k\cdot\nabla\ln p_s)\cdot\Delta B_k \qquad (2.73)$$

- using the form of 2.67 to evaluate the second term on the right-hand side of 2.71

$$(\vec{v}\cdot\nabla\ln p)_k=\frac{p_s}{\Delta p_k}\cdot\left\{\Delta B_k+C_k\cdot\frac{1}{\Delta p_k}\cdot\left(\ln\frac{p_{k+1/2}}{p_{k-1/2}}\right)\right\}\cdot\vec{v}_k\cdot\nabla\ln p_s \qquad (2.74)$$

2.1.4. Time integration scheme

A semi-implicit time scheme is used for equations of divergence, temperature and surface pressure, based on the work of Robert et al. (1972). The growth of spurious computational modes is inhibited by a time filter (Asselin, 1972). In addition, a semi-implicit method for the zonal advection terms in the vorticity equation is used, following results obtained by Robert (1981, 1982). He showed that in a semi-implicit shallow water equation model the time-step criterion was determined by the explicit treatment of the vorticity equation. Facilities also exist for selective damping of short model scales to allow use of longer timesteps. These are incorporated within the horizontal diffusion. The semi-implicit schemes are formally given by:

$$\delta_t\xi \;=\; ZT-\frac{1}{2a}\beta_Z\frac{U_r(\mu)}{1-\mu^2}\frac{\partial\Delta_{tt}\xi}{\partial\lambda} \qquad (2.75)$$

$$\delta_t D \;=\; DT-\nabla^2 G-\frac{1}{2}\beta_{DT}\nabla^2\{\gamma\delta_{tt}T+R_d T_r\Delta_{tt}\ln p_s\} \qquad (2.76)$$

$$\delta_t T \;=\; TT-\frac{1}{2}\beta_{DT}\tau\Delta_{tt}D \qquad (2.77)$$

$$\delta_t\ln p_s \;=\; PT-\frac{1}{2}\beta_{DT}\nu\Delta_{tt}D \qquad (2.78)$$

Here the terms ZT, DT, G, TT and PT represent those on the right-hand sides of equations 2.15, 2.16, 2.3 and 2.10, apart from the diffusion terms, which are neglected here. Adiabatic components are evaluated at the current time, t, and parameterized components are generally evaluated using values of fields at the previous timestep, $t-\Delta t$.

The remaining terms on the right-hand sides of 2.75 - 2.78 are corrections associated with the semi-implicit time schemes, and are discussed in more detail below. The operators δ_t and Δ_{tt} are given by

$$\delta_t X = \frac{(X^+ - X_f^-)}{2\Delta t} \tag{2.79}$$

$$\Delta_{tt} X = X^+ + X_f^- - 2X \tag{2.80}$$

where X represents the value of a variable at time t, X^+ the value at time $t + \Delta t$, and X_f^- a filtered value at time $t - \Delta t$. A further operator that will be used is

$$\tilde{\Delta}_{tt} X = X_f^- - 2X \tag{2.81}$$

The time filtering is defined by

$$X_f = X + \epsilon_f(X_f^- - 2X + X^+) \tag{2.82}$$

and it is computationally convenient to split it into two parts;

$$\tilde{X}_f = X + \epsilon_f(X_f^- - 2X) \tag{2.83}$$

$$X_f = \tilde{X}_f + \epsilon_f X^+ \tag{2.84}$$

The timestep Δt depends on resolution, while $\epsilon_f = 0.1$ is independent of the resolution.

The semi-implicit treatment of vorticity

Referring to equation 2.75, an explicit treatment of the vorticity equation is obtained by setting $\beta_Z = 0$. Otherwise $\beta_Z = 1$ and $U_r(\mu)$ is a zonally-uniform reference zonal velocity, multiplied by $\cos\theta$. Terms describing advection by this reference velocity are represented implicitly by the arithmetic mean of values at times $t + \Delta t$ and $t - \Delta t$, while the remainder of the tendencies are represented explicitly by values at time t. $U_r(\mu)$ may vary in the vertical.

For the vorticity equation, 2.15 is used to write

$$ZT = \frac{1}{\alpha(1-\mu^2)}\frac{\partial(F_V + P_V)}{\partial\lambda} - \frac{1}{a}\frac{\partial(F_U + P_U)}{\partial\mu} \tag{2.85}$$

where the horizontal diffusion term has for convenience been neglected. Transforming into Fourier space gives:

$$\xi_m^+ = b_m(\mu) = \left[\left(\xi_f^- + \frac{2\,im\Delta t}{a(1-\mu^2)}(F_V + P_V)\right)_m - 2\,im\Delta t\alpha(\mu)\tilde{\Delta}_{tt}\xi_m - \frac{2\Delta t}{a}\frac{\partial(F_U + P_U)_m}{\partial\mu}\right] \tag{2.86}$$

The factor $b_m(\mu)$ renders the right-hand side of this equation unsuitable for direct integration by parts, but a suitable form is found from the relation

$$b_m(\mu)\frac{\partial(F_U + P_U)}{\partial\mu} = \frac{\partial\{b_m(\mu)(F_U + P_U)\}}{\partial\mu} - c_m(\mu)(F_U + P_U) \tag{2.87}$$

where

$$c_m(\mu) = \frac{\partial\{b_m(\mu)\}}{\partial\mu} \tag{2.88}$$

This gives

$$\xi_m^+ = \tilde{Z}_{\lambda m}(\mu) + \frac{\partial\tilde{Z}_{\mu m}(\mu)}{\partial\mu} \tag{2.89}$$

where

$$\tilde{Z}_{\lambda m}(\mu) = b_m(\mu)(\xi_f^-)_m + 2\Delta t\left(imb_m(\mu)\left[\frac{(F_V + P_V)_m}{a(1-\mu^2)} - \alpha(\mu)\tilde{\Delta}_{tt}\xi_m\right] + \frac{1}{a}c_m(\mu)(F_U + P_U)_m\right)$$

and

$$\tilde{Z}_{\lambda m}(\mu) = -\frac{2\Delta t}{a}b_m(\mu)(F_U + P_U)_m \tag{2.90}$$

New values $(\xi_n^m)^+$ are obtained from 2.89 by Gaussian quadrature, using integration by parts as illustrated by 2.39 and 2.45 for the continuous form of the equations.

$U_r(\mu)$ is the arithmetic mean of the maximum and minimum velocities multiplied by $cos\theta$, as computed for each latitude and model level at timestep $t - \Delta t$. Different values are thus used for different levels. In ECHAM5, $\beta_Z = 1$ is used.

The semi-implicit treatment of divergence, temperature and surface pressure

Referring to equations 2.76 - 2.78, an explicit treatment of the divergence, temperature and surface pressure equations is obtained by setting $\beta_{DT} = 0$. For $\beta_Z = 1$, the nature of the semi-implicit correction is such that gravity wave terms for small amplitude motion about a basic state with isothermal temperatue T_r and surface pressure p_r are treated implicitly by the arithmetic mean of values at times $t + \Delta t$ and $t - \Delta t$, while the remainder of tendencies are represented explicitly by values at time t. The choice of an isothermal reference temperature is governed by considerations of the stability of the semi-implicit time scheme (Simmons et al., 1978), while the appropriate choice of p_r for the hybrid vertical coordinate is discussed by Simmons and Burridge (1981) and Simmons and Strüfing (1981).

γ, τ and ν in equations 2.76 - 2.78 are operators obtained from linearizing the finite-difference forms specified in section 2.1.3 about the reference state $(T_r, \ p_r)$. Their definitions are

$$(\gamma T)_k = \alpha_k^r R_d T_k + \sum_{j=k+1}^{NLEV} R_d T_j \ln\left(\frac{p_{j+1/2}^r}{p_{j-1/2}^r}\right) \tag{2.91}$$

$$(\tau D)_k = \kappa T_r \left\{ \frac{1}{\Delta p_k^r} \ln\left(\frac{p_{j+1/2}^r}{p_{j-1/2}^r}\right) S_{k-1/2}^r + \alpha_k^r D_k \right\} \tag{2.92}$$

and

$$\nu D = \frac{S_{NLEV+1/2}^r}{p^r} \tag{2.93}$$

where

$$
\begin{aligned}
p_{k+1/2}^r &= A_{k+1/2} + p_r B_{k+1/2} \\
\Delta p_k^r &= p_{k+1/2}^r - p_{k-1/2}^r \\
S_{k+1/2}^r &= \sum_{j=1}^{k} D_j \Delta p_j^r
\end{aligned}
\tag{2.94}
$$

and the α_k^r are defined by 2.63 and 2.64 , but with half-level pressures replaced by reference values $p_{k+1/2}^r$.

Expanding 2.76 - 2.78 using 2.79 and 2.80, and writing l to denote $\ln p_S'$, we obtain

$$
\begin{aligned}
D^+ &= D_f^- + 2\Delta t(DT) - 2\Delta t\nabla^2\{G + \frac{\beta_{DT}}{2}[\gamma(T^+ + T_f^- - 2T) \\
&\quad + R_d T_r(l^+ + l_f^- - 2l)]\}
\end{aligned}
\tag{2.95}
$$

$$T^+ = T_1 - \Delta t\beta_{DT}\tau D^+ \tag{2.96}$$

and

$$l^+ = l_1 - \Delta t\beta_{DT}\nu D^+ \tag{2.97}$$

where

$$T_1 = T_f^- + 2\Delta t(TT) - \Delta t\beta_{DT}\tau\tilde{\Delta}_{tt}D \tag{2.98}$$

and

$$l_1 = l_f^- + 2\Delta t(PT) - \Delta t\beta_{DT}\nu\tilde{\Delta}_{tt}D \tag{2.99}$$

Substituting 2.96 and 2.97 into 2.95 then gives

$$(1 - \Gamma\nabla^2)D^+ = DT' \tag{2.100}$$

where

$$\begin{aligned}
\Gamma &= (\beta_{DT})^2(\Delta t)^2(\gamma\tau + R_d T_r \nu) & (2.101) \\
DT' &= D_f^- + 2\Delta t(DT) + \nabla^2 R = \tilde{D}_\lambda + \tilde{D}_\mu + \nabla^2 R & (2.102)
\end{aligned}$$

with

$$\begin{aligned}
\tilde{D}_\lambda &= D_f^- + \frac{2\Delta t}{a(1-\mu^2)}\frac{\partial(F_U + P_U)}{\partial\lambda} & (2.103) \\
\tilde{D}_\mu &= \frac{2\Delta t}{a}\frac{\partial(F_V + P_V)}{\partial\mu} & (2.104)
\end{aligned}$$

and

$$R = -2\Delta t\left\{G + \frac{B_{DT}}{2}(\gamma T_2 + R_d T_r l_2)\right\} \tag{2.105}$$

Here

$$\begin{aligned}
T_2 &= T_1 + T_f^- - 2T & (2.106) \\
l_2 &= l_1 + l_f^- - 2l & (2.107)
\end{aligned}$$

The sequence of these semi-implicit calculations in the model is thus as follows. The expressions 2.98, 2.99 and 2.105 - 2.107 are computed on the Gaussian grid to form the gridpoint values of R. The spectral expansion of DT' is then derived by Gaussian quadrature, using integration by parts as illustrated by 2.40 and 2.46 for the continuous form of the equations. Since

$$\{(1 - \Gamma\nabla^2)D^+\}_n^m = \left(1 + \frac{n(n+1)}{a^2}\Gamma\right)(D^+)_n^m, \tag{2.108}$$

the spectral coefficients of divergence at time $t + \Delta t$ are given from 2.40 by

$$(D^+)_n^m = \left(1 + \frac{n(n+1)}{a^2}\Gamma\right)^{-1}(DT')_n^m, \tag{2.109}$$

where this operation involves, for each (m, n), multiplication of the vector of $NLEV$ values of $(DT')_n^m$ by a pre-computed $NLEV \times NLEV$ matrix whose elements are independent of time and determined by writing the operators γ, τ and ν in matrix and vector form. Finally, 2.96 and 2.97 are applied in spectral space to compute spectral coefficients of T and $\ln p'_S$ at time $t + \Delta t$ in terms of the spectral coefficients of T_1 and l_1 (again determined by Gaussian quadrature) and those of D^+. In ECHAM5, $\beta_{DT} = 0.75$, $T_r = 300$ K and $p_r = 800$ hPa.

2.1.5. Nudging of dynamical variables

The general circulation model `ECHAM6` calculates the state of the atmosphere starting at certain initial conditions and integrating over time. The state of the atmosphere may be represented by a vector $\vec{\xi}_t$ at a time $t \in \mathbb{R}_+$ in a certain abstract space $\mathbb{S}$. The state vector moves with time in $\mathbb{S}$ and describes some trajectory. The trajectory $t \mapsto \vec{\xi}_t$ is unambiguously determined by the initial and boundary conditions, and the model equations. However, even if two initial states are very close to each other, the trajectories drift apart with time and their mutual distance becomes larger than any bound provided that we wait long enough. It is therefore impossible to simulate any real historical trajectory $t \mapsto \vec{\zeta}_t$ even if the initial state was set with all care because of the discretization errors in the model. We cannot even expect that the trajectories remain close to each other. If it is important for longer simulations to reproduce some real historical trajectory $t \mapsto \vec{\zeta}_t$ at least in its main characteristics, the "nudging" technique can help to achieve this goal. The idea is to use a relaxation mechanism that approaches the simulated trajectory $t \mapsto \vec{\xi}_t$ to a given trajectory $t \mapsto \vec{\zeta}_t$.

Let $F : \mathbb{S} \to \mathbb{S}$ describe the time evolution of $\vec{\xi}_t$ by the model equations without nudging:

$$\frac{d}{dt}\vec{\xi}_t = F(\vec{\xi}_t). \tag{2.110}$$

We add a relaxation term to this equation that approaches $\vec{\xi}_t$ to $\vec{\zeta}_t$. To this end, let $\boldsymbol{\kappa} : \mathbb{S} \to \mathbb{S}$ be a (diagonal) matrix of relaxation coefficients and set:

$$\frac{d}{dt}\vec{\xi}_t = F(\vec{\xi}_t) - \boldsymbol{\kappa}(\vec{\xi}_t - \vec{\zeta}_t) \tag{2.111}$$

If $\boldsymbol{\kappa}$ has small values, the "nudging term" $\boldsymbol{\kappa}(\vec{\xi}_t - \vec{\zeta}_t)$ does not influence $\frac{d}{dt}\vec{\xi}_t$, but it dominates $F(\vec{\xi}_t)$ for large values of $\boldsymbol{\kappa}$. Each matrix element of $\boldsymbol{\kappa}$ can be interpreted as the inverse of a corresponding relaxation time. Short relaxation times mean a dominant nudging term, at longer relaxation times, the influence of nudging is reduced.

`ECHAM6` provides two possibilities of solving differential equation (2.111): (i) an implicit method and (ii) an explicit method.

Implicit nudging

The discretization of equation (2.111) with respect to time for implicit nudging is the following:

$$\frac{\vec{\xi}_{t+\Delta t} - \vec{\xi}_t}{\Delta t} = F(\vec{\xi}_{t+\Delta t}) - \boldsymbol{\kappa}(\vec{\xi}_{t+\Delta t} - \vec{\zeta}_{t+\Delta t}) \tag{2.112}$$

In the above equation, Δt is the integration time step. Some authors like Krishnamurti et al. (1991) set $2\Delta t$ instead because the integration time step is two times longer than the time step in many time integration schemes.

Equation (2.112) could be solved using a similar procedure as it is implemented for the solution of equation (2.110) in `ECHAM6`. The implicit form of discretization of equation (2.110) can be

written as $(\vec{\xi}^*_{t+\Delta t} - \vec{\xi}_t)/\Delta t = F(\vec{\xi}^*_{t+\Delta t})$ describing the integration from a state $\vec{\xi}_t$ to a state $\vec{\xi}^*_{t+\Delta t}$ using the model equation (2.110) without nudging. On the other hand, we may approximate $F(\vec{\xi}_{t+\Delta t})$ in equation (2.112) by $F(\vec{\xi}^*_{t+\Delta t})$ and get

$$\vec{\xi}_{t+\Delta t} - \vec{\xi}^*_{t+\Delta t} = -\Delta t \boldsymbol{\kappa}(\vec{\xi}_{t+\Delta t} - \vec{\zeta}_{t+\Delta t})$$

Solving for $\vec{\xi}_{t+\Delta t}$ yields:

$$\vec{\xi}_{t+\Delta t} = (1 + \Delta t \boldsymbol{\kappa})^{-1}(\vec{\xi}^*_{t+\Delta t} + \Delta t \boldsymbol{\kappa} \vec{\zeta}_{t+\Delta t}) \tag{2.113}$$

or reformulated for any projection ξ, ζ on an arbitrary axis of $\mathbb{S}$ representing e.g. temperature or divergence of the wind field and τ being the corresponding relaxation time ($\boldsymbol{\kappa}$ diagonal):

$$\xi_{t+\Delta t} = \frac{\tau}{\tau + \Delta t}\xi^*_{t+\Delta t} + \frac{\Delta t}{\tau + \Delta t}\zeta_{t+\Delta t}. \tag{2.114}$$

The new $\xi_{t+\Delta t}$ is therefore a linear combination of the prediction $\xi^*_{t+\Delta t}$ calculated with "free" `ECHAM6` and the nudging data $\zeta_{t+\Delta t}$ at that time. For small relaxation times, we get

$$\lim_{\tau \to 0} \xi_{t+\Delta t} = \zeta_{t+\Delta t}. \tag{2.115}$$

This means that we simply replace the original prediction by the nudging data. For very large relaxation times, we get:

$$\lim_{\tau \to \infty} \xi_{t+\Delta t} = \lim_{\tau \to \infty} \frac{1}{1 + \Delta t/\tau}\xi^*_{t+\Delta t} = \xi^*_{t+\Delta t}. \tag{2.116}$$

This means that the original prediction of free `ECHAM6` is used and the nudging data do not have any influence on the trajectory $t \mapsto \vec{\xi}_t$.

Explicit nudging

The discretization of equation (2.111) with respect to time for explicit nudging is a bit different from its implicit form (2.112):

$$\frac{\vec{\xi}_{t+\Delta t} - \vec{\xi}_t}{\Delta t} = F(\vec{\xi}_t) - \boldsymbol{\kappa}(\vec{\xi}_t - \vec{\zeta}_t) \tag{2.117}$$

From this follows with $(\vec{\xi}^*_{t+\Delta t} - \vec{\xi}_t)/\Delta t = F(\vec{\xi}_t)$:

$$\vec{\xi}_{t+\Delta t} = \vec{\xi}^*_{t+\Delta t} - \Delta t \boldsymbol{\kappa}\left(\vec{\xi}_t - \vec{\zeta}_t\right)$$

For small $\Delta t \boldsymbol{\kappa}$ (small time steps compared to the relaxation times), one may approximate $\Delta t \boldsymbol{\kappa} \vec{\xi}_t$ by $\Delta t \boldsymbol{\kappa} \vec{\xi}^{\,*}_{t+\Delta t}$ leading to

$$\vec{\xi}_{t+\Delta t} = (1 - \Delta t \boldsymbol{\kappa}) \vec{\xi}^{\,*}_{t+\Delta t} + \Delta t \boldsymbol{\kappa} \vec{\zeta}_t \tag{2.118}$$

This means for any projection:

$$\xi_{t+\Delta t} = \left(1 - \frac{\Delta t}{\tau}\right) \xi^*_{t+\Delta t} + \frac{\Delta t}{\tau} \zeta_{t+\Delta t} \tag{2.119}$$

Very long relaxation times τ lead to the following limit:

$$\lim_{\tau \to \infty} \xi_{t+\Delta t} = \xi^*_{t+\Delta t} \tag{2.120}$$

We therefore just accept the original prediction of the time integration and ignore the nudging data. On the other hand, very short relaxation times show a wrong behaviour of equation (2.119):

$$\lim_{\tau \to 0} \xi_{t+\Delta t} = \xi^*_{t+\Delta t} + \left(\zeta_{t+\Delta t} - \xi^*_{t+\Delta t}\right) \lim_{\tau \to 0} \frac{\Delta t}{\tau} = \mathrm{sgn}\left(\zeta_{t+\Delta t} - \xi^*_{t+\Delta t}\right) \infty \tag{2.121}$$

In general, the nudging equations (2.114) or (2.119) are applied in spectral space to the logarithm of the surface pressure, the 3–d temperature, and 3–d vorticity and divergence of the wind field. For each model layer and variable, the relaxation time can be set individually. There is also a possibility to exclude spectral coefficients of certain order from the nudging procedure. In general, the nudging mechanism is often used to reproduce large scale dynamic phenomena as they are present in analysis data but the boundary layer dynamics and local convection and diffusion processes are intended to be treated by the parameterizations implemented in `ECHAM6`. In such cases, the boundary layer and higher order spectral coefficients should be excluded from nudging. For a more detailed discussion of the choice of relaxation times, see the article of Jeuken et al. (1996).

In early versions of the nudging procedure, it was possible to nudge the sea surface temperature also, but this leads to problems due to hysteresis effects.

2.2. Transport

The flux form semi-Lagrangian scheme employed in ECHAM6 for passive tracer transport has been introduced by Lin and Rood (1996). This type of advection scheme combines typical features of Eulerian, flux form schemes (i.e., exact mass conservation to machine precision) with the unconditional stability for all Courant numbers typical of standard (non conservative) semi-Lagrangian schemes. For Courant numbers smaller than one, the Lin-Rood schemes reverts to a multidimensional flux form scheme which takes properly into account transverse fluxes, such as those developed by Colella, LeVeque, Leonard and others (see references in Lin and Rood (1996)). In the constant velocity case at Courant number smaller than one, it is in fact identical with the Colella *Corner Transport Upwind* scheme. The scheme is described here for application to incompressible flows, its generalization to compressible fluids is described in Lin and Rood (1996).

Consider the conservative formulation of passive advection in an incompressible fluid

$$\frac{\partial Q}{\partial t} + \nabla \cdot (\mathbf{v}Q) = 0, \tag{2.122}$$

where Q is the tracer concentration and the continuity equation is given by

$$\nabla \cdot \mathbf{v} = 0. \tag{2.123}$$

It is to be remarked that there is an inherent coupling of (2.122) to the continuity equation, since in the case of constant tracer concentration (2.122) reduces to (2.123). This property should be also guaranteed by the discretization of (2.122).

Assuming a C-type grid staggering in which normal velocity components are defined at the grid sides and scalar quantities (to be interpreted as cell averages) are defined at the cell center, a flux form discretization of (2.122) is given by

$$Q_{i,j}^{n+1} = Q_{i,j}^n - \left(\mathcal{X}_{i+\frac{1}{2},j} - \mathcal{X}_{i-\frac{1}{2},j} \right) - \left(\mathcal{Y}_{i,j+\frac{1}{2}} - \mathcal{Y}_{i,j-\frac{1}{2}} \right) \tag{2.124}$$

where $\mathcal{X}_{i+\frac{1}{2},j} \mathcal{Y}_{i,j+\frac{1}{2}}$ and $\mathcal{X}_{i-\frac{1}{2},j} \mathcal{Y}_{i,j-\frac{1}{2}}$ are approximations of the Q fluxes in the E-W and N-S directions, respectively, integrated in time over the time step Δt. In order to achieve unconditional stability, in the Lin-Rood scheme the fluxes are computed as the sum of an *integer* and a *fractional* flux

$$\mathcal{X}_{i-\frac{1}{2},j} = \mathcal{X}_{i-\frac{1}{2},j}^{int} + \mathcal{X}_{i-\frac{1}{2},j}^{fr}.$$

The integer fluxes represent the contribution to the flux that arises in case of Courant numbers larger than one at the cell side $i - \frac{1}{2}$. More specifically, defining

$$C_{i-\frac{1}{2},j}^x = \frac{\Delta t u_{i-\frac{1}{2},j}^{n+\frac{1}{2}}}{\Delta x} = K_{i-\frac{1}{2},j}^x + c_{i-\frac{1}{2},j}^x$$

$$K_{i-\frac{1}{2},j}^x = INT(C_{i-\frac{1}{2},j}^x) \qquad I = INT(i - C_{i-\frac{1}{2},j}^x)$$

(where INT has the same meaning as the corresponding *Fortran95* intrinsic function) and assuming e.g. a positive velocity, the integer flux is defined as

$$\mathcal{X}^{int}_{i-\frac{1}{2},j} = \sum_{k=1}^{K^x_{i-\frac{1}{2},j}} Q^n_{i-k,j}.$$

Thus, the integer flux represents the mass transport through all the cells crossed completely by a Lagrangian trajectory ending at $(i - \frac{1}{2}, j)$ at timestep $n + 1$ during a time interval Δt.

The fractional flux is defined as the Van Leer flux

$$\mathcal{X}^{fr}_{i-\frac{1}{2},j} = c^x_{i-\frac{1}{2},j}\left[Q^g_{I,j} + \frac{Q^g_{I+1,j} - Q^g_{I-1,j}}{4}\Big(SIGN(1, c^x_{i-\frac{1}{2},j}) - c^x_{i-\frac{1}{2},j} \Big) \right] \tag{2.125}$$

where $SIGN$ has the same meaning as the corresponding *Fortran95* intrinsic function.

The intermediate value $Q^g_{i,j}$ used in the computation of the Van Leer flux can be interpreted as a first order finite difference approximation of

$$\frac{\partial Q}{\partial t} + v\frac{\partial Q}{\partial y} = 0,$$

advanced in time $\Delta t/2$ from timestep n along the Lagrangian trajectory ending at $(i - \frac{1}{2}, j)$ at timestep $n + 1$.

More precisely,

$$Q^g_{i,j} = \frac{\left(Q^n_{i,J} + Q^n_{i,j} \right)}{2} + \frac{|c^y_{i,j}|}{2}\left(Q^n_{i,J^*} - Q^n_{i,J} \right)$$

where

$$C^y_{i,j} = \frac{\Delta t}{2\Delta y}\left(v^{n+\frac{1}{2}}_{i,j-\frac{1}{2}} + v^{n+\frac{1}{2}}_{i,j+\frac{1}{2}} \right)$$

$$c^y_{i,j} = C^y_{i,j} - INT(C^y_{i,j}) \qquad J = j - INT(C^y_{i,j}) \qquad J^* = J - SIGN(1, C^y_{i,j}).$$

The Lin and Rood scheme satisfies some fundamental requirements for a tracer advection algorithm:

- mass conservation: by construction, since it is formulated in flux form;

- consistency with the discretization of the continuity equation: setting $q = 1$ yields a discretization of (2.123) by the same scheme,

- monotonicity of the 1D advection schemes: if a flux limiter is applied to the centered difference $Q^g_{I+1,j} - Q^g_{I-1,j}$ in (2.125) (see references in Lin and Rood (1996)), the one dimensional flux operators are guaranteed to be monotonic, although this in general does not ensure that the full multidimensional scheme is monotonic as well;

37

- preservation of linear tracer correlations: if q_1, q_2 are the concentrations of two different tracers such that $q_2^n = \alpha q_1^n + \beta$, with α, β two constants, then the values q_1^{n+1}, q_2^{n+1} obtained by time update with the Lin and Rood scheme still satisfy $q_2^{n+1} = \alpha q_1^{n+1} + \beta$.

2.3. Horizontal diffusion

Unlike the other physical parameterizations which are computed in grid point space, the horizontal diffusion can conveniently be formulated in spectral space. Moreover, the treatment of horizontal diffusion differs from that of the other processes in that it does not involve a physical model of subgrid-scale processes, but rather a numerically convenient form of scale selective diffusion with coefficients determined empirically to ensure a realistic behavior of the resolved scales. As in many other models, the horizontal diffusion tendency is expressed in the form of a hyper-Laplacian,

$$\frac{\partial \chi}{\partial t} = -(-1)^q K_\chi \nabla^{2q} \chi \tag{2.126}$$

where χ is vorticity, divergence or temperature (no horizontal diffusion is applied to water components or trace constituents), K_χ is a constant diffusion coefficient for the respective variable, and $q > 0$ is an integer. The time rate of change of spectral component χ_n is given by

$$\frac{\partial \chi_n}{\partial t} = -K_\chi \left\{ n(n+1)a^{-2} \right\}^q \chi_n \tag{2.127}$$

where a is the Earth's radius and n is wavenumber. For convenience, K_χ can be replaced by the e-folding damping time τ of the highest resolvable wavenumber n_0

$$\tau(n_0) \equiv \tau_0 = K_\chi^{-1} \left\{ n_0(n_0+1)a^{-2} \right\}^{-q} \tag{2.128}$$

so that (2.127) can be expressed in terms of the order of the scheme, $2q$, and damping time τ_0. The scale selectivity of the scheme increases with increasing q. Both damping time and order depend on the horizontal resolution. Furthermore, in order to avoid spurious wave reflection at the upper boundary of the model, the diffusion is enhanced in the upper layers by gradually decreasing the order of the scheme (Table 2.3).

Table 2.3.: Damping time τ_0 in hours (independent of model level) and order, $2q$, of horizontal diffusion scheme applied at different model levels

Level	T31 ($\tau_0 = 12$)	T63 ($\tau_0 = 7$)	T127 ($\tau_0 = 1.5$)	T255 ($\tau_0 = 0.5$)
version with 47 levels				
1–4	2	2	—	—
5–7	4	4	—	—
8–9	6	6	—	—
10–11	8	8	—	—
12–47	10	8	—	—
version with 95 levels				

Table 2.3.: `horizontal diffusion` — continued				
1–10	—	2	2	2
11–20	—	4	4	4
21–25	—	6	4	4
26–95	—	8	6	6

2.4. Radiative Transfer

Beginning with ECHAM 6.2 radiative transfer is computed using PSrad (Pincus and Stevens, 2013), a two-stream model that descends from the RRTMG codes (Mlawer et al., 1997; Iacono et al., 2008) developed by Atmospheric and Environmental Research (AER). Irradiances are computed separately for the longwave and shortwave portions of the spectrum. Scattering is neglected in longwave calculations and sources internal to the atmosphere are neglected in shortwave calculations, both of which simplify the resulting equation sets. Spectral discretization is determined by the "correlated-k" method used to treat absorption by gases, so that upward and downward irradiances are calculated over a predetermined number of pseudo-wavelengths denoted by $\tilde{\nu}_g$. Below we describe the correlated-k method and why it is adopted, the longwave and shortwave radiative transfer solvers, their required input data and how that is used to determine the radiative (or optical) properties of the atmosphere and surface, as well as details of the numerical implementation.

Below we adopt the radiance/irradiance terminology because it is shorter than referring to radiative intensity/flux. The radiance at a point is a function of the incident angle of the radiative beam passing through that point, the irradiance is the sum of all beams (integral over angles in the hemisphere) that pass through a unit area.

2.4.1. Spectral discretization: the correlated k method for gaseous absorption

The dynamical equations are sensitive to the divergence of broadband irradiances, with most of the radiant energy being carried in the wavelength interval ranging from 1 mm to 100 nm, and the break between the longwave and shortwave bands is roughly 4 microns. Formally the broadband irradiance is defined by the intergral of the irradiance spectral density over the wavelengths of interest, so that if one is interested in wavelenghts $\lambda_1 < \nu \leq \lambda_2$

$$I = \int_{\lambda_1}^{\lambda_2} I_\lambda \mathrm{d}\lambda.$$

This integral can be approximated by a sum over discrete frequencies, but because the spectral properties of the atmosphere vary strongly as a function of wavelength, with nearly singular line-like features at specific wavelengths, the required number of frequencies to well approximate the integral is prohibitively large given the balance between desired accuracy and computational resources.

To address this shortcoming the spectrum is divided into bands, and within a band the band-averaged irradiance is approximated by a sum over a discrete set of pseudo wavelengths, $\tilde{\lambda}_{b,g}$, where we have chosen b to index the band and g to index the pseudo wavelength for a particular band. Psuedo wavelengths are defined by discretizing the distribution of the absorption features, $g_b(k)$, within a band, where here k denotes the magnitude of the absorption. This method effectively defines pseudo-absorbers that represent the collective effects of different absorbers discretized on the basis of their absorption strength rather than on their basis of the frequency at which they absorb. The method assumes that through the column over which the radiative transfer is performed the distributions are correlated, so that wavelengths which are strongly absorbing are strongly absorbing throughout the entire column — hence the correlated k nomenclature. The correlation requirement can be better satisfied by adopting a band structure that isolates particular absorption features. Because the discretization is based on the distribution of absorption strengths within a band $k(g_b)$, which is inverted

λ_b^{-1} $[cm^{-1}]$	b	N_b	Absorbers $p > 100$ hPa	$p < 100$ hPa
10-250	1	8	H_2O, SC, FC	H_2O, FC
250-500	2	14	H_2O, SC, FC	H_2O, FC
500-630	3	16	H_2O, CO_2, N_2O, SC, FC	H_2O, CO_2, N_2O, FC
630-700	4	14	H_2O, CO_2, SC	O_3, CO_2
700-820	5	16	H_2O, CO_2, SC	O_3, CO_2
820-980	6	8	H_2O, CO_2, CFC11, CFC12, SC	CFC11, CFC12
980-1080	7	12	H_2O, O_3, CO_2, SC	O_3, CO_2
1080-1180	8	8	H_2O, CFC12, CFC22, CO_2, N_2O, SC	O_3, CFC12, CFC22, CO_2, N_2O
1180-1390	9	12	H_2O, CH_4, N_2O, SC	CH_4
1390-1480	10	6	H_2O	H_2O
1480-1800	11	8	H_2O, SC	H_2O
1800-2080	12	8	H_2O, CO_2, SC	-
2080-2250	13	4	H_2O, N_2O, SC	-
2250-2380	14	2	CO_2, SC	CO_2
2380-2600	15	2	N_2O, CO_2, SC	-
2600-3000	16	2	H_2O, CH_4, SC	-

Table 2.4.: Band structure for longwave radiative transfer: Wavenumbers in band, band number, number of g points in each band, gaseous absorbers used in high and low pressure regions of the atmosphere, SC and FC denote the self and foreign continuum

cumulative distribution function, it is smoother than the absorption spectrum $k(\lambda)$ and can be approximated by a smaller number of discrete terms. Thus it is computationally more efficient. Because the discretisation is over the cumulative distribution, $g(k)$, as a function of absorption one often speaks of the radiative transfer being calculated over g-points, what we call pseudo-wavelengths, $\tilde{\lambda}_{b,g}$, above.

Thus in the correlated k-method the integrated irradiance, I_b, in some band, b, is approximated by the sum, such that

$$I_b = \sum_{g=1,N_b} w_{b,g} I_{b,g} \quad \text{where} \quad \sum_{g=1,n_{g,b}} w_{b,g} = 1. \qquad (2.129)$$

The weights, $w_{b,g}$ are chosen based on the relative contribution of each pseudo frequency to the broadband irradiance.

The band structure used by the RRTMG k-distribution (and by PSrad, which adopts this distribution directly) is given in Table 2.4 and 2.5 for the long and shortwave spectral regions respectively. Overall the method requires calculation at 140 g-points in the longwave, and 112 g-points in the shortwave. Note that band 29, which is treated by the shortwave solver, is out of sequence (having smaller wavenumbers than band 28), this arises because it was added later to treat the contribution from the solar source in the regions covered by bands 6-15 in the longwave.

λ_b^{-1}	b	N_b	Absorbers	
$[cm^{-1}]$			$p > 100$ hPa	$p < 100$ hPa
820- 2600	29	12	H_2O, CO_2, SC, FC	H_2O, CO_2
2600- 3250	16	6	H_2O, CH_4, SC, FC	CH_4
3250- 4000	17	12	H_2O, CO_2, SC, FC	H_2O, CO_2
4000- 4650	18	8	H_2O, CH_4, SC, FC	CH_4
4650- 5150	19	8	H_2O, CO_2, SC, FC	CO_2
5150- 6150	20	10	H_2O , SC, FC	H_2O
6150- 7700	21	10	H_2O, CO_2, SC, FC	H_2O, CO_2
7700- 8050	22	2	H_2O, O_2, SC, FC	O_2
8050-12850	23	10	H_2O , SC, FC	-
12850-16000	24	8	H_2O, O_2, O_3, SC, FC	O_2, O_3
16000-22650	25	6	H_2O, O_3	O_3
22650-29000	26	6	-	-
29000-38000	27	8	O_3	O_3
38000-50000	28	6	O_2, O_3	O_2, O_3

Table 2.5.: Band structure for shortwave radiative transfer: Wavenumbers in band, band number, number of g points in each band, gaseous absorbers used in high and low pressure regions of the atmosphere, SC and FC denote the self and foreign continuum

2.4.2. Shortwave

In the shortwave part of the spectrum, where sunlight is the external source of radiation and internal sources are negligible the equations for two stream radiative transfer is written as

$$\frac{\mathrm{d}I^\uparrow}{\mathrm{d}\tau} = \alpha I^\uparrow - \beta I^\downarrow - \gamma^\uparrow \frac{S}{\mu_0} \tag{2.130}$$

$$\frac{\mathrm{d}I^\downarrow}{\mathrm{d}\tau} = \beta I^\uparrow - \alpha I^\downarrow + \gamma^\downarrow \frac{S}{\mu_0} \tag{2.131}$$

$$\frac{\mathrm{d}S}{\mathrm{d}\tau} = -\frac{S}{\mu_0}. \tag{2.132}$$

These equations describes the changes in direct (collimated) solar radiation S and in the diffuse upward and downward irradiances $I^\uparrow$ and $I^\downarrow$ as a function of the optically-relevant vertical coordinate optical depth (τ). The factors α, β and $\gamma^{\uparrow,\downarrow}$ parameterize how the scattering effects diffuse irradiance, and are functions the optical properties of the atmosphere (single scattering albedo $\tilde{\omega}$ and asymmetry factor g, not to be confused with the cumulative distribution function for the absorption) as well as the solar zenith angle μ_0.

The relative sizes of cloud drops and the wavelengths of solar radiation mean that diffraction causes much of the light that interacts with clouds to be scattered almost directly forward. In ECHAM, as in most applications, the optical properties of the atmosphere are "delta-scaled" to remove this contribution. (Delta-scaling dates to Fritz (1954) and became widespread with the introduction of the delta-Eddington approximation of Joseph et al. (1976)). Delta-scaling

replaces the original optical properties τ, $\tilde{\omega}$, and g with their scaled counterparts:

$$
\begin{aligned}
\tau_\delta &= (1 - \tilde{\omega} f)\tau \\
\tilde{\omega}_\delta &= \tilde{\omega}(1 - f)/(1 - \tilde{\omega} f) \\
g_\delta &= (g - f)/(1 - f)
\end{aligned}
\tag{2.133}
$$

where the forward scattering fraction f is often defined as $f \equiv g^2$. Rescaling distorts the partitioning of the downward irradiance between the direct and the diffuse beam, it leads to a good representation of the total irradiance. To the extent that a more accurate representation of the diffuse irradiance is desired it can be estimated by rescaling the direct irradiance and subtracting this from the net.

The two stream equations (2.130) are general (e.g., Meador and Weaver, 1980) but the precise values of the coefficients depend on which particular flavor of two stream algorithm one adopts. PSrad follows RRTMG in adopting the practical improved flux method (PIFM) developed by Zdunkowski et al. (1980), for which

$$
f = g^2 \quad \text{and} \quad \beta = \tilde{\omega}\frac{3(1 - g)}{4}
\tag{2.134}
$$

and

$$
\begin{aligned}
\alpha &= \beta + 2(1 - \tilde{\omega}) \tag{2.135} \\
\gamma^\uparrow &= \beta\left(\frac{2}{3}(1 + g) - \mu_0\right) \tag{2.136} \\
\gamma^\downarrow &= \beta\left(\frac{2}{3}(1 + g) + \mu_0\right) \tag{2.137}
\end{aligned}
$$

To close the mathematical description one must specify at the (total) radiative properties of the atmosphere (in ECHAM, this includes contributions from gases, clouds, and aerosols), the cosine of the solar zenith angle, and boundary conditions (the top-of-atmosphere incident solar radiation and the surface albedos for direct and diffuse radiation). This description must be determined for each spectral quadrature point. The two stream equations then provide the reflectance and transmittance for direct (collimated) radiation (R_i, T_i) and diffuse radiation (r_i, t_i) for each layer i.

The two stream equations are solved by specifying a transfer matrix which expresses the transmission and reflectance of diffuse and direct radiation across or from any set of contiguous levels. The total upward and downward irradiance at any level can then be expressed directly as a function of the reflectance and transmission coefficients for the contiguous layers above and below. Following Oreopoulos and Barker (1999)

$$
I_i^\uparrow = \mu_0 S \left\{ \frac{T_{1,i-1}^{\mathrm{dir}} R_{i,N} + \left[T_{1,i-1} - T_{1,i-1}^{\mathrm{dir}}\right] r_{i,n}}{1 - r_{i-1,1} r_{i,N}} \right\}
\tag{2.138}
$$

$$
I_i^\downarrow = \mu_0 S \left\{ T_{1,i-1}^{\mathrm{dir}} + \frac{T_{1,i-1}^{\mathrm{dir}} R_{i,N} r_{1,i-1} + \left[T_{1,i-1} - T_{1,i-1}^{\mathrm{dir}}\right]}{1 - r_{i-1,1} r_{i,N}} \right\},
\tag{2.139}
$$

where $i = 1, 2, \ldots, N$ with $i = 1$ denoting the upper most level. The reflectance and transmission of the direct beam are given recursively. Generalizing from the two layer system presented

by Oreopoulos and Barker (1999) results in the following equations for the transmittance and reflectance with $R_j \equiv R_{j,j}$, $T_j \equiv T_{j,j}$, $r_j \equiv r_{j,j}$, and $t_j \equiv t_{j,j}$:

$$T_{1,i-1} = T_{1,i-2}^{\text{dir}} T_{i-1} + \frac{t_{i-1}\left\{\left[T_{1,i-2} - T_{1,i-2}^{\text{dir}}\right] + T_{1,i-2}^{\text{dir}} R_{i-1} r_{1,i-2}\right\}}{1 - r_{1,i-2} r_{i-1}} \quad (2.140)$$

$$R_{i,N} = R_{i,N-1} + \frac{t_{1,N-1}\left\{\left[T_{i,N-1} - T_{i,N-1}^{\text{dir}}\right] r_N + T_{i,N-1}^{\text{dir}} R_N\right\}}{1 - r_{i,N-1} r_N} \quad (2.141)$$

with

$$T_{1,i-1}^{\text{dir}} = \prod_{j=1}^{i-1} \exp\left(\frac{-\tau_j'}{\mu_0}\right), \quad (2.142)$$

denoting the transmission of the direct beam only. Here a single subscript indicates the reflectance or transmittance of a single layer and two subscripts the cumulative property of all layers between the two index values. The total transmission and reflectance of the direct beam also depends on the transmission and reflectance of the diffuse irradiance, which is given for a composite layer as follows:

$$t_{i,N-1} = \frac{t_{i,N-2} t_{N-1}}{1 - r_{i,N-2} r_{N-1}}, \quad \text{and} \quad r_{1,i-1} = r_{1,i-2} + \frac{t_{1,i-2}^2 r_{i-1}}{1 - r_{1,i-2} r_{i-1}}. \quad (2.143)$$

Thus given input data the bulk of the radiative solver is spent working upward and downward through all the layers to compute the reflectance and transmission coefficients for each contiguous block of layers that is bounded either by the top of the atmosphere above, or the surface below. Because these transmission and reflectance coefficients depend on the radiative properties of the atmosphere, they must be computed for each of the g-points, which corresponds to 112 calls to the RRTMG shortwave solver.

Zenith Angle Correction

The actual shortwave computation is based on an effective solar zenith angle $\theta_{0,\text{eff}} = \arccos(\mu_{0,\text{eff}})$ which accounts for curvature of the atmosphere and its effect on the length of the optical path of the direct solar beam with respect to a plane parallel atmosphere following Paltridge and Platt (1976). Altitude dependencies as well as refraction are disregarded. This correction is given as

$$\mu_{0,\text{eff}} = \frac{0.001277}{\sqrt{\mu_0^2 + 0.001277 \cdot (2 + 0.001277)} - \mu_0} \quad (2.144)$$

where the numerical factor is the ratio of scale height of the atmosphere and the mean radius of the earth. The correction provided by $\mu_{0,\text{eff}}$ is such that the effective solar zenith angle remains lower than $88.56°$, so that the shortwave transfer calculation has a minimum irradiation of 2.5% of I_0, except for the variation due to the sun Earth distance. At zero solar zenith angle $\mu_{0,\text{eff}}$ is identical to μ_0.

2.4.3. Longwave radiation

The treatment of radiative transfer by the longwave solver differs from that in the shortwave by the presence of diffusive sources within the atmosphere, the replacement of the direct

external source (the solar beam) with a diffuse external source (Earth's surface). Scattering is neglected, which considerably simplifies the radiative transfer so that for each layer the broadband radiance within a wavelength interval is

$$R = \int_{\lambda_1}^{\lambda_2} d\lambda \left\{ R_0(\lambda) + \int_{t_v}^{1} (B(\lambda, T(t'_\lambda)) - R_0(\lambda)) \, dt' \right\}, \qquad (2.145)$$

where $R_0(\lambda)$ is the radiance entering the layer and $B(\lambda, T(t'_\lambda))$ is the Planck function for the temperature, T, at a point along the optical path. Transmittance, t is used as the coordinate along the path and depends on λ.

In the correlated-k method adopted by RRTMG the integral over wavenumbers is replaced by an integration over the cumulative distribution function, such that the integral for the broadband radiance can be more efficiently replaced by a sum, such that

$$R = \sum_j w_j \cdot \left\{ B_{\text{eff},j} + (R_{0,j} - B_{\text{eff},j}) \cdot \exp(-k_j \cdot \frac{\rho \delta z}{\cos \phi}) \right\}, \quad \text{where} \quad \sum_j w_j = \lambda_2 - \lambda_1. \;\; (2.146)$$

where $B_{\text{eff},j} = B_{\text{eff}}(g, T_g)$ is an effective Planck function valid for the group of wavenumbers described by a given g, and is allowed to vary linearly with the layer's transmittance so as to maintain continuity of the flux across layer boundaries, the absorption coefficient for a given g-point, $k_j = k(g, p, T)$ is dependent on the ambient conditions. The diffusivity factor r is the secant of ϕ. For bands, 1, 4 and 10-16 the standard diffusivity approximation, with $r = 1.66$ is employed. For the remaining bands r varies with the diffusivity as a function of the water vapor path, Υ, such that

$$r = \max\left[1.5, \min\left[1.8, a_0 + a_1 \exp\left(a_w \Upsilon\right)\right]\right] \qquad (2.147)$$

with constants a_i dependent on band.

2.4.4. Radiative Properties

To perform the radiative transfer calcuations the radiative properties of the atmosphere must be known. These can be derived given knowledge of the atmospheric state and composition. The state is determined by the humidity and the temperature of the atmosphere, the composition requires a specification of the amount of radiatively active gases, aerosol particles, cloud liquid and ice. Precipitating liquid and ice does not presently contribute to the radiative transfer.

2.4.5. Treatment of partial cloudiness

Two-stream theory is based on the assumption of a homogeneous atmosphere, but columns within ECHAM6 may contain significant internal variability through the presence of partly cloudy layers.

Partly-cloudy layers require the specification of an "overlap assumption" describing the vertical structure of cloudiness – essentially a prescription as to whether clouds in a given layer lie directly beneath clouds above them or not. ECHAM6 uses the "maximum-random" overlap assumption of Geleyn and Hollingsworth (1979), in maximum overlap is applied contiguous

partly-cloudy layers and random overlap applied when partly-cloudy layers are separated by clear skies.

If only a single layer within a column were partly cloudy one could compute irradiance for clear- and cloudy-skies and weight the result by the cloud fraction. This solution quickly becomes impractical when $n > 1$ layers are partly cloudy, since the number of possible combinations of cloud and clear sky increases as $n! + 2$. Fully sampling the configuration space would make the treatment of radiative transfer in inhomogeneous atmospheres prohibitively expensive.

PSrad treats cloud overlap using the Monte Carlo Independent Column Approximation (McICA, see Pincus et al., 2003). Discrete samples are constructed, some of which contain cloud and some not, such that a large ensemble reproduces the distribution of cloud fraction at each model level and the overlap assumption being applied. One random sample is constructed for each pseudo-wavelength and spectral integration proceeds as usual. The result is that in- dividual calculations contain unbiased estimates of the all-sky irradiance with random noise superimposed.

Care must be taken in the generation of random samples for McICA so that results do not depend on the assignment of columns to processors, to the time since the last restart, etc. To this end a high-quality random number generator is seeded at the beginning of each radiation calculation using model time and absolute geographic location.

2.4.6. Implementation and Numerical Aspects

For efficiency reasons the radiative transfer computation in ECHAM6 is called less frequently than the dynamics and other parameterizations. Typically the radiation time step Δt_rad is set to 2 hours. At each radiation time step t_rad the transfer calculation is executed at all grid points of the Gaussian grid used in the GCM. At each grid point the scheme provides profiles of the net radiative irradiances I_SW and I_LW in the shortwave and longwave spectrum, respectively, based on the profiles of absorber mixing ratios q_i and temperature T at the previous time step $t_\text{rad} - \Delta t$. For the shortwave computation the radiative transfer calculation uses the effective solar zenith angle $\vartheta_{0,eff}$ at time $t_\text{rad} + \Delta t_\text{rad}/2$, i.e. halfway across the following radiation time interval, which includes a correction for high zenith angles that maintains a minimal irradiation for zenith angles exceeding $90°$. This correction is necessary to provide non-zero irradiances in areas which are crossed by the day/night terminator during the radiation time interval.

$$I_\text{LW}(t_\text{rad}) = I_\text{LW}(q_i(t_\text{rad} - \Delta t), T(t_\text{rad} - \Delta t)) \tag{2.148}$$

$$I_\text{SW}(t_\text{rad}) = I_\text{SW}(q_i(t_\text{rad} - \Delta t), T(t_\text{rad} - \Delta t), \vartheta_{0eff}(t_\text{rad} + \Delta t_\text{rad}/2)) \tag{2.149}$$

The resulting longwave irradiances are kept constant over the whole radiation time interval, while the shortwave irradiances are corrected for the local change in solar irradiation at the top of the atmosphere within the radiation time interval. The computation of the current shortwave irradiance is based on the local zenith angle at time t with a cut-off at $90°$ zenith angle, $\vartheta_{0,\text{eff}}$.

$$I_\text{LW}(t_\text{rad} \leq t < t_\text{rad} + \Delta t_\text{rad}) = I_\text{LW}(t_\text{rad}) \tag{2.150}$$

$$I_{\mathrm{SW}}(t_{\mathrm{rad}} \leq t < t_{\mathrm{rad}} + \Delta t_{\mathrm{rad}}) = I_{\mathrm{SW}}(t_{\mathrm{rad}}) \cdot \frac{F_0(t\vartheta_0)}{F_0(\vartheta_{0,\mathrm{eff}})} \qquad (2.151)$$

PSrad also implements the capability of using predetermined subsets of spectral quadrature points as a proxy for broadband calculations following Pincus and Stevens (2013). When this choice is invoked the frequency of radiation calculations should match (or be a small multiple of) the "physics time step."

The heating rate Q_{rad} in a cell is computed from the difference of the total net irradiance $F_{\mathrm{rad}} = I_{\mathrm{LW}} + I_{\mathrm{SW}}$ at the lower and upper boundary of a cell, and the heat capacity C_p of moist air[1]. The mass of air is derived from the pressure difference between the lower and upper boundary of a cell, making use of the hydrostatic assumption.

---

[1]Within the radiation time interval the longwave cooling $Q_{\mathrm{LW}}(t)$ in a cell of constant mass may vary slightly due to the time dependence of the water vapour mixing ratio $q_{\mathrm{v}}(t)$. In dry air, as for instance above the troposphere, $Q_{\mathrm{LW}}(t)$ is essentially constant over the radiation time interval.

2.5. Turbulent transport and surface fluxes

Mixing by unresolved small-scale turbulent eddies causes exchange of momentum and scalar quantities between the atmosphere, ocean and land, and within the interior of the atmosphere and oceans. The purpose of a turbulence closure scheme is to parameterize these turbulent fluxes in the atmosphere. ECHAM applies a turbulent kinetic energy (TKE) scheme modified from that described by Brinkop and Roeckner (1995). The scheme applies Reynolds averaging, whereby the full flow is separated into a resolved mean-flow part, and unresolved turbulent fluctuations. Relative to the second-order closure schemes presented by Mellor and Yamada (1974), the current implementation applies empirical stability functions, rather than solving all ten budget equations for the second-order moments, applies a simple mixing-length scale, and the scheme neglects advection of TKE by the resolved flow. Generally, the tendency of a prognostic variable, ψ, due to turbulent motion is then:

$$\left(\frac{\partial \psi}{\partial t}\right)_{\text{turb}} = -\frac{\partial \overline{w'\psi'}}{\partial z}, \tag{2.152}$$

where w is the vertical velocity, primes denote turbulent fluctuations, and the overbar indicates Reynolds averaging.

It is the purpose of the turbulence closure scheme to diagnose, or predict, the vertical profile of the turbulent fluxes as a function of the model mean state. The scheme is formulated separately for mixing internally in the atmosphere and for the exchange with the surface. Between atmospheric model levels fluxes are assumed to have the form:

$$\overline{w'\psi'} = -K_\psi \frac{\partial \psi}{\partial z}, \tag{2.153}$$

while at the surface fluxes are assumed to have the form:

$$\overline{w'\psi'}_{\text{sfc}} = -C_\psi |\vec{V}| (\psi_{\text{nlev}} - \psi_{\text{sfc}}), \tag{2.154}$$

where K_ψ is the diffusion coefficient and C_ψ is the bulk exchange coefficient, both with respect to ψ, while nlev indicates lowest model level, and sfc surface quantities, respectively. $|\vec{V}|$ is the absolute value of the difference between the surface velocity and the wind velocity at the lowest model level. At the top of the atmosphere (TOA) the turbulent fluxes are further assumed to vanish:

$$\overline{w'\psi'}_{\text{TOA}} = 0. \tag{2.155}$$

Below we explain how K_ψ and C_ψ are determined.

2.5.1. Conservative variables and definitions

Vertical turbulent mixing is done on the six prognostic variables temperature (T), zonal and meridional winds (u, v), specific humidity (q_v), cloud liquid water content (q_l), cloud ice water content (q_i), as well as any tracers that may be defined. To account for dry adiabatic expansion, the mixing of temperature is done on the dry static energy, which is the sum of the specific enthalpy and the geopotential energy:

$$h = c_p T + gz, \tag{2.156}$$

where g is gravity and z is height. In many ways, mixing h is equivalent to mixing potential temperature, which is more common. These variables are conserved during dry adiabatic processes. Quantities used in this chapter are:

Potential temperature:	θ	$=$	$T\left(\frac{p_{00}}{p}\right)^{\frac{R_d}{c_{pd}}}$
Reference pressure:	p_{00}	$=$	10^5 Pa
Constant:	ϵ	$=$	$R_v/R_d - 1$
Virtual potential temperature:	θ_v	$=$	$\theta\left[1 + \epsilon q_v - q_l - q_i\right]$
Liquid water potential temperature:	θ_l	$=$	$\theta\left[1 - \frac{L}{c_{pd}T}\left(q_l + q_i\right)\right]$
Virtual dry static energy:	h_v	$=$	$gz + c_pT\left[1 + \left(\frac{c_{pv}}{c_{pd}} - 1\right)q_v\right]$
Total water content:	q_t	$=$	$q_v + q_l + q_i$
Surface friction velocity:	u_*	$=$	$\left[\left(\overline{w'u'}\right)^2_{\text{sfc}} + \left(\overline{w'v'}\right)^2_{\text{sfc}}\right]^{1/4}$
Convective velocity scale:	w^*	$=$	$\left[gz_{\text{pbl}}(\overline{w'\theta_v'})_{\text{sfc}}/\bar{\theta}_v\right]^{1/3}$
Monin-Obukhov length scale:	L	$=$	$-u_*^3\bar{\theta}_v/\left[\kappa g\left(\overline{w'\theta_v'}\right)_{\text{sfc}}\right]$
von Karmans constant:	κ	$=$	0.4
Boundary layer height:	z_{pbl}		
Gravity:	g		

2.5.2. TKE closure model

In the atmosphere, away from the surface, the turbulent closure model assumes that the turbulent viscosity and diffusivities have the form:

$$K_\psi = l\, S_\psi\, \sqrt{E}, \tag{2.157}$$

where l is the turbulent mixing-length, S_ψ is a stability function and $E = \overline{u'u'} + \overline{v'v'} + \overline{w'w'}$ is the turbulent kinetic energy. E is predicted by solving a simplified version of the TKE-budget equation:

$$\frac{\partial E}{\partial t} = -\overline{w'u'}\frac{\partial u}{\partial z} - \overline{w'v'}\frac{\partial v}{\partial z} + \frac{g}{\theta_v}\overline{w'\theta_v'} - \delta - \frac{\partial \overline{w'E'}}{\partial z}, \tag{2.158}$$

where the first two terms on the right-hand-side are shear production terms, the third is the buoyancy term, δ is dissipation of E by molecular viscosity and the last term is the third-order vertical turbulent transport of E. To solve the prognostic TKE-equation (2.158) it is necessary to make a series of closure assumptions and characterize the stability of the flow, here using the moist Richardson number.

Moist Richardson number

It is assumed that the stability of the turbulent flow is characterized by the non-dimensional local gradient Richardson number, Ri, which is formally defined as the ratio of the static

stability to the shear:

$$Ri = \frac{N^2}{S^2},$$ (2.159)

where N is the Brunt-Väisälä frequency and S is the mean-flow vertical shear. The Brunt-Väisälä frequency depends on whether the flow is in clear or cloudy skies, so to approximate the grid-scale flow stability, a so-called moist Ri is defined:

$$Ri = \frac{\frac{g}{\theta_v}\left(A\frac{\partial\theta_l}{\partial z} + \theta D\frac{\partial q_t}{\partial z}\right)}{\left(\frac{\partial u}{\partial z}\right)^2 + \left(\frac{\partial v}{\partial z}\right)^2},$$ (2.160)

where:

$$A = \begin{cases} 1 + \epsilon q, & \text{in clear-sky} \\[2em] 1 + \epsilon q_t - \frac{L\,q_s}{R_v T} \cdot \frac{\left(\frac{L}{c_{pd}T}\left(1 + \epsilon q_t\right) - \frac{R_v}{R_d}\right)}{\left(1 + \frac{L^2 q_s}{R_v c_{pd} T^2}\right)}, & \text{in cloud} \end{cases}$$ (2.161)

$$D = \begin{cases} \epsilon, & \text{in clear-sky} \\ \frac{L}{c_p T}A - 1, & \text{in cloud} \end{cases}$$ (2.162)

For each grid cell, A and D are first computed for the cloudy and clear-sky parts separately. The grid-cell mean is derived using the cloud fraction as the weighting factor and then used in Equation (2.160).

Turbulent mixing length

The turbulence mixing length used in Equation (2.153) is computed as in Blackadar (1962):

$$l = \frac{\kappa z}{1 + \kappa z/\lambda}$$ (2.163)

in which κ is the von Karman constant ($\kappa = 0.4$), and z is the geopotential height above the surface. The asymptotic mixing length λ reads

$$\lambda = \begin{cases} \lambda_o, & \text{if } z \leq z_{\text{pbl}}, \\ (\lambda_o - \lambda_\infty)\exp\left(-\frac{z - z_{\text{pbl}}}{z_{\text{pbl}}}\right) + \lambda_\infty, & \text{if } z > z_{\text{pbl}}, \end{cases}$$ (2.164)

with z_{pbl} being the PBL height as defined below. The asymptotic mixing length is a constant ($\lambda_o = 150$ m) in the boundary layer, and it decreases exponentially with height above the boundary layer approaching λ_∞ ($= 1$ m) in the lower stratosphere.

To calculate λ it is necessary to estimate the boundary layer height. The scheme distinguishes two types of boundary layers, i.e. neutrally and stably stratified boundary layer (SBL) and convective boundary layer (CBL). The height of the SBL is assumed approximately to be:

$$z_{\text{sbl}} = 0.3\,u_*/f,$$ (2.165)

with f being the Coriolis parameter. The top of the convective boundary layer is identified when, at a certain height z_{cbl}, the virtual dry static energy s_v exceeds the value at the lowest

model level. The boundary layer height is then assumed to be the largest of the two definitions:

$$z_{\text{pbl}} = \max(z_{\text{sbl}}, z_{\text{cbl}}). \tag{2.166}$$

In the model there is an additional constraint that the geopotential at the top of the boundary layer does not exceed $5 \times 10^4 \, \text{m}^2 \, \text{s}^{-2}$. The boundary layer height is diagnosed using geopotential height at full model levels.

Stability functions

The stability factor S_ψ in Eqn. (2.157) is defined as a product of the neutral coefficient $S_{N\psi}$ and the stability functions g_ψ:

$$S_\psi = S_{N\psi} \, g_\psi. \tag{2.167}$$

The neutral stability coefficients are constants given by Mellor and Yamada (1982):

$$S_{Nh} = 3\sqrt{2}A_2\gamma_1, \tag{2.168}$$

$$S_{Nm} = S_{Nh} \frac{A_1}{A_2} \left(\frac{\gamma_1 - C_1}{\gamma_1} \right), \tag{2.169}$$

with $A_1 = 0.92$, $A_2 = 0.74$, $B_1 = 16.6$, $C_1 = 0.08$ and $\gamma_1 = 1/3 - 2A_1/B_1$. The stability functions are:

$$g_m = \begin{cases} \dfrac{1}{1 + 2cRi \left(\sqrt{1 + Ri} \right)^{-1}} & \text{if } Ri \geq 0 \\[3ex] 1 - \dfrac{2cRi}{1 + 3c^2l^2 \left[\left(\frac{\Delta z}{z} + 1 \right)^{1/3} - 1 \right]^{3/2} \left[\frac{\sqrt{-Ri}}{(\Delta z)^{3/2}\sqrt{z}} \right]} & \text{if } Ri < 0 \end{cases} \tag{2.170}$$

$$g_h = \begin{cases} \dfrac{1}{1 + 2cRi \sqrt{1 + Ri}} & \text{if } Ri \geq 0 \\[3ex] 1 - \dfrac{3cRi}{1 + 3c^2l^2 \left[\left(\frac{\Delta z}{z} + 1 \right)^{1/3} - 1 \right]^{3/2} \left[\frac{\sqrt{-Ri}}{(\Delta z)^{3/2}\sqrt{z}} \right]} & \text{if } Ri < 0 \end{cases} \tag{2.171}$$

where z is the geopotential height above surface, Δz the layer thickness, and $c = 5$ is a constant. Ri is the moist Richardson number defined earlier.

Dissipation

The TKE dissipation term, δ, in Equation (2.158) is assumed to have the form (Kolmogorov 1941):

$$\delta \propto \frac{E^{\frac{3}{2}}}{l}, \tag{2.172}$$

where here the length-scale in the denominator is the dissipation length-scale. This length-scale is assumed to equal the mixing-length, and then it can be shown that:

$$\delta = S_{Nm}^3 \frac{E^{\frac{3}{2}}}{l}. \tag{2.173}$$

Third-order TKE transport

The turbulent transport of TKE term in Equation (2.158) is modeled by assuming the form of the flux in Equation (2.153) and that the relevant exchange coefficient is the turbulent viscosity, K_m. Then the transport term is modeled as:

$$\frac{\partial \overline{w'E'}}{\partial z} = \frac{\partial}{\partial z}\left(-K_m \frac{\partial E}{\partial z}\right) \tag{2.174}$$

TKE surface boundary condition

The formulation of the bottom boundary condition for TKE is dependent on the surface-layer stability only under convectively unstable situations Mailhot and Benoit (1982):

$$E_{\text{sfc}} = \begin{cases} S_{Nm}^{-2}u_*^2, & \frac{z}{L} \geq 0 \\ \left[S_{Nm}^{-2} + \left(-\frac{z}{L}\right)^{2/3}\right]u_*^2 + 0.2w_*^2, & \frac{z}{L} < 0 \end{cases} \tag{2.175}$$

where u_* is the friction velocity, w_* is the convective velocity scale and L is the Monin-Obukhov length-scale defined earlier. The surface buoyancy flux $\left(\overline{w'\theta_v'}\right)_{\text{sfc}}$ is computed as described in Section 2.5.3. With a few steps of simple manipulation one can rewrite Eqn. (2.175) into:

$$E_{\text{sfc}} = \begin{cases} S_{Nm}^{-2}u_*^2 \\ S_{Nm}^{-2}u_*^2 + 0.2\left[gz_{\text{pbl}}\dfrac{\left(\overline{w'\theta_v'}\right)_{\text{sfc}}}{\bar{\theta}_v}\right]^{\frac{2}{3}} + \left[\kappa gz_{\text{nlev}}\dfrac{\left(\overline{w'\theta_v'}\right)_{\text{sfc}}}{\bar{\theta}_v}\right]^{\frac{2}{3}} \end{cases} \tag{2.176}$$

where the surface-layer mean virtual potential temperature is $\bar{\theta}_v = 0.5\left(\theta_{v,\text{nlev}} + \theta_{v,\text{sfc}}\right)$. In the code we use this formula in order to avoid floating point problem when $u_* = 0$, e.g. when simulations are carried out with the surface momentum flux switched off.

Prognostic temperature variance

Although not directly used in the TKE closure model, for completeness we here mention that the code contains a prognostic equation for virtual potential temperature variance, $\sigma_{\theta_v}^2$. This quantity is used by the convection scheme to estimate the updraft buoyancy excess. The prognostic equation of this quantity is:

$$\frac{\partial \sigma_{\theta_v}^2}{\partial t} = -2\overline{w'\theta_v'}\frac{\partial \theta_v}{\partial z} - \frac{\sigma_{\theta_v}^2}{\tau} - \frac{\partial \overline{w'\sigma_{\theta_v}^2}}{\partial z}. \tag{2.177}$$

Changes in the sub-grid variance of virtual potential temperature are assumed to be caused by buoyancy production, molecular dissipation and vertical turbulent transport. The dissipation time-scale is assumed to be $\tau = l\,S_{Nm}^{-3}/\sqrt{E}$. The turbulent flux profile used in the buoyancy production term is approximated by Equation (2.153). The numerical solution is done analogously to the TKE equation.

2.5.3. Interaction with the surface

The surface fluxes in ECHAM are calculated using the bulk-exchange formula, Equation (2.154). To achieve this it is necessary to define empirical expressions for the bulk transfer coefficients, C_ψ, which are usually obtained from Monin-Obukhov similarity theory by integrating the flux-profile relationships from the surface up to the lowest model layer. This results in implicit expressions that requires iterative numerical methods to solve. Therefore, approximate analytical expressions are applied close to those suggested by Louis (1979). In ECHAM these depend on the moist Richardson number evaluated between the surface and the first model level. This is often called the bulk Richardson number. We first separate the coefficient into a product of coefficient and a universal function:

$$C_\psi = C_{N,\psi} f_\psi \tag{2.178}$$

where $C_{N,\psi}$ is the neutral limit transfer coefficient and f_ψ is an empirical function to be determined. The turbulence formulation in ECHAM distinguishes only between momentum ($\psi = m$) and scalars ($\psi = h$).

Neutral limit coefficients

The neutral limit coefficients depend only on surface roughness lengths and the height of the first model level, z_{nlev}, which we shall simply designate z in this section:

$$
\begin{aligned}
C_{N,m} &= \frac{\kappa^2}{[\ln(z/z_{0m} + 1)]^2} &\tag{2.179}\\
C_{N,h} &= \frac{\kappa^2}{\ln(z/z_{0m} + 1)\ln(z/z_{0h} + 1)}, &\tag{2.180}
\end{aligned}
$$

where κ is von Karmans constant, z_{0m} is the aerodynamic roughness length for momentum and z_{0h} is the roughness length with respect to scalars.

Roughness lengths

The roughness lengths over land are specified based the orography and vegetation. These are read in from a file with a global map, and assumed to not exceed 1 m. Over snow covered land z_{0h} is set to 10^{-3} m. If land is partially covered with snow, the blending height concept is applied by taking a weighted average of the bulk transfer coefficients from each surface type, not by averaging the roughness lengths. Over sea ice $z_{0m} = z_{0h} = 10^{-3}$ m. Over open ocean the aerodynamic roughness length is calculated after the Charnock (1955) formula:

$$z_{0m} = \max\left[0.018 u_*^2/g, 1.5 \cdot 10^{-5}\text{m}\right], \tag{2.181}$$

where u_* is the friction velocity and g is gravity. The roughness length for scalars is assumed to be related to the aerodynamic roughness as:

$$z_{0h} = z_{0m} \cdot \exp\left(2 - 86.276 z_{0m}^{0.375}\right). \tag{2.182}$$

Surface-layer stability functions

Under neutral to stably stratified conditions ($Ri \geq 0$) the vertical transfer is reduced according to:

$$f_m = \frac{1}{1 + 2cRi \left(\sqrt{1 + Ri}\right)^{-1}} \tag{2.183}$$

$$f_h = \frac{1}{1 + 2cRi\sqrt{1 + Ri}}, \tag{2.184}$$

where $c = 5$. Under unstable conditions ($Ri < 0$), instead the transfer coefficients are enhanced:

$$f_m = 1 - \frac{2cRi}{1 + 3c^2 C_{N,m}\sqrt{-Ri\left(\frac{z}{z_{0m}} + 1\right)}} \tag{2.185}$$

$$f_h = 1 - \frac{3cRi}{1 + 3c^2 C_{N,m}\sqrt{-Ri\left(\frac{z}{z_{0m}} + 1\right)}}. \tag{2.186}$$

However, over open ocean and unstable conditions ($Ri < 0$), the scalar transfer stability function is defined:

$$f_h = (1 + C_R^\gamma)^{1/\gamma}, \quad \text{where} \tag{2.187}$$

$$C_R = \beta \frac{\Delta\theta_v^{1/3}}{C_{N,h}|\vec{V}|}, \tag{2.188}$$

while $\beta = 0.001$, $\gamma = 1.25$, and $\Delta\theta_v$ is the virtual potential temperature difference between the surface and the lowest model level.

Accounting for evapotranspiration

The surface flux over land of specific humidity $\left(\overline{w'q_v'}\right)_{\text{sfc}}$, and therefore also virtual dry static energy $\left(\overline{w'h_v'}\right)_{\text{sfc}}$, includes evapotranspiration by a modification of equation (2.154):

$$\left(\overline{w'q_v'}\right)_{\text{sfc}} = -C_h|\vec{V}|\left[\beta(z)q_v(z) - \beta_{\text{sfc}}q_{v,\text{sfc}}\right], \tag{2.189}$$

$$\left(\overline{w'h_v'}\right)_{\text{sfc}} = -C_h|\vec{V}|\left[\beta(z)h_v(z) - \beta_{\text{sfc}}h_{v,\text{sfc}}\right], \tag{2.190}$$

where $\beta(z)$ and β_{sfc} are introduced to account for evapotranspiration.

Handling fractional surface coverage

The current implementation of the turbulent mixing schemes allows for fractional land, ocean and sea ice coverages. The grid-box mean surface exchange coefficients of momentum and heat

are defined as:

$$\overline{u'w'}_{\text{sfc}} = \sum_{i=1}^{3} F_i \left(C_m \left| \vec{V} - \vec{V}_{\text{sfc},i} \right| \right)_i [u(z) - u_{\text{sfc},i}] \tag{2.191}$$

$$\overline{v'w'}_{\text{sfc}} = \sum_{i=1}^{3} F_i \left(C_m \left| \vec{V} - \vec{V}_{\text{sfc},i} \right| \right)_i [v(z) - v_{\text{sfc},i}] \tag{2.192}$$

$$\overline{w'h'}_{\text{sfc}} = \sum_{i=1}^{3} F_i \left(C_h \left| \vec{V} - \vec{V}_{\text{sfc},i} \right| \right)_i [h(z) - h_{\text{sfc},i}] \tag{2.193}$$

where i indicates land, ocean and sea ice, respectively, F_i is the surface type fractional cover, h is the dry static energy, $\vec{V}_{\text{sfc},i} = (u_{\text{sfc},i}, v_{\text{sfc},i})$ is the velocity of the ocean surface current, while $\vec{V}_{\text{sfc},i} = 0$ over land and sea ice. The surface boundary condition for TKE is obtained analogously to momentum by evaluating Equation (2.176) for each surface type and then aggregating. Likewise, the area-weighted grid-box mean friction velocity is then $u_* = \sum_{i=1}^{N_{\text{st}}} F_i \, u_{*,i}$. There is no surface flux of any hydrometeors over any surface type. Other tracers, e.g., aerosols or gas-phase chemical species, can have emission sources at the surface.

2.5.4. Numerical solution

The turbulent mixing parameterization is expressed in the height coordinate, z, however, ECHAM uses the pressure-based terrain following coordinate. One can then express the Equations (2.152) and (2.153):

$$\left(\frac{\partial \psi}{\partial t} \right)_{\text{turb}} = -\frac{\partial \overline{\omega'\psi'}}{\partial p} = \frac{\partial}{\partial p} \left[\rho g K_\psi \left(-\frac{\partial \psi}{\partial z} \right) \right] \tag{2.194}$$

Vertical discretization

We first consider the vertical discretization of Eqn. (2.194). ECHAM uses the hybrid vertical coordinate with Lorenz-type staggering. Horizontal wind, temperature and all tracers are defined at the mid level of each vertical layer. A straightforward vertical discretization reads:

$$\frac{\partial}{\partial p} \left[\rho g K_\psi \left(-\frac{\partial \psi}{\partial z} \right) \right] = \begin{cases} \dfrac{1}{\Delta p_k} \left[(\rho g K_\psi)_{k+1/2} \dfrac{\Delta \psi_{k+1/2}}{\Delta z_{k+1/2}} \right] , & k = 1 \\[3mm] \dfrac{1}{\Delta p_k} \left[(\rho g K_\psi)_{k+1/2} \dfrac{\Delta \psi_{k+1/2}}{\Delta z_{k+1/2}} - (\rho g K_\psi)_{k-1/2} \dfrac{\Delta \psi_{k-1/2}}{\Delta z_{k-1/2}} \right] , & k = 2, ..., \text{nlev} - 1 \\[3mm] \dfrac{1}{\Delta p_k} \left[(\rho g)_{k+1/2} (\text{surface flux}) - (\rho g K_\psi)_{k-1/2} \dfrac{\Delta \psi_{k-1/2}}{\Delta z_{k-1/2}} \right] , & k = \text{nlev} \end{cases}$$

$$\tag{2.195}$$

where $\Delta p_k = p_{k+1/2} - p_{k-1/2}$, $\Delta \psi_{k+1/2} = \psi_{k+1} - \psi_k$ and $\Delta z_{k+1/2} = z_k - z_{k+1}$. Note that Δp_k and $\Delta z_{k+1/2}$ are both positive by definition.

Temporal discretization

Now consider the temporal discretization. Since turbulent mixing is a very fast process compared to the typical time step used by global hydrostatic models, an implicit time stepping

scheme is employed. To integrate the model from time instance $t - \Delta t$ to $t + \Delta t$, a trapezoidal method is used. The temporal derivative in Equation (2.194) is approximated by:

$$\left(\frac{\partial \psi}{\partial t}\right)_{\text{turb},k} = \frac{\psi_k^{(t+\Delta t)} - \psi_k^{(t-\Delta t)}}{2\Delta t} \; . \tag{2.196}$$

For Equation (2.195), the temporal average:

$$\hat{\psi} = \alpha \, \psi^{(t+\Delta t)} + (1 - \alpha) \, \psi^{(t-\Delta t)}, \tag{2.197}$$

is used for the prognostic variable ψ and all the other quantities are computed at the current time step t. Here α denotes the implicitness factor which is set to a value of 1.5. Note that the time-stepping scheme used to solve the vertical diffusion equation uses only the time steps $t - \Delta t$ and $t + \Delta t$, and not the actual time t. We use this notation because ECHAM in general applies a leap-frog time step scheme which involves all three time steps.

The tri-diagonal system

To keep the formulation compact, let

$$\tilde{\psi}_k \;\; = \;\; \hat{\psi}_k/\alpha\,, \quad k = 1, ..., \text{nlev} \tag{2.198}$$

and define symbolically

$$\tilde{\psi}_0 = 0\,, \quad \tilde{\psi}_{\text{nlev}+1} = \psi_{\text{sfc}}/\alpha\,. \tag{2.199}$$

Let

$$K_{k+1/2}^* \;\; = \;\; \begin{cases} 0\,, & k = 0 \\[2mm] \dfrac{\alpha 2 \Delta t g \, (\rho K)_{k+1/2}}{\Delta z_{k+1/2}}, & k = 1, ..., \text{nlev - 1} \\[3mm] \delta \alpha 2 \Delta t g \rho_{k+1/2} C_\psi \left| \vec{V}_k - \vec{V}_{sfc} \right|\,, & k = \text{nlev} \end{cases} \tag{2.200}$$

where $\delta = 1$ if surface flux is considered, and $\delta = 0$ otherwise, for example for cloud water and cloud ice, and for horizontal winds if a slip boundary condition is desired. Consider first the simple case in which a grid cell is completely occupied by one surface type. Substitute Eqns. (2.197) and (2.196) into (2.195) and perform some further manipulation, we get

$$-\frac{K_{k-1/2}^*}{\Delta p_k} \tilde{\psi}_{k-1} + \left(1 + \frac{K_{k-1/2}^*}{\Delta p_k} + \frac{K_{k+1/2}^*}{\Delta p_k}\right) \tilde{\psi}_k - \frac{K_{k+1/2}^*}{\Delta p_k} \tilde{\psi}_{k+1} = \frac{\psi_k^{(t-\Delta t)}}{\alpha} \,, k \leq \text{nlev} - 1 \tag{2.201}$$

$$-\frac{K_{k-1/2}^*}{\Delta p_k} \tilde{\psi}_{k-1} + \left(1 + \frac{K_{k-1/2}^*}{\Delta p_k} + \frac{K_{k+1/2}^*}{\Delta p_k}\beta_k\right) \tilde{\psi}_k - \frac{K_{k+1/2}^*}{\Delta p_k}\beta_{k+1} \tilde{\psi}_{k+1} = \frac{\psi_k^{(t-\Delta t)}}{\alpha} \,, k = \text{nlev} \tag{2.202}$$

A more general version of the bottom level equation (2.202) reads

$$-\frac{K_{k-1/2}^*}{\Delta p_k} \tilde{\psi}_{k-1} + \left(1 + \frac{K_{k-1/2}^*}{\Delta p_k}\right) \tilde{\psi}_k - \frac{2\Delta t \, (\rho g)_{k+1/2}}{\Delta p_k}\mathcal{F}_{k+1/2} \;\; = \;\; \frac{\psi_k^{(t-\Delta t)}}{\alpha}, k = \text{nlev} \tag{2.203}$$

If either the surface value $\tilde{\psi}_{k+1/2}$ in Equation (2.202) or the surface flux $\mathcal{F}_{k+1/2}$ in Equation (2.203) is known, then the system (2.199) – (2.203) form a tri-diagonal linear algebraic system with the unknowns being $\tilde{\psi}_k$, $(k = 1, \ldots, \text{nlev})$. Gauss-elimination, followed by back substitution is used to solve the linear problem. After obtaining the this, one can derive the solution:

$$\psi_k^{(t+\Delta t)} \;\; = \;\; \tilde{\psi}_k + (1 - 1/\alpha) \, \psi_k^{(t-\Delta t)} \tag{2.204}$$

$$\left(\frac{\partial \psi}{\partial t}\right)_{\text{turb},k} \;\; = \;\; \frac{\psi_k^{(t+\Delta t)} - \psi_k^{(t-\Delta t)}}{2\Delta t} = \frac{\tilde{\psi}_k - \psi_k^{(t-\Delta t)}/\alpha}{2\Delta t} \tag{2.205}$$

for all the layers $k = 1, \ldots, \text{nlev}$.

2.5.5. Solving the TKE-equation

The TKE equation (2.158) is solved in two steps. First, the local terms, shear production, buoyancy and dissipation terms are applied, second, the non-local vertical transport.

Step 1: The TKE equation can be rewritten using the closure assumptions to:

$$\frac{\partial E}{\partial t} = \underbrace{\left\{ lS_m \left[\left(\frac{\partial u}{\partial z} \right)^2 + \left(\frac{\partial v}{\partial z} \right)^2 \right] - lS_h \left(\frac{g}{\theta_v} \frac{\partial \theta_v}{\partial z} \right) \right\}}_{\equiv B} \sqrt{E} - \underbrace{\left(S_{Nm}^{-3} l \right)^{-1}}_{\equiv C} \sqrt{E^3} . \tag{2.206}$$

The budget equation can be converted into an equation of $\sqrt{E}$:

$$\frac{\partial \sqrt{E}}{\partial t} = \frac{B}{2} - \frac{C}{2} \left(\sqrt{E} \right)^2 , \tag{2.207}$$

and discretized using implicit time stepping for $\sqrt{E}$ and explicit steps for B and C:

$$\frac{\sqrt{E}^{(*)} - \sqrt{E}^{(t-\Delta t)}}{2\Delta t} = \frac{B^{(t)}}{2} - \frac{C^{(t)}}{2} \left(\sqrt{E}^{(*)} \right)^2 . \tag{2.208}$$

The equation has an analytical solution reading

$$\sqrt{E}^{(*)} = \frac{-1 + \sqrt{1 + 2\Delta t\, C \left(2\Delta t\, B + 2\sqrt{E}^{(t-\Delta t)} \right)}}{2\Delta t\, C} . \tag{2.209}$$

Step 2: After obtaining the intermediate value $\sqrt{E}^{(*)}$, the effect of turbulent transport is taken into account by solving the equation

$$\frac{\partial E}{\partial t} = -\frac{\partial \overline{w'E}}{\partial z}. \tag{2.210}$$

The turbulent flux is parameterized in the same way as for the other prognostic variables. Bearing in mind that $\sqrt{E}^{(*)}$ is already available, and that the equation needs to be solved at layer interfaces, we get the following discrete equation:

$$\frac{E_{k+1/2}^{(t+\Delta t)} - E_{k+1/2}^{(*)}}{2\Delta t} = \frac{g}{\Delta p_{k+1/2}} \left[\overline{(\rho\, K_{\text{tke}})}_{k+1}^z \frac{\Delta \hat{E}_{k+1}}{\Delta z_{k+1}} - \overline{(\rho\, K_{\text{tke}})}_k^z \frac{\Delta \hat{E}_k}{\Delta z_k} \right] , k = 1, \ldots, \text{nlev} - 1. \tag{2.211}$$

with $\Delta p_{k+1/2} = p_{k+1} - p_k$, $\Delta \hat{E}_k = \hat{E}_{k+1/2} - \hat{E}_{k-1/2}$, $\Delta z_k = z_{k-1/2} - z_{k+1/2}$. The notation $\overline{()}^z$ denotes a simple arithmetic averaging from half levels to full levels. The exchange coefficients are

$$(K_{\text{tke}})_{k+1/2} = \begin{cases} 0 & \text{for } k = 0 \\ l_{k+1/2}\, (S_m)_{k+1/2}\, \sqrt{E}_{k+1/2}^{(*)} & \text{for } k = 1, \ldots, \text{nlev-1} \\ (K_m)_{\text{sfc}} & \text{for } k = \text{nlev} \end{cases} \tag{2.212}$$

Using the boundary condition for TKE, Equation (2.176), it is now possible to solve the TKE equation.

Solving for virtual dry static energy and specific humidity surface fluxes

For these two variables we account for evapotranspiration by Equation (2.189) in the vertical diffusion equation Equation (2.201). This is solved separately for each surface type when performing the Gaussian elimination for the lowest model level. The solutions, $\tilde{\psi}_{\mathrm{nlev},i}$, are then aggregated by:

$$\tilde{\psi}_{\mathrm{nlev}} = \frac{\sum_{i=1}^{3} F_i \, K^*_{nlev+1/2,i} \, \tilde{\psi}_{\mathrm{nlev},i} \beta_{nlev,i}}{\sum_{i=1}^{3} F_i \, K^*_{nlev+1/2,i} \beta_{nlev,i}} \tag{2.213}$$

with $K^*_{nlev+1/2,i}$ computed from Eqn. (2.200) and $\rho_{k+1/2} = p_{\mathrm{sfc}}/(R_d T_{v,\mathrm{nlev}})$. The resulting grid-box mean value $\tilde{\psi}_{\mathrm{nlev}}$ is then used in the back-substitution to obtain the solution in the upper layers. Equation (2.213) ensures a conservative aggregation of surface fluxes.

2.6. Cumulus convection

As in ECHAM4 and ECHAM5, a mass flux scheme (Tiedtke, 1989) is applied for cumulus convection with modifications for penetrative convection according to Nordeng (1994). The contribution of cumulus convection to the large scale budgets of heat, moisture and momentum is represented by an ensemble of clouds consisting of updrafts and donwdrafts in a steady state. The bulk equations for mass, heat, moisture, cloud water and momentum for an ensemble of cumulus updrafts are

$$\frac{\partial M_u}{\partial z} = E_u - D_u \tag{2.214}$$

$$\frac{\partial}{\partial z}(M_u s_u) = E_u \bar{s} - D_u s_u + L \bar{\rho} c_u \tag{2.215}$$

$$\frac{\partial}{\partial z}(M_u q_u) = E_u \bar{q} - D_u q_u - \bar{\rho} c_u \tag{2.216}$$

$$\frac{\partial}{\partial z}(M_u l_u) = -D_u l_u + \bar{\rho} c_u - \bar{\rho} P_u \tag{2.217}$$

$$\frac{\partial}{\partial z}(M_u u_u) = E_u \bar{u} - D_u u_u \tag{2.218}$$

$$\frac{\partial}{\partial z}(M_u v_u) = E_u \bar{v} - D_u v_u \tag{2.219}$$

where the subscript u denotes updraft variables and the overbar denotes large-scale variables. E is entrainment, D is detrainment, $s = c_p T + gz$ the dry static energy, ρ the air density, q is specific humidity, l the cloud water mixing ratio, c_u the release of latent heat from condensation, P_u the conversion of cloud water to precipitation, and u and v are the components of the horizontal wind vector. A corresponding set of equations is used for the cumulus downdrafts which are assumed to originate from mixing of cloud air with environmental air which has been cooled to its wet bulb temperature by evaporation of precipitation generated in the updrafts. The cloud water detrainment in (2.217) is used as a source term in the stratiform cloud water/ice equations (2.242, 2.243).

2.6.1. Organized entrainment

In Tiedtke (1989), organized entrainment is consistent with the closure and is based on a moisture convergence hypothesis. Nordeng (1994), on the other hand, assumes organized entrainment to take place as inflow of air into the cloud when cloud parcels accelerate upwards, i.e. when the buoyancy is positive. Organized detrainment takes place where the air decelerates, i.e. when the buoyancy becomes negative. Organized entrainment and detrainment are therefore related to the cloud activity itself. Fractional entrainment and detrainment rates, ϵ_i and δ_i (Turner, 1963), are introduced so that for an individual updraft i, $E_i = M_i \epsilon_i$ and $D_i = M_i \delta_i$, and for the cloud ensemble

$$E = M\epsilon = \sum_i M_i \epsilon_i = \sum_i E_i \tag{2.220}$$

$$D = M\delta = \sum_i M_i \delta_i = \sum_i D_i \tag{2.221}$$

where the cloud ensemble mass flux is defined as

$$M = \sum_i M_i = \sum_i \overline{\rho}\sigma_i w_i \tag{2.222}$$

with fractional area σ_i and vertical velocity w_i. Equation (2.214) can then be expressed as

$$\frac{1}{M}\frac{\partial M}{\partial z} = \epsilon - \delta \tag{2.223}$$

where the subscript u denoting the updraft has been omitted for convenience (in the following as well). According to Simpson and Wiggert (1969), the steady state vertical momentum equation for an individual updraft is given by

$$w_i \frac{\partial w_i}{\partial z} = b_i - \epsilon_i w_i^2 \tag{2.224}$$

where b_i is the buoyancy term which may include water loading and non-hydrostatic effects. Assuming that the fractional area σ_i of each individual updraft is constant with height (except in the ouflow part, see later), organized entrainment, according to (2.222) and (2.223), can be written as

$$\epsilon_i = \frac{1}{M_i}\frac{\partial M_i}{\partial z} = \frac{1}{w_i}\frac{\partial w_i}{\partial z} + \frac{1}{\overline{\rho}}\frac{\partial \overline{\rho}}{\partial z} \tag{2.225}$$

whenever the buoyancy is positive ($\delta_i = 0$). By integrating (2.224) upwards, starting at cloud base ($z = 0$), and using (2.220), (2.224) and (2.225), the organized entrainment rate of the cloud ensemble becomes

$$\epsilon = \frac{b}{2\left(w_0^2 + \int_o^z b\,dz\right)} + \frac{1}{\overline{\rho}}\frac{\partial \overline{\rho}}{\partial z} \tag{2.226}$$

with the ensemble buoyancy $b = \frac{g}{\overline{T}_v}(T_v - \overline{T}_v) - gl$.

2.6.2. Organized detrainment

Organized detrainment is defined as the loss of total massflux due to detrainment of those clouds which are losing their buoyancy, i.e.

$$D = E - \frac{\partial M}{\partial z} = \sum_i \overline{\rho}\sigma_i w_i \left(\frac{1}{w_i}\frac{\partial w_i}{\partial z} + \frac{1}{\overline{\rho}}\frac{\partial \overline{\rho}}{\partial z}\right) - \frac{\partial}{\partial z}\sum_i \overline{\rho}\sigma_i w_i = -\sum_i \overline{\rho}w_i\frac{\partial \sigma_i}{\partial z} \tag{2.227}$$

Since the fractional area of each individual member of the ensemble is assumed to be constant with height, except for the detrainment level, the only contribution to the sum in (2.227) comes from those members of the ensemble which detrain at this level (k), i.e.,

$$D = -\sum_k \overline{\rho}w_k\frac{\partial \sigma_k}{\partial z} \approx \frac{\overline{\rho}\sigma_k w_k}{\Delta z} = \frac{M_k}{\Delta z} \tag{2.228}$$

where Δz is the depth over which the detrainment takes place. Thus, organized detrainment is equal to the change of mass flux with height. Since the in-cloud vertical velocities are primarily a function of the height above cloud base and, hence, $w_k \approx w$, and due to the assumption that individual clouds do not change their area fraction before they start to detrain, the individual cloud cover change is equal to the total, i.e.,

$$\frac{\partial \sigma_k}{\partial z} = \frac{\partial \sigma}{\partial z} \tag{2.229}$$

so that, according to (2.228) and (2.229), the organized detrainment may be parameterized as

$$D = -\frac{M}{\sigma} \frac{\partial \sigma}{\partial z} \tag{2.230}$$

It remains to determine the variation of cloud cover with height. Having obtained the level where clouds start to detrain (z_d), an analytical function $\sigma = \sigma(z)$ is specified with boundary values $\sigma(z_d) = \sigma_0$ and $\sigma = (z_t) = \sigma_0$, where z_t is the highest possible cloud level obtained from undiluted ascent starting at cloud base. In the parameterization, the spectrum of clouds detraining at different levels is realized through the following function

$$\sigma(z) = \sigma_0 \cos\left[\frac{\pi}{2} \frac{(z - z_d)}{(z_t - z_d)}\right] \tag{2.231}$$

Except for being continuous at $z = z_d$, and satisfying the boundary conditions specified above, there is no physical reason for chosing this particular function.

2.6.3. Adjustment closure

The adjustment-type closure suggested by Nordeng (1994) relates the cloud base mass flux to convective instability. The dominant part of convective heating and drying, respectively, is due to compensating subsidence in the environment Fritsch and Chapell (1980)

$$\frac{\partial \overline{T}}{\partial t} \approx \frac{1}{\overline{\rho} c_p} M \frac{\partial \overline{s}}{\partial z} \tag{2.232}$$

$$\frac{\partial \overline{q}}{\partial t} \approx \frac{1}{\overline{\rho}} M \frac{\partial \overline{q}}{\partial z} \tag{2.233}$$

where M is the massflux.

Convective activity is expressed in terms of $CAPE$ (convective available potential energy) which is estimated from the parcel ascent incorporating the effects of water loading,

$$CAPE = \int_{base}^{top} \left(\frac{g}{\overline{T}_v}\left[T_v - \overline{T}_v\right] - gl\right) dz \tag{2.234}$$

where cloud ensemble values are used for T_v and l. The change of $CAPE$ due to convective heating/moistening is approximated by

$$\frac{\partial}{\partial t}CAPE \approx -\int_{base}^{top} \frac{g}{\overline{T}_v}\frac{\partial \overline{T}_v}{\partial t}dz = -M_B \int_{base}^{top} \left(\frac{[1+\delta\overline{q}]}{c_p\overline{T}_v}\frac{\partial \overline{s}}{\partial z} + \delta\frac{\partial \overline{q}}{\partial z}\right)\eta\frac{g}{\rho}dz \qquad (2.235)$$

with normalized mass flux η defined as $M = M_B \cdot \eta(z)$ where M_B is the cloud base mass flux. By assuming that convection acts to reduce $CAPE$ towards zero over a specified time scale τ, the time rate of change is approximated by

$$\frac{\partial}{\partial t}CAPE \approx -\frac{CAPE}{\tau} \qquad (2.236)$$

so that the cloud base mass flux can be obtained from (2.235) and (2.236) according to

$$M_B = \frac{CAPE}{\tau}\left\{\int_{base}^{top}\left[\frac{(1+\delta\overline{q})}{c_p\overline{T}_v}\frac{\partial \overline{s}}{\partial z} + \delta\frac{\partial \overline{q}}{\partial z}\right]\eta\frac{g}{\rho}dz\right\}^{-1}. \qquad (2.237)$$

Since η is not known before the total mass flux is known, $CAPE$ is estimated through a first guess $M_B = M_B^*$ obtained from first applying the moisture convergence scheme. Thus, the cloud base mass can finally be written as

$$M_B = \frac{CAPE}{\tau} = M_B^*\left\{\int_{base}^{top}\left[\frac{(1+\delta\overline{q})}{c_p\overline{T}_v}\frac{\partial \overline{s}}{\partial z} + \delta\frac{\partial}{\partial z}\overline{q}\right]M^*\frac{g}{\rho}dz\right\}^{-1}. \qquad (2.238)$$

Following Nordeng (1994), who argued that τ should be smaller (larger) with increasing (decreasing) horizontal resolution, we apply an algorithm similar to that used in the ECMWF model, $\tau[s] = \min(3 \cdot 3600, 2 \cdot 3600 \cdot 63/N)$, where N denotes the spectral resolution.

2.6.4. Trigger of cumulus convection

The aim is to relate the parcel buoyancy to the standard deviation of virtual potential temperature at the lifting level. To this end, the balance equation for the variance of the virtual potential temperature is solved within the vertical diffusion scheme:

$$\frac{\partial \overline{\Theta_v'^2}}{\partial t} = -2\overline{\omega'\Theta_v'}\frac{\partial \overline{\Theta_v}}{\partial z} - \frac{\partial \overline{\omega'\Theta_v'^2}}{\partial z} - \varepsilon(\overline{\Theta_v'^2}) \tag{2.239}$$

$$\frac{\partial \overline{\Theta_v'^2}}{\partial t} = -2\overline{\omega'\Theta_v'}\frac{\partial \overline{\Theta_v}}{\partial z} - \frac{\partial \overline{\omega'\Theta_v'^2}}{\partial z} - \varepsilon(\overline{\Theta_v'^2}) \tag{2.240}$$

representing the sum of the production, turbulent transfer and dissipation terms. The buoyancy flux is parameterized in analogy to the fluxes of heat, moisture etc. $\overline{\omega'\Theta_v'} = -K_h\frac{\partial \overline{\Theta_v}}{\partial z}$ with $K_h = S_h(Ri)l_{\mathrm{mix}}\sqrt{TKE}$, where S_h is a non-dimensional stability function depending on the Richardson number Ri, TKE is the turbulence kinetic energy, and the mixing length is defined as $l_{\mathrm{mix}} = kz/(1 + kz/\lambda)$ with $k = 0.4$ and $l = 150m$ (asymptotic mixing length). Thus, the production term can be written as $2K_h(\frac{\partial \overline{\Theta_v}}{\partial z})^2$ (defined at 'half levels'). The turbulent transport is calculated analogously to TKE (at 'half levels'). The dissipation term is parameterized in terms of TKE and a dissipation length scale $\varepsilon(\overline{\Theta_v'^2}) = \overline{\Theta_v'^2}\sqrt{TKE}/(6*l_{\mathrm{mix}})$ (Deardorff (1974); see also the dissipation of total water variance in Roeckner et al. (2003), equations 10.19 and 10.20). The balance equation is solved implicitly by using the 'fractional steps' method.

The result is used to parameterize the buoyancy of air parcels lifted dry adiabatically upward within the convection scheme. In previous versions of ECHAM, the buoyancy depends on the difference of virtual temperature between the air parcel and the environment. A constant of 0.5K is added as trigger of cumulus convection, thereby taking into account some degree of subgrid-scale variability in virtual temperature. In ECHAM6, the trigger constant is replaced by $b\sqrt{\overline{\Theta_v'^2}}$, where b is a tuning parameter (currently set to 1). This term is calculated at the lifting level (corresponding to the half level klev-1 in 'cubase' and 'cuasc'), and then applied identically at all sub-cloud levels and at cloud base as well. Thus, the buoyancy of the air parcel is determined by its properties (mean and variance) at the lifting level and on the vertical profile of virtual temperature in the large-scale environment (as before). Note that lower and upper thresholds for the standard deviation of virtual potential are applied (0.1 and 1.0 degree, respectively).

2.7. Large-scale cloud scheme

The scheme for the respresentation of stratiform clouds consists of prognostic equations for the vapor, liquid, and ice phase, respectively, a cloud microphysical scheme (Lohmann and Roeckner (1996); with some revisions), and a diagnostic cloud cover scheme (Sundqvist et al., 1989). The statistical cloud cover scheme (Tompkins, 2002) used in ECHAM5 is available on request (see Roeckner et al. (2003) for details).

2.7.1. Governing equations

The governing equations for the grid-cell mean mass mixing ratios of water vapor, $\bar{r}_v$, cloud liquid water, $\bar{r}_l$, and cloud ice, $\bar{r}_i$, are written in symbolic form as follows (units are $\mathrm{kgkg}^{-1}\mathrm{s}^{-1}$)

$$\frac{\partial \bar{r}_v}{\partial t} = Q_{\mathrm{Tv}} + Q_{\mathrm{evr}} + Q_{\mathrm{evl}} + Q_{\mathrm{sbs}} + Q_{\mathrm{sbis}} + Q_{\mathrm{sbi}} - Q_{\mathrm{cnd}} - Q_{\mathrm{dep}} - Q_{\mathrm{tbl}} - Q_{\mathrm{tbi}} \quad (2.241)$$

$$\frac{\partial \bar{r}_l}{\partial t} = Q_{\mathrm{Tl}} + Q_{\mathrm{mli}} + Q_{\mathrm{mlis}} + Q_{\mathrm{cnd}} + Q_{\mathrm{tbl}} - Q_{\mathrm{evl}} - Q_{\mathrm{frh}} - Q_{\mathrm{frs}} - Q_{\mathrm{frc}}$$
$$- Q_{\mathrm{aut}} - Q_{\mathrm{racl}} - Q_{\mathrm{sacl}} \quad (2.242)$$

$$\frac{\partial \bar{r}_i}{\partial t} = Q_{\mathrm{Ti}} + Q_{\mathrm{sed}} + Q_{\mathrm{dep}} + Q_{\mathrm{tbi}} - Q_{\mathrm{mli}} - Q_{\mathrm{sbi}} + Q_{\mathrm{frh}} + Q_{\mathrm{frs}} + Q_{\mathrm{frc}} - Q_{\mathrm{agg}} - Q_{\mathrm{saci}} \quad (2.243)$$

with

Q_{Tv} Transport of $\bar{r}_v$ by advection (Q_{Av}), diffusion (Q_{Dv}) and changes due to convection

Q_{Tl} Transport of $\bar{r}_l$ by advection (Q_{Al}), diffusion (Q_{Dl}) and convective detrainment (Q_{Cl})

Q_{Ti} Transport of $\bar{r}_i$ by advection (Q_{Ai}), diffusion (Q_{Di}) and convective detrainment (Q_{Ci})

Q_{evr} Evaporation of rain falling into the respective layer

Q_{evl} Instantaneous evaporation of r_l transported into the cloud-free part of the grid cell

Q_{sbs} Sublimation of snow

Q_{sbis} Sublimation of r_i in the sedimentation flux

Q_{sbi} Instantaneous sublimation of r_i transported into the cloud-free part of the grid cell

Q_{cnd} Condensation of r_v (if $Q_{\mathrm{cnd}} > 0$), or evaporation of r_l (if $Q_{\mathrm{cnd}} < 0$)

Q_{dep} Deposition of r_v (if $Q_{\mathrm{dep}} > 0$), or sublimation of r_i (if $Q_{\mathrm{dep}} < 0$)

Q_{tbl} Generation ($Q_{\mathrm{tbl}} > 0$) or dissipation ($Q_{\mathrm{tbl}} < 0$) of r_l through turbulent fluctuations

Q_{tbi} Generation ($Q_{\mathrm{tbi}} > 0$) or dissipation ($Q_{\mathrm{tbi}} < 0$) of r_i through turbulent fluctuations

Q_{mli} Instantaneous melting of r_{i} if the temperature exceeds the freezing point

Q_{mlis} Melting of r_{i} in the sedimentation flux

Q_{frh} Homogeneous freezing of r_{l}

Q_{frs} Stochastical and heterogeneous freezing of r_{l}

Q_{frc} Contact freezing of r_{l}

Q_{aut} Autoconversion of r_{l}

Q_{racl} Accretion of r_{l} by rain

Q_{sacl} Accretion of r_{l} by snow

Q_{sed} Sedimentation of $\bar{r}_{\mathrm{i}}$, including losses due to Q_{sbis} and Q_{mlis}

Q_{agg} Aggregation of r_{i}

Q_{saci} Accretion of r_{i} by snow

Note that the transport terms as well as the sedimentation of cloud ice is calculated from the respective grid-cell mean values (denoted by an overbar), while the microphysical processes are calculated from in-cloud values (without overbar). The phase changes sketched above result in the following temperature change

$$\left(\frac{\partial T}{\partial t}\right)_{\mathrm{ph}} = \left(\frac{\partial T}{\partial t}\right)_{\mathrm{vapor}\leftrightarrow\mathrm{liquid}} + \left(\frac{\partial T}{\partial t}\right)_{\mathrm{vapor}\leftrightarrow\mathrm{solid}} + \left(\frac{\partial T}{\partial t}\right)_{\mathrm{liquid}\leftrightarrow\mathrm{solid}} \tag{2.244}$$

with

$$\left(\frac{\partial T}{\partial t}\right)_{\mathrm{vapor}\leftrightarrow\mathrm{liquid}} = \frac{L_{\mathrm{v}}}{c_{\mathrm{p}}}(Q_{\mathrm{cnd}} + Q_{\mathrm{tbl}} - Q_{\mathrm{evr}} - Q_{\mathrm{evl}}) \tag{2.245}$$

$$\left(\frac{\partial T}{\partial t}\right)_{\mathrm{vapor}\leftrightarrow\mathrm{solid}} = \frac{L_{\mathrm{s}}}{c_{\mathrm{p}}}(Q_{\mathrm{dep}} + Q_{\mathrm{tbi}} - Q_{\mathrm{sbs}} - Q_{\mathrm{sbi}} - Q_{\mathrm{sbis}}) \tag{2.246}$$

$$\left(\frac{\partial T}{\partial t}\right)_{\mathrm{liquid}\leftrightarrow\mathrm{solid}} = \frac{L_{\mathrm{f}}}{c_{\mathrm{p}}}(Q_{\mathrm{frh}} + Q_{\mathrm{frs}} + Q_{\mathrm{frc}} + Q_{\mathrm{sacl}} - Q_{\mathrm{mli}} - Q_{\mathrm{mlis}} - Q_{\mathrm{mls}}) \tag{2.247}$$

where L_{v}, L_{s}, L_{f} is the latent heat of vaporization, sublimation, and fusion, respectively, c_{p} is the specific heat of moist air at constant pressure, Q_{mls} is the melting of snow falling into the respective layer, and 'solid' refers to both cloud ice and snow.

2.7.2. Cloud cover

Fractional cloud cover C is parameterized as a non-linear function of grid-mean relative humidity r (Sundqvist et al., 1989). For $r > r_0$, where $r_0 < r_{\mathrm{sat}}$ is a subgrid-scale condensation threshold and r_{sat} ($=1$ in general) is the saturation value,

$$C = 1 - \sqrt{1 - C_0} \tag{2.248}$$

$$C_0 = \frac{r - r_0}{r_{\text{sat}} - r_0} \tag{2.249}$$

and $C = 0$ otherwise. Condensational growth of cloud droplets occurs if $r > r_0$. Oppositely, an existing cloud is diluted by evaporation if $r < r_0$. The condensation threshold r_0 is specified as a function of height (or pressure), fitted to the results obtained by Xu and Krueger (1991) from experiments with a high-resolution cumulus ensemble model,

$$r_0(p) = r_{0,\text{top}} + (r_{0,\text{surf}} - r_{0,\text{top}})\, \mathrm{e}^{[1-(p_{\text{s}}/p)^{\text{n}}]} \tag{2.250}$$

where p is pressure, p_{s} is surface pressure, $r_{0,\text{top}} = 0.7$ and $r_{0,\text{surf}} = 0.9$ are the upper and lower values of r_0, and $n = 4$ is a fitting parameter. The function (2.250) is used for all cloud types except for marine stratus under a low-level inversion. If such an inversion is detected below about 700 hPa, r_0 is reduced to 0.7 below the inversion and $r_{\text{sat}} = 0.9$ so that, according to (2.248) and (2.249) $C = 1$ is reached already before the whole layer is saturated. This ad hoc parameter setting allows formation of thin stratus clouds under a subsidence inversion which otherwise would not be captured due to the insufficient vertical resolution of the model. The lack of marine stratus clouds is one of the most persistent problems in GCMs.

2.7.3. Sedimentation and cloud microphysics

Condensation/evaporation and deposition/sublimation

Condensational growth of cloud droplets ($Q_{\text{cnd}} > 0$) occurs if the grid-mean relative humidity r exceeds the specified threshold r_0 so that the fractional cloud cover $C > 0$:

$$Q_{\text{cnd}} = C(\Delta q_{\text{f}} - \Delta q_{\text{s}}) \tag{2.251}$$

where $\Delta q_{\text{f}} > 0$ is the *humidity forcing*, i.e. convergence of $q = r_{\text{v}}$ resulting from all previously calculated transport processes (advection, vertical diffusion, convection), and

$$\Delta q_{\text{s}} = \frac{\left(\Delta T_{\text{f}} + C\frac{L_{\text{v}}}{c_{\text{p}}}\Delta q_{\text{f}}\right)\frac{\partial q_{\text{s}}}{\partial T}}{1 + C\frac{L_{\text{v}}}{c_{\text{p}}}\frac{\partial q_{\text{s}}}{\partial T}} \tag{2.252}$$

is the change of saturation water vapor mixing ratio resulting from all previously calculated processes (temperature advection, adiabatic cooling, radiation, vertical diffusion, convection). Oppositely, dissipation ($Q_{\text{cnd}} < 0$) of an existing cloud ($C > 0$) is caused by moisture divergence ($\Delta q_{\text{f}} < 0$) and/or net heating of the grid-box ($\Delta q_{\text{s}} > 0$).

Note that humidity changes due to evaporation of rain/cloud water and sublimation of snowfall/cloud ice are not included in Δq_{f}. These phase changes (Δq_{e}) are limited to the clear-sky part of the grid-box and do not affect cloud formation/dissipation at the respective timestep. However, since these processes change the grid-mean humidity, they are able to modify the cloud cover and, hence, the amount of condensation at the next timestep.

The total changes per timestep of humidity and temperature are given by

$$\Delta q = \Delta q_{\mathrm{f}} + (1 - C)\Delta q_{\mathrm{e}} - Q_{\mathrm{cnd}} \tag{2.253}$$

$$\Delta T = \Delta T_{\mathrm{f}} + \frac{L_{\mathrm{v}}}{c_{\mathrm{p}}} Q_{\mathrm{cnd}} \tag{2.254}$$

Depositional growth ($Q_{\mathrm{dep}} > 0$) and sublimation ($Q_{\mathrm{dep}} < 0$) of cloud ice is calculated in a way analogous to condensation/evaporation if one of the following conditions apply

(i) $T < -35°\mathrm{C}$ or

(ii) $T < 0°\mathrm{C}$ and $x_{\mathrm{i}} >$ threshold value γ_{thr} where x_{i} is the in-cloud ice water mixing ratio

with Q_{cnd} and L_{v} in Eqs. (2.251) - (2.254) replaced by Q_{dep} and L_{s}, respectively.

Condition (ii) can be considered as a simple parameterization of the Bergeron-Findeisen process describing the fact that the equilibrium vapor pressure over water is greater than the saturation vapor pressure over ice, at the same temperature. Therefore, in mixed phase clouds, the water droplets tend to move to the lower pressure over the ice. The vapor will be condensed and freeze onto the ice crystal, causing it to grow larger.

Sedimentation of cloud ice

Sedimentation of cloud ice is formally treated like vertical advection, i.e. the algorithm is applied to grid-cell mean values so that the flux divergence is given by

$$\left(\frac{\partial \overline{r}_{\mathrm{i}}}{\partial t}\right)_{\mathrm{sed}} = \frac{1}{\rho}\frac{\partial \overline{F}_{\mathrm{i}}}{\partial z} = \frac{1}{\rho}\frac{\partial \left(\rho \overline{v}_{\mathrm{i}} \overline{r}_{\mathrm{i}}\right)}{\partial z} \tag{2.255}$$

where the fall velocity is parameterized as $\overline{v}_{\mathrm{i}} = \alpha \left(\rho \overline{r}_{\mathrm{i}}\right)^{\beta}$ with $\alpha = 3.29$ and $\beta = 0.16$ (Heymsfield and Donner, 1990). Equation (2.255) can be expressed in discrete form as

$$Q_{\mathrm{sed}} \equiv \left(\frac{\partial \overline{r}_{\mathrm{i}}}{\partial t}\right)_{\mathrm{sed}} \approx \frac{1}{\rho \Delta z}\left(\overline{F}_{\mathrm{i}}^{\mathrm{top}} - \rho \overline{v}_{\mathrm{i}} \overline{r}_{\mathrm{i}}\right) \tag{2.256}$$

where $\overline{F}_{\mathrm{i}}^{\mathrm{top}}$ is the incoming sedimentation flux which has already been subject to sublimation and melting. By keeping $\overline{F}_{\mathrm{i}}^{\mathrm{top}}$ as well as $\overline{v}_{\mathrm{i}}$ constant during a time step interval, (2.256) can be solved analytically (Rotstayn (1997); see also section 2.7.3). The flux leaving the respective layer, $\overline{F}_{\mathrm{i}}^{\mathrm{bot}}$, is obtained by integrating (2.256) over the layer, giving

$$\overline{F}_{\mathrm{i}}^{\mathrm{bot}} = \overline{F}_{\mathrm{i}}^{\mathrm{top}} - \rho \Delta z Q_{\mathrm{sed}}. \tag{2.257}$$

As the integration proceeds from the top of the model down to the surface, the flux at the bottom of a layer can be used as incoming flux for the layer beneath. In the lowest model layer ($k = N$), the flux $\overline{F}_{\mathrm{i}}^{\mathrm{bot}}(k = N) \equiv \overline{F}_{\mathrm{i}}(p_{\mathrm{s}})$, representing the ice sedimentation at the surface, where p_{s} is surface pressure, is added to the snow flux according to (2.280).

Freezing of cloud liquid water and melting of cloud ice

At temperatures $T < -35°C$, the total amount of cloud liquid water freezes homogeneously and instantaneously, during one time step Δt, to cloud ice Levkov et al. (1992) so that

$$Q_{\text{frh}} = \frac{\overline{r}_1}{\Delta t}. \tag{2.258}$$

For stochastical and heterogeneous freezing in the temperature range -35°C $\leq T < 0$°C, we use the extrapolated equation by Bigg (1953) down to the cloud droplet size (Levkov et al., 1992; Murakami, 1990).

$$Q_{\text{frs}} = Ca_1\{\exp[b_1(T_0 - T)] - 1\}\frac{\rho r_1^2}{\rho_{\text{w}}N_1} \tag{2.259}$$

where the constants $a_1 = 100$ m^{3}s^{-1} and b_1=0.66 K^{-1} are taken from laboratory experiments, $T_0 = 273.15$ K is the freezing point, $\rho_{\text{w}} = 1000$ kgm^{-3} is the density of water, ρ the air density, T the grid-cell mean temperature, r_1 the in-cloud liquid water mixing ratio, N_1 is the cloud droplet number concentration, and C the fractional cloud cover. N_1 is prescribed within the atmospheric boundary layer ($= 220\cdot10^6$ m^{-3} over land and $80 \cdot 10^6$ m^{-3} over sea, respectively). Above the boundary layer, N_1 decreases exponentially to 50 m^{-3} in the upper troposphere over both land and ocean.

Brownian diffusion contact nucleation results from random collisions of aerosol particles with supercooled cloud droplets. It may be written as (e.g. Levkov et al. (1992))

$$Q_{\text{frc}} = Cm_{\text{io}}F_1DF_{\text{ar}} \tag{2.260}$$

where $m_{\text{io}} = 10^{-12}$ kg is the initial mass of a nucleated ice crystal, $DF_{\text{ar}} = 1.4 \cdot 10^{-8}$ m^{-2}s^{-1} the aerosol diffusivity (Pruppacher and Klett, 1978), and $F_1 = (4\pi R_{\text{vl}}N_1N_{\text{a}})/\rho$. The concentration of active contact nuclei is approximated as $N_{\text{a}} = \max[N_{\text{a0}}(T_0 - T - 3), 0]$, with $N_{\text{a0}} = 2 \cdot 10^5$ m^{-3}, and the mean volume droplet radius, R_{vl}, is obtained from

$$\frac{4}{3}\pi R_{\text{vl}}^3 N_1\rho_{\text{w}} = r_1\rho. \tag{2.261}$$

Following Levkov et al. (1992), cloud ice is assumed to melt completely when $T > T_0$, giving

$$Q_{\text{mli}} = \frac{\overline{r}_{\text{i}}}{\Delta t}. \tag{2.262}$$

Precipitation formation in warm clouds, cold clouds and in mixed-phase clouds

In warm clouds ($T > 0$°C) and also in mixed phase clouds (-35°C $\leq T < 0$°C), the cloud liquid water content can be diminished by autoconversion of cloud droplets, Q_{aut}, growth of rain drops by accretion of cloud droplets, Q_{racl}, and growth of snow crystals by accretion of cloud droplets, Q_{sacl}. The autoconversion rate is derived from the stochastic collection equation

which describes the time evolution of a droplet spectrum changing by collisions among droplets of different size (Beheng, 1994) which gives

$$Q_{\text{aut}} = C\gamma_1 \left[a_2 n^{-b_2} \left(10^{-6} N_l \right)^{-b_3} \left(10^{-3} \rho r_l \right)^{b_4} \right] / \rho \tag{2.263}$$

where $a_2 = 6 \cdot 10^{28}$, $n = 10$ is the width parameter of the initial droplet spectrum described by a gamma distribution, $b_2 = 1.7$, $b_3 = 3.3$, $b_4 = 4.7$, and γ_1 is a tunable parameter which determines the efficiency of the autoconversion process and, hence, cloud lifetime.

Raindrops, once formed, continue to grow by accretion of cloud droplets. The accretion rate is derived from the stochastic collection equation (Beheng, 1994)

$$Q_{\text{racl}} = \min(C, C_{\text{pr}}) a_3 r_l \rho r_{\text{rain}} + \gamma_2 \rho Q_{\text{aut}} \Delta t \tag{2.264}$$

where r_{rain} is the mass mixing ratio of rain falling into a fraction C_{pr} of the respective grid-cell, and $a_3 = 6 \, \text{m}^3 \text{kg}^{-1} \text{s}^{-1}$. The second term in the bracket is the local rainwater production during a time step by autoconversion, and γ_2 is a tunable parameter. The remaining precipitation process occurring in the cloud liquid water equation, Q_{sacl}, will be discussed below together with the analogous process for cloud ice, Q_{saci}.

The conversion rate from cloud ice to snow by aggregation of ice crystals has been adopted from Levkov et al. (1992), based on the work of Murakami (1990)

$$Q_{\text{agg}} = C\gamma_3 \frac{\rho r_i^2 a_4 E_{\text{ii}} X \left(\frac{\rho_0}{\rho} \right)^{1/3}}{-2\rho_i \log \left(\frac{R_{\text{vi}}}{R_{\text{s0}}} \right)^3} \tag{2.265}$$

where $a_4 = 700 \, \text{s}^{-1}$ is an empirical constant, $E_{\text{ii}} = 0.1$ is the collection efficiency between ice crystals, $X = 0.25$ is the dispersion of the fall velocity spectrum of cloud ice, $\rho_0 = 1.3 \, \text{kgm}^{-3}$ is a reference density of air, $\rho_i = 500 \, \text{kgm}^{-3}$ is the density of cloud ice, R_{vi} is the mean volume ice crystal radius, $R_{\text{s0}} = 10^{-4} \, \text{m}$ is the smallest radius of a particle in the snow class, and γ_3 is a tunable parameter. From simultaneous measurements of ρr_i, R_{vi} and the effective radius of ice crystals, R_{ei}, Moss (1996; personal communication) derived the following relationships

$$R_{\text{ei}} = a_5 \left(10^3 \rho r_i \right)^{b_5} \tag{2.266}$$

$$R_{\text{ei}}^3 = R_{\text{vi}}^3 \left(a_6 + b_6 R_{\text{vi}}^3 \right) \tag{2.267}$$

with R_{ei}, R_{vi} in μm, $a_5 = 83.8$, $b_5 = 0.216$, $a_6 = 1.61$, $b_6 = 3.56 \cdot 10^{-4}$, so that after solving for (2.267)

$$R_{\text{vi}}[m] = 10^{-6} \left(\sqrt{2809 R_{\text{ei}}^3 + 5113188} - 2261 \right)^{1/3}. \tag{2.268}$$

The accretional growth of snow through riming and collecting of ice crystals is based on Lin et al. (1983) and Levkov et al. (1992). Snow crystals are assumed to be exponentially distributed (Gunn and Marshall, 1958)

$$n_{\mathrm{s}}(D_{\mathrm{s}}) = n_{0s} \exp(-\lambda_{\mathrm{s}} D_{\mathrm{s}}) \tag{2.269}$$

where $n_{\mathrm{s}}(D_{\mathrm{s}})$ is the concentration of particles of diameters D_{s} per unit size interval, D_{s} is the diameter of the snow particle, $n_{0\mathrm{s}} = 3 \cdot 10^6$ m^{-4} is the intercept parameter obtained from measurements (Gunn and Marshall, 1958), and λ_{s} is the slope of the particle size distribution and is written as (Potter, 1991)

$$\lambda_{\mathrm{s}} = \left(\frac{\pi \rho_{\mathrm{s}} n_{0\mathrm{s}}}{\rho r_{\mathrm{snow}}} \right)^{1/4} \tag{2.270}$$

where $\rho_{\mathrm{s}} = 100$ kgm^{-3} is the bulk density of snow and r_{snow} is the mass mixing ratio of snow. Snow crystals settle through a population of supercooled cloud droplets, colliding and coalescing with them (riming). The rate of change in the snow mixing ratio is based on geometric sweep-out concept integrated over the size distribution (2.269)

$$Q_{\mathrm{sacl}} = \min(C, C_{\mathrm{pr}}) \gamma_4 \frac{\pi E_{\mathrm{sl}} n_{0\mathrm{s}} k_{\mathrm{s}} r_{\mathrm{l}} \Gamma(3 + b_7)}{4 \lambda_{\mathrm{s}}^{3+b_7}} \left(\frac{\rho_0}{\rho} \right)^{1/2} \tag{2.271}$$

where $k_{\mathrm{s}} = 4.83$ m^{2}s^{-1}, $b_7 = 0.25$, $E_{\mathrm{sl}} = 1$ is the collection efficiency of snow for cloud droplets (Lin et al., 1983) and γ_4 is a tunable parameter. The accretion rate of ice crystals by snow is similar to (2.271) and is expressed as

$$Q_{\mathrm{saci}} = \min(C, C_{\mathrm{pr}}) \frac{\pi E_{\mathrm{si}} n_{0\mathrm{s}} k_s r_{\mathrm{i}} \Gamma(3 + b_7)}{4 \lambda_{\mathrm{s}}^{3+b_7}} \left(\frac{\rho_0}{\rho} \right)^{1/2} \tag{2.272}$$

where the collection efficiency of snow for cloud ice is assumed to be temperature dependent according to $E_{\mathrm{si}} = \exp[-a_7(T_0 - T)]$ with $a_7 = 0.025$. Note that $r_{\mathrm{i}} = 0$ for $T > T_0$ (c.f.,(2.262)) so that $Q_{\mathrm{saci}} = 0$ in this case. Analogous to (2.264), ρr_{snow} used in (2.271) and (2.272) through (2.270) consists of two parts. The first one is a contribution from the snow flux into the respective grid-cell (c.f., section 2.7.3), and the second one, $\gamma_2 \rho Q_{\mathrm{agg}} \Delta t$, is due to local snow generation through aggregation of ice crystals (2.265).

Evaporation of rain and sublimation of snow and ice

The evaporation of rain is obtained by integration of the evaporation for a single rain drop of diameter D_{r} over the Marshall-Palmer distribution (Marshall and Palmer, 1948). The rate of change can then be expressed as

$$Q_{evr} = C_{\mathrm{pr}} \frac{2\pi n_{0\mathrm{r}} S_{\mathrm{l}}}{\rho(A' + B')} \left[\frac{a_8}{\lambda_{\mathrm{r}}^2} + \frac{b_8 S_{\mathrm{c}}^{1/3}}{\lambda_{\mathrm{r}}^{\delta_{\mathrm{r}}/2}} \Gamma\left(\frac{\delta_{\mathrm{r}}}{2} \right) \left(\frac{k_{\mathrm{r}}\rho}{\mu} \right)^{1/2} \left(\frac{\rho_0}{\rho} \right)^{1/4} \right] \tag{2.273}$$

where $A' = L_v^2/(K_a R_v T^2)$, $B' = 1/(\rho r_{sl} D_v)$, K_a is the thermal conductivity of air, R_v is the gas constant for water vapor, D_v is the diffusivity of vapor in the air, $n_{0r} = 8 \cdot 10^6$ m^{-4} is the intercept parameter, r_{sl} is the saturation water vapor mixing ratio with respect to liquid water, $S_l = 1 - r_v/r_{sl}$ is the respective sub-saturation, $S_c = \mu/(\rho D_v)$ is the Schmidt number, μ is the dynamic viscosity of air, $\delta_r = 5.5$, $a_8 = 0.78$, $b_8 = 0.31$, $k_r = 141.4$ m^{2}s^{-1}, and the slope of the size distribution is defined as

$$\lambda_r = \left(\frac{\pi \rho_w n_{0r}}{\rho r_{rain}} \right)^{1/4}. \tag{2.274}$$

Instead of (2.273) we use a simplified form obtained after minor simplifications and evaluation of parameters after Rotstayn (1997)

$$Q_{evr} = C_{pr} \frac{a_9 S_l}{\rho^{1/2}(A' + B')} \left(\frac{P_r}{C_{pr}} \right)^{b_9} \tag{2.275}$$

where P_r is the rain flux [kgm^{-2}s^{-1}], $a_9 = 870$ and $b_9 = 0.61$.

Analogously, the sublimation of snow is obtained by integrating the sublimation for a single particle of diameter D_s over the Gunn-Marshall distribution (2.269). The time rate of change can then be expressed as

$$Q_{sbs} = C_{pr} \frac{2\pi n_{0s} S_i}{\rho(A'' + B'')} \left[\frac{a_8}{\lambda_s^2} + \frac{b_8 S_c^{1/3}}{\lambda_s^{\delta_s/2}} \Gamma\left(\frac{\delta_s}{2} \right) \left(\frac{k_s \rho}{\mu} \right)^{1/2} \left(\frac{\rho_0}{\rho} \right)^{1/4} \right], \tag{2.276}$$

where $A'' = L_s^2/K_a R_v T^2)$, $B'' = 1/(\rho_{si} D_v)$, r_{si} is the saturation water vapor mixing ratio with respect to ice, $S_i = 1 - r_v/r_{si}$ is the respective sub-saturation, $\delta_s = 5.25$ and $k_s = 4.83$ m^{2}s^{-1} (Levkov et al., 1992). The expression (2.276) is used for sublimation of both snowfall, Q_{sbs}, and falling ice, Q_{sbis}. Note that in Q_{sbis} the slope parameter λ_s (2.270) includes the ice mixing ratio, r_{ised}, instead of r_{snow} (see section 2.7.3).

Precipitation

The total amount of non-convective precipitation at a certain pressure level, p, is obtained by integrating the relevant processes from the top of the model ($p = 0$) to the respective pressure level. The fluxes of rain and snow [kgm^{-2}s^{-1}] can then be expressed as

$$P_{rain}(p) = \frac{1}{g} \int_0^p (Q_{aut} + Q_{racl} - Q_{evr} + Q_{mls}) \, dp \tag{2.277}$$

$$P_{snow}(p) = \frac{1}{g} \int_0^p (Q_{agg} + Q_{sacl} + Q_{saci} - Q_{sbs} - Q_{mls}) \, dp \tag{2.278}$$

with the snow melt, Q_{mls}, defined in (2.284). The sedimentation (see section 2.7.3) is given by

$$\bar{F}_i(p) = -\frac{1}{g} \int_0^p Q_{sed} \, dp \geq 0 \tag{2.279}$$

where Q_{sed} includes the effects of sublimation Q_{sbis}, and melting, Q_{mlis}. At the surface $(p = p_{\text{s}})$, the sedimentation is added to the snow fall so that the total snow flux is given by

$$P_{\text{snow}}(p_{\text{s}}) = \frac{1}{g} \int_0^{p_{\text{s}}} \left(Q_{\text{agg}} + Q_{\text{sacl}} + Q_{\text{saci}} - Q_{\text{sbs}} - Q_{\text{mls}} \right) dp + \bar{F}_{\text{i}}(p_{\text{s}}). \tag{2.280}$$

Melting of falling ice and snow is calculated from the heat budget in case the air temperature exceeds the freezing point. The excess heat in the respective model layer with pressure thickness, Δp, is then used for melting all or part of the snow and/or ice sedimentation according to

$$\frac{c_{\text{p}} \left(\tilde{T} - T_0 \right)}{\Delta t} \frac{\Delta p}{g} = \max(L_{\text{f}} \hat{M}, 0) \tag{2.281}$$

where $\tilde{T}$ includes all processes except melting, and $\hat{M}$ is the preliminary amount of melting. The actual amount of melting depends not only on the excess heat, according to (2.281), but also on the available snow fall, P_{snow}, and/or incoming sedimentation flux, $\bar{F}_{\text{i}}^{\text{top}}$:

$$M_{\text{snow}} = min(P_{\text{snow}}, \hat{M}) \tag{2.282}$$
$$M_{\text{ice}} = min(\bar{F}_{\text{i}}^{\text{top}}, \hat{M}) \tag{2.283}$$

The temperature change associated with melting (c.f., (2.247)) can be written as

$$\left(\frac{\partial T}{\partial t} \right)_{\text{melt}} = -\frac{L_{\text{f}}}{c_{\text{p}}} (Q_{\text{mls}} + Q_{\text{mlis}}) \tag{2.284}$$

with $Q_{\text{mls}} \equiv M_{\text{snow}} \cdot g / \Delta p$ and $Q_{\text{mlis}} \equiv M_{\text{ice}} \cdot g / \Delta p$.

The precipitation fluxes (2.277) - (2.280) represent grid-cell averages, while the accretion processes (2.264), (2.271) and (2.272) as well as evaporation of rain (2.275) and sublimation of snow (2.276) depend on the fractional area, C_{pr}, of a grid-cell covered with precipitation. Our approach for estimating C_{pr} is a slight modification of that employed by Tiedtke (1993), as defined in Jakob and Klein (1999)

$$C_{\text{pr}}^k = \max \left(\hat{C}_{\text{pr}}, \frac{C^k \Delta Pr^k + \hat{C}_{\text{pr}} Pr^{k-1}}{\Delta Pr^k + Pr^{k-1}} \right) \tag{2.285}$$

where Pr^{k-1} is the total precipitation flux, $P_{\text{rain}} + P_{\text{snow}}$, at model level $k - 1$, ΔPr^k is the amount of precipitation produced locally in the layer beneath, C^k is the fractional cloud cover in layer k and

$$\hat{C}_{\text{pr}} = \left(\begin{array}{l} C^k \text{ for } \left(\Delta Pr^k \geq Pr^{k-1} \right) \\ C_{\text{pr}}^{k-1} \text{ for } \left(\Delta Pr^k < Pr^{k-1} \right) \end{array} \right). \tag{2.286}$$

According to (2.285) and (2.286), the vertical profile of C_{pr} is related to the profiles of both fractional cloud cover and precipitation. In case the local precipitation production exceeds the incoming flux, the precipitation fraction is given by $C_{\text{pr}}^k = C^k$. Note also that $C_{\text{pr}}^k = 0$ for $\Delta Pr^k + Pr^{k-1} = 0$.

Mixing ratios of rain, falling ice and snow

The mass mixing ratio of rain, r_{rain}, is related to the rain flux by

$$\rho r_{\text{rain}} = P_{\text{rain}}/(C_{\text{pr}} v_{\text{r}}) \tag{2.287}$$

where $P_{\text{rain}}/C_{\text{pr}}$ is the rain flux within the fraction of the grid-cell covered with rain, and v_{r} is the mass-weighted fall velocity of rain drops parameterized according to Kessler (1969)

$$v_{\text{r}} = a_{10} \left(\frac{\rho r_{\text{rain}}}{n_{0\text{r}}} \right)^{1/8} \left(\frac{\rho_0}{\rho} \right)^{1/2} \tag{2.288}$$

with the intercept parameter $n_{0\text{r}} = 8 \cdot 10^6$ m^{-4} and $a_{10} = 90.8$. By using (2.288) in (2.287) we obtain

$$\rho r_{\text{rain}} = \left(\frac{P_{\text{rain}}}{C_{\text{pr}} a_{10} (n_{0\text{r}})^{-1/8} \sqrt{\rho_0/\rho}} \right)^{8/9}. \tag{2.289}$$

According to (2.255), the mass mixing ratio of falling ice can be obtained from

$$r_{\text{ised}} = \overline{F}_{\text{i}}^{\text{top}}/(\rho v_{\text{i}}) \tag{2.290}$$

where v_{i} is the fall velocity of cloud ice, $\overline{F}_{\text{i}}^{\text{top}}$ is the grid-cell mean sedimentation flux and v_{i} parameterized as in (2.255) by employing the Heymsfield and Donner (1990) approach

$$v_{\text{i}} = a_{11} (\rho r_{\text{ised}})^{b_{10}} \tag{2.291}$$

with $a_{11} = 3.29$ and $b_{10} = 0.16$. By using (2.291) in (2.290) we obtain

$$\rho r_{\text{ised}} = \left(\frac{\overline{F}_{\text{i}}^{\text{top}}}{a_{11}} \right)^{1/(1+b_{10})}. \tag{2.292}$$

Analogously, the mass mixing ratio of snow within the fraction C_{pr} of the grid-cell covered with snow is obtained from the snow fall rate according to

$$\rho r_{\text{snow}} = \left(\frac{P_{\text{snow}}}{C_{\text{pr}} a_{11}} \right)^{1/(1+b_{10})}. \tag{2.293}$$

Solution method and parameter choice

The cloud microphysical terms are solved in a split manner, i.e. sequentially. In the following, a subscript n denotes the value of a variable before application of the respective process, while $n+1$ denotes the updated value after application of the process. A major part of the microphysics is solved analytically (Q_{frs}, Q_{aut}, Q_{agg}, Q_{racl}, Q_{sacl}, and Q_{saci}), and these terms can formally be written as

$$\frac{\partial \Psi}{\partial t} = -F_\Psi \Psi^z \tag{2.294}$$

where $F_\Psi > 0$ is kept constant during the respective time interval, Δt, and $z \geq 1$. In the linear case, i.e. for all accretion processes (Q_{racl}, Q_{sacl}, Q_{saci}), the solution of (2.294) is given by

$$\Psi_{n+1} = \Psi_n \exp(-F_\Psi \Delta t). \tag{2.295}$$

For $z > 1$, i.e. for $Q_{\text{frs}}(z = 2)$, $Q_{\text{aut}}(z = 4.7)$ and $Q_{\text{agg}}(z = 2)$, the solution of (2.294) is given by

$$\Psi_{n+1} = \Psi_n \left[1 + F_\Psi \Delta t (z-1) \Psi_n^{z-1} \right]^{1/(1-z)}. \tag{2.296}$$

An analytical solution can also be obtained for the ice sedimentation equation (2.256) which can be written in the form

$$\frac{\partial \Psi}{\partial t} = A - B\Psi \tag{2.297}$$

where A and B are constants. The solution after one time step interval, Δt, is given by

$$\Psi_{n+1} = \Psi_n \exp(-B\Delta t) + \frac{A}{B}[1 - \exp(-B\Delta t)]. \tag{2.298}$$

In the sedimentation equation, $\overline{F}_i^{\text{top}}$ is included in A, while the fall velocity v_i is included in B. Both are assumed constant during the respective time step interval.

The microphysics scheme includes a large number of parameters, $(a_1, a_2, ..., a_{11})$ and $(b_1, b_2, ..., b_{10})$, which are kept constant as part of the parameterizations. On the other hand, $(\gamma_1, \gamma_2, \gamma_3, \gamma_4)$, in (2.263), (2.264), (2.265), and (2.271), respectively, are used as 'tuning' parameters. This can be justified to some extent because these parameterizations are based on detailed microphysical models and cannot be applied to large-scale models without adjustment. The following values are used in `ECHAM6`: $\gamma_1 = 15$; $0 \leq \gamma_2 \leq 0.5$ depending on model resolution; $\gamma_3 = 95$; $\gamma_4 = 0.1$; $\gamma_{\text{thr}} = 5 \cdot 10^{-7}$ kgkg^{-1}.

2.8. Parameterization of the momentum flux deposition due to a gravity wave spectrum

The parameterization of the effects of a gravity wave spectrum is based on the Doppler spread theory of propagation and dissipation of a gravity wave spectrum as formulated by Hines (1991a,b,c, 1993). The simplifications to the Doppler spread theory necessary for developing the parameterization are discussed in Hines (1997a,b). Here the version of the parameterization formulated following Hines (1997a,b) that has been implemented in the middle atmosphere (MA) version of ECHAM5 (Manzini et al. (2006); Giorgetta et al. (2006)) is presented. The impact of the Doppler spread parameterization in the middle atmosphere of the previous model cycle (MAECHAM4) has been discussed by Manzini et al. (1997) and Manzini and McFarlane (1998).

2.8.1. Hines Doppler spread theory

During the last decades, an increasing number of observations by a variety of techniques has contributed to the current characterization of atmospheric gravity waves (among others, Allen and Vincent (1995); Eckermann et al. (1994); Hamilton (1991); Smith et al. (1987); Dewan and Good (1986); Hirota (1984)). The forcing mechanisms generating the gravity waves are most likely located in the troposphere, and may include convective activity, shear instabilities, frontal systems, transient flow over topography. In the middle atmosphere, the gravity waves appear to propagate predominantly upward from their tropospheric source regions and they appear to form a broad background spectrum of waves.

On the basis of these observations, the Hines Doppler spread theory (henceforth, HDST) assumes an interacting and upward propagating gravity wave spectrum with tropospheric sources. The HDST does not directly deal with the forcing mechanisms of the gravity waves. The HDST considered in the current parameterization only assumes that the variety of the forcing mechanisms gives rise to a broad band and continuous spectrum. Within this framework, quasi monochromatic waves cannot be take into account, although extensions are possible (Hines, 1997b).

Evidence that the vertically propagating gravity waves are dissipating and therefore interacting with the large scale flow has been derived form the observations that the amplitude of the spectrum at high vertical wavenumbers tends not to change with height, in spite of the growth expected in response to the decrease in atmospheric density, a behavior usually termed saturation (Smith et al., 1987; Dewan and Good, 1986). A variety of processes can be responsible for saturation (see Fritts (1984, 1989) for reviews). According to the HDST, as the gravity waves propagate upwards from the troposphere to the mesosphere, an essential role in the saturation process is played be the nonlinear advective interaction exerted on each wave component of the spectrum by the gravity wave wind field induced by the other waves.

The HDST builds upon gravity wave theory for small amplitude waves propagating in a mean flow that is uniform horizontally and temporally and slowly varying in altitude (for a review of gravity wave theory see Andrews et al. (1987)). The core aspects of the Hines Doppler spread theory (Hines, 1991a,b,c, 1993) are here briefly summarized:

1. The effects of the wind field induced by the other waves on each wave component of the spectrum at a given height are assumed to be approximately determined by treating the

wave induced wind field as a background horizontal wind field, slowly varying in altitude while horizontally and temporally uniform. As the waves propagate upward, their vertical wavenumber spectrum is therefore modified, and in turn the spectral characteristics of the wave induced wind field are also modified. In a statistical sense, the modification induced by the advective nonlinear interaction is found to be a Doppler spreading of the vertical wavenumber spectrum towards high wavenumbers.

2. In conformity with wave theory, wave action density is conserved as the waves propagate upwards, until the gravity wave spectrum as a whole becomes unstable and the waves at high vertical wavenumbers break down into turbulence. For parameterization purposes the transition to turbulence is taken to occur at a specific vertical wavenumber, the *maximum permissible vertical wavenumber m_M*, and the breaking waves (with $m > m_M$) are removed from the spectrum. Within the HDST it is possible to assume a more complex and smooth transition to turbulence. The momentum carried by the waves that have been removed is deposited into the large scale background flow.

3. In agreement with wave-mean flow interaction theory (Andrews et al., 1987), within the HDST formulation the background large scale flow has the effect of producing Doppler shifts of the vertical wavenumber. In the presence of a background large scale flow, differential momentum flux deposition (hence forcing of the large scale flow) can therefore occur also for an isotropic gravity wave spectrum. Consequently, it becomes necessary to take into account the variations in the azimuth of wave propagation. Note that in the absence of a background large scale flow and for an isotropic gravity wave spectrum, the momentum flux would be deposited isotropically and no *net* deposition of momentum flux would occur.

4. An aspect of the Hines formulation crucial to the practical development of a parameterization is that at any given height, the spectral characteristics of the gravity waves are determined by a modification of the gravity wave spectrum at a specified low altitude. The calculation of the spectral evolution with altitude is therefore by-passed in the parameterization, by keeping track of the portion of the gravity wave spectrum at the specified low altitude which continue to propagate upward. The largest vertical wavenumber of the spectrum at the specified low altitude that continues to propagate upward at the current height of interest is called the *cutoff vertical wavenumber m_C*. The vertical evolution of m_C is the key computation of the parameterization. A drastic reduction of the gravity wave quantities describing the vertical evolution of the gravity wave spectrum is therefore achieved, a requirement for any parameterization of practical use in a general circulation model.

2.8.2. The Hines Doppler Spread Parameterization (HDSP)

The quantity that has to be evaluated is the deposition of the horizontal momentum transferred by the vertically propagating gravity waves (what is referred to as momentum flux deposition). As commonly done in a general circulation model, only vertical propagation is considered, assuming that a gridbox is large enough that oblique propagation (outside the vertical column) can be neglected. For each gridbox, the dependence in the azimuth of wave propagation must be discretized: the total number of azimuths considered is defined to be J. It is assumed (although not necessary) that the J azimuths are equally spaced around the azimuth circle.

Within this framework, the HDSP requires the specification of the input gravity wave spectrum

at some low altitude (within the forcing region). Thereafter, the momentum flux deposition is determined in function of the large scale flow and buoyancy frequency, the input gravity wave spectrum at a specified low altitude, and a limited number of height varying gravity wave related quantities, the most important being the horizontal wind variance and the cutoff vertical wavenumber. These quantities are defined and derived below.

At any given height, the broad band gravity wave spectrum is characterized by the power spectral density H_j^2 of the horizontal winds associated with the gravity waves at that height in the j-th azimuth. The power spectral density is a function of horizontal wavenumber k (a directional wavenumber in the j-azimuth) and vertical wavenumber m. The spectrum is assumed to be separable in k and m. For convenience, k and m are made positive for upward propagating waves.

The *horizontal wind variance* at the height of interest that is contributed by the waves propagating in the j-th azimuth is the integral over all positive horizontal and vertical wavenumbers of the power spectral density:

$$s_j^2 = \int_0^{m_M} \int_0^\infty H_j^2 dk dm \tag{2.299}$$

The integral in the vertical wavenumber is limited by the maximum permissible vertical wavenumber m_M (see point 2 in section 2.8.1). The s_j^2 are derived in section 2.8.2.

At any given height, the *total rms horizontal wind speed σ_T* is contributed by gravity waves propagating in all azimuths:

$$\sigma_T = \left(\sum_{j=1}^J s_j^2 \right)^{1/2} \tag{2.300}$$

At any given height, the *total rms horizontal wind speed σ_j in the j-th azimuth* depends on the variance from waves in the j-th azimuth and in all other azimuths, non-orthogonal to the j-th direction. These contributions must be added up, and they are found by projecting the s_j^2 wind variances on the azimuth of interest. The total rms horizontal wind speed σ_j in the j-th azimuth is:

$$\sigma_j = \left(\sum_{p=1}^J s_p^2 \cos(\alpha_p - \alpha_j)^2 \right)^{1/2} \tag{2.301}$$

where α_p and α_j are respectively the p- and j-th azimuth.

The height where the gravity wave spectrum is specified is defined to be the *initial (or launching) height*, and any gravity wave quantity at the initial height is given the subscript I.

Cutoff vertical wavenumber

At any given height, the dispersion relation for an individual gravity wave with azimuth j in a background flow that is horizontally and temporally uniform, is:

$$\omega/k = N/m + V_j + v_j \tag{2.302}$$

where k is the horizontal wavenumber, m the vertical wavenumber, ω the ground based frequency, N the buoyancy frequency, and V_j and v_j are respectively the large scale background flow and the wave induced wind field in the j-th azimuth. For convenience, k, ω and m are made positive for upward propagating waves. Given that ω and k are height independent, from the combination of equation (2.302) as written for the initial height and for some overlying height of interest, it is obtained:

$$N/m = N_I/m_I + V_{jI} - V_j - v_j \tag{2.303}$$

assuming that the induced wave field at the initial height is negligible. Equation (2.303) expresses the mapping between the vertical wavenumber m at the height of interest and the corresponding vertical wavenumber m_I at the initial height. In equation (2.303), N_I and V_{jI} are respectively the buoyancy frequency and the j-directed large scale background flow at the initial height.

Equation (2.303) shows that as $V_j + v_j$ increases, the vertical wavenumber m is Doppler shifted to infinity and into negative values. Before reaching negative values, at sufficiently large vertical wavenumbers, the spectrum is likely to become unstable and dissipative processes are likely to take place (the vertical wavelength is reduced, critical level conditions are approached). In practice, it is assumed that this transition occurs at a specific vertical wavenumber m_M (large, positive and less than infinity), the maximum permissible vertical wavenumber of the spectrum at the height of interest (already introduced, see point 2 in section 2.300). The waves with wavenumbers equal or larger than m_M are supposed to be dissipated and are removed from the spectrum. The vertical wavenumber m_M may be reached by a wave when the wave induced wind field v_j increases to the value:

$$v_{jM} = N_I/m_I - N/m_M + V_{jI} - V_j \tag{2.304}$$

The probability for the induced wind field to meet condition (2.304) was first derived in Hines (1993) for the case of no large scale background flow and m_M equal to infinity, in order to determine the cutoff vertical wavenumber m_C (see point 4 in section 2.8.1). In Hines (1993) it was found that the probability for a wave to survive to some height decreases rapidly as m_I enters a particular critical range. On the basis of this rapid transition and further approximations (Hines, 1997a), an expression for v_{jM} is found in order to evaluate a provisional (i.e., subject to two conditions expressed below) cutoff vertical wavenumber in the j-th azimuth for the general case of a positive and finite m_M and a nonzero background flow:

$$\{m_j\}_{TRIAL} = N_I(N/m_M + V_j - V_{jI} + \Phi_1\sigma_j)^{-1} \tag{2.305}$$

with v_{jM} expressed in terms of the total rms wind speed in the j-th azimuth σ_i. The coefficient Φ_1 that appears in (2.305) is a nondimensional factor that lays in the range: $1.2 < \Phi_1 < 1.9$, deduced in Hines (1993, 1997a). In (2.305) the cutoff vertical wavenumber m_C is a function of azimuth and is denoted m_j.

The maximum permissible wavenumber m_M was determined in Hines (1991b) by the condition of marginal instability of the total wave system. In Hines (1997a) the derivation is extended by approximation to the case of a nonzero background flow, so that:

$$N/m_M = \Phi_2 \sigma_T \tag{2.306}$$

where Φ_2 is a second nondimensional factor that lays in the range: $0.1 < \Phi_2 < 0.4$ deduced in Hines (1991b, 1997a). The limits of Φ_2 are intended to roughly correspond to 17% or 8% of space time being convectively unstable, with and additional 10% or 4 % being dynamically unstable. Inserting (2.306) in (2.305), the provisorial cutoff wavenumber in the j-th azimuth becomes:

$$\{m_j\}_{TRIAL} = N_I(\Phi_2 \sigma_T + V_j - V_{jI} + \Phi_1 \sigma_j)^{-1} \tag{2.307}$$

Equation (2.307) is the fundamental equation of the HDSP. The first term on the right-hand side of equation (2.307) represents the effect of instability of the spectrum as a whole at the height of interest. The $V_j - V_{jI}$ term represents the effect of Doppler shifting by the background winds, common for instance also to parameterizations based on Lindzen (1981). The $\Phi_1 \sigma_j$ term (unique to this theory) represents the nonlinear effect of localized Doppler shifting on individual waves by all the other waves.

The two above mentioned conditions to be imposed on $\{m_j\}_{TRIAL}$ are: (1) the cutoff wavenumber must be monotonically non increasing with height, (2) the cutoff wavenumber must be positive. Equation (2.307) shows that these conditions can be achieved, because there always exists a positive m_j at the initial height, where $V_j - V_{jI}$ is zero.

Horizontal wind variance

At the height of interest and in the j-th azimuth, an elementary contribution of the power spectral density H_j^2 of the horizontal winds associated with the gravity waves to the horizontal wind variance is written:

$$H_j^2 dk dm = \rho^{-1} \rho_I s_{jI}^2 K_j(k) M_j(m) dk dm \tag{2.308}$$

where ρ is the atmospheric density and ρ_I is its value at the initial height. K_j and M_j are respectively the horizontal and vertical wavenumber spectra in the j-th azimuth (the spectrum is assumed to be separable in k and m). The integrals of $K_j dk$ and $M_j dm$ over all positive values are taken to be normalized to 1 at the initial height. As required by the definition of spectral density, the integral of the horizontal wind power spectral density at the initial height is therefore equal to s_{jI}^2, the horizontal wind variance at the initial height.

The theory and the parameterization as developed to date consider that the K_j spectrum is unchanging with height, while the M_j spectrum evolves in response to the background large scale flow, buoyancy frequency, and nonlinear interactions.

Thereafter, the conservation of the vertical flux of the horizontal momentum (or equivalently wave action, see point 2 in section 2.8.1) is used to compute the horizontal wind variance. Given that the vertical flux of the horizontal momentum transported by the waves that are not yet removed from the spectrum is conserved, the portion of the spectra not removed at the height of interest and that at the initial height are related by:

$$(HW)_j dm = \rho^{-1}\rho_I (HW)_{jI} dm_I \qquad (2.309)$$

where an elemental range dm_I of the initial spectrum is mapped into the range dm at the height of interest. $(HW)_j$ represents the covariance spectrum of the horizontal and vertical velocity fluctuations associated with the gravity waves, the vertical flux of horizontal momentum transferred by the waves, at the height of interest. $(HW)_{jI}$ is the covariance at the initial height.

Following gravity wave theory, the vertical velocity perturbation is in phase with the horizontal velocity perturbation and is given by k/m times the horizontal velocity, hence:

$$H_j^2 dm = \rho^{-1}\rho_I H_{jI}^2 (m/m_I) dm_I \qquad (2.310)$$

the horizontal wavenumber k being constant with height.

The determination of the horizontal wind variance in the j-th azimuth at the height of interest can therefore be achieved by integration of the right-hand side of equation (2.310) over all positive m_I up to the cut off vertical wavenumber m_j. For this purpose, m on the right must be written as a function of m_I. This can be done by means of (2.303), with the induced wind field contribution v_j ignored, under the approximation that the spreading effect is significant only for waves at large vertical wavenumber, and that the contribution of those waves to the total wind variance is small Hines (1991a):

$$m/m_I = N/N_I (1 - (V_j - V_{jI})m_I/N_I)^{-1} \qquad (2.311)$$

Substituting (2.311) into (2.310) and integrating over all positive k and m, the horizontal wind variance at any height is obtained:

$$s_j^2 = \rho^{-1}\rho_I N N_I^{-1} s_{jI}^2 \int_0^{m_j} M_{jI}(m_I)(1 - N_I^{-1}(V_j - V_{Ji})m_I)^{-1} dm_I \qquad (2.312)$$

The determination of the evoluted M_j spectrum is therefore by-passed by the mapping between the spectrum at the current height and the initial spectrum. The initial spectrum M_{jI} and the cutoff vertical wavenumber m_j are all what is needed to compute the horizontal wind variance.

Momentum flux deposition

At any given height, the vertical flux density of the j-directed horizontal momentum that is transferred upward by the j-directed waves is:

$$F_j = \rho \int_0^{m_M} \int_0^\infty (HW)_j dk dm \qquad (2.313)$$

where (HW) is the covariance spectrum of the horizontal and vertical velocity fluctuations associated with the gravity waves already introduced. Using again the conservation of horizontal momentum for the portion of the spectra not removed, the j-directed flux density at the height of interest can be written in terms of the spectrum at the initial height:

$$F_j = \rho_1 s_{jI}^2 K^* \int_0^{m_j} M_{jI}(m_I) m_I^{-1} dm_I \qquad (2.314)$$

Where K^* is obtained by the integration of $kK_j dk$ over all positive k, and by neglecting the dependence on azimuth for simplicity (although not necessary). K^* can be considered a weighted average of the directional horizontal wavenumber, and is called the *characteristic horizontal wavenumber*. In (2.314) the integral in vertical wavenumber m_I is limited by the m_j cutoff vertical wavenumber. Height variations in F_j are therefore expressed by the dependence in height of the m_j cutoff vertical wavenumber.

In order to compute the rate of horizontal momentum flux deposition at each gridpoint of the general circulation model, the momentum flux must be expressed in the cardinal eastward and northward azimuths, respectively. The rate of horizontal momentum flux deposition is thereafter given by the vertical convergence of the momentum flux in the cardinal directions.

2.8.3. Summary

The parameters that must be specified at the initial (launching) height are the total rms gravity wave wind speed σ_{TI}, the initial vertical wavenumber spectrum M_{jI}, and the s_{jI}^2 variances, which sum over the azimuths must be σ_{TI}^2, as defined in (2.300). In addition, the location of the initial height, the characteristic horizontal wavenumber K^*, and the nondimensional factors Φ_1 and Φ_2 must be specified.

Given that the current knowledge about the global and seasonal distributions of these gravity wave parameters is very limited, simple choices have been made so far, based on the generalization of observations of gravity wave variances and spectra, for instance Allen and Vincent (1995); Fritts and Nastrom (1992); Vincent et al. (1997).

The vertical wavenumber spectrum at the initial height is assumed to follow a power law form in the initial vertical wavenumber, extending from $m_I = 0$ to the cutoff vertical wavenumber m_{jI} at the initial height. Its integral must be normalized to 1 at the initial height, therefore:

$$M_{jI}(m_I) = (s+1) m_{jI}^{-s-1} m_I^s \qquad (2.315)$$

where s is the slope. The cutoff vertical wavenumber m_{jI} at the initial height is computed from (2.307) with $V_j = V_{jI}$:

$$m_{jI} = N_I(\Phi_2\sigma_{TI} + \Phi_1\sigma_{jI})^{-1} \tag{2.316}$$

The computation of the cutoff vertical wavenumber m_j thereafter proceeds upward. At the first step upward and above the m_j is obtained by (2.307), subjected to the conditions of being monotonically non increasing with height and positive. In principle, above the initial height the horizontal wind variance at that vertical level should be used in (2.307). However, the horizontal wind variance at that vertical level depends in turn on the cutoff vertical wavenumber that has to be evaluated. An iteration procedure would therefore be required. As Hines (1997a) has suggested, in case the vertical resolution of the general circulation model is sufficiently high, the iteration can be avoided by using in the computation of the m_j at any vertical level above the initial height the horizontal wind variance at the level immediately below. This approach is used in the parameterization implemented in the ECHAM model.

2.8.4. Implementation Details

The Hines gravity wave drag parameterization is by default activated in ECHAM6 at the standard resolutions T63L47 and T63L95, which both resolve the atmosphere up to 0.01 hPa. The setup generally depends on the model resolution, and is described below for the standard resolutions T63L47 and T63L95. However, the setup can be modified through the control parameters of the *gwsctl* Fortran namelist.

The launching height H_I of the parameterized gravity waves source spectrum is set to the model level, which above sea is at 680 hPa. For the L47 as well as the L95 vertical grid this is the 10th level above the surface.

The total root-mean-square gravity wave wind speed σ_{TI} is prescribed as a global constant, if *lrmscon_lat* = .FALSE. This is the default setting for ECHAM6 T63 L47.

Alternatively, if *lrmscon_lat* = .TRUE., σ_{TI} can be prescribed by a simple function of latitude allowing to distinguish the source strength near the equator from that in other latitudes. $\sigma_{TI}(\phi)$ is set to $\sigma_{TI,hi}$ for $|\phi| >= \phi_{hi}$ and $\sigma_{TI,lo}$ for $|\phi| <= \phi_{lo}$ Between latitudes ϕ_{hi} and ϕ_{lo} σ_{TI} is linearly interpolated between $\sigma_{TI,hi}$ and $\sigma_{TI,lo}$. This degree of freedom to specify an equatorial source strengths different from that in mid and high latitudes has been introduced to allow the tuning of the period of the QBO simulated in ECHAM6 configurations with high vertical resolution. For ECHAM6 T63 L95 the following parameters are used: $\phi_{lo} = 5deg$, $\phi_{hi} = 10deg$, $\sigma_{TI,lo} = 1.2m/s$, and $\sigma_{TI,hi} = 1.0m/s$.

The source spectrum is assumed to be isotropic with respect to the wind at the launch level. The s_{jI}^2 variances are distributed equally over 8 azimuth angles. Further the characteristic horizontal wavenumber K^* is set to 126 km.

Table 2.6.: Parameters, symbols and control parameters of namelist GWSCTL

Parameter	Symbol	Namelist parameters
Initial height	H_I	*emiss_lev*
Global rms wind at H_I	σ_{TI}	*rmscon*, used if *lrmscon_lat=.FALSE.*
Low latitude rms wind at H_I	$\sigma_{TI,lo}$	*rmscon_lo*, used if *lrmscon_lat=.TRUE.*
High latitude rms wind at H_I	$\sigma_{TI,hi}$	*rmscon_hi*, used if *lrmscon_lat=.TRUE.*
Low latitude limit for $\sigma_{TI,lo}$	ϕ_{lo}	*lat_rmscon_lo*, used if *lrmscon_lat=.TRUE.*
High latitude limit for $\sigma_{TI,hi}$	ϕ_{hi}	*lat_rmscon_hi*, used if *lrmscon_lat=.TRUE.*
Typical horizontal wavenumber	K^*	*kstar*

2.9. Parameterized gravity wave drag from subgrid scale orography

The Subgrid Scale Orographic Parameterization (hereafter SSOP) developed by Lott and Miller (1997) and Lott (1999) that has been implemented in the `ECHAM6` model is aimed at representing the effects of orographic variations on scales smaller than the typical horizontal resolution of a climate model.

The orography may affect the atmospheric flow in many ways. The SSOP considered in `ECHAM6` takes into account two main mechanisms of interaction between the orography and the atmospheric flow:

1. momentum transfer from the earth to the atmosphere accomplished by orographic gravity waves and

2. the drag exerted by the subgrid scale mountains when the air flow is blocked at low levels.

The part of the SSOP concerning the propagation and dissipation of the orographic gravity waves follows the formulation of Palmer et al. (1986) and Miller et al. (1989). In addition, the SSOP has options for including the effects of low level trapped lee waves and of subgrid scale orographic lift (Lott, 1999).

Concerning the specification of the gravity wave forcing, the SSOP includes a relatively detailed description of the subgrid scale orography (based on the work of Baines and Palmer (1990)) in order to take into account anisotropic orography and directional effects.

2.9.1. Representation of the subgrid scale orography

At one gridpoint, it is assumed that the subgrid scale orography can be described by seven parameters: the standard deviation μ, the anisotropy γ, the slope σ, the orientation θ, the minimum Z_{min}, the maximum Z_{max}, and the mean Z_{mea} elevation of the orography.

These parameters are evaluated offline for each gridpoint from the US Navy (10'x10') topographic dataset. The last three parameters are taken directly from the US Navy data set (for each horizontal model resolution considered), while the first four parameters are derived from topographic gradients relationships as formulated by Baines and Palmer (1990). In order to derive relationships between the low level flow and the orientation of the orography, it is assumed that the subgrid scale orography has the shape of an elliptical mountain. Thereafter, in each gridbox a typical number of elliptical mountains is considered. For a brief description and additional references see Lott and Miller (1997).

Concerning the large scale flow, it is assumed that the model mean orography is the optimal representation (e.g. the so-called envelope orography used sometimes in low resolution models is excluded).

2.9.2. Gravity wave drag from subgrid-scale orography

In case that the subgrid scale mountains are high enough, the vertical motion of the air is limited and part of the low level flow (below the mountain top) is blocked and a drag should

be provided at the model levels that intersect the subgrid scale orography (the so-called low level drag). Given a non-dimensional height of the mountain: $H_n = NH/U$, where H is the maximum elevation of the mountain, U the wind speed and N the Brunt-Visïla frequency, it can be shown theoretically that part of the low level flow is blocked for $H_n >> 1$. For $H_n << 1$ all the flow goes over the mountain and gravity waves are generated by the vertical motion of the air (Lott and Miller, 1997).

In the parameterization, it is distinguished between the incident flow, flowing above the mountain and forcing the gravity waves, and the blocked flow, associated with the low level drag. The incident flow is defined as the average of the wind speed, the Brunt-Visïla frequency, and the fluid density between the model ground, Z_{mea}, and the mountain peak, Z_{max}. This flow is referenced as U_H, N_H, and ρ_H, respectively. Concerning the blocked flow, the parameter of interest is the height of the blocked flow, Z_b defined as the highest level that satisfies the condition:

$$\int_{Z_b}^{Z_{max}} \frac{N}{U_p} dz \leq H_{NC} \tag{2.317}$$

where the wind speed U_p is calculated by resolving the wind $\overrightarrow{U}$ in the direction of the incident flow. The parameter H_{NC} tunes the depth of the blocked flow layer and is of order one.

The low level drag for each layer below Z_b is given by:

$$\overrightarrow{D}_b(z) = -\rho C_d max \left(2 - \frac{1}{r}, 0\right) \frac{\sigma}{2\mu} \left(\frac{Z_b - z}{Z_b - Z_{mea}}\right) \left(B\cos^2\psi_H + C\sin^2\psi_H\right) \frac{\overrightarrow{U}\left|\overrightarrow{U}\right|}{2} \tag{2.318}$$

where ψ_H is the angle between the incident flow and the normal orographic ridge direction, the constants B and C are functions of the anisotropy, and r is the aspect ratio of the ridge as seen by the incident flow (see Lott and Miller (1997) and Lott (1999)).

If there is low level flow blocking, it is therefore assumed that the effective height, Z_{eff}, of the orography seen by the atmospheric flow is reduced to $Z_{max} - Z_b$. In case that there is no low level flow blocking, $Z_{max} - Z_{min}$ is instead used as effective height.

Taking into account the difference in orientation between a orographic ridge and the incident flow and the typical number of ridges within a gridbox, the gravity wave stress at the source level is given by:

$$\tau = \rho_H G U_H N_H Z_{eff}^2 \frac{\sigma}{4\mu} \left|\overrightarrow{P}\right| \tag{2.319}$$

where the parameter G tunes the gravity wave stress amplitude and is of order one. The directional vector $\overrightarrow{P}$ is given by:

$$\overrightarrow{P} = (B\cos^2\psi_H + C\sin^2\psi_H; (B - C)\sin\psi_H\cos\psi_H) \tag{2.320}$$

2.9.3. Gravity wave drag

Above the source level the gravity wave stress is constant, except when the waves encounter a critical level or when they break. Given that the gravity wave drag is the vertical derivative of the gravity wave stress, the gravity waves produce a drag on the resolved flow only when a critical level is reached or when they become unstable and break, in agreement with wave-mean flow theory.

A critical level is encountered when the background wind turns with height so that it becomes zero in the plane of the low level stress. If this happens, the gravity wave stress is set to zero at that level.

The part of the SSOP that concerns gravity wave breaking follows the original formulation of Palmer et al. (1986), that uses a breaking condition based on the Richardson number and the Lindzen (1981) saturation hypothesis to determine the stress at the breaking level.

At each model level a minimum Richardson number that includes the gravity wave influence on the static stability and wind shear is evaluated:

$$Ri_{min} = Ri \frac{1 - (N\delta h/U)}{\left\{ 1 + Ri^{1/2}(N\delta h U) \right\}^2} \tag{2.321}$$

where $Ri = (N/(dU/dz))^2$ is the background (resolved) flow Richardson number, N the background static stability, U the background wind speed (derived from the projection of the wind vector in the plane of the low level stress), and δh is the amplitude of the vertical displacement induced by the gravity waves. δh is derived following a steady two dimensional model of gravity waves and is given by:

$$\delta h^2 = G \frac{\rho_H N_H U_H}{\rho N U} Z_{eff}^2 \tag{2.322}$$

Ri_{min} is a lower bound (hence 'minimum') to the Richardson number, in the sense that it is the minimum value that can be anticipated from a steady two dimensional model of gravity wave propagation (Palmer et al., 1986).

It is assumed that instability occurs if $Ri_{min} < Ri_c$, where Ri_c is the critical Richardson number equal to 0.25. This condition takes into account the occurrence of both convective overturning and shear instability.

If the critical Richardson number is reached, the waves are assumed to saturate: their amplitude is limited to the value at which instability occurs (Lindzen, 1981). The wave vertical displacement is therefore computed from the Ri_{min} equation with $Ri_{min} = Ri_c$. This vertical displacement, ε, is thereafter used in the gravity wave stress at the breaking height, the saturation stress:

$$\tau_s = \rho \frac{U^3}{N} \varepsilon^2 \frac{\sigma}{2\mu} \tag{2.323}$$

The equation for the saturation stress is obtained following Lindzen (1981). Thereafter, above the breaking level, the gravity wave stress remains constant and equal to the saturation stress, if the condition for instability is not reached again.

In the parameterization, the calculation of the gravity wave stress proceeds from the bottom to the top of the vertical column. The procedure of evaluating the Richardson number and the search for instability is therefore applied from the bottom up, and can produce more than one breaking level.

2.10. Water Vapor in the Middle Atmosphere

In the stratosphere and mesosphere the major source of water vapor, besides transport from the troposphere, is the oxidation of methane. In order not to underestimate middle atmospheric water vapor, `ECHAM6` includes a submodel that parameterizes methane oxidation as well as the photolysis of water vapor. By default this submodel is however switched off. The formulation of the processes follows the respective implementation in the ECMWF IFS (see IFS documentation Cy36r1, part IV, chapter 9 for details). The scheme adds the two tendency terms Q_{methox} and Q_{photo} to the right hand side of the prognostic equation for the grid-cell mean mass mixing ratio of water vapor $\bar{r}_v$ (eq. 2.241).

Q_{methox} describes the parameterization of methane oxidation and is defined as

$$Q_{\text{methox}} = (r_{v,\text{lim}} - \bar{r}_v)/\tau_{\text{methox}}. \tag{2.324}$$

$r_{v,\text{lim}}$ is set to the value of 4.25 ppm and hence independent of the methane mixing ratio acting on radiation. The dependence of τ_{methox} in days on atmospheric pressure p in hPa is given by

$$\tau_{\text{methox}} = \begin{cases} 100 & p \leq 0.5 \\ 100\left[1 + \alpha_1 \frac{\{\ln(p/0.5)\}^4}{\ln(100/p)}\right] & 0.5 < p < 100 \\ \infty & p \geq 100 \end{cases} \tag{2.325}$$

with

$$\alpha_1 = \frac{19\ln 10}{(\ln 20)^4}. \tag{2.326}$$

This means that water vapor production by methane is strongest in the mesosphere and not considered in the troposphere.

Q_{photo} describes the photolysis of water vapor and is defined as

$$Q_{\text{photo}} = -\bar{r}_v/\tau_{\text{photo}}. \tag{2.327}$$

The dependence of τ_{photo} in days on pressure in hPa given by

$$\tau_{\text{photo}} = \begin{cases} 3 & p \leq 0.001 \\ \left[\exp\left\{\alpha_2 - 0.5(\ln 100 + \alpha_2)\left(1 + \cos\frac{\pi\ln(p/0.2)}{\ln 0.005}\right)\right\} - 0.01\right]^{-1} & 0.001 < p < 0.2 \\ \infty & p \geq 0.2 \end{cases} \tag{2.328}$$

with

$$\alpha_2 = \ln\left(\frac{1}{3} + 0.01\right). \tag{2.329}$$

This definition ensures that the photolysis of water vapor contributes significantly to the water vapor budget only above about 0.1 hPa where τ_{photo} reaches values of below 100 days.

The vertical profile of the photochemical lifetime of water vapor $(1/\tau_{\text{methox}} + 1/\tau_{\text{photo}})^{-1}$ combined from the two parameterized processes above agrees reasonably to a respective profile given in Fig. 5.23 of Brasseur and Solomon (2005).

3. Land

The documentation for JSBACH is in progress. Most of the JSBACH components can be found in (Raddatz et al. (2007)) and under http://www.mpimet.mpg.de/wissenschaft/land-im-erdsystem/globale-vegetationsmodellierung/jsbach-publikationen.html. For further information please contact Christian Reick (christian.reick@zmaw.de).

4. Slab Ocean and Sea Ice

4.1. Slab ocean

As an option, the sea surface temperatures, $SSTs$, and sea-ice thickness, h_i, can be calculated using a slab ocean model. The $SSTs$ are computed from the ocean surface heat balance. The slab ocean model represents the surface ocean as a slab of specified depth h. In the model the mixed layer depth h is set to $50m$. The slab ocean model is a thermodynamical model that does not contain any explicit computation of ocean dynamics. The ocean dynamics are represented by a prescribed ocean heat transport divergence which may also be interpreted as a heat-flux correction. The prognostic variable in the ocean is the mixed layer temperature T_m. The heat budget of a constant-depth mixed layer h can be written as:

$$C_m \frac{\partial T_m}{\partial t} = H - F_O \qquad (4.1)$$

where T_m is the sea surface temperature SST, $H =$ net surface heat flux (including all radiative and turbulent fluxes), $F_O =$ the divergence of ocean heat transport and $C_m = \rho_{sea} h c_{sea}$ is the heat capacity of the slab. The sea water density ρ_{sea} is set to $1025\, kg\, m^{-3}$ and the heat capacity of sea water c_{sea} to $3994\, J\, kg^{-1}\, K^{-1}$. While F_O is unknown, its monthly climatology, F_{clim}, can be derived from equation 4.1 by replacing T_m by the observed SST climatology, T_{clim}, and H by its climatology, H_{clim}. For consistency, H_{clim} has to be computed from the uncoupled AGCM with T_{clim} used as lower boundary forcing, resulting in

$$F_{clim} = H_{clim} - C_m \frac{\partial T_{clim}}{\partial t}. \qquad (4.2)$$

This simple approach of approximating F_O in equation 4.1 by its monthly climatology has the main advantage that systematic errors in simulated $SSTs$ are practically avoided while SST variability is captured through the variability of H. The main limitation is that variability of ocean heat transport is neglected. The heat flux divergence F_{clim} is applied also, with appropriate area weighting, in those regions where sea-ice is observed, according to climatology, except when the observed ice fraction is larger than 0.9. Then the heat flux divergence F_{clim} is set to zero. To compute the net climatological surface heat flux H_{clim} a 'long' (10-20 years) standalone ECHAM6 simulation has to be performed forced by prescribed climatological SSTs. Please note that if changes are made to ECHAM6 physical or dynamical parameters, a new heat-flux climatology has to be computed.
Equations 4.1 and 4.2 give:

$$C_m \frac{\partial T_m}{\partial t} = H - F_O \approx H - F_{clim} = H - H_{clim} + C_m \frac{\partial T_{clim}}{\partial t}. \qquad (4.3)$$

This may be written as:

$$C_m \frac{\partial (T_m - T_{clim})}{\partial t} = H - H_{clim}. \qquad (4.4)$$

Thus, the model predicts only the deviations from the observed seasonal cycle of SST, forced by anomalies in the net surface heat fluxes. Therefore, the mean (long-term averaged) climatological seasonal cycle of SST as simulated by the slab ocean model is similar to the observed one.
The term F_{clim} in equation 4.2 may also be interpreted as a "heat-flux correction" Q of the slab ocean model, i. e.

$$C_m \frac{\partial T_m}{\partial t} = H - Q \qquad (4.5)$$

with

$$Q = F_{clim} = H_{clim} - C_m \frac{\partial T_{clim}}{\partial t}. \qquad (4.6)$$

The heat-flux correction Q has to be provided to the slab ocean model in every month (each year the same) and is then interpolated in time onto the respective time step (in the same way as for all other surface variables that are prescribed as monthly means).

For more details see subroutines *ml_ocean.f90* and *ml_flux.f90*.

4.2. Sea Ice

4.2.1. Calculation of sea ice melting separately for bare/snow covered ice and meltponds

Bare ice or snow covered ice: The melt rate is calculated from the net surface heat flux over ice and the conductive heat flux, with the net surface solar radiation prescribed for bare/snow covered ice using the respective surface albedo (palsobs). The ice temperature for this part of the grid box is given by

$$T_{i,bare}^{n+1} = \frac{H_{Bare} + \frac{C_i}{\Delta t}T_{i,bare}^n + \frac{\kappa_i}{h_{i,\text{eff}}}T_0}{\frac{C_i}{\Delta t} + \frac{\kappa_i}{h_{i,\text{eff}}}} \tag{4.7}$$

where

C_i = heat capacity of the surface ice layer (currently 5 cm)

Δt = time step

$h_{i,\text{eff}}^n = h_i^n + \left(\frac{\kappa_i \rho_w}{\kappa_s \rho_s}\right) h_s^n$ = effective thickness of the ice/snow layer

h_i^n = thickness of sea ice at the previous time step

h_s^n = thickness of snow (water equivalent) at the previous time step

κ_s = thermal conductivity of snow

κ_i = thermal conductivity of ice

ρ_w, ρ_i = density of water, ice

H_{bare} = net heat flux over bare/snow covered ice using the respective surface albedo

$T_{i,bare}^n$ = ice temperature at the previous time step

T_0 = water temperature below the ice (-1.8°C for ocean)

Melting of sea ice over the <u>bare-ice</u> fraction of the grid-box can be estimated from

$$F_{melt,b} = (T_i^* - T_{melt}) \times \left(\frac{C_i}{\Delta t} + \frac{\kappa_i}{h_{i,eff}^n}\right) > 0 \tag{4.8}$$

for $T_i^* > T_{melt}$, where $T_i^* = T_{i,bare}^{n+1}$ is the ice temperature at the surface given by ((4.7)) and T_{melt} is the temperature at the melting point (273.15 K). By using ((4.7)) in ((4.8)), the melt

rate can be written as

$$F_{melt,b} = \frac{C_i}{\Delta t}\left(T_{i,bare}^n - T_{melt}\right) + H_{bare} - \frac{\kappa_i}{h_{i,eff}^n}\left(T_{melt} - T_0\right) \tag{4.9}$$

If $T_{i,bare}^n$ is already at the melting point, the first term vanishes. The melt rate is then given by the net heat flux H_{bare} minus the conductive heat flux which is positive (downward) for melting sea ice because $T_{melt} > T_0$. For lake ice, this term vanishes during the melting period. If $T_{i,bare}^n$ is still below the melting point, part of the excess heat $F_{melt,b} > 0$ is used to increase the ice temperature up to the melting point.

Open melt ponds: Same as above, but the net surface heat flux H_{pond} is now calculated for water conditions, using the melt pond albedo for deriving the net surface solar radiation. The ice temperature below the pond can then be written as

$$T_{i,pond}^{n+1} = \frac{H_{pond} + \frac{C_i}{\Delta t}T_{i,pond}^n + \frac{\kappa_i}{\left(h_i^n - h_p^n\right)}T_0}{\frac{C_i}{\Delta t} + \frac{\kappa_i}{\left(h_i^n - h_p^n\right)}} \tag{4.10}$$

where $h_p = \underline{\text{local}}$ pond depth = grid-mean pond depth divided by the melt pond fraction f_p. Generally, when the pond is open, $T_{i,pond}^n = T_{melt}$, but $T_{i,pond}^n < T_{melt}$ just before the melt pond is formed. In this case, $T_{i,pond}^n$ is set to $T_{i,bare}^n$. The melt rate is given analogously to ((4.8)):

$$F_{melt,p} = (T_i^\star - T_{melt}) \times \left(\frac{C_i}{\Delta t} + \frac{\kappa_i}{\left(h_i^n - h_p^n\right)}\right) > 0 \tag{4.11}$$

for $T_i^\star > T_{melt}$, where $T_i^\star = T_{i,pond}^{n+1}$ is the ice temperature below the pond given by ((4.10)). Using ((4.10)) in ((4.11)), the melt rate can also be written as (c.f., ((4.9)))

$$F_{melt,p} = \frac{C_i}{\Delta t}\left(T_{i,pond}^n - T_{melt}\right) + H_{pond} - \frac{\kappa_i}{\left(h_i^n - h_p^n\right)}\left(T_{melt} - T_0\right) \tag{4.12}$$

The total melt rate is a weighted average of the melt rate over bare ice ((4.9)) and melt ponds ((4.12)), respectively, with the melt pond fraction f_p as weighting factor:

$$F_{melt} = (1 - f_p)F_{melt,b} + f_p F_{melt,p} \tag{4.13}$$

Analogously, the total conductive heat flux through the ice is given as

$$H_c = (1 - f_p)H_{c,bare} + f_p H_{c,pond} \tag{4.14}$$

with the individual fluxes defined as

$$H_{c,bare} = \frac{\kappa_i}{h_{i,\text{eff}}^n}\left(T_{i,bare}^{n+1} - T_0\right) \text{ positive downward} \tag{4.15}$$

$$H_{c,pond} = \frac{\kappa_i}{\left(h_i^n - h_p^n\right)}\left(T_{i,bare}^{n+1} - T_0\right) \tag{4.16}$$

Preliminary results: Compared to the standard model used in the cmip5 simulations, the summer (JJA) melt rate is enhanced by $5 - 10 W/m^2$ along the Canadian and Siberian coasts (most prominently during 1976-2005). This corresponds to change in sea ice thickness of about 25 cm. In addition, the downward conductive heat flux during summer is enhanced as well, due to the reduced ice depth below the melt ponds (c.f., eq. ((4.16))). This tends to reduce the melt rate at the surface but increases the melting at the bottom of the ice.

4.2.2. Snow on ice

Snow on lake ice and sea ice (subroutines s_licetemp; s_sicetemp)

$$\rho_w \frac{\Delta H_s}{\Delta t} = S + f_s E_s - M_s \qquad [kg/(m^2 s)]$$

$$\Delta h_s = \frac{\delta t}{\rho_w} (S + f_s E_s - M_s) = \text{ zsnowd + zevsnd + zsmelt} \qquad [m]$$

symbol	variable	code	unit
h_s	snow water equivalent	psni	m
ρ_w	densitiy of water	rhoh2o	kg/m^3
Δt	time step	zdtime	s
S	snowfall	psnow	$kg/(m^2 s)$
f_s	snow fraction	pcvsi	—
E_s	sublimation*	pevapi	$kg/(m^2 s)$
M_s	snow melt		$kg/(m^2 s)$

*downward (upward) fluxes are positive (negative)
Snow melt occurs when the skin temperature $T_i > T_0 = T_{melt}$, where T_i is calculated from the surface heat fluxes:

$$\begin{aligned} F_s &= SW + LW + SH + LH & \text{(zsflx)} \\ SW &= \text{ net surface solar radiation} & \text{(zsofli; see below)} \\ LW &= \text{ net surface longwave radiation} & \text{(ptrfli)} \\ SH &= \text{ sensible heat flux} & \text{(pahfsi)} \\ LH &= \text{ latent heat flux} & \text{(pahfli)} \end{aligned}$$

'zsofli' represents the net surface solar radiation **over the snow/ice covered part of the grid box**, i.e., excluding the meltpond area. 'psofli' is the net surface solar radiation over the ice (including meltponds). Since the mean ice albedo (palsoi) includes bare ice, snow on ice and also meltponds, the incoming solar radiation at the surface is given by $F_{in} = \text{psofli}/(1 - \text{palsoi})$. 'palsobs' represents the albedo of bare ice and snow on ice so that $\text{zsofli} = F_{in}(1 - \text{palsobs})$ is the net surface solar radiation over bare ice or snow (excluding meltponds).
In addition to the surface heat fluxes, the skin temperature is also affected by the conductive

heat flux throught the ice/snow layer.

$$F_c = \frac{a_i}{h_{\text{eff}}} (T_i - T_0) \qquad\qquad \text{(negative upward: } T_i < T_0)$$

α_i = thermal conductivity of ice $\qquad\qquad$ [$2.1656 W/(mK)$]

α_s = thermal conductivity of snow $\qquad\qquad$ [$0.31 W/(mK)$]

ρ_s = density of snow $\qquad\qquad$ [$300 kg/m^3$]

h_s = thickness of snow in water equivalent

T_i = skin temperature at the ice/snow surface

T_0 = freezing/melting temperature $\qquad\qquad$ [$273.15 K$]

$h_{i,\text{eff}} = h_i + \left(\frac{\alpha_i \rho_w}{\alpha_s \rho_s} \right) h_s$ is effective thickness of the ice/snow layer

The heat budget of a thin ice layer ($h_0 = 0.05m$) is given by

$$C_i \frac{\delta T_i}{\Delta t} = F_s - F_c \qquad\qquad [W/m^2]$$

$$C_i = \rho_i c_{pi} h_0 \qquad\qquad [Ws/m^2 K]$$

$$\rho_i = \text{ density of ice} \qquad\qquad [917 kg/m^3]$$

$$c_{pi} = \text{ specific heat of ice} \qquad\qquad [2106 Ws/(kgK)]$$

New: adding the heat capacity of the snow layer (17 February 2010)

$$C_{is} = C_i + C_s \qquad \text{with } C_s = \rho_c c_{ps} h_s$$

Then, a preliminary skin temperature $T^\star$ can be calculated:

$$C_{is} \frac{(T^\star - T_i^n)}{\Delta t} = F_s - \frac{\alpha_i}{h_{\text{eff}}} (T^\star - T_0) \text{ where } T_i^n \text{ is the skin temperature at the previous timestep.}$$

$$T^\star = \frac{F_s + \frac{C_{is}}{\Delta t} T_i^n + \frac{\alpha_i}{h_{\text{eff}}} T_0}{\frac{C_{is}}{\Delta t} + \frac{\alpha_i}{h_{\text{eff}}}}$$

For $T^\star \leq T_0$, the new skin temperature is $T_i^{n+1} = T^\star$. For $T^\star > T_0$, the new skin temperature is calculated from the excess heat $F_{melt} = \left(\frac{C_{is}}{\Delta t} + \frac{\alpha_i}{h_{\text{eff}}} \right) (T^\star - T_0)$ which is used for melting of snow (first) and ice (as soon as the snow is melted away completely). The melt rate is given by $M_s F_{melt}/L_f$ [$kg/(m^2 s)$] where L_f [Ws/kg] is the latent heat of fusion. The change in snow height (m water equivalent) is given by $\Delta h_s = \min\left(h_s^n, M_s \frac{\Delta t}{\rho_w} \right) = $ zsmelt > 0, where h_s^n is the snow water equivalent [m] at the previous timestep. The corresponding increment in skin temperature is given by $\Delta T_i = \Delta h_s \frac{\rho_w L_f}{\Delta t \left(\frac{C_{is}}{\Delta t} + \frac{\alpha_i}{h_{\text{eff}}} \right)}$, corresponding to 'zsmelt/zmelfac' in the code, and $T_i^{n+1} = T^\star - \Delta T_i$. The heat that was used for melting the snow, $\Delta h_s \frac{\rho_w L_f}{\Delta t}$ [W/m^2], is saved as 'zsmelres' in the diagnostics (code 209). After adjusting snow thickness and skin temperature (melting, cooling), the resulting skin temperature is checked again. If $T_i^{n+1} > T_0$, the excess heat is saved as $F_{melt} = \left(\frac{C_{is}}{\Delta t} + \frac{\alpha_i}{h_{\text{eff}}} \right) (T^{n+1} - T_0)$, corresponding to 'pqres' in the model, and the new skin temperature is set to the melting point $T_i^{n+1} = T_0$. In the lake model (s_lake), F_{melt} is used for melting the ice. For sea ice, F_{melt} is saved as diagnostics (code 209) and also passed to the ocean in the coupled model (daily mean).

4.2.3. New sea ice albedo scheme

The sections hereafter closely follow the article written by Pedersen et al. (2009). Some small modifications were necessary since the article describes the albedo scheme for use in the context of the ECHAM5 model and not `ECHAM6`. We follow the structure of the complex albedo parameterization in a small–scale thermodynamic sea ice model to construct a new sea ice albedo scheme for the four surface types; snow–covered sea ice α_s, bare sea ice α_i, melt ponds α_mp, and open water α_w. The sea ice albedo is defined as

$$\alpha_\text{ice} = \alpha_\text{s} f_\text{s} + \alpha_\text{i} f_\text{i} + \alpha_\text{mp} f_\text{mp}, \tag{4.17}$$

with the respective area fractions f_s, f_i, f_mp. The snow cover fraction f_s is calculated from the snow depth (`ECHAM6`'s original description Roesch (2000)), the melt pond fraction f_mp from the melt pond depth (discussed in the melt pond section hereafter), and the bare ice fraction f_i is extracted from the sum of the others.

The total albedo is weigthted according to the grid mean ice concentration

$$\alpha = \alpha_\text{ice} f_\text{ice} + \alpha_w (1 - f_\text{ice}), \tag{4.18}$$

where f_ice is the sea ice concentration from `ECHAM6`.

In `ECHAM6`, the number of spectral bands has been increased to six (five bands in the UV–visible (VIS) and nine bands in the near–infrared (NIR)). We use one parameterization for the three VIS bands and another for the three NIR bands. The broadband albedo is calculated by weighting the VIS and NIR albedos with the irradiance spectra. Separate schemes are developed for the diffuse and direct components of the solar radiation, and weighted according to the cloud cover fraction computed in `ECHAM6`. The individual albedo components, described in the next sections, are also summarized in Tab. 4.1. The wavelength ranges for the different schemes differ slightly from the wavelength range used in `ECHAM6`; however, the solar spectrum is roughly divided at 689 nm for all schemes.

Snow–Covered Sea Ice

Two main groups of snow albedo schemes are common in GCMs: temperature–dependent schemes (including ECHAM5) and prognostic schemes. In a previous study the temperature–dependent schemes were found not to capture the winter snow metamorphosis and spring melting very well as the albedo was fixed to threshold values Pedersen and Winther (2005). The prognostic schemes have an iterative albedo dependence, with separate decay factors for melting and nonmelting snow, and reset the albedo to its maximum after new snowfall above a prescribed precipitation threshold. They are found to capture the seasonal cycle better than the temperature–dependent schemes Pedersen and Winther (2005).

Both types of schemes were originally created for snow on land, but can be used for snow–covered sea ice, by compensating for an underlying surface of bare ice. We suggest to replace the original, empirical temperature–dependent scheme in `ECHAM6` with the more physically based prognostic scheme BATS (Biosphere–Atmosphere Transfer Scheme Dickinson et al. (1986)). BATS includes all processes relevant to capturing the changes in snow albedo, and it separates

Table 4.1.: New sea ice albedo parameterization scheme in `ECHAM6`[*]

Albedo of Surface Type	VIS 200–689 nm	NIR 689–12195 nm
Snow–covered sea ice, α_s		
Direct	BATS equations	BATS equations
Diffuse	BATS equations	BATS equations
Bare sea ice, α_i	$0.13\ln(h_\mathrm{i}) + 0.1$[†]	
Direct		$0.047\ln(h_\mathrm{i}) + 0.074$[†]
Diffuse		$0.049\ln(h_\mathrm{i}) + 0.085$[†]
Melt pond, α_mp		
Direct	$0.336 + \exp(-9.457 d_\mathrm{mp} - 1.061)$	$0.017 + \exp(-18.904 d_\mathrm{mp} - 0.909)$
Diffuse	$0.413 + \exp(-24.014 d_\mathrm{mp} - 1.086)$	$0.061 + \exp(-17.449 d_\mathrm{mp} - 1.075)$

[*]Scheme separates between snow–covered sea ice α_s, bare sea ice α_i, melt ponds α_mp, and open water for visible (VIS) and near–infrared (NIR) bands and diffuse and direct radiation. h_i is the ice thickness in cm, and d_mp is the melt pond depth in m. BATS equations from Dickinson et al. (1986).

[†]For ice thicknesses equal to or above 1.6 m for VIS and 1.0 m for NIR, constant albedos of 0.76 for VIS and 0.29 for NIR direct and 0.31 for NIR diffuse are used.

between VIS and NIR bands, as well as between diffuse and direct radiation. It was shown to accurately represent the temporal snow albedo decay when implemented in ECHAM4. In fact, BATS was the preferred snow albedo scheme for ECHAM4 (Roesch (2000)). The BATS snow scheme has been validated against observations by Roesch (2000) and Yang et al. (1997), with good correspondence.

Bare sea ice

We take advantage of the extensive sets of sea ice albedos collected by Brandt et al. (2005) in the Antarctic sea ice zone over several years. The spectral albedos for different sea ice types were measured and integrated to obtain VIS ($\lambda < 689\,\mathrm{nm}$) and NIR ($\lambda > 689\,\mathrm{nm}$) sea ice albedos. As clouds only weakly absorb at VIS wavelengths, the visible albedo is the same under cloudy and clear skies, while for NIR, the observations were split into a diffuse and direct component. On the basis of Brandt et al. (2005), we propose a simple least squares fit parameterization of the form

$$\alpha_\mathrm{i} = a\log(h_\mathrm{i}) + b, \tag{4.19}$$

where a and b are the model parameters and h_i is the ice thickness in cm (Fig. 4.1 and Tab. 4.1). For ice thicknesses equal to or above 1.6 m for VIS and 1.0 m for NIR, the upper threshold values from Tab. 4.1 are used.

Melt ponds

The inclusion of melt ponds in the albedo scheme is very important from a physical perspective, because of their extensive presence during summer Perovich et al. (2002); Tschudi et al. (2001);
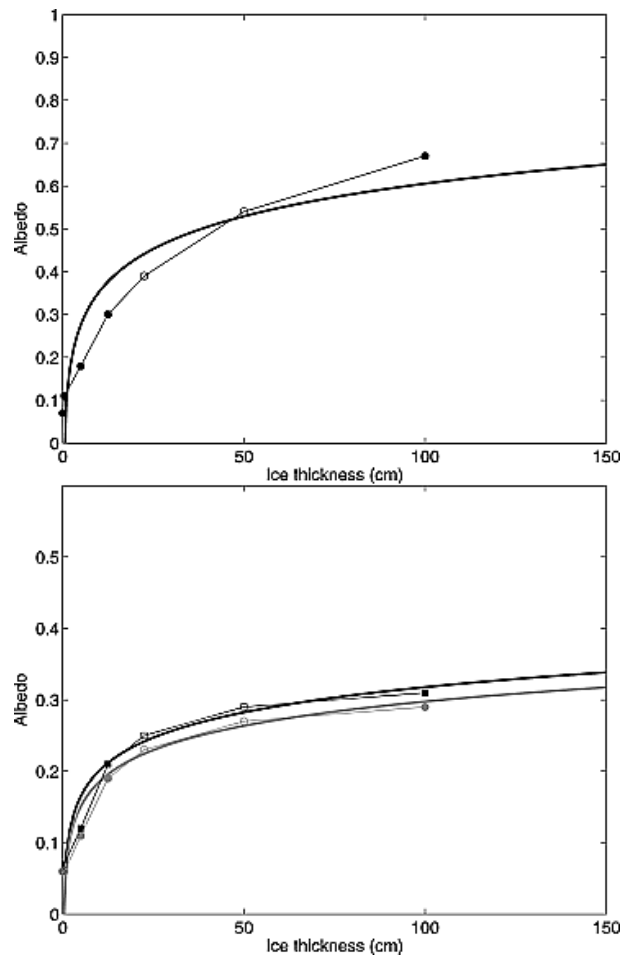
Figure 4.1.: Sea ice albedo as a function of ice thickness for (top) visible (VIS, $\lambda < 689\,\mathrm{nm}$) and (bottom) near–infrared (NIR, $\lambda > 689\,\mathrm{nm}$) spectral bands after Brandt et al. (2005). The filled symbols are measurements, while the open are interpolated values. The depths are the mean squares fit of the form $\alpha_i = a\log(h_i) + b$, where a and b are given in Tab. 4.2. A distinction is made between direct (black) and diffuse (gray) irradiance for NIR in Fig. 4.1 (bottom). Reprinted by permission from John Wiley and Sons. Copyright 2009 by the American Geophysical Union.

Table 4.2.: Constants for bare sea ice albedo[*]

	a	b	Upper threshold
VIS	0.13	0.10	0.76
NIR direct	0.047	0.074	0.29
NIR diffuse	0.049	0.085	0.31

[*] Bare sea ice albedo is of the form $\alpha_i = a\log(h_i) + b$ proposed from data from Brandt et al. (2005) for visible (VIS, $\lambda < 689\,\mathrm{nm}$) and near–infrared (NIR, $\lambda > 689\,\mathrm{nm}$) (direct and diffuse). The upper threshold values are used for ice thicknesses equal to or above $1.6\,\mathrm{m}$ for VIS and $1.0\,\mathrm{m}$ for NIR.

Fetterer and Untersteiner (1998); Perovich and Tucker III (1997), and the large portion of solar energy absorbed by the melt water (Podgorny and Grenfell (1996)). Both Schramm et al.

(1997) and Morassutti and LeDrew (1996) provide useful melt pond albedo parameterizations as a function of pond depth. However, such schemes cannot be used directly because melt pond depth, and also the more important melt pond fraction (see equation (4.17)), is not available in GCMs.

We propose a basic model for melt pond evolution based on the daily surface ice melt rate from ECHAM6. The temporal evolution of a melt pond is calculated from the mass balance equation

$$\frac{\partial p_\mathrm{d}}{\partial t} = -\frac{\rho_\mathrm{i}}{\rho_\mathrm{w}}\left(\frac{\partial h_\mathrm{i}}{\partial t} + \frac{\partial p_\mathrm{di}}{\partial t}\right) - \left(\frac{\partial p_\mathrm{d}}{\partial t}\right)_s, \tag{4.20}$$

where p_d is the pond depth in m and ρ_w, ρ_i are the densities of water and ice, respectively (Fig. 4.2). The first term on the right hand side represents the melt pond growth through the surface melting of sea ice; the second term refers to the growth or melting of pond ice p_di; and the last term is the constant seepage rate. Pond ice forms if the temperature of the pond, T_w, falls below the freezing point, T_0, where T_w is calculated from the heat budget equation

$$C_\mathrm{w}\frac{\partial T_\mathrm{w}}{\partial t} = H_\mathrm{sfc}. \tag{4.21}$$

C_w is the heat capacity of the pond and H_sfc is the sum of all radiative and turbulent heat fluxes at the surface of the ice–free pond. For $T_\mathrm{w} < T_0$, a slab of ice is formed according to

$$p_\mathrm{di} = \left(\frac{C_\mathrm{w}}{L_\mathrm{f}\rho_\mathrm{i}}\right)(T_0 - T_\mathrm{w}), \tag{4.22}$$

where L_f is the latent heat of fusion. T_w is then reset to T_0 and is kept fixed, independent of the sign of H_sfc, because the pond water is forming on top of the ice. The surface temperature of the ice, T_i, is calculated from the heat budget of a thin slab of ice (1 cm) at the surface

$$C_\mathrm{i}\frac{\partial T_\mathrm{i}}{\partial t} = H_\mathrm{sfc} + H_\mathrm{c}, \tag{4.23}$$

where C_i is the heat capacity of the thin upper slab of pond ice and H_c is the conductive heat flux through the ice given by

$$H_\mathrm{c} = \frac{\kappa_\mathrm{i}}{p_\mathrm{di}}(T_0 - T_\mathrm{i}) \geq 0, \tag{4.24}$$

where κ_i is the thermal conductivity of ice.

Melt pond formation will not start before the snow on top of the sea ice has melted away. If a slab of pond ice $p_\mathrm{di} \geq 1\,\mathrm{cm}$ is forming, the melt pond fraction is set to zero. The final closing of the melt pond in fall is generally caused by vanishing melting and constant seepage, resulting in $p_\mathrm{d} \leq 0$, or by freezing if the pond is totally frozen or if a thick ice layer has been formed ($p_\mathrm{di} = 10\,\mathrm{cm}$). In all these cases the pond is closed, i.e., p_d is set to zero.

To provide an estimate of the melt pond fraction, we propose to calculate it from the melt pond depth (similar to what is done for the snow cover fraction in GCMs) using a parameterization
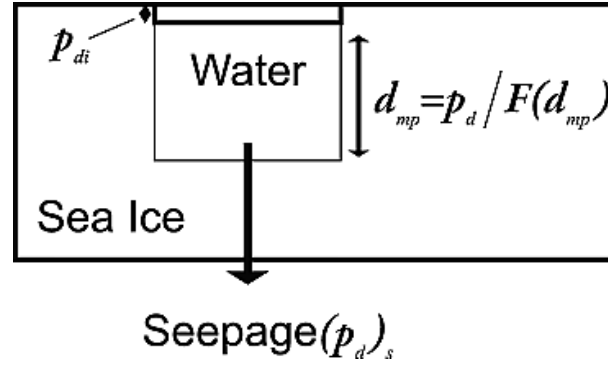
Figure 4.2.: A schematic drawing of a melt pond describing a few of the variables in equations (4.20)–(4.24). Reprinted by permission from John Wiley and Sons. Copyright 2009 by the American Geophysical Union.

Table 4.3.: Constants for melt pond fraction as a function of melt pond depth for multiyear ice

a	b	c	d	e	f	g	h	i
-0.00724636	0.14438	-1.19140	5.25995	-13.37101	19.53030	-15.27019	5.26674	-0.12549

of the results from a number of simulations using a small–scale melt pond model (Lüthje et al. (2006)). The model treats the ice surface as a porous medium. Melt water drains through the ice to the ocean at a constant rate $(0.8\,\mathrm{cm/d})$ and the melt water left on the surface percolates to lower lying areas to form melt ponds. The melt rate is kept constant during the melt season, but is enhanced where melt ponds form, to simulate the lower albedo of the melt ponds. The model discretizes the space and time domain using a finite differences scheme. For relating the melt pond depth and fraction covered for different climate scenarios, the model was run with the same input parameters as described in details by Lüthje et al. (2006) in the study of Pedersen et al. (2009). The melt rate for the ice surface was varied from $1.0\,\mathrm{cm/d}$ to $3.0\,\mathrm{cm/d}$ (in steps of $0.1\,\mathrm{cm/d}$), while the enhanced melt rate under the melt ponds was kept at twice the ice surface melt rate. This was done for both a MYI and a FYI setting, resulting in a total of 42 model runs, with a melt season of 71 days. The mean daily fraction of the surface covered by melt ponds is plotted against the daily mean melt pond depth in Fig. 4.3 (for FYI and MYI separately).

To connect the melt pond fraction to the melt pond depth for MYI (Fig. 3, top), an 8–degree polynomial was fitted to the data points:

$$f_{\mathrm{mp}} = ad_{\mathrm{mp}}^8 + bd_{\mathrm{mp}}^7 + cd_{\mathrm{mp}}^6 + dd_{\mathrm{mp}}^5 + ed_{\mathrm{mp}}^4 + fd_{\mathrm{mp}}^3 + gd_{\mathrm{mp}}^2 + hd_{\mathrm{mp}} + i \qquad (4.25)$$

where d_{mp} is th melt pond depth in m, and the constants a to i are given in Tab. 4.3. Fig. 4.3 (top) shows melt pond depths up to 2.5 m for unrealistically high melt rates $(2.5 - 3.0$ cm/d) during the end of the 71 simulated days. Such depths are not realistic, and were only included to avoid reaching outside the range of possible melt pond depth. For FYI, the connection between fraction and depth is more complex (Fig. 4.3, bottom). For small melt rates, the relationship is similar to that for MYI, but for more realistic melt rates, the relationship is
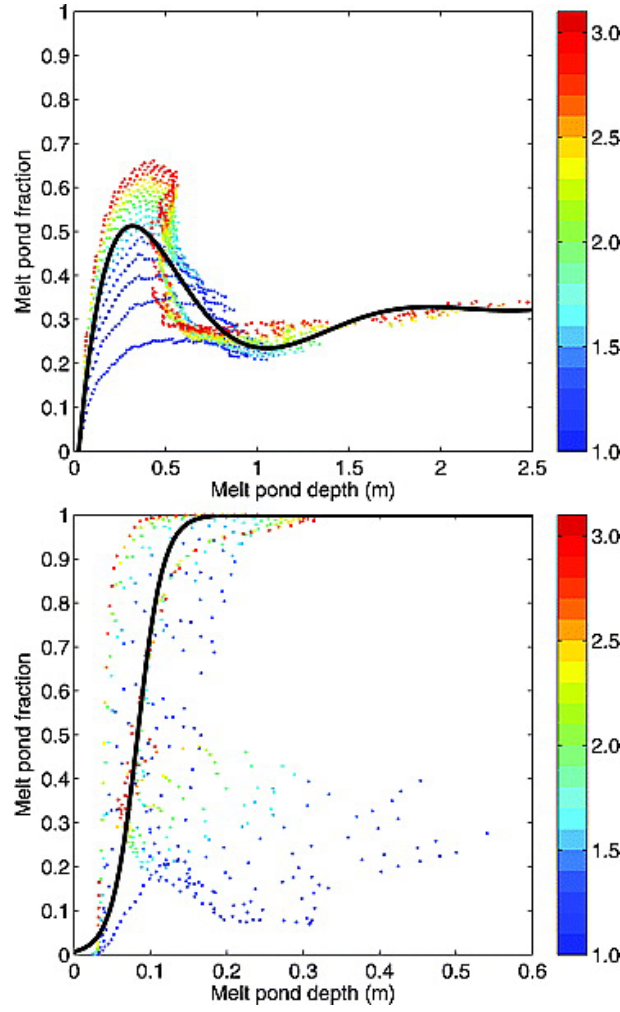
Figure 4.3.: Melt pond depth versus meltpond fraction for (top) multiyear ice (MYI) and (bottom) first year ice (FYI). The thick lines represent the best fit to the data. For MYI the best fit is represented by a 8–degree polynomial (equation(4.25)), and for TYI it is represented by a hyperbolic tangent (equation (4.26)). The scatter plot is based on the melt pond model by Lüthje et al. (2006) by using melt rates ranging from $1\,\mathrm{cm/d}$ to $3\,\mathrm{cm/d}$ (in steps of $0.1\,\mathrm{cm/d}$) as indicated by the color bar. Reprinted by permission from John Wiley and Sons. Copyright 2009 by the American Geophysical Union.

better described by a hyperbolic tangent function,

$$f_{\mathrm{mp}} = 0.5\tanh(30d_{\mathrm{mp}} - 2.5) + 0.5. \tag{4.26}$$

Since melt ponds on FYI are mostly important in the beginning and middle of the melt season, before the ice breaks up, the fit is created to correspond best with this data, and less with the model data from later in the melt season.

Regression equations were used for calculating the melt pond albedo from melt pond depth from observations of melt pond albedo in the Canadian Arctic Archipelago in spring and

Table 4.4.: Constants for melt pond albedo[*]

	a	b	c
VIS direct	0.336	9.457	1.061
VIS diffuse	0.413	24.014	1.086
NIR direct	0.017	18.904	0.909
NIR diffuse	0.061	17.449	1.075

[*]Melt pond albedo α_{mp} is of the form $\alpha_{\mathrm{mp}} = a + \exp(-bd_{\mathrm{mp}} - c)$ as a function of melt pond depth d_{mp} from Morassutti and LeDrew (1996) for visible (VIS) and near–infrared (NIR) and direct and diffuse radiation.

summer by Morassutti and LeDrew (1996):

$$\alpha_{\mathrm{mp}} = a + \exp(-bd_{\mathrm{mp}} - c) \tag{4.27}$$

where a, b, and c are regression coefficients, determined for VIS ($400 - 689\,\mathrm{nm}$) and NIR ($689 - 1000\,\mathrm{nm}$) bands under different light conditions (Tab. 4.4). The exponential albedo decay is large for the first $10 - 20\,\mathrm{cm}$ of pond depth, and for deeper melt ponds the albedo is relatively constant. An overview of the impact of melt ponds on Arctic sea ice is given in the model study of Roeckner et al. (2012).

5. Atmosphere surface coupling

The documentation for JSBACH is in progress. Most of the JSBACH components can be found in (Raddatz et al. (2007)) and under http://www.mpimet.mpg.de/wissenschaft/land-im-erdsystem/globale-vegetationsmodellierung/jsbach-publikationen.html. For further information please contact Christian Reick (christian.reick@zmaw.de).

6. Model resolutions and resolution dependent parameters

6.1. Model resolutions and resolution-dependent parameters

ECHAM 6.0 contains several poorly constrained parameters relating to orographic and non-orographic gravity wave drag, clouds, convection and horizontal diffusion adjusted, or tuned, to yield an acceptable climate and a sufficiently stable model execution. Some of these parameters are adjusted individually for each horizontal and/or vertical discretization of the model. The ECHAM 6.0 model was rigorously tested to run coupled to the MPIOM ocean model in two resolutions, and in atmosphere-only mode in one higher resolution. Additionally, the model can be run in a set of lower and one higher resolutions for testing purposes.

6.1.1. Available model resolutions

For coupled simulations T63L47 was used with the MPIOM GR15 (1.5 degree) ocean resolution in MPI-ESM-LR. T63L95 was used with a higher resolved MPIOM TP04 ocean grid (0.4 degree) in MPI-ESM-MR. For both these setups, spun-up ocean initial states exist from the control simulations submitted to the CMIP5 archive. The model was also tested in atmosphere-only mode with satisfactory results at T127L95. The former model is designated MPI-ESM-HR in the CMIP5 archive. Correspondingly spun-up ocean initial state is not available for these resolution. See table for an overview:

ECHAM 6.0	MPIOM	Status, tested for:	CMIP5 designator
T63L47	GR15	Coupled and Uncoupled	MPI-ESM-LR
T63L95	TP04	Coupled and Uncoupled	MPI-ESM-MR
T127L95	N/A	Atmosphere-only	MPI-ESM-HR

6.1.2. Resolution-dependent parameters

The parameters that are resolution dependent for maintaining the radiation balance and, thereby, the global mean temperature for the supported resolutions are Cloud mass-flux above the level of non-buoyancy (CMFCTOP), and the Conversion rate from cloud water to rain in convective clouds (CPRCON). See Tiedtke (1989) for details. The parameter settings are given in the table.

The extra-tropical northern hemisphere tropospheric winds are tuned using orographic wave drag. This is done adjusting the orographic gravity wave drag strength, GKDRAG and GKWAKE, which we tend to set equal. The largest sub-grid scale orographic peaks must exceed the mean topography by GPICMEA, while the sub-grid scale orography standard deviation must exceed GSTD, before the scheme is activated. For details see Lott (1999). Resolution-dependent parameters are given in the table.

Non-orographic wave drag is modeled using a fixed background wave source field. The strength a meridional shape of the source field is adjusted to yield a good representation of the stratospheric circulation and variability, in particular the quasi-biennial oscillation. If LRMSCON_LAT is set to .true. the source field is latitude-dependent. At latitudes equator-ward of +/- LAT_RMSCON_LO = 5 degrees the source strength is RMSCON_LO, and at latitudes

poleward of +/- LAT_RMSCON_HI = 10 degrees the strength is set to RMSCON_HI, which is 1.0 for all resolutions. Between these latitudes the strength is interpolated. The parameters may be controlled at runtime through the 'gwsctl' namelist, and their default values for the supported resolutions are given in the Table:

Parameter	Subroutine	T63L47	T63L95	T127L95
CMFCTOP	mo_cumulus_flux	0.21	0.23	0.205
CPRCON	mo_cumulus_flux	$2.0 \cdot 10^{-4}$	$2.0 \cdot 10^{-4}$	$1.3 \cdot 10^{-4}$
GKDRAG	mo_ssodrag	0.50	0.25	0.50
GKWAKE	mo_ssodrag	0.50	0.25	0.50
GPICMEA	mo_ssodrag	400 m	400 m	200 m
GSTD	mo_ssodrag	100 m	100 m	50 m
RMSCON_LO	setgws	1.2	1.2	1.05

6.1.3. Code implementation

The resolution-dependent parameters are hard-coded into several subroutines. Thereby, the model configures itself when it is executed at a certain resolution. That also means that it requires code-modifications to run the model in a different resolution than those that are implemented. Some of the affected subroutines are listed in the Table. Each subroutine contains a series of IF- or CASE-statements that configures the model according to horizontal and/or vertical resolution. If a resolution is not supported by the code, execution will typically finish with an error message: 'Truncation not supported'.

In addition to the parameters treated here for the supported resolutions, a number of parameters vary among the unsupported resolutions, and the settings of these have not been evaluated. These pertain to snow and ice albedos (mo_surface_ice.f90), cloud optical properties (mo_newcld_optics.f90) and cloud microphysics (mo_cloud.f90). Horizontal diffusion and sponge-layer parameters are also set for each resolution in mo_hdiff.f90 and in setdyn.f90, while the time-step length needs to be set in mo_time_control.f90. See chapter 2.1 for details.

7. External data

7.1. Solar irradiation

The total solar irradiance Ψ of the earth is defined as the incoming solar energy at the top of the atmosphere per area, normed to a sun–earth distance of 1 astronomical unit, and integrated over the whole range of wavelengths $[0, \infty[$ (units: W/m^2). The solar irradiance $\lambda \mapsto \psi(\lambda)$ is the incoming solar energy at the top of the atmosphere per area and wavelength of electromagnetic radiation, also normed to a sun–earth distance of 1 astronomical unit (units: $W/m^2/nm$). Solar irradiance ψ and therefore Ψ vary with time. The variation patterns depend on the wave length and are therefore different for the various spectral bands of `ECHAM6`. For the old 6–band radiation scheme of ECHAM5, only the total solar irradiance Ψ was prescribed and the distribution onto the spectral bands was fixed. This means that for a spectral band $[\lambda_1, \lambda_2]$, the incoming energy

$$\psi_{\lambda_1, \lambda_2} := \int\limits_{\lambda_1}^{\lambda_2} \psi(\lambda) \, d\lambda$$

was determined from fixed fractions $\xi_{\lambda_1, \lambda_2} := \psi_{\lambda_1, \lambda_2}/\Psi$. For the new 14–band SRTM radiation scheme implemented in `ECHAM6` (section 2.4.2), the incoming solar irradiance of each band $\psi_{\lambda_1, \lambda_2}$ can vary independently with time.

7.1.1. Historic

For historic and future solar irradiance data we follow as closely as possible the recommendations for CMIP5 as provided by the SPARC/SOLARIS project as given on the web site (`http://www.geo.fu-berlin.de/en/met/ag/strat/forschung/SOLARIS/Input_data/CMIP5_solar_irradiance.html`). Historic data for the period 1850 until 2008 was reconstructed based on observations and proxy data by J. Lean (Naval Research Laboratory, Washington D.C., USA). Detailed information on the reconstruction is provided at the above mentioned web site. Total solar irradiance variations were reconstructed as described by Fröhlich and Lean (2004) based on time series of sunspots and faculae. The spectral dependence of the solar irradiance and its variability was determined from the spectral dependence of the sunspot blocking and facular brightening, as described in detail by Lean (2000). Data are provided for wavelengths from 100 to 100000 nm with a spectral resolution of 1 nm for small wavelengths and increasing with wavelength. For use in `ECHAM6` the original data have been averaged over the wavelength bins of the SRTM code as given in table 7.1 and scaled in order to provide the full TSI in the wavlength range covered by the SRTM scheme. Additionally, as recommended by SPARC/SOLARIS, the orginal data have been multiplied by a factor of 0.9965. This was done in order to obtain a TSI close to 1361 W/m^2 as suggested by recent observations instead of about 1368 W/m^2 assumed earlier. The temporal resolution of the original data is annually until 1881 and monthly starting in 1882. For use in `ECHAM6` we have linearly interpolated the annual data available before 1882 to monthly values in order to provide consistent data sets over the full historic period. However, it should be kept in mind that short period variability of solar irradiance used as input in the CMIP5 simulations is larger after than before 1882 (see Fig. 7.1).

7.1.2. Scenarios

For the future scenarios it is recommended to repeat solar cycle 23, i.e. irradiance data of the period May 1996 to July 2008 for August 2008 to Oct 2020, Nov 2020 to Jan 2033, etc. This means that data files for the 49 years from 2008 to 2056 can be used as input for the years 2057 to 2105 and further repeated for later periods. The time series of monthly TSI integrated from the spectral irradiances used for the period 1850–2100 is presented in Fig. 7.1.

Monthly averaged spectral irradiance data for the years 1850–2100 are stored in yearly files `swflux_14band_yyyy.nc`, `yyyy` being the year. These files contain the monthly mean values of Ψ as `TSI` and $\psi_{\lambda_1, \lambda_2}$ as `SSI` in W/m^2. These variables are read into `ECHAM6` and linearly interpolated with respect to time to the actual model radiation time step.
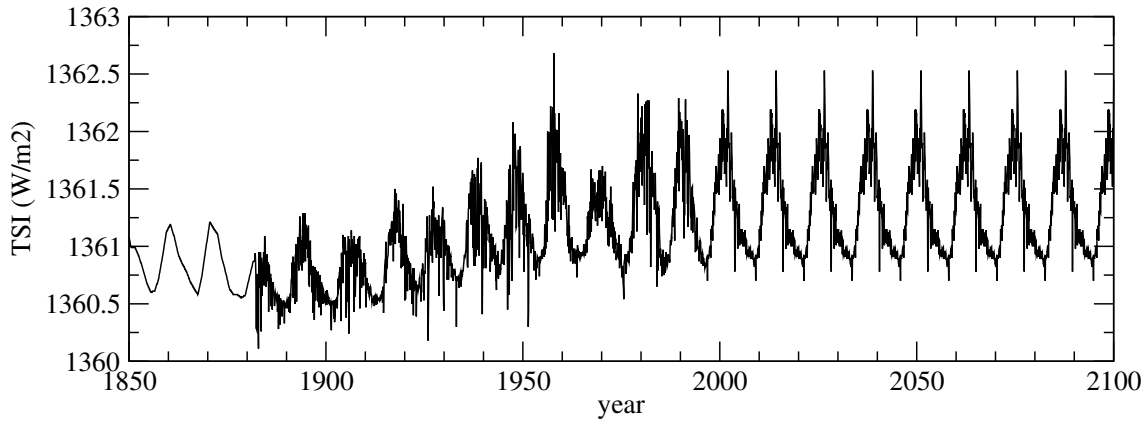
Figure 7.1.: Monthly averaged total solar irradiance (TSI) resulting from the spectrally resolved irradiance used in CMIP5 simulations with `ECHAM6`.

7.1.3. Climatologies

Several choices of climatological solar irradiance (i.e. constant solar irradiance that is independent of time) are available: The original "SRTM" values, a solar irradiance averaged over the years 1844–1856 ("preindustrial") that was used in the preindutrial control simulations of CMIP5, and a solar irradiance averaged over the years 1979–1988 ("amip"). In the latter two cases averaging was performed over data from the time dependent historic data set as described below. For simulations with constant solar irradiance it is recommended to use the "preindustrial" or "amip" climatological values which provide total solar irradiances (TSI) of close to 1361 W/m^2 to which `ECHAM6` has been tuned. The original TSI of "SRTM" is of about 1368 W/m^2 (see table 7.1). All the mentioned climatologies do not have to be read in from external files but can be accessed by specific choices of namelist parameters.

Table 7.1.: $\psi_{\lambda_1,\lambda_2}$ in W/m^2 as defined for the original SRTM radiation scheme (SRTM), for the preindustrial period (preind), and the amip period (amip). The resulting total solar irradiance (solar constant) Ψ is 1368.222 W/m^2 for the original SRTM scheme, 1360.875 W/s^2 for the preindustrial period, and 1361.371 W/m^2 for the amip period.

band/nm	3077 – 3846	2500 – 3077	2151 – 2500	1942 – 2151
index	1	2	3	4
$\psi_{\lambda_1,\lambda_2}$ (SRTM)	12.1096	20.3651	23.7297	22.4277
$\psi_{\lambda_1,\lambda_2}$ (preind)	11.9500	20.1461	23.4030	22.0944
$\psi_{\lambda_1,\lambda_2}$ (amip)	11.9505	20.1477	23.4039	22.0946
band/nm	1626 – 1942	1299 – 1626	1242 – 1299	788 – 1242
index	5	6	7	8
$\psi_{\lambda_1,\lambda_2}$ (SRTM)	55.6266	102.932	24.2936	345.742
$\psi_{\lambda_1,\lambda_2}$ (preind)	55.4168	102.512	24.6954	347.472
$\psi_{\lambda_1,\lambda_2}$ (amip)	55.4140	102.513	24.6981	347.536
band/nm	625 – 788	442 – 625	345 – 442	263 – 345
index	9	10	11	12
$\psi_{\lambda_1,\lambda_2}$ (SRTM)	218.187	347.192	129.495	50.1522
$\psi_{\lambda_1,\lambda_2}$ (preind)	217.222	343.282	129.300	47.0762
$\psi_{\lambda_1,\lambda_2}$ (amip)	217.292	343.422	129.403	47.1426
band/nm	200 – 263	3846 –12195		
index	13	14		
$\psi_{\lambda_1,\lambda_2}$ (SRTM)	3.07994	12.8894		
$\psi_{\lambda_1,\lambda_2}$ (preind)	3.17212	13.1807		
$\psi_{\lambda_1,\lambda_2}$ (amip)	3.17213	13.1808		

7.2. CO2, CH4, N2O, CFCs

7.2.1. 1850-present, present to 2100 and beyond

The data sets for pre-industrial, historical and future concentrations of well mixed greenhouse gases have been provided by IIASA as global mean time series at:
`http://www.iiasa.ac.at/web-apps/tnt/RcpDb/`

For historical times and the future until 2100 the Representative Concentration Pathway (RCP) scenarios are used. RCP 4.5 is a stabilization scenario where total radiative forcing is stabilized before 2100 (Thomson et al., 2011). RCP 8.5 is characterized by increasing greenhouse gas emissions over time (Riahi et al., 2011). RCP 2.6, also known as RCP 3-PD, first peaks at 3.1 Wm^{-2} around mid-century, and then declines to 2.6 Wm^{-2} by 2100 (van Vuuren et al., 2011).

For the years 2100 to 2300 the proper RCP scenarios have been extended, for the purpose of climate modelling (Meinshausen et al., 2011).

Further information on the original data can be found on the given IIASA website.

Starting from the original data in ASCII-Format the greenhouse gases relevant for `ECHAM6` (CO2, CH4, N2O, CFC-11 and CFC-12) were extracted and simply rewritten in netcdf-Format. Units are ppmv for CO2, ppbv for CH4 and N2O, and pptv for CFC-11 and CFC-12.

7.3. Ozone

Ozone absorbs in the solar wave length spectrum but also in the thermal wave length spectrum thus acting as a greenhouse gas. According to Brasseur et al. (1999, p.528) it contributes about 16% to the total radiative forcing due to increases in greenhouse gas concentrations for the period from 1900 to 1990. The mass mixing ratio of ozone in the atmosphere strongly varies with altitude and geographical latitude. The variation with geographical longitude at fixed latitude and altitude are less pronounced but not negligible. Therefore, it is preferable to use 3–dimensional ozone data. The ozone concentration also depends on time, but climatological data may be useful for non–transient simulations.

7.3.1. Historic

The data set for historic ozone concentrations was created within the projects AC&C and SPARC for simulations (e.g. CMIP5) that do not take interactive chemistry into account (Cionni et al. (2011)). The ozone data are prepared using satellite (SAGE I and II) and radiosonde data for the stratosphere and model data (CAM3.5 and NASA-GISS PUCCINI) for the troposphere. These historic ozone data include the ozone reduction in the stratosphere caused by ozone depleting species. A short description of the construction is given on: `http://www.pa.op.dlr.de/CCMVal/AC&CSPARC_O3Database_CMIP5.html`.

Ozone data are provided in terms of 3–dimensional monthly averages. However, in the stratosphere the data set does not vary with longitude, so that only in the troposphere real 3D information is available.

Original data exist only for altitudes with pressures larger than 1 hPa. Since the standard vertical resolutions include model layers with pressures as low as 0.01 hPa, the dataset was extended upward by Chris Bell (University of Reading) applying the following formula:

$$O_3(z) = O_3(1 \text{ hPa}) * \exp(-(z - z(1 \text{ hPa}))/H), \tag{7.1}$$

with H set to 7 km and $O_3(z)$ denoting the ozone concentration at altitude z.

The resulting 3–dimensional ozone data for the years 1850–2008 are given as monthly mean values on 39 pressure levels which are listed in Table 7.2. The data are organized in yearly files `T{RES}_ozone_CMIP5_`*yyyy*`.nc` where `{RES}` represents the horizontal resolution and *yyyy* the respective year between 1850 and 2008. These files contain the pressure levels in the variable `plev` and the ozone volume mixing ratio in the variable `O3`. Height interpolation is performed by `ECHAM6`.

Table 7.2.: Pressure levels in Pa of ozone climatology

1	3	5	10	20	30	50	100
150	200	300	500	700	1000	1500	2000
3000	5000	7000	8000	10000	15000	20000	25000
30000	40000	50000	60000	70000	85000	100000	

7.3.2. Scenarios

Future ozone scenarios for the period 2008–2099 are provided from the same source mentioned in the case of historic data. In the case of the future the data set is based on multi–model projections provided in the framewok of the SPARC Chemistry-Climate Model Validation Activity (CCMVAL, see Cionni et al. (2011); Eyring et al. (2010)). As in the case of historical ozone the original dataset also did only extend up to 1 hPa and was extended upward by Chris Bell. This dataset however does not include a solar cycle. For CMIP5 simulations with `ECHAM6`solar cycle 23 is repeated for the future, i.e. the solar variability for the period May 1996 to July 2008 is repeated for August 2008 to October 2020, November 2020 to January 2033, etc. (see section 7.1). In order to obtain future ozone concentrations consistent with the assumptions for solar irradiance a multi-linear regression analysis was performed for the historical ozone data using the solar irradiance at a wavelength of 180.5 nm and the EESC (Equivalent Effective Stratospheric Chlorine) content as regressors. The resulting regression coefficients for the ozone dependence on solar irradiance and the assumed future irradiance at 180.5 nm were then used to add a solar cycle dependence to the future stratospheric ozone. Tropospheric data (for $p \geq 100$ hPa) have not been modified as the solar cycle dependence calculated from the historic data for this altitude regime is negligible.

AC&C/SPARC ozone projections are available only until 2099. For the years starting with 2100 the original ozone data for the year 2099 are used, but modulated by a solar cycle effect as described above for the years until 2099. Data files were prepared until the year 2399.

The total column ozone for various geographical regions for the years 1850 to 2099 is presented in Fig. 7.2.
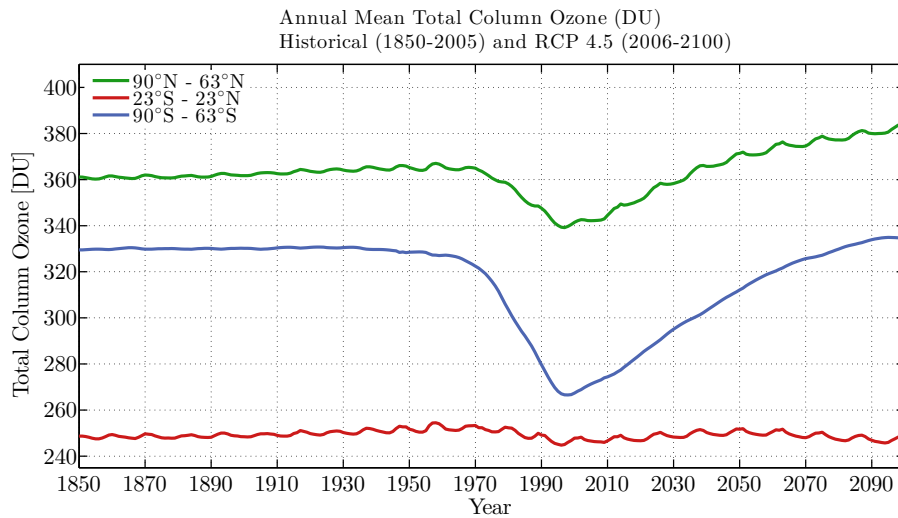
Figure 7.2.: Annual total column ozone for various geographical regions for the years 1850 to 2099. Figure courtesy by Alexander Haumann

As in the case of historical data, 3–dimensional ozone data for the years 2009–2399 are given as monthly mean values on 39 pressure levels. The data are organized in yearly files `T{RES}_ozone_CMIP5_{rcp}_`*yyyy*`.nc` where `{RES}` represents the horizontal resolution and *yyyy* the respective year. {rcp} can have the values RCP26, RCP45 or RCP85, and indicates the respective representative concentration pathway (i.e. future greenhouse gas scenario) for which the data set is valid. While in the stratosphere (for $p < 100$ hPa) all data sets are equal,

the AC&C/SPARC projections differ for tropospheric ozone.

7.3.3. Climatologies

In some cases, mean values of historic ozone concentration over time may be used as climatological boundary condition. Therefore, monthly mean ozone concentrations over eleven years for the years 1850–1860 (`T{RES}_ozone_CMIP5_1850-1860.nc` to be used for preindustrial simulations and the years 1979-1988 (`T{RES}_ozone_CMIP5_1979-1988.nc`) are also provided. In both cases the averaging was performed over about one full solar cycle in order to avoid potential biasing from biased solar irradiance.

7.4. Aerosols

Aerosols affect the distribution of radiative energy in the atmosphere by scattering and absorption of electromagnetic radiation. This is the direct aerosol effect. Aerosols also modify cloud optical properties and influence the cloud formation processes and precipitation. Since this also acts on radiation, but the aerosol particles are involved by the intermediate of clouds, this is called the indirect aerosol effect. The radiative transfer calculation of `ECHAM6` needs time dependent 3–d fields of (1) the extinction ζ by aerosols, (2) the single scattering albedo ω (SSA), and (3) the asymmetry factor g for a detailed consideration of the direct aerosol effect. These quantities depend on the wavelength of the electromagnetic radiation and have to be provided for each of the 14 solar radiation bands and the 16 thermal radiation bands used in `ECHAM6`. In the thermal radiation range, the knowledge of ζ and ω is sufficient, since the radiative transfer calculation does not account for scattering in this wavelength regime.

7.4.1. Tropospheric aerosols

In this section, we describe the generation of a data set of optical properties of tropospheric aerosols for the historic period of 1850 to 2000 and for three different future emission scenarios (Moss et al. (2010)) until 2100. Tropospheric aerosol is partly anthropogenic and highly diverse in concentration, size, and composition.

We combine complete and consistent background maps of monthly mean aerosol optical properties from global model results with high quality monthly averages from ground based remote sensing. All equations are valid for monthly means. We distinguish between fine mode aerosols with particle radii smaller than $0.5\,\mu$m and coarse mode aerosols with radii equal or larger than $0.5\,\mu$m. Coarse mode aerosols are assumed to be of natural origin comprising dust and sea salt. Fine mode aerosols consist of sulfate and organic matter including black carbon. The general procedure consists of 7 steps: (1) Establishing 2–d maps of column properties of the aerosol optical depth (AOD), single scattering albedo, and the Ångström parameter at 550 nm for the year 2000, (2) separating the AOD into one due to fine and one due to coarse mode aerosols for the year 2000, (3) defining the microphysical properties of the coarse mode, (4) spreading the optical properties to all wavelengths, (5) defining altitude profiles, (6) establishing an anthropogenic (fine mode) AOD for the year 2000, (7) extending the anthropogenic AOD back to the year 1850 and forward to the year 2100 using selected future emission scenarios.

(1) 2–d maps of column aerosol optical properties for the year 2000

In a first step, monthly mean values of the total aerosol optical depth τ of each column together with one value of the single scatter albedo ω, and Ångström parameter α for that column were determined for light of a wavelength of 550 nm. The background data are based on maps of medians of an ensemble of up to 15 different global models all applying a complex aerosol module. All models simulated the respective quantities for present day conditions in the frame work of the AeroCom project (Kinne et al. (2006)). The resulting maps were blended by the use of AERONET ground based sun–/sky–photometer data (Holben et al. (1998)): We first associated a "factor of influence" around each AERONET site being equal to one at the exact location of the site and tending to zero with increasing distance from the site. The rate of decrease depends on how well the measurements of this site repesent the aerosol optical properties of its surroundings. The original medians were then multiplied by the factor

of influence times the ratio of the AERONET measurement value and the original median. Thus, we obtain a map of τ, ω, α with AERONET–similar values near the AERONET sites and median values of the model ensemble at remote places. The above method provides the monthly mean optical properties on a $1° \times 1°$ longitude–latitude grid for all aerosols.

(2) Splitting the AOD into fine and coarse mode contributions for the year 2000

In order to split the aerosol optical depth into a part for fine and coarse mode, we use the Ångström parameter. It is assumed that the Ångström parameter is zero for the coarse mode and that it varies between 1.6 and 2.2 for the fine mode depending on humidity. Details of this procedure are described by Kinne (2012).

(3) Definition of the coarse mode microphysical properties

In order to derive the coarse mode aerosol optical properties at 550 nm, the respective composition and particle size has to be known. It is assumed that the coarse mode aerosols are ten times less absorbing than the fine mode aerosols. The initial guess of the coarse mode single scattering albedo $\omega_{c,0}$ depends on the total aerosol single scattering albedo ω and the ratio of the aerosol optical depth of the fine mode τ_f and the total aerosol optical depth τ:

$$\omega_{c,0} = 1 - \frac{1 - \omega}{1 + 9\frac{\tau_f}{\tau}}$$

This choice determines the mixing ratio of dust and sea salt aerosols in the coarse mode. For latitudes between 35° S and 45° N, the fraction of dust was assumed to increase with coarse mode aerosol optical depth. In the initial guess, it is assumed that dust particles have an effective radius of $1.5\,\mu m$ and sea salt particles have an effective radius of $2.5\,\mu m$. However, the size of the dust particles can be set to larger values in order to avoid unrealistic small values for the single scattering albedo of the fine mode aerosols. In such cases, the single scattering albedo of the fine mode is kept at values given by:

$$\omega_{f,0} = 1 - \left(\frac{1}{10}\mathrm{e}^{-3\tau} + \frac{1}{4}\frac{\tau_f}{\tau} \right). \tag{7.2}$$

(4) Spreading the optical properties to all wavelengths

The coarse mode aerosol optical properties for all wavelengths are then determined by Mie scattering calculations from the knowledge of the refractive indices (see Tab. 7.3), the size, and the composition of the coarse mode. Thus, the fine mode aerosol optical properties at 550 nm is also determined.

The aerosol optical properties of the fine mode aerosols are required at solar wavelengths only since the interaction of these small particles with light in the thermal spectral range is negligible. In the solar spectral range, the aerosol optical depth is given by

Table 7.3.: Wavelengths of the 14 bands in the short wavelength range and the 16 bands in the long wavelength range as they are used in the radiation calculation of `ECHAM6` and the refractive indices of sulfate, dust (Sokolik et al. (1998)), and sea salt (Nilsson (1979))

λ_{v}/nm	sulfate	dust	sea salt
solar radiation			
200 – 263	$1.450 + i1.0 \times 10^{-9}$	$1.450 + i0.025$	$1.510 + i1 \times 10^{-5}$
263 – 345	$1.450 + i1.0 \times 10^{-9}$	$1.450 + i0.020$	$1.510 + i1 \times 10^{-6}$
345 – 442	$1.445 + i1.0 \times 10^{-9}$	$1.450 + i0.0025$	$1.500 + i2 \times 10^{-8}$
442 – 625	$1.432 + i1.0 \times 10^{-9}$	$1.450 + i0.001$	$1.490 + i1 \times 10^{-8}$
625 – 778	$1.427 + i5.2 \times 10^{-8}$	$1.450 + i0.00095$	$1.480 + i1 \times 10^{-7}$
778 – 1242	$1.422 + i1.3 \times 10^{-6}$	$1.450 + i0.00075$	$1.470 + i1 \times 10^{-4}$
1242 – 1299	$1.413 + i7.9 \times 10^{-6}$	$1.450 + i0.00060$	$1.470 + i3.3 \times 10^{-4}$
1299 – 1626	$1.406 + i9.0 \times 10^{-5}$	$1.450 + i0.00080$	$1.460 + i5.5 \times 10^{-4}$
1626 – 1942	$1.393 + i5.1 \times 10^{-4}$	$1.450 + i0.0010$	$1.450 + i1 \times 10^{-3}$
1942 – 2151	$1.382 + i1.3 \times 10^{-3}$	$1.450 + i0.0015$	$1.450 + i1.5 \times 10^{-3}$
2151 – 2500	$1.364 + i2.1 \times 10^{-3}$	$1.460 + i0.0025$	$1.440 + i2.5 \times 10^{-2}$
2500 – 3077	$1.295 + i5.5 \times 10^{-2}$	$1.460 + i0.0060$	$1.400 + i8 \times 10^{-3}$
3077 – 3846	$1.361 + i1.4 \times 10^{-1}$	$1.460 + i0.0118$	$1.480 + i1.3 \times 10^{-2}$
3846 – 12195	$1.400 + i2.6 \times 10^{-1}$	$1.170 + i0.10$	$1.400 + i1.4 \times 10^{-2}$
thermal radiation			
3078 – 3846	$1.380 + i1.5 \times 10^{-1}$	$1.468 + i0.011$	$1.480 + i0.00156$
3846 – 4202	$1.397 + i1.3 \times 10^{-1}$	$1.480 + i0.0044$	$1.478 + i0.00175$
4202 – 4444	$1.396 + i1.2 \times 10^{-1}$	$1.487 + i0.0053$	$1.488 + i0.00246$
4444 – 4808	$1.385 + i1.2 \times 10^{-1}$	$1.502 + i0.0092$	$1.483 + i0.00251$
4808 – 5556	$1.348 + i1.5 \times 10^{-1}$	$1.525 + i0.0228$	$1.459 + i0.00288$
5556 – 6757	$1.385 + i1.7 \times 10^{-1}$	$1.423 + i0.054$	$1.505 + i0.0180$
6757 – 7194	$1.277 + i1.5 \times 10^{-1}$	$1.439 + i0.0976$	$1.450 + i0.00543$
7194 – 8474	$1.180 + i4.5 \times 10^{-1}$	$1.248 + i0.105$	$1.401 + i0.0138$
8474 – 9259	$1.588 + i6.7 \times 10^{-1}$	$1.613 + i0.439$	$1.638 + i0.0293$
9259 – 10204	$1.777 + i6.0 \times 10^{-1}$	$2.739 + i0.783$	$1.563 + i0.0179$
10204 – 12195	$1.799 + i3.3 \times 10^{-1}$	$1.816 + i0.299$	$1.485 + i0.0140$
12195 – 14286	$1.724 + i1.6 \times 10^{-1}$	$1.697 + i0.189$	$1.408 + i0.0192$
14286 – 15873	$1.601 + i1.9 \times 10^{-1}$	$1.518 + i0.231$	$1.447 + i0.0344$
15873 – 20000	$1.758 + i4.0 \times 10^{-1}$	$1.865 + i0.546$	$1.763 + i0.111$
20000 – 28571	$1.850 + i2.7 \times 10^{-1}$	$2.552 + i0.741$	$1.754 + i0.250$
28571 – 1000000	$1.850 + i2.7 \times 10^{-1}$	$2.552 + i0.741$	$1.628 + i0.997$

$$\tau_{\mathrm{f}}(\lambda_i) = \tau_{\mathrm{f}}(550\,\mathrm{nm}) \left(\frac{\lambda_i}{550\,\mathrm{nm}} \right)^{\alpha_{\mathrm{f}}}, \quad i = 1, \ldots, 14$$

for the 14 solar spectral bands. The single scattering albedo at $550\,\mathrm{nm}$ is used for shorter wavelengths and reduced towards longer wavelengths. The wavelength dependent asymmetry factor g_{f} of the fine mode is parametrized as function of the Ångström parameter α and solar wavelength λ by

$$g_{\mathrm{f}}(\lambda) = \max \left\{ 0.72 - 0.14\alpha_{\mathrm{f}} \sqrt{\frac{\lambda}{\lambda_0} - \frac{1}{4}}, 0.1 \right\}, \quad \lambda_0 = 1\,\mu\mathrm{m}, \quad 0.25\,\mu\mathrm{m} \le \lambda \le 3\,\mu\mathrm{m}$$

The aerosol optical properties of the year 2000 are now defined. These data serve as a basis for temporal extension.

(5) Definition of altitude profiles

To obtain an altitude profile of the aerosol optical depth, data from global model studies with ECHAM5–HAM were adopted. The single scattering and the asymmetry factor of fine and coarse mode do not change with altitude. Since the model distinguishes between fine mode and coarse mode aerosol, local monthly altitude distributions were separately described for fine mode aerosol and for coarse mode aerosol.

(6) Establishing an anthropogenic (fine mode) AOD for the year 2000

We assume that all anthropogenic aerosols belong to the fine mode aerosols. The Laboratoire de Météorologie Dynamique (LMD) model simulated the aerosol optical properties for the year 2000 and the pre–industrial period (Boucher and Pham (2002)). It is assumed that the emissions are all of natural origin for the pre–industrial period. The pre–industrial fine mode aerosol optical depths $\tau_{\mathrm{f,pre}}^{(\mathrm{LMD})}$ are everywhere lower than those for the fine mode of the year 2000 $\tau_{\mathrm{f,2000}}^{(\mathrm{LMD})}$. The anthropogenic aerosol optical depth of the year 2000 $\tau_{\mathrm{a,2000}}$ is then derived from the fine mode aerosol optical depth of the year 2000 $\tau_{\mathrm{a,2000}}$:

$$\tau_{\mathrm{a,2000}} := \tau_{\mathrm{f,2000}} \times f_{\mathrm{a,2000}}, \quad \text{with} \quad f_{\mathrm{a,2000}} := \frac{\tau_{\mathrm{f,2000}}^{(\mathrm{LMD})} - \tau_{\mathrm{f,pre}}^{(\mathrm{LMD})}}{\tau_{\mathrm{f,2000}}^{(\mathrm{LMD})}}$$

We assume that the natural aerosols do not change over time, neither in concentration nor size or composition. The composition of the anthropognic aerosols is also kept constant in time but its concentration changes.

(7) Extending the anthropogenic AOD back and forward in time

The only quantity that is allowed to vary with time is the anthropogenic aerosol optical depth. This means that pre–industrial fine mode and coarse mode aerosol optical properties are constant in time. The altitude profile associated with the aerosol optical depth of coarse and

fine mode are also kept constant in time. This implies that we assume the same composition and altitude distribution of pre–industrial fine mode aerosol and fine mode aerosol for the year 2000. Nevertheless, note that all aerosol optical properties can change their altitude profile with time because of the weighted mean values over the various aerosol types that will be discussed in the section about the implementation.

Historic The contribution of the anthropogenic aerosols to the aerosol optical depth due to fine mode aerosols is estimated in the following way: First, an ECHAM5–HAM (Stier et al. (2005)) hindcast simulation using National Institute for Environmental Studies (NIES) emissions was performed for the years 1850–2000. The output of the fine mode aerosol optical depth was interpolated to a $1° \times 1°$ longitude–latitude grid and monthly 10–year means were calculated. From these, anthropogenic fractions for the year j can be determined by

$$f_{\mathrm{a},j}^{(\mathrm{HAM})} = \frac{\tau_{\mathrm{f},j}^{(\mathrm{HAM})} - \tau_{\mathrm{f,pre}}^{(\mathrm{HAM})}}{\tau_{\mathrm{f},2000}^{(\mathrm{HAM})} - \tau_{\mathrm{f,pre}}^{(\mathrm{HAM})}}.$$

The ratios were then linearly interpolated to all years 1860 to 2000. Then, the anthropogenic contribution to the aerosol optical depth $\tau_{\mathrm{a},2000}$ was multiplied with this ratio resulting in the anthropogenic part of the aerosol optical depth for year j:

$$\tau_{\mathrm{a},j} = \tau_{\mathrm{a},2000} \times f_{\mathrm{a},j}^{(\mathrm{HAM})}.$$

Scenarios

Anthropogenic aerosols have been predicted to be an important forcing for the future climate. For an ideal climate projection, one would utilize a fully coupled Earth system model with online aerosol computations, but such experiments are computationally very expensive. An alternative could be to use an atmosphere–only model with a detailed aerosol submodel, to perform simulations with prescribed emission scenarios through the projection period (with sea surface temperatures from coupled model runs without interactive aerosols), to store the simulated aerosol properties, and to use them as a forcing for the Earth system model. In this case, aerosol model simulations would need to be performed for each scenario, which would still be expensive. As a flexible and inexpensive alternative, we generate future scenarios of aerosol radiative properties using the Kinne aerosol climatology of the year 2000, the CMIP5 emission scenarios (RCP2.6, RCP4.5, and RCP8.5, see the description by Moss et al. (2010)), and ECHAM5–HAM (Stier et al. (2005)) model simulations. This approach is based on the following assumptions:

1. Vertical profiles of the aerosol optical depth will not change significantly in the future.

2. Changes in the vertically integrated aerosol optical depth (column AOD) are approximately linear functions of the changes in emissions.

3. When forced by fixed emissions (with seasonal cycle but without interannual variability or trend), the 10–year average of column AOD simulated by ECHAM5–HAM is a good representation of the steady state.

4. Contributions of anthropogenic emissions to the total AOD from the 10 regions identified by the CMIP5 emission scenarios are largely independent and do not interact with each other strongly.

The first step for constructing the AOD scenarios is to build a "database" that quantifies the impact of a change in the emissions in one of the 10 regions on the global column AOD. For each of the 10 regions we performed a 10–year simulation using the aerosol climate model ECHAM5–HAM but with the regional emissions reduced to 50% of the year 2000 level. For this purpose, we used ECHAM5–HAM in the T42L19 resolution. As boundary conditions of the atmosphere, the climatological sea surface temperature and sea ice concentration are used. We only consider the aerosol optical depth caused by fine mode aerosols since fine mode aerosols are dominated by the anthropogenic aerosols whereas coarse mode aerosols are of mostly natural origin. The AOD of the fine mode aerosols is not affected by the statistical variability of coarse mode particles. Thus, we reduce the statistical noise in our results. The resulting 10–year mean column fine mode AOD is then compared with a control experiment with the year 2000 emissions. The grid points at which the fine mode AOD changes are statistically significant are identified, and a map of differences $\Delta\tau_l^{(f)}$ of the fine mode AOD under a 50% emission reduction in region l ($\tau_{l,50\%}^{(f)}$) and the reference AOD of the year 2000 ($\tau_{2000}^{(f)}$) for each region $l = 1, \ldots, 10$ is stored:

$$\Delta\tau_l^{(f)} = \tau_{l,50\%}^{(f)} - \tau_{2000}^{(f)}$$

Only the sulfur emissions were reduced in the simulations, because sensitivity simulations indicated that a change of carbonaceous aerosol emissions does not contribute to the AOD change as significantly as changes in sulfur emissions do.

In the second step, for any prescribed global emission at any time instance j we compute the difference between each regional mean emission $q_{l,j}$ of region l and the corresponding year 2000 value $q_{l,2000}$, and then the ratio $\xi_{l,j}$ between this difference and the difference between 50% regional mean of the year 2000 given by $q_{l,50\%}$ and the corresponding emission for the year 2000:

$$\xi_{l,j} := \frac{q_{l,j} - q_{l,2000}}{q_{l,50\%} - q_{l,2000}}.$$

The global fine mode AOD resulting from the emissions $q_{l,j}$ is then calculated by superposition:

$$\tau_j^{(f)} = \max\left\{\sum_{l=1}^{10} \xi_{l,j}\Delta\tau_l^{(f)} + \tau_{2000}^{(f)}, \tau_{pre}^{(f)}\right\},$$

where $\tau_{pre}^{(f)}$ is the pre–industrial fine mode aerosol optical depth. It serves as a lower limit of the fine mode aerosol optical depth. Fine mode AOD data from the year 2000 to 2100 have been created by using this method. These data can then be used to define a scaling factor with respect to the AOD of the year 2000.

The main advantage of this method is that one can easily estimate future change of aerosol radiative properties for any given emission scenario without having to repeat the simulation

with the global aerosol model, as long as the assumptions listed above are valid. On the other hand, the method also has some limitations. For example, at a certain gridbox the reponse of the fine mode AOD to emission changes might be non–linear, so the assumption mentioned above may cause some error. Furthermore, in both the historical and scenario aerosol climatology, aerosol compositions are assumed to be fixed. This will also bring some error into the estimation.

Nevertheless, it is believed that in terms of global patterns and regional average, the estimated fine mode AOD projections under various scenarios are comparable to those predicted by an online global aerosol model. The estimated data for the year 2050 and 2100 were compared with ECHAM5–HAM simulations using emissions for the same year. In terms of main features of the global distribution and regional mean values, the estimated fine mode AOD agrees well with the predicted ones.

Summary of assumptions

Natural aerosol is assumed to remain constant over time. However, natural aerosol loads depend strongly on meteorological, synoptical and surface conditions so that at least locally strong inter–annual variations for natural aerosols can be expected. This is especially relevant since the AOD of natural aerosol dominates anthropogenic aerosol in many regions of the world.

Anthropogenic aerosol is only found in the fine–mode. This is not completely true, since dust is partly of anthropogenic origin, mainly due to man–made changes to land–cover. However, since this anthropogenic contribution is generally a minor fraction of the dust and in addition highly speculative and uncertain, this anthropogenic coarse mode contribution has been ignored.

Fine mode aerosol composition does not change with time. It should be noted that in both historical extrapolations and future–scenario simulations only changes to the AOD are considered. However, the BC aerosol type had relatively strong contributions in the 1930ies, while the sulfate aerosols gain more importance in the 1960ies and 1970ies. Similarly, changes in the fine–mode composition for future anthropogenic aerosol can be expected.

Future scenarios are based on changes in sulfate emissions and the superposition principle is applied. However, other aerosol types from anthropogenic sources may become more important in the future. Because of the non–linearity of aerosol physics, the superposition principle may become inaccurate.

Implementation

For the shortwave (SW) or solar spectral bands, coarse and fine mode aerosol optical properties (column AOD $\tau_{sw}^{(f,c)}$, single scattering albedo $\omega_{sw}^{(f,c)}$, and asymmetry factor $g_{sw}^{(f,c)}$) have to be combined. Since fine and coarse mode are assigned different normed extinction profiles, $\zeta^{(f)}$ and $\zeta^{(c)}$, any changes in the ratio between coarse–mode and fine–mode column AOD will modify the vertical profiles of the single scattering albedo and the asymmetry factor.

For the longwave (LW) or IR spectral bands only the coarse mode aerosol contributes, as fine–mode aerosol is too small to play a significant role at these wavelengths. Since the IR

radiative transfer code does not account for scattering the required properties are the spectrally resolved column AOD $\tau_{\text{lw}}^{(c)}$, the column single scattering albedo $\omega_{\text{lw}}^{(c)}$ and coarse–mode altitude distribution via the normed extinction profile $\zeta^{(c)}$.

The altitude dependent optical depth is calculated in the following way. Let $(\Delta z_l)_{l=1,L}$ be the geometrical layer thickness of the ECHAM6 layers $1, \ldots, L$. Let the normed $\zeta^{(\text{f,c})}$ extinction of the climatology be given for layers $1, \ldots, K$ and

$$k : \begin{cases} \{1, \ldots, L\} & \to & \{1, \ldots, K\} \\ l & \mapsto & k_l \end{cases}$$

be the function that gives the layer k_l of the climatology inside of which the mid point of a given layer l of ECHAM6 is located. For simplicity, we attribute to this ECHAM6 layer l the normed extinction $\zeta_{k_l}^{(\text{f,c})}$. In general,

$$Z := \sum_{l=1}^{L} \zeta_{k_l}^{(\text{f,c})} \Delta z_l \neq 1$$

even if $\sum_{k=1}^{K} \zeta_k^{(\text{f,c})} \Delta y_k = 1$ for the layer thickness $(y_k)_{k=1,K}$ of the climatology. We want to have the same total optical depth in the simulation with ECHAM6 as in the climatology. Thus, we introduce renormalized extinctions

$$\tilde{\zeta}_{k_l}^{(\text{f,c})} := \zeta_{k_l}^{(\text{f,c})} / Z$$

With these renormalized extinctions, we can calculate the optical depths $\tau_{\text{sw,lw},l}^{(\text{f,c})}$ for each layer $l = 1, L$ of ECHAM6:

$$\tau_{\text{sw,lw},l}^{(\text{f,c})} = \tau_{\text{sw,lw}}^{(\text{f,c})} \tilde{\zeta}_{k_l}^{(\text{f,c})} \tag{7.3}$$

The total column optical depth is then exactly the given optical depth $\tau_{\text{sw,lw}}^{(\text{c,f})}$ of the climatology.

For the SW bands, the optical properties of the combined fine and coarse aerosol modes are obtained by the usual mixing rules. This results in the layer dependent optical depth $\tau_{\text{sw},l}$, the layer dependent single scattering albedo $\omega_{\text{sw},l}$, and the layer dependent asymmetry factor $g_{\text{sw},l}$ for each ECHAM6 layer $l = 1, L$:

$$\tau_{\text{sw},l} = \tau_{\text{sw},l}^{(\text{f})} + \tau_{\text{sw},l}^{(\text{c})} \tag{7.4}$$

$$\omega_{\text{sw},l} = \frac{\tau_{\text{sw},l}^{(\text{f})} \omega_{\text{sw}}^{(\text{f})} + \tau_{\text{sw},l}^{(\text{c})} \omega_{\text{sw}}^{(\text{c})}}{\tau_{\text{sw},l}} \tag{7.5}$$

$$g_{\text{sw},l} = \frac{\tau_{\text{sw},l}^{(\text{f})} \omega_{\text{sw}}^{(\text{f})} g_{\text{sw}}^{(\text{f})} + \tau_{\text{sw},l}^{(\text{c})} \omega_{\text{sw}}^{(\text{c})} g_{\text{sw}}^{(\text{c})}}{\omega_{\text{sw},l}} \tag{7.6}$$

Table 7.4.: File names of files containing tropospheric aerosol optical properties for a year yyyy and scenario `rcpzz`. The resolution of echam is `{RES}`.

File name	Explanation
`T{RES}_aeropt_kinne_sw_b14_coa.nc`	Aerosol optical properties of coarse mode aerosols in the solar range of the spectrum. The aerosols are of natural origin (dust, sea salt) and independent of the year for historic times.
`T{RES}_aeropt_kinne_lw_b16_coa.nc`	Aerosol optical properties of coarse mode aerosols in the thermal range of the spectrum. The aerosols are of natural origin (dust, sea salt) and independent of the year for historic times.
`T{RES}_aeropt_kinne_sw_b14_fin[_rcpzz]_yyyy.nc`	Aerosol optical properties of fine mode aerosols in the solar range of the spectrum. These aerosols are of anthropogenic origin and therefore depend on the year.

For the LW bands, the absorption optical depth is defined by:

$$\tau_{\text{lw},l}^{(\text{abs})} = \tau_{\text{lw}} \tilde{\zeta}_{k_l}^{(\text{c})} (1 - \omega_{\text{lw}}) \tag{7.7}$$

The fine mode aerosols of anthropogenic origin have an effect in the solar spectrum only and are the sole time dependent quantities. Tab. 7.4 gives an overview of the files used in `ECHAM6`.

7.4.2. Stratospheric aerosols

Stratospheric aerosols modify the heating in the stratosphere and have some influence on the radiation budget in the troposphere. The optical properties of these aerosols are mainly determined by the size and concentration of sulfuric acid droplets that form from SO_2 gas in the stratosphere. The SO_2 gas is either of volcanic origin or is formed from sulfur containing species from other sources at the surface of the earth. Ash aerosols from volcanic eruptions are of minor importance and play a role on short time scales of a few days to weeks only. Consequently, the data set of optical properties of stratospheric aerosols only accounts for the effect of volcanic aerosols released by eruptions reaching the stratosphere. Since the concentration and size distribution of sulfuric acid droplets in the stratosphere are determined by complex chemical processes, advective transport, and sedimentation processes in the stratosphere, the resulting aerosol optical properties are highly variable in space and time. Nevertheless, due to fast transport in East–West direction, the optical properties exhibit small variations for different

longitudes at the same latitude but vary strongly with latitude. Therefore, zonal mean values of the optical properties may describe the effect of volcanic aerosols on the radiation budget with sufficient accuracy.

Volcanic aerosols from 1850 until 1999

The data set of volcanic forcing for the historic period from 1850 to 1999 has been provided by G. Stenchikov. It is an extended version of the Pinatubo aerosol data set (PADS) derived by Stenchikov et al. (1998) from stellite measurements of aerosol extinction and effective radii after the Pinatubo eruption and successfully applied in climate model studies (Stenchikov et al. (2004, 2009); Thomas et al. (2009a,b)). This data set contains monthly mean zonal averages of the aerosol extinction ζ_v, the single scattering albedo ω_v, and the asymmetry factor g_v as a function of altitude, wavelength, and time. Furthermore, the integral aerosol optical depth of a column τ_v is given as a function of wavelength and time. The data set comprises the years 1850 to 1999. The data are given at 40 different mid-level pressures listed in table 7.5 together with the corresponding interface pressures. The interpolation with respect to altitude is performed in a similar way as for the tropospheric aerosols.

Table 7.5.: Pressure levels, mid level pressures (top), pressure at interfaces (bottom) in Pa

1		3		7		13		22	
0	2	2	4	4	10	10	16	16	28
35		52		76		108		150	
28	42	42	62	62	90	90	126	126	174
207		283		383		516		692	
174	240	240	326	326	440	440	592	592	792
922		1224		1619		2133		2802	
792	1052	1052	1396	1396	1842	1842	2424	2424	3180
3670		4793		6236		8066		10362	
3180	4160	4160	5426	5426	7046	7046	9086	9086	11638
13220		16748		21059		26192		32082	
11638	14802	14802	18694	18694	23424	28960	28960	28960	35204
38675		45908		53672		61799		70056	
35204	42146	42146	49670	49670	57674	57674	65924	65924	74188
78139		85673		92219		97287		100368	
74188	82090	82090	89256	89256	95182	95182	99392	99392	101344

The aerosol optical properties are provided at 30 wavelength bands which are listed in table 7.6. We give the index of the corresponding spectral bands in the `ECHAM6` radiation code in column three and four of the table. The definition of wavelength band 30 is different for the new data set and the radiation code of `ECHAM6`.

Table 7.6.: Wavelength bands for optical properties of volcanic aerosols in nm

band index	$\lambda_\mathrm{v}/$nm		ECHAM6 band	
1	200 –	263	solar 13	
2	263 –	345	solar 12	
3	345 –	442	solar 11	
4	442 –	625	solar 10	
5	625 –	778	solar 9	
6	778 –	1242	solar 8	
7	1242 –	1299	solar 7	
8	1299 –	1626	solar 6	
9	1626 –	1942	solar 5	
10	1942 –	2151	solar 4	
11	2151 –	2500	solar 3	
12	2500 –	3077	solar 2	
13	3077 –	3846	solar 1	thermal 16
14	3846 –	12195	solar 14	
15	3333 –	3846	—	
16	3846 –	4202		thermal 15
17	4202 –	4444		thermal 14
18	4444 –	4808		thermal 13
19	4808 –	5556		thermal 12
20	5556 –	6757		thermal 11
21	6757 –	7194		thermal 10
22	7194 –	8474		thermal 9
23	8474 –	9259		thermal 8
24	9259 –	10204		thermal 7
25	10204 –	12195		thermal 6
26	12195 –	14286		thermal 5
27	14286 –	15873		thermal 4
28	15873 –	20000		thermal 3
29	20000 –	40000		thermal 2
30	40000 –	250000		thermal 1

The aerosol optical properties of the volcanic aerosols in the solar wavelength range (τ_{v}, ω_{v}, g_{v}) and the thermal wavelength range ($\tau_{\mathrm{v}}^{(\mathrm{lw})}$, $\omega_{\mathrm{v}}^{(\mathrm{lw})}$) are added to the given aerosol optical properties in the solar wavelength range (τ, ω, g) and the thermal wavelength range ($\tau^{(\mathrm{lw})}$, $\omega^{(\mathrm{lw})}$) by the usual mixing rules (see equations (7.8)–(7.11)) although the tropospheric and stratospheric aerosols are separated by region. Nevertheless, this procedure assures generality and allows for an overlap of these regions.

$$
\begin{aligned}
\tau_{\mathrm{total}} &:= \tau + \tau_{\mathrm{v}} & (7.8)\\
\omega_{\mathrm{total}} &:= \frac{\tau\omega + \tau_{\mathrm{v}}\omega_{\mathrm{v}}}{\tau_{\mathrm{total}}} & (7.9)\\
g_{\mathrm{total}} &:= \frac{\tau\omega g + \tau_{\mathrm{v}}\omega_{\mathrm{v}}g_{\mathrm{v}}}{\tau_{\mathrm{total}}\omega_{\mathrm{total}}} & (7.10)\\
\tau_{\mathrm{total}}^{(\mathrm{lw})} &:= \tau^{(\mathrm{lw})} + \tau_{\mathrm{v}}^{(\mathrm{lw})}(1 - \omega_{\mathrm{v}}^{(\mathrm{lw})}) & (7.11)
\end{aligned}
$$

Volcanic aerosols from 790 until 2010

The historic record of stratospheric volcanic aerosols by G. Stenchikov (see the previous section) comprises the period from 1850 until 1999 only. Volcanic eruptions prior to this period can be taken into account by the use of the longterm data set by T. Crowley that gives information about the volcanic forcing in terms of total aerosol optical depth and the effective radius since 790. In that case, no information about the height distribution of the aerosols is available. T. Crowley estimated the total aerosol optical depth at 550 nm for four latitude bands (30°N – 90°N, 0°N – 30°N, 30°S – 0°N, 90°N – 30°S). For each of these latitude bands, he also gives an estimate of the effective radius of the aerosols. These original values for the aerosol optical depth and the effective radius are linearly interpolated for latitudes in $[15°\mathrm{N}, 45°\mathrm{N}[$ (between the values for the latitude bands 30°N – 90°N, 0°N – 30°N), $[15°\mathrm{S}, 15°\mathrm{N}[$ (between the values for the latitude bands 0°N – 30°N, 30°S – 0°N), and $[45°\mathrm{S}, 15°\mathrm{S}[$ (between the values for the latitude bands 30°S – 0°N, 90°N – 30°S).

For the radiation calculation, it is assumed that the volcanic aerosols consist of 75% sulfate aerosols. Certain wavelength and radius dependence tables prepared by S. Kinne are used to estimate the aerosol optical properties from the the aerosol optical depth at 550 nm and the effective radius r_{err} assuming a logarithmic normal distribution. For each particle radius r and wavelength λ a table provides the ratio $(r, \lambda) \mapsto \xi(r, \lambda) := \zeta(r, \lambda)/\zeta(r, 550)$ where ζ is the extinction coefficient, the single scattering albedo $(r, \lambda) \mapsto \omega(r, \lambda)$, and the asymmetry factor $(r, \lambda) \mapsto g(r, \lambda)$. Since ζ is assumed to be constant in a model layer, the extinction is proportional to the aerosol optical depth in one layer. Therefore, the space, time, and wavelength dependent volcanic aerosol optical properties τ_{v} are given for any position $\vec{x}$ in the atmosphere and time t by:

$$
\begin{aligned}
\tau_{\mathrm{v}}(\vec{x}, t, \lambda) &= \xi(r_{\mathrm{eff}}(\vec{x}, t), \lambda) \times \tau_{550}(\vec{x}, r) & (7.12)\\
\omega_{\mathrm{v}}(\vec{x}, t, \lambda) &= \omega(r_{\mathrm{eff}}(\vec{x}, t), \lambda) & (7.13)\\
g_{\mathrm{v}}(\vec{x}, t, \lambda) &= g(r_{\mathrm{eff}}(\vec{x}, t), \lambda) & (7.14)
\end{aligned}
$$

The aerosol optical properties of the volcanic or stratospheric aerosols are linearly interpolated in time and then added to the aerosol optical properties according to the common mixing rules

resulting in the following overall aerosol optical properties τ_{total}, ω_{total}, g_{total}. In the case of solar wavelenghts, the full mixing rules are applied:

$$\tau_{\text{total}} = \sum_{i=1}^{l} \tau_i \tag{7.15}$$

$$\omega_{\text{total}} = \frac{\sum_{i=1}^{l} \omega_i \tau_i}{\tau_{\text{total}}} \tag{7.16}$$

$$g_{\text{total}} = \frac{\sum_{i=1}^{l} g_i \omega_i \tau_i}{\tau_{\text{a}} \omega_{\text{total}}} \tag{7.17}$$

In the case of thermal wavelengths, only the aerosol optical depth has to be provided, but only the "absorbence" is taken into account:

$$\tau_{\text{total}} = \sum_{i=1}^{l} \tau_i (1 - \omega_i) \tag{7.18}$$

For historic volcanic eruptions, there is no information available about the vertical distribution of volcanic aerosols from measurements, but we know that the altitude distribution depends on the neutral buoyancy height of the volcanic plume at which the aerosols form. Furthermore, we know that the neutral buoyancy height is also limited because of the gravity effect on the plume as described by Herzog and Graf (2010); Timmreck et al. (2009) and by personal communication of H.–F. Graf 2005. From this, we conclude that the aerosols are located mainly in the stratosphere. The exact altitude position is not of first order relevance for the radiation budget in the troposphere provided that the total aerosol optical depth is correct. On the other hand, the influence on the dynamics of the stratosphere depends on the exact altitude but is not so relevant for simulations with a focus on the climate. We therefore decided to use an altitude profile that is similar to the injection height of SO_2 as it was observed from satellite after the Pinatubo eruption, see Sparks et al. (1997). The following pressure dependent weight function w is used at all geographical locations:

$$p \mapsto w(p) = \frac{1}{4} \times \mathbf{1}_{[30\text{hPa},40\text{hPa}[}(p) + \frac{1}{2} \times \mathbf{1}_{[40\text{hPa},50\text{hPa}[}(p) + \frac{1}{4} \times \mathbf{1}_{[50\text{hPa},60\text{hPa}[}(p) \tag{7.19}$$

where $\mathbf{1}_A$ is the characteristic function of set A. Let $\vec{y}$ represent a location on the surface of the Earth and be $(\vec{y}, r) \mapsto \tau_{\text{crow}}(\vec{y}, r)$ the aerosol optical depth at 550 nm and a certain effective radius r provided by T. Crowley, then $\tau_{550} = w \times \tau_{\text{crow}}$. The time, space and wavelength dependent optical properties of the volcanic aerosols are then given by equations (7.12–7.14). As in the case of the HAM derived volcanic aerosol properties, the full mixing rules are applied in the case of the solar radiation according to equations (7.15–7.17). In the case of the thermal radiation, the simplified equation (7.18) is used.

7.5. Sea surface temperature and ice cover

7.5.1. Historic

The historical sea surface temperature (SST) and sea ice cover (SIC) data are taken from PCMDI's Atmospheric Model Intercomparison Project (status: Nov. 2009):
`http://www-pcmdi.llnl.gov/projects/amip/`

The basic observational data set was made available by NCAR and was constructed following the procedure described by Hurrell et al. (2008). More information can be found on the given web site.

The data were downloaded as Grib files from
`http://www-pcmdi.llnl.gov/projects/amip/AMIP2EXPDSN/BCS/amipobs_dwnld.php`
and bilinearly remapped to the needed model grid. SST and SIC boundary conditions for 1979 to 2008 are used for the AMIP experiment of CMIP5.

7.5.2. Climatologies

Sea surface temperature and sea ice cover climatologies for `ECHAM6` are based on our coupled pre–industrial control simulations over 500 years for CMIP5, the so–called piControl experiments. These climatologies have been used for the so-called "sstClim" experiment of CMIP5. Climatologies are derived from three different piControl simulations resulting from different model configurations:

- MPI-ESM-LR

- MPI-ESM-MR

- MPI-ESM-P

7.5.3. Aqua planet

For CMIP5 aqua planet simulations the climatological input files have been modified following the requirements at
`http://www.atmos.ucla.edu/~brianpm/cfmip2_aqua.html`

Sea ice cover has been set to zero. Sea surface temperature is constant, symmetric about equator and zonally uniform, following the APE "Qobs" functional form:

$$T(\phi) = \begin{cases} T_0 + \Delta T_{max} \cdot (2 - \sin^2(\frac{3\phi}{2}) - \sin^4(\frac{3\phi}{2}))/2. & , |\phi| < \pi/3 \\ T_0 & , \text{otherwise (high latitudes)} \end{cases} \quad (7.20)$$

where $\Delta T_{max} = 27K$, $T_0 = 273.15K$.

7.6. Land data

7.6.1. Land sea maps

There are a couple of land-sea masks, dependent on the horizontal resolution of ECHAM6 and MPI-OM. Table 7.7 shows the available masks.

ECHAM6 \ MPI-OM	GR30	GR15	TP04	TP6M
T31	x	-	-	-
T63L47	-	x	-	-
T63L95	-	-	x	-
T127	-	-	x	-
T255	-	-	-	x

Table 7.7.: Available land sea masks dependent on ECHAM6 and MPI-OM resolution.

7.6.2. Orography

Subgrid scale orography

See. 2.9.1.

7.6.3. Vegetation maps

The documentation for JSBACH is in progress. Most of the JSBACH components can be found in (Raddatz et al. (2007)) and under http://www.mpimet.mpg.de/wissenschaft/land-im-erdsystem/globale-vegetationsmodellierung/jsbach-publikationen.html. For further information please contact Christian Reick (christian.reick@zmaw.de).

8. Errata

In the course of evaluating the MPI–ESM and ECHAM6 simulations a number of bugs have been identified which impact the simulations. We list these bugs here and give a description of their effects.

8.1. Bug in anthropogenic aerosol data set

In implementing the new aerosol climatology (see Section 7.4.1) a data formatting error led to a somewhat weaker anthropogenic aerosol forcing than was foreseen in the original data set, with the effect most pronounced over the heavily populated regions of the northern hemispheric continents. The adjusted all sky aerosol forcing for the AMIP period, calculated as the difference between the top–of–atmosphere fluxes for the AMIP period with the aerosol load for this period (including the formatting bug) and a run for the same period but with the pre–industrial tropospheric aerosol loading is -0.34 W m^{-2}. If the calculation is repeated but with the formatting bug removed the adjusted forcing increases to -0.50 W m^{-2}. For reference, the difference in the clear sky shortwave adjusted forcing between the two simulations is nearly three times as large (0.42 W m^{-2}) suggesting that much of the missing forcing attributable to the formatting error is offset by additional adjustments, compensating effects in the long wave, and cloud masking effects. Use of the correct aerosol only has a small impact in the representation of the clear sky reflected solar irradiance, decreasing the root mean square error relative to CERES from 6.6 to 6.5 W m^{-2}. This error is present in the external data set version `r0001` only, the newer versions have corrected aerosol data.

8.2. Energy conservation violation

In preparing `ECHAM6.2` emphasis was given to achieving energy conservation in the physics and surface coupling. This was achieved through a number of bug-fixes, including inconsistent use of specific heats, the coupling between convection and cloud schemes, discretization errors in the convection and turbulent diffusion schemes. After these corrections the atmospheric physics conserve energy, and the surface energy budget is consistent. However, the atmosphere still leaks a small amount of energy, presumably due to issues in the dynamical core.

A. The unparameterized equations

A.1. Introduction

To derive the governing equations given by (2.1)–(2.6) and (2.11)–(2.14), we take start from the unparameterized equations for a mixture of dry air, water vapour, liquid water and ice, and work for convenience in a Cartesian coordinate system. An individual component is denoted by a subscript i, where $i = d, v, l$, or i for dry air, water vapour, liquid water or ice, respectively. The specific mass of component k, denoted by q_k, is defined by

$$q_k = \frac{m_k}{m} = \frac{\rho_k}{\rho} \tag{A.1}$$

where

m_k	is the mass of component of k in a small material volume moving with the local velocity of the atmosphere,
$m = \sum m_k$	is the total mass of the material volume,
ρ_k	is the density of component k, and
$\rho = \sum \rho_k$	is the density of the atmosphere.

The rate of change of m_k is denoted by $\dot{m}_k$. This change occurs because of

    a. internal phase changes,

    b. rainfall, snowfall, and surface exchanges.

The rate of change due to (a) alone is denoted by $\dot{m}_{ki}$, and that due to (b) by $\dot{m}_{ke}$. Then

$$\dot{m}_k = \dot{m}_{ki} + \dot{m}_{ke} \tag{A.2}$$
$$\dot{m}_{di} = \dot{m}_{de} = 0 \tag{A.3}$$

$$\sum_i \dot{m}_{ki} = 0 \tag{A.4}$$

The rate of change of total mass is given by

$$\dot{m} = \sum_i \dot{m}_k = \sum_i \dot{m}_{ke} \tag{A.5}$$

The rate of change of density of component k satisfies the equation

$$\dot{\rho}_k = \frac{\rho}{m} \dot{m}_k \tag{A.6}$$

provided (as is reasonable) volume changes due to precipitation or phase changes are neglected. The net rate of change of density, $\dot{\rho}$, is then given by

$$\dot{\rho} = \frac{\rho}{m} \sum_k \dot{m}_k = \frac{\rho}{m} \dot{m} \tag{A.7}$$

A.2. The advective form of the unparameterized equations

A.2.1. The material derivative

The material derivative is denoted by $\frac{d}{dt}$. Its definition is

$$\frac{d}{dt} \equiv \frac{\partial}{\partial t} + \vec{v} \cdot \nabla \tag{A.8}$$

where $\vec{v}$ here denotes the three-dimensional velocity vector, and ∇ the ususal three-dimensional vector operator. Horizontal vectors and operators will subsequently be denoted by a subscript h.

A.2.2. The equation of state

We consider a volume V of atmosphere, of which dry air and water vapour occupy a volume V_{d+v}. The equations of state for dry air and water vapour are

$$p_d V_{d+v} = m_d R_d T \tag{A.9}$$

and

$$p_v V_{d+v} = m_v R_v T \tag{A.10}$$

where p_d and p_v are partial pressures. Dalton's Law then shows that the total pressure p is given from A.10 by

$$p = \frac{m_d R_d T + m_v R_v T}{V_{d+v}}. \tag{A.11}$$

Introducing the specific volumes of liquid water v_l, and ice v_i,

$$V_{d+v} = V - m_l v_l - m_i v_i = \frac{m}{\rho}(1 - \rho(q_l v_l + q_i v_i)) \tag{A.12}$$

and A.11 becomes

$$p = \rho T \frac{R_d q_d + R_v q_v}{1 - \rho(q_l v_l + q_i v_i)}. \tag{A.13}$$

or

$$p = \rho T R_d \frac{1 + \left(\frac{1}{\epsilon} - 1\right) q_v - q_l - q_i}{1 - \rho(q_l v_l + q_i v_i)}. \tag{A.14}$$

136

where

$$\epsilon = R_d/R_v \tag{A.15}$$

A.2.3. Mass conservation

Conservation of mass for element k leads to the equation

$$\frac{d\rho_k}{dt} + \rho_k(\nabla \cdot \vec{v}) = \dot{\rho}_k = \frac{\rho \dot{m}_k}{m} \tag{A.16}$$

Summing over k then gives

$$\frac{d\rho}{dt} + \rho(\nabla \cdot \vec{v}) = \frac{\rho \dot{m}}{m} = \dot{\rho} \tag{A.17}$$

In addition, by definition

$$\frac{dm_k}{dt} = \dot{m}_k \tag{A.18}$$

which gives

$$\frac{dq_k}{dt} = \frac{\dot{m}_k}{m} - \frac{m_k \dot{m}}{m^2} = \frac{1}{m}(\dot{m}_k - q_k \dot{m}) \tag{A.19}$$

A.2.4. The velocity equation

The advective form of the equations for the horizontal components of velocity is unaltered by mass changes. The horizontal velocity components thus satisfy the equation

$$\frac{d\vec{v}_h}{dt} = -\frac{1}{\rho}\nabla_h p - 2(\vec{\Omega} \times \vec{v}_h)_h \tag{A.20}$$

where $\vec{\Omega}$ is the earth's rotation vector. Changes due to molecular stresses are neglected.

A.2.5. The thermodynamic equation

As discussed by Dufour and Van Mieghem (1975, Eq. 5.21), the first law of thermodynamics may be written

$$\delta Q + \alpha dp = d_i H = d_i \left(\sum m_k h_k \right) \tag{A.21}$$

where the h_k are specific enthalpies, $\alpha = 1/\rho$ is the specific volume and the subscript i denotes changes independent of the mass changes due to precipitation. As molecular diffusion is neglected, δQ represents the heat received by the atmospheric element due to radiation and to heat exchange with falling rain or snow.

Under the usual assumptions of perfect gas behaviour for dry air and water vapour, and neglect of variations of the specific enthalpies of water and ice with pressure, we can write

$$h_k = h_k^0 + C_{pk}T \tag{A.22}$$

and (A.21) becomes

$$mC_p dT = \alpha dp + \delta Q - \sum_k h_k d_i m_k \tag{A.23}$$

where

$$C_p = \sum_k C_{pk} q_k \tag{A.24}$$

Thus considering a material volume of the atmosphere, we obtain the thermodynamic equation

$$C_p \frac{dT}{dt} = \frac{1}{\rho}\frac{dp}{dt} + Q_R + Q_M - \sum_k h_k \frac{\dot{m}_{ki}}{m} \tag{A.25}$$

where Q_R and Q_M are the heating rates due to respectively radiation and the heat transferred from falling rain or snow.

A.3. The flux forms of the equations

It is convenient to define the differential operator $\frac{D}{Dt}$ by

$$\frac{DX}{Dt} = \frac{dX}{dt} + X(\nabla \cdot \vec{v}) = \frac{\partial X}{\partial t} + \nabla \cdot (X\vec{v}) \tag{A.26}$$

Note that

$$\rho = \frac{dx}{dt} = \frac{D\rho x}{Dt} \text{ if } \dot{\rho} = 0 \tag{A.27}$$

Equations (A.19), (A.20) and (A.25) may then be written

$$\frac{D\rho}{Dt} = \frac{\rho}{m}\dot{m} = \dot{\rho} \tag{A.28}$$

$$\frac{D\rho q_k}{Dt} = \frac{\rho}{m}\dot{m}_k = \dot{\rho}_k \tag{A.29}$$

$$\frac{D\rho\vec{v}_h}{Dt} = \dot{\rho}\vec{v}_h - \nabla_h p - 2\rho(\vec{\Omega}\times\vec{v}_h)_h \tag{A.30}$$

$$C_p\frac{D\rho T}{Dt} = C_p\dot{\rho}T + \frac{dp}{dt} + \rho(Q_R + Q_M) - \rho\sum_k h_k\frac{\dot{m}_{ki}}{m} \tag{A.31}$$

From the definition (A.24) of C_p we obtain

$$\frac{DC_p\rho T}{DT} = C_p\frac{D\rho T}{DT} + \rho T\frac{d}{dt}\sum_k C_{pk}q_k \tag{A.32}$$

and using (A.24) and (A.31) gives

$$\frac{DC_p\rho T}{Dt} = C_p\dot{\rho}T + \frac{dp}{dt} + \rho\left(Q_R + Q_M\right) - \rho\sum_k\left(h_k^0 + C_{pk}T\right)\frac{\dot{m}_{ki}}{m} \\ + \rho T\sum_k C_{pk}\left(\frac{\dot{m}_k}{m} - \frac{q_k\dot{m}}{m}\right) \tag{A.33}$$

Using (A.2), (A.7) and (A.24), we obtain from (A.33):

$$\frac{DC_p\rho T}{Dt} = \frac{dp}{dt} + \rho\left(Q_R + Q_M\right) - \rho\sum_k h_k^0\frac{\dot{m}_{ki}}{m} + \rho T\sum_k C_{pk}\frac{\dot{m}_{ke}}{m} \tag{A.34}$$

A.4. The introduction of diffusive fluxes

We now introduce a separation of dependent variables into components that will be explicitly resolved in the model and components the effect of which will require parameterization.

If the bar operator represents an average over unresolved scales in space and time, then we write:

$$\begin{aligned} X &= \overline{X} + X' \text{ with } \overline{X'} = 0 \\ \text{and } X &= \overline{\overline{X}} + X'' \text{ with } \overline{\overline{X}}'' = 0 \\ \text{where } \overline{\overline{X}} &= \frac{\overline{\rho X}}{\overline{\rho}} \text{ is a mass weighted average.} \end{aligned}$$

It follows that

$$\frac{\overline{\overline{D}}\,\overline{\rho}\,\overline{\overline{X}}}{Dt} = \frac{\overline{D\rho X}}{Dt} - (\nabla \cdot \overline{\rho \vec{v}'' X''})$$

$$\frac{\overline{\overline{dX}}}{dt} = \frac{\overline{dX}}{dt} - \left(\overline{\vec{v}'' \cdot \nabla X}\right)$$

$$\overline{\rho XY} = \overline{\rho XY} = \overline{\rho}\,\overline{\overline{X}}\,\overline{\overline{Y}} + \overline{\rho X'' Y''}$$

Using these results, equations (A.27) - (A.29) and (A.33) become

$$\frac{\overline{\overline{D}}\,\overline{\rho}}{Dt} = \dot{\overline{\rho}} = \overline{\rho}\left(\frac{\overline{\overline{\dot{m}}}}{m}\right) \tag{A.35}$$

$$\frac{\overline{\overline{D}}\,\overline{\rho}\,\overline{\overline{q_k}}}{Dt} = \dot{\overline{\rho}}_k - \left(\nabla \cdot \overline{\rho\vec{v}'' q_k''}\right) = \overline{\rho}\left(\frac{\overline{\overline{\dot{m}_k}}}{m}\right) - \left(\nabla \cdot \overline{\rho\vec{v}'' p_k''}\right) \tag{A.36}$$

$$\frac{\overline{\overline{D}}\,\overline{\rho}\,\overline{\overline{\vec{v}_h}}}{Dt} = \overline{\dot{\rho}\vec{v}_h} - \nabla_h\overline{p} - 2\overline{\rho}\left(\vec{\Omega} \times \overline{\overline{\vec{v}_h}}\right)_h - \left(\nabla \cdot \overline{\rho\vec{v}''\vec{v}_h''}\right) \tag{A.37}$$

$$= \overline{\rho}\left(\frac{\overline{\overline{\dot{m}}}}{m}\right)\overline{\overline{\vec{v}_h}} - \nabla_h\overline{\rho} - 2\overline{\rho}\left(\vec{\Omega} \times \overline{\overline{\vec{v}_h}}\right)_h - \left(\nabla \cdot \overline{\rho\vec{v}''\vec{v}_h''}\right) - \overline{\rho\left(\frac{\dot{m}}{m}\right)'' \vec{v}_h''}$$

and

$$\frac{\overline{\overline{D}}}{Dt}\left(\overline{\rho}\,\overline{\overline{C_p}}\,\overline{\overline{T}} + \overline{\rho C_p'' T''}\right) = \frac{\overline{\overline{d\overline{p}}}}{dt} + \overline{\rho}\left(\overline{\overline{Q_R}} + \overline{\overline{Q_M}}\right) - \overline{\rho}\sum_k h_k^0\left(\frac{\overline{\overline{\dot{m}_{ki}}}}{m}\right)$$

$$+ \overline{\rho}\,\overline{\overline{T}}\sum_k C_{pk}\left(\frac{\overline{\overline{\dot{m}_{ke}}}}{m}\right) + \overline{\vec{v}'' \cdot \nabla p} - \left(\nabla \cdot \overline{\rho\vec{v}'' C_p T''}\right) \tag{A.38}$$

$$+ \sum_k C_{pk}\overline{\rho T''\left(\frac{\dot{m}_{ke}}{m}\right)''}$$

The equation of state A.13 gives

$$p = \rho RT \tag{A.39}$$

where $R = (R_d q_d + R_v q_v)/\{1 - \rho(q_l v_l + q_i v_i)\}$

whence

$$\overline{p} = \overline{\rho RT} = \overline{\rho}\,\overline{\overline{R}}\,\overline{\overline{T}} + \overline{\rho R'' T''} \tag{A.40}$$

Using $\overline{\overline{C_p}} = \sum C_{pk}\overline{\overline{q_k}}$, (A.36) and (A.38) may be written

$$\overline{\overline{C_p}}\frac{\overline{\overline{D}}\overline{\rho}\overline{\overline{T}}}{Dt} = \frac{\overline{\overline{dp}}}{dt} + \overline{\rho}\left(\overline{\overline{Q_R}} + \overline{\overline{Q_M}}\right) - \overline{\rho}\sum_k \overline{\overline{h_k}}\left(\frac{\overline{\overline{\dot{m}_{ki}}}}{m}\right) + \overline{\rho}\overline{\overline{C_p}}\,\overline{\overline{T}}\left(\frac{\overline{\overline{\dot{m}}}}{m}\right)$$

$$+ \quad \overline{v''\nabla p} - \nabla \cdot \overline{\rho\vec{v}''(C_pT)''} + \overline{\overline{T}}\sum_k C_{pk}\nabla\cdot\overline{\rho\vec{v}''q_k''} \qquad\qquad \text{(A.41)}$$

$$- \quad \frac{\overline{\overline{D}}}{Dt}(\overline{\rho C_p''T''}) + \sum_k C_{pk}\overline{\rho T''\left(\frac{\dot{m}_{ke}}{m}\right)}$$

A.5. Approximations and definitions

At this stage, we make two approximations. The first is to neglect the higher-order correlations

$$\overline{\rho T''\left(\frac{\dot{m}_{ke}}{m}\right)''}, \quad \frac{\overline{\overline{D}}}{Dt}\overline{\left(\rho C_p''T''\right)}, \quad \overline{\rho T''R''} \text{ and } \overline{\rho\left(\frac{\dot{m}}{m}\right)''\vec{v}_h}.$$

This is equivalent to assuming higher-order terms are important only when eddy velocities and derivatives are involved. The second is to neglect the term in the equation of state, or equivalently to neglect the volume occupied by liquid water and ice compared with that occupied by dry air and water vapour.

In addition we introduce the following notation:

a. The vertical flux of a variable X, $\overline{\rho w''X''}$, is denoted by J_X. Here w is the vertical velocity component.

b. The term $\overline{v''\cdot\nabla p}$ is added to the term $\frac{\partial}{\partial z}\overline{\rho w''(C_pT)''}$ and the resulting sum is expressed as the derivative $\frac{\partial J_S}{\partial z}$ of the vertical flux of dry static energy, plus a term which is written $\overline{\rho Q_D}$ and regarded as representing unorgnized transfers between enthalpy and sub-grid scale kinetic energy. The latter is parameterized by the heating implied by the dissipation of kinetic energy due to the parameterized vertical momentum fluxes $J_{\vec{v}_h}$.

c. The net effect of horizontal fluxes is represented only by their contribution K_X to the tendency of variable X.

d. The term $-\overline{\rho}\sum_k\overline{\overline{h_k}}\left(\frac{\overline{\overline{\dot{m}_{ki}}}}{m}\right)$ representing the latent heat release associated with internal phase changes is written $\overline{\rho Q_L}$.

A.6. Return to the advective form

With the above approximations and definitions, we obtain from the equations of Appendix A.4, on dropping the bar operators

$$\frac{d\rho}{dt} + \rho\nabla\cdot\vec{v} = \rho\frac{\dot{m}}{m} \qquad\qquad\qquad \text{(A.42)}$$

$$\frac{dq_k}{dt} = S_{q_k} - \frac{1}{\rho}\frac{\partial J_{q_k}}{\partial z} + K_{q_k} \tag{A.43}$$

$$\frac{d\vec{v}_h}{dt} = -\frac{1}{\rho}\nabla_h p - 2\left(\vec{\Omega} \times \vec{v}_h\right)_h - \frac{1}{\rho}\frac{\partial J_{\vec{v}_h}}{\partial z} + K_{\vec{v}_h} \tag{A.44}$$

$$\frac{dT}{dt} = \frac{1}{\rho C_p}\frac{dp}{dt} + \frac{1}{C_p}\left(Q_R + Q_L + Q_M + Q_D - \frac{1}{\rho}\left[\frac{\partial J_S}{\partial z} - T\sum_k C_{pk}\frac{\partial J_{q_k}}{\partial z}\right]\right) + K_T \tag{A.45}$$

where

$$S_{q_k} = \frac{\dot{m}_k}{m} - q_k\frac{\dot{m}}{m}. \tag{A.46}$$

In addition we have the equation of state

$$p = \rho T\left(R_d q_d + R_v q_v\right). \tag{A.47}$$

and the hydrostatic equation

$$\frac{\partial p}{\partial z} = -g\rho. \tag{A.48}$$

A.7. The model equations

The model equations (2.1)–(2.6) and (2.11)–(2.14) are finally obtained by neglecting density changes due to precipitation or evaporation, setting $\dot{m} = 0$ in (A.42). This approximation is traditionally made, although it is open to question.

In addition, Q_M is set to zero, an approximation of the same order as the assumption of no variation of latent heat with temperature that is made in the parameterizations.

The governing equations are

$$\begin{aligned}
\frac{d\vec{v}_h}{dt} &= -\frac{1}{\rho}\nabla_h p - 2\left(\vec{\Omega} \times \vec{v_h}\right)_h - \frac{1}{\rho}\frac{\partial J_{\vec{v}_h}}{\partial z} + K_{\vec{v}_h} && \text{(A.49)} \\
\frac{dT}{dt} &= \frac{R_d T_v}{p C_p}\frac{dp}{dt} + \frac{1}{C_p}\left(Q_R + Q_L + Q_D - \frac{1}{\rho}\left[\frac{\partial J_s}{\partial z} - C_{pd}T(\delta - 1)\frac{\partial J_{q_v}}{\partial z}\right]\right) + K_T && \text{(A.50)} \\
\frac{dq_i}{dt} &= S_{q_i} - \frac{1}{\rho}\frac{\partial J_{q_i}}{\partial z} && \text{(A.51)} \\
p &= \rho R_d T_v && \text{(A.52)} \\
\frac{\partial p}{\partial z} &= -g\rho && \text{(A.53)}
\end{aligned}$$

with

$$T_v = T \left(1 + \left(\frac{1}{\epsilon} - 1 \right) q_v \right) \tag{A.54}$$

In this case

$$C_p = C_{pd} \left(1 - q_v \right) + C_{pv} q$$

which is written

$$C_p = C_{pd} \left(1 + \left(\delta - 1 \right) q_v \right) \tag{A.55}$$

where $\delta = \frac{C_{pv}}{C_{pd}}$.

The model equations then follow from a change from z - to η-coordinates, the formalism for which is given by Kasahara (1974), and from rewriting the adiabatic terms in their usual form for a spherical geometry.

B. Orbital Variations

B.1. Introduction

In the mid-19th century, Croll (1867b,a) proposed an astronomical theory linking the Pleistocene[1] ice ages with periodic changes in the Earth's orbit around the Sun. Croll's ideas were later refined and elaborated by Milankovitch (1941). Since this theory was put forward, much evidence has been found to support it.

The original Milankovitch theory identifies three types of orbital variations which could act as climate forcing mechanisms, obliquity of the Earth's axis, eccentricity of the Earth orbit around the Sun, and precession of the equinoxes. Each variation has its specific time period.

To allow proper representation of orbital variations for climate simulations in `ECHAM6`, two orbits are given. The first one is based on very precise orbit determination principles to reflect short term variations for todays climate. It is using the VSOP (Variations Séculaires des Orbites Planétaires) analytical solution by Bretagnon and Francou (1988). This analytical solution is representing the todays orbit for an interval of -4000 and +8000 years with respect to the epoch J2000.0 very accurate. The second orbit given is using the basic Kepler laws only, allowing for simple adjustment for paleoclimate studies using the long term series expansions for obliquity, eccentricity, and precession by Laskar and Boudin (1993).

Before starting to describe the used orbits, the three basic orbital parameters for variations in climate are described as there are the obliquity i, the eccentricity e, and the precession expressed as the longitude of the perihelion ω with respect to the equinox.

B.1.1. Obliquity

Today the Earth is tilted on its rotational axis at an angle of 23.4°C relative to a perpendicular to the orbital plane of the Earth. Over a ~41000 year time period, this angle of inclination fluctuates between 22°C and 24.5°C, influencing the latitudinal distribution of solar radiation.

Obliquity does not influence the total amount of solar radiation received by the Earth, but affects the distribution of insolation in space and time. As obliquity increases, so does the amount of solar radiation received at high latitudes in summer, whilst insolation decreases in winter. Changes in obliquity have little effect at low latitudes, since the strength of the effect decrease towards the equator. Consequently, variations in the Earth's axial tilt affect the strength of the latitudinal temperature gradient. Increased tilt has the effect of raising the annual receipt of solar energy at high latitudes, with a consequent reduction in the latitudinal temperature gradient.

---

[1]2 Million to 10 thousand years ago

Obliquity (periodicity ~ 41000 years)
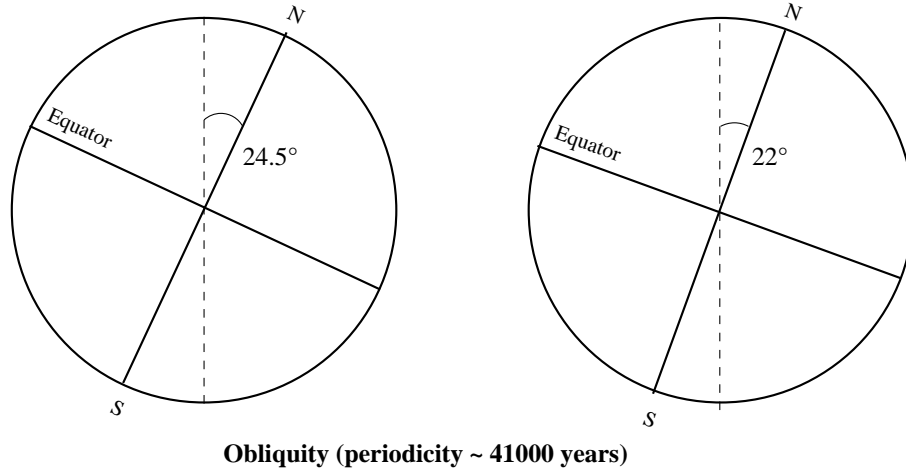
Figure B.1.: Obliquity

B.1.2. Eccentricity

The Earth's orbit around the Sun is not perfectly circular but follows an elliptical path (see Figure B.2). A second orbital variation involves the strength of the ellipse, or eccentricity. This parameter, e, is determined by Equation B.1.

$$e = \frac{1}{2}\frac{(a^2 - b^2)}{a} \tag{B.1}$$

When the orbit is circular, the semimajor axis a and semiminor axis b are equal and $e = 0$. The Earth's orbit has been found to vary from being near circular ($e = 0.005$) to markedly elliptical ($e = 0.06$) with two primary periodicities of approximately 96000 and 413000 years (Berger, 1976). The current value of e is 0.0167 (Meeus, 1998). Variations in eccentricity influence the total amount of solar radiation incident at the top of the Earth's atmosphere. With maximum eccentricity, differences in solar radiation receipt of about 30 % may occur between perihelion and aphelion (Goodess et al., 1992).

Orbital eccentricity (periodicity ~ 96000 years)
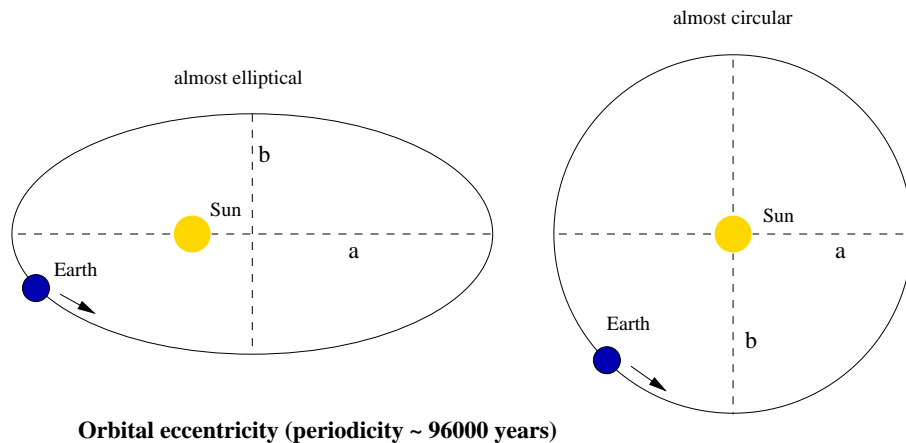
Figure B.2.: Eccentricity

B.1.3. Precession

The third orbital variation is that of precession. The Sun lies at one of the focal points of the Earth's orbital ellipse. Due to the gravitational interaction of other planetary bodies in the solar system, primarily the Moon and the planet Jupiter, the perihelion (the point at which the Earth passes closest to the Sun) moves in space with a consequent shifting or precessing of the elliptical orbit. This phenomenon is known as the precession of the equinoxes, and effects the intensity of the seasons.

Precession of equinoxes (periodicity ~ 22000 years)
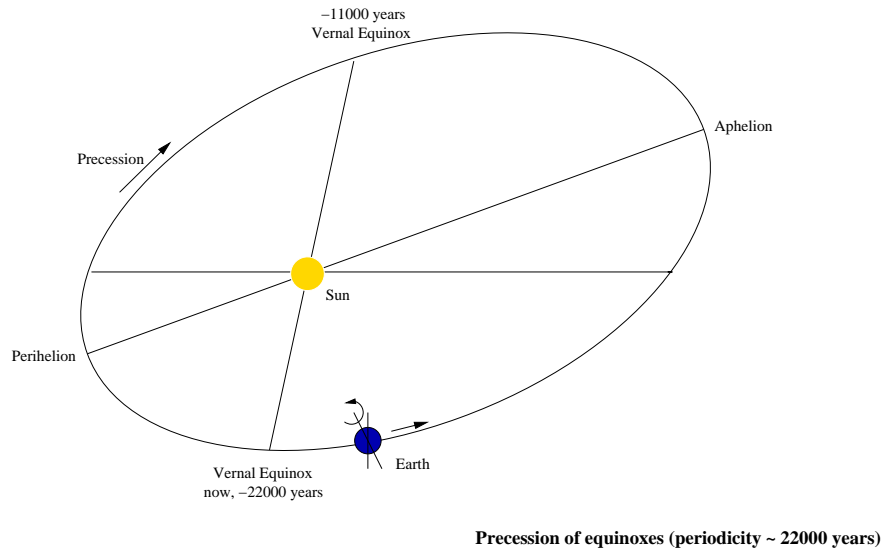
Figure B.3.: Precession

Precession has two components: an axial precession, in which the torque of the other planets exerted on the Earth's equatorial bulge causes the rotational axis to gyrate like a spinning top, and an elliptical precession, in which the elliptical orbit of the Earth itself rotates about one focus. The net effect describes the precession of the equinoxes with a period of 22000 years. This term is modulated by eccentricity which splits the precession into periods, of 19000 and 23000 years (Crowell and North, 1991).

Like obliquity, precession does not affect the total amount of solar energy received by the Earth, but only its hemispheric distribution over time. If the perihelion occurs in mid-June i.e. when the Northern Hemisphere is tilted toward the Sun, then the receipt of summer solar radiation in Northern Hemisphere will increase. Conversely, if the perihelion occurs in December, the Northern Hemisphere will receive more solar radiation in winter. It should be clear that the direction of changes in solar radiation receipt at the Earth's surface is opposite in each hemisphere.

B.2. Precise orbit determination based on VSOP87

B.2.1. VSOP — Variations Séculaires des Orbites Planétaires

From an analytical solution of the motion of the planets expressed with elliptic elements (Bretagnon, 1982) the position of planets is expressed as a Poisson series expansion. Different

sets of coordinate representations have been derived. The solution used in `ECHAM6`for the position of Earth is based on heliocentric spherical coordinate variables and the reference frame is the mean equinox and ecliptic of date.

The position of Earth is given by the heliocentric latitude L and longitude B and the distance from the Sun R.

This coordinates are given by the following Poisson series:

$$L = \sum_{n=1}^{6} L_n \sum_{k=1}^{k_N} a_{k_n} \cos(b_{k_n} + c_{k_n} \tau^n) \tag{B.2}$$

$$B = \sum_{n=1}^{2} B_n \sum_{k=1}^{k_N} a_{k_n} \cos(b_{k_n} + c_{k_n} \tau^n) \tag{B.3}$$

$$R = \sum_{n=1}^{5} R_n \sum_{k=1}^{k_N} a_{k_n} \cos(b_{k_n} + c_{k_n} \tau^n) \tag{B.4}$$

where τ is reckoned in thousands of Julian years from epoch J2000.0

$$\tau = \frac{\text{Julian date} - 2451545}{365250} \tag{B.5}$$

The coefficients for the Poisson series expansions are given in tables B.1 till B.13 in appendix B.5.

To derive the required coordinates of the Sun with respect to Earth the calculated heliocentric spehrical coordinates have to be transformed to geocentric spherical coordinates.

First step is a transformation of the Sun's and Earth's position to heliocentric rectangular coordinates with:

$$\vec{X}_s = f(L_s, B_s, R_s) \quad \text{and} \quad \vec{X}_e = f(L_e, B_e, R_e) \tag{B.6}$$

$\vec{X}$ are the heliocentric rectangular coordinates, (L, B, R) are the heliocentric spherical coordinates. The subscripts s and e are denoting the Sun and Earth respectively. The transformation function f is given by:

$$\begin{aligned} X &= R \cos L \cos B \\ Y &= R \sin L \cos B \\ Z &= R \sin B \end{aligned} \tag{B.7}$$

The geocentric rectangular coordinates are than given by:

$$\vec{x} = \vec{X}_s - \vec{X}_e \tag{B.8}$$

147

$\vec{x}$ has to be transformed to geocentric spherical coordinates by the inverse f^{-1} of equation B.7:

$$
\begin{aligned}
l &= \arctan \frac{y}{x} \quad \text{with} \quad l = l + 2\pi \quad \text{for} \quad l < 0 & \text{(B.9)} \\
b &= \arcsin \frac{z}{r} \\
r &= \sqrt{x^2 + y^2 + z^2}
\end{aligned}
$$

The next step is the transformation from the ecliptic geocentric to equatorial geocentric coordinates. This requires the obliquity (or inclination) i of Earth. This is a slowly varying property of the Earth's orbit, see section B.1.1. For the calculation of the actual obliquity a polynomial series developed by Laskar and Boudin (1993) is used:

$$
\begin{aligned}
i = \ & 84381.448 & \text{(B.10)} \\
& -4680.93U - 1.55U^2 + 1999.25U^3 - 51.38U^4 - 249.67U^5 \\
& -39.05U^6 + 7.12U^7 + 27.87U^8 + 5.79U^9 + 2.45U^10
\end{aligned}
$$

U is the time given as $U = 0.01\tau$. The transformation to equatorial geocentric coordinates is given by:

$$
\begin{aligned}
\alpha &= \arctan \left(\frac{\cos b \sin l \cos i - \sin b \sin i}{\cos b \cos L} \right) \quad \text{with} \quad \alpha = \alpha + 2\pi \quad \text{for} \quad \alpha < 0 \quad \text{(B.11)} \\
\delta &= \arcsin \left(\sin b \cos i + \cos b \sin i \sin l \right)
\end{aligned}
$$

There is another effect which has to be considered in determining the Sun's position in geocentric coordinates and this is the aberration. Aberration is the angular discrepancy between the apparent position of a star and its true position, arising from the motion of an observer relative to the path of the beam of light observed. This motion is the result of velocity components like the speed of the diurnal rotation of the Earth and its orbital speed in revolving around the sun. The change in Earth's position due to aberration regarding the Sun is given by:

$$
\begin{aligned}
\Delta\alpha &= -9.93639 \, 10^{-5} \frac{(\cos \alpha \cos \lambda \cos i + \sin \alpha \sin \lambda)}{\cos \delta} & \text{(B.12)} \\
\Delta\delta &= -9.93639 \, 10^{-5} \cos \lambda \left(\sin i \cos \delta - \sin \alpha \sin \delta \cos i \right) + \cos \alpha \sin \delta \sin \lambda & \text{(B.13)}
\end{aligned}
$$

where λ is the longitude and e the eccentricity of the Sun given by

$$
\lambda = L_0 + C \tag{B.14}
$$

where L_0 is the Sun's longitude of the ascending node, and C the position of the Sun, these are in terms of mean anomaly M and eccentricity e (in degrees), and time t in hundreds of Julian years:

$$L_0 = 280.46646 + 36000.76983\,t + 0.0003032\,t^2 \tag{B.15}$$

$$M = 357.52910 + 35999.05028\,t - 0.0001561\,t^2 \tag{B.16}$$

$$e = 0.016708617 - 0.000042040\,t + 0.0000001236\,t^2 \tag{B.17}$$

$$\tag{B.18}$$

$$C = e\,(2 - 0.25\,e^2)\sin M + 1.25\,e^2 \sin 2M + 1.083\,e^3 \sin 3M$$

with

$$t = \frac{\text{Julian date} - 2451545}{36525}$$

So, the final position is

$$\alpha = \alpha + \Delta\alpha \tag{B.19}$$

$$\delta = \delta + \Delta\delta \tag{B.20}$$

Finaly the mean sidereal time in degrees has to be determined:

$$\theta_0 = \left(280.46061837 + 360.98564736629 \cdot 36525\,t + 0.000387933\,t^2 - \frac{t^3}{38710000}\right) \tag{B.21}$$

$$\text{with}\theta_0 = \theta_0 \mathrm{mod} 360$$

B.2.2. Nutation

Nutation is a small wobble of the Earth's rotational axis with an amplitude of about 9 arcsec and period of up to 18.6 years. Traditionally, nutation is represented by variations in ecliptic longitude and obliquity (the angle between the ecliptic and the equator). Current models represent the nutation quantities with well-defined series (Seidelmann, 1982).

The nutation of the Earth is handled by the following equations and added before the transformation from the geocentric ecliptic to the geocentric equatorial coordinate system is performed.

Five auxilliar variables must be calculated which allows the further expansion of a sine/cosine series for the nutation. The five variables are

- longitude of the mean ascending node of the lunar orbit on the ecliptic, measured from the mean equinox of date

$$\Omega = 125.0445222 - 1934.1362608\,t + 0.00207833\,t^2 + 2.220e - 6\,t^3 \tag{B.22}$$

- mean longitude of the Sun minus the mean longitude of the Sun's perigee

$$M = 357.5277233 + 35999.0503400\,t - 0.00016030\,t^2 - 3.330e - 6\,t^3 \tag{B.23}$$

149

- mean longitude of the Moon minus the mean longitude of the Moon's perigee

$$M' = 134.9629814 + 477198.8673981\,t + 0.00869720\,t^2 + 1.778e - 5\,t^3 \qquad (B.24)$$

- mean longitude of the Moon minus the mean longitude of the Moon's node

$$F = 93.2719103 + 483202.0175381\,t - 0.00368250\,t^2 + 3.056e - 6\,t^3 \qquad (B.25)$$

- mean elongation of the Moon from the Sun

$$D = 297.8503631 + 445267.1114800\,t - 0.00191420\,t^2 + 5.278e - 6\,t^3 \qquad (B.26)$$

The table B.14 with the require coeeficients is given in appendix B.5.

B.3. Kepler based orbit for paleoclimate applications

The three components of the orbital variations, obliquity, eccentricity, and precession together effect both the total flux of incoming solar radiation and also the temporal and spatial distribution of terrestrial insolation. These variations have the potential to influence the energy budget of the climate system (Milankovitch, 1941; Berger, 1978), and can therefore be regarded as possible causes of climate change over long time scales.

Milankovitch (1941) considered the changing seasonal (precession) and latitudinal (obliquity) patterns of incoming radiation to be critical factors in the growth of continental ice sheets and in the initiation of ice ages. He hypothesised that when axial tilt was small (large latitudinal temperature gradient), eccentricity was large and perihelion occurred during the Northern Hemisphere winter (warmer winters and colder summers), such a configuration would allow the persistence of accumulated snow throughout the summer months in the Northern Hemisphere. Additionally, the warmer winters and stronger atmospheric general circulation due to the increased temperature gradient would increase the amount of water vapour at the high latitudes available for snowfall.

To allow for paleoclimate studies, `ECHAM6`provides an Kepler based orbit which has as basic parameters, to be defined externally, the long term varying orbit parameters obliquity, eccentricity, and, as measure for the precession, the longitude of perihelion from the equinox of date.

Used for the calculation of the position of the Sun is Lacaille's formula which links the true anomaly ν and the eccentric anomaly E:

$$\tan\frac{\nu}{2} = \sqrt{\frac{1+e}{1-e}}\,\tan\frac{E}{2} \qquad (B.27)$$

with $\nu = \omega$, where ω is the longitude of perihelion. This allows the calculation of the eccentric anomaly which is required for the Kepler equation linking the eccentric and the mean anomaly M:

$$M = E - e\sin E \qquad (B.28)$$

First, calculate the mean anomaly M of the current longitude λ from the true anomaly ν:

$$M = \lambda - M(\omega) \quad \text{with} \quad M(\omega) = \nu - e \sin \nu \tag{B.29}$$

The true and mean anomaly are identical at the vernal equinox. For solving the Kepler equation B.28 the Newton method is used:

$$E^{m+1} = E^m - \frac{K(E^m)}{K'(E^m)}$$

with

$$K(E) = M - E + e \sin E = 0 \quad \text{and} \quad K'(E) = 1 + e \cos E$$

so the final iteration expression to solve is:

$$E^{m+1} = E^m - \frac{M - E^m + e \sin E^m}{1 + e \cos E^m} \tag{B.30}$$

This iterative solver does converge for most initial values, but not for all. This has been taken into account. For more details see Meeus (1998).

The final distance between Earth and Sun is given by

$$R = \left(\frac{1}{1 - e \cos E} \right)^2 \tag{B.31}$$

and the true anomaly ν with Lacaille's formula (equation B.27). The true longitude is $\lambda = \nu + \omega$ and the declination of the Sun (with i the obliquity (or inclination):

$$\delta = \sin i \sin \lambda \tag{B.32}$$

and the right ascension:

$$\alpha = \tan \frac{\cos i \sin \lambda}{\cos \lambda} \tag{B.33}$$

B.4. Differences in the daily insolation due to the two given orbits

The astronomical orbital parameters have to be transformed into the solar constant scaled by the distance Earth — Sun R and the local zenith angle Z.

For comparison of the two given orbits the difference in the orbit parameters against the JPL DE405 are shown. The first set is for the AMIP2 period 1978 to 1996 and the second set for 1870 till 2150.
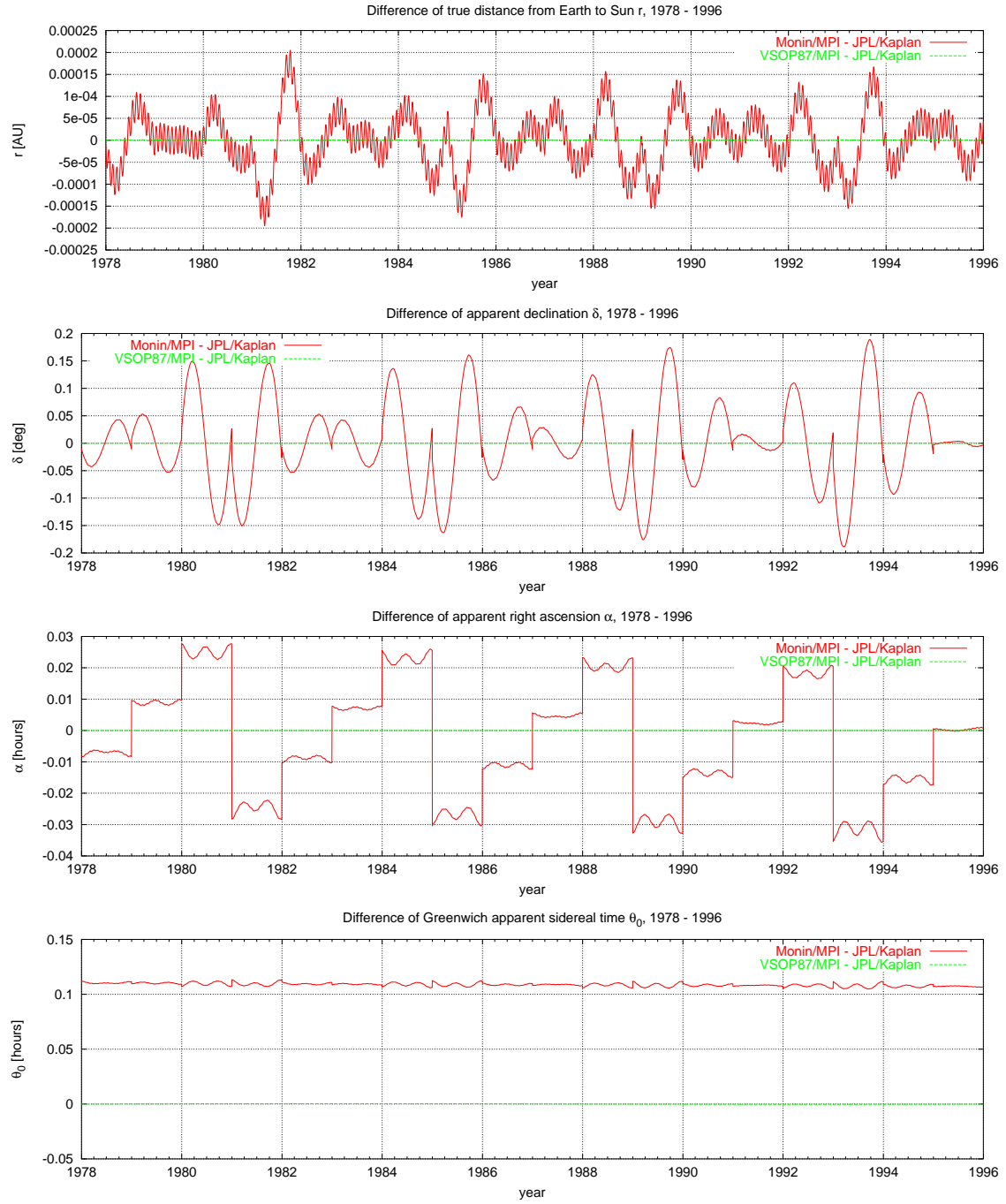
Figure B.4.: Differences between the VSOP87 and Monin orbit with respect to JPL's DE405 for the peride 1978 till 1996
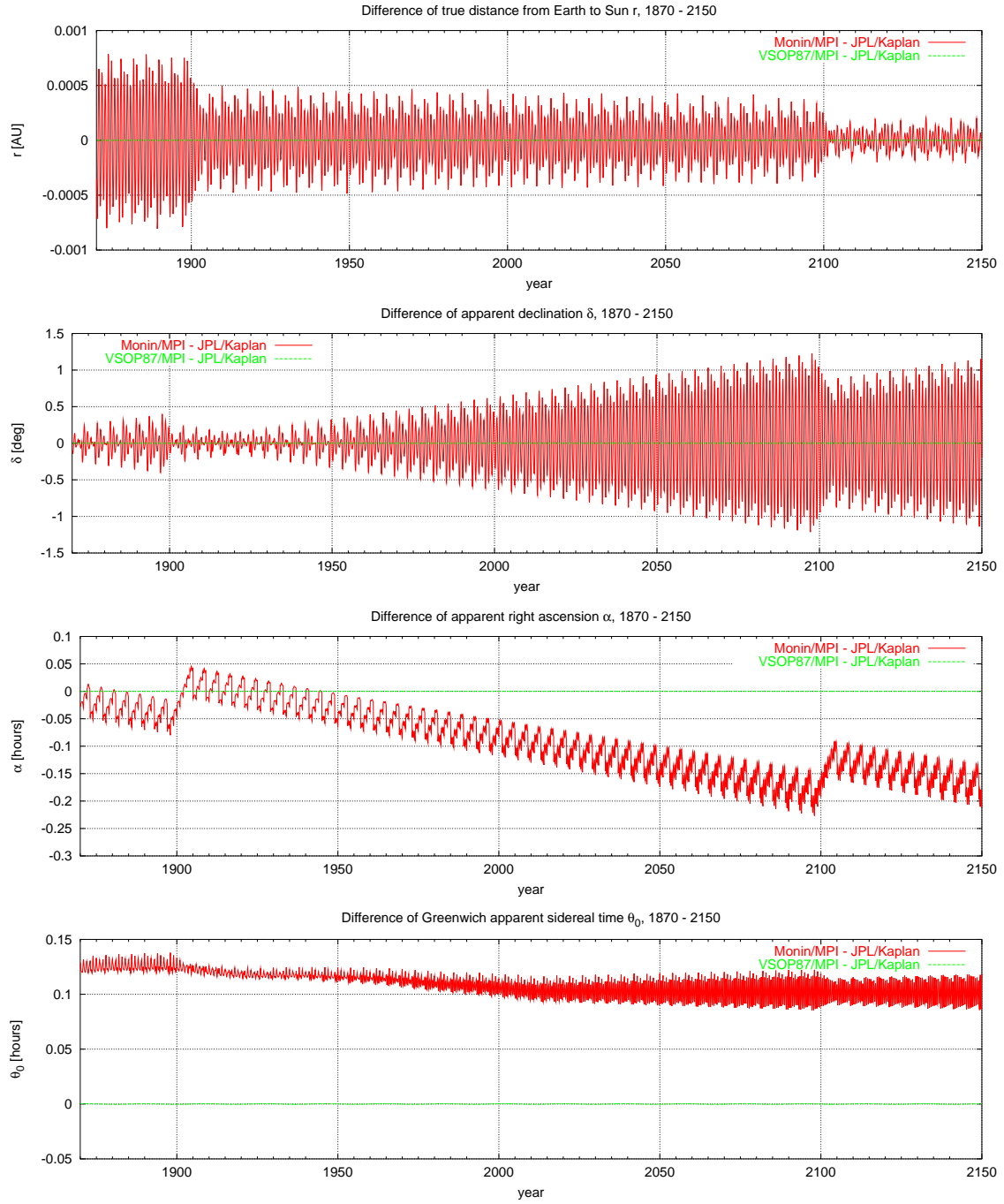
Figure B.5.: Differences between the VSOP87 and Monin orbit with respect to JPL's DE405 for the peride 1870 till 2150

B.5. Orbit tables

The coefficients for the Poisson series expansions required for the VSOP87 orbit calculation.

L1		
a_k	b_k	c_k
1.753470456730000e+00	0.00000000000e+00	0.000000000000000e+00
3.341656456000000e-02	4.66925680417e+00	6.283075849991400e+03
3.489427500000000e-04	4.62610241759e+00	1.256615169998280e+04
3.497056000000000e-05	2.74411800971e+00	5.753384884896800e+03
3.417571000000000e-05	2.82886579606e+00	3.523118349000000e+00
3.135896000000000e-05	3.62767041758e+00	7.771377146812050e+04
2.676218000000000e-05	4.41808351397e+00	7.860419392439200e+03
2.342687000000000e-05	6.13516237631e+00	3.930209696219600e+03
1.324292000000000e-05	7.42463563520e-01	1.150676976979360e+04
1.273166000000000e-05	2.03709655772e+00	5.296909650946000e+02
1.199167000000000e-05	1.10962944315e+00	1.577343542447800e+03
9.902500000000000e-06	5.23268129594e+00	5.884926846583200e+03
9.018550000000000e-06	2.04505443513e+00	2.629831979980000e+01
8.572229999999999e-06	3.50849156957e+00	3.981490034082000e+02
7.797859999999999e-06	1.17882652114e+00	5.223693919802200e+03
7.531410000000000e-06	2.53339053818e+00	5.507553238667400e+03
5.052640000000000e-06	4.58292563052e+00	1.884922754997420e+04
4.923790000000000e-06	4.20506639861e+00	7.755226113240000e+02
3.566550000000000e-06	2.91954116867e+00	6.731030280000000e-02
3.170870000000000e-06	5.84901952218e+00	1.179062908865880e+04
2.841250000000000e-06	1.89869034186e+00	7.962980068163999e+02
2.710390000000000e-06	3.14886076490e-01	1.097707880469900e+04
2.428100000000000e-06	3.44811409060e-01	5.486777843175000e+03
2.061600000000000e-06	4.80646606059e+00	2.544314419883400e+03
2.053850000000000e-06	1.86947813692e+00	5.573142801433100e+03
2.022610000000000e-06	2.45767795458e+00	6.069776754553400e+03
1.555160000000000e-06	8.33060738070e-01	2.132990954380000e+02
1.322120000000000e-06	3.41118275555e+00	2.942463423291600e+03
1.261840000000000e-06	1.08302630210e+00	2.077539549240000e+01
1.151320000000000e-06	6.45449116830e-01	9.803210682000000e-01
table B.1 to be continued ...		

L1		
a_k	b_k	c_k
1.028510000000000e-06	6.35998467270e-01	4.694002954707600e+03
1.018950000000000e-06	9.75692218240e-01	1.572083878487840e+04
1.017240000000000e-06	4.26679821365e+00	7.113547000800000e+00
9.920600000000000e-07	6.20992940258e+00	2.146165416475200e+03
9.760700000000001e-07	6.81012722700e-01	1.554203994342000e+02
8.580300000000000e-07	5.98322631256e+00	1.610006857376741e+05
8.512800000000000e-07	1.29870743025e+00	6.275962302990600e+03
8.471100000000000e-07	3.67080093025e+00	7.143069561812909e+04
7.963700000000000e-07	1.80791330700e+00	1.726015465469040e+04
7.875600000000000e-07	3.03698313141e+00	1.203646073488820e+04
7.465100000000000e-07	1.75508916159e+00	5.088628839766800e+03
7.387400000000000e-07	3.50319443167e+00	3.154687084895600e+03
7.354700000000000e-07	4.67926565481e+00	8.018209311238001e+02
6.962700000000000e-07	8.32975969660e-01	9.437762934887000e+03
6.244899999999999e-07	3.97763880587e+00	8.827390269874801e+03
6.114800000000000e-07	1.81839811024e+00	7.084896781115200e+03
5.696300000000000e-07	2.78430398043e+00	6.286598968340400e+03
5.611600000000000e-07	4.38694880779e+00	1.414349524243060e+04
5.557700000000000e-07	3.47006009062e+00	6.279552731642400e+03
5.199200000000000e-07	1.89149458340e-01	1.213955350910680e+04
5.160500000000000e-07	1.33282746983e+00	1.748016413067000e+03
5.114500000000000e-07	2.83068645010e-01	5.856477659115400e+03
4.900000000000000e-07	4.87350650330e-01	1.194447010224600e+03
4.103600000000000e-07	5.36817351402e+00	8.429241266466601e+03
4.093800000000000e-07	2.39850881707e+00	1.965104848109800e+04
3.920000000000000e-07	6.16832995016e+00	1.044738783960440e+04
3.677000000000000e-07	6.04133859347e+00	1.021328554621100e+04
3.659600000000000e-07	2.56955238628e+00	1.059381930189200e+03
3.595400000000000e-07	1.70876111898e+00	2.352866153771800e+03
3.556600000000000e-07	1.77597314691e+00	6.812766815086000e+03
3.329100000000000e-07	5.93094994590e-01	1.778984561978500e+04
3.041200000000000e-07	4.42944641350e-01	8.399684731811189e+04
3.004700000000000e-07	2.73975123935e+00	1.349867409658800e+03
2.535200000000000e-07	3.16470953405e+00	4.690479836358600e+03

Table B.1.: First summand of heliocentric latitude (VSOP87D)

L2		
a_k	b_k	c_k
6.283319667474910e+03	0.00000000000e+00	0.000000000000000e+00
table B.2 to be continued ...		

L2		
a_k	b_k	c_k
2.060588630000000e-03	2.67823455584e+00	6.283075849991400e+03
4.303430000000000e-05	2.63512650414e+00	1.256615169998280e+04
4.252640000000000e-06	1.59046980729e+00	3.523118349000000e+00
1.192610000000000e-06	5.79557487799e+00	2.629831979980000e+01
1.089770000000000e-06	2.96618001993e+00	1.577343542447800e+03
9.347800000000000e-07	2.59212835365e+00	1.884922754997420e+04
7.212200000000000e-07	1.13846158196e+00	5.296909650946000e+02
6.776800000000000e-07	1.87472304791e+00	3.981490034082000e+02
6.732700000000000e-07	4.40918235168e+00	5.507553238667400e+03
5.902700000000000e-07	2.88797038460e+00	5.223693919802200e+03
5.597600000000000e-07	2.17471680261e+00	1.554203994342000e+02
4.540700000000000e-07	3.98030798050e-01	7.962980068163999e+02
3.636900000000000e-07	4.66247398350e-01	7.755226113240000e+02
2.895800000000000e-07	2.64707383882e+00	7.113547000800000e+00
2.084400000000000e-07	5.34138275149e+00	9.803210682000000e-01
1.909700000000000e-07	1.84628332577e+00	5.486777843175000e+03
1.850800000000000e-07	4.96855124577e+00	2.132990954380000e+02
1.729300000000000e-07	2.99116864949e+00	6.275962302990600e+03
1.623300000000000e-07	3.21648304700e-02	2.544314419883400e+03
1.583200000000000e-07	1.43049285325e+00	2.146165416475200e+03
1.461500000000000e-07	1.20532366323e+00	1.097707880469900e+04
1.246100000000000e-07	2.83432285512e+00	1.748016413067000e+03
1.187700000000000e-07	3.25804815607e+00	5.088628839766800e+03
1.180800000000000e-07	5.27379790480e+00	1.194447010224600e+03
1.151400000000000e-07	2.07502418155e+00	4.694002954707600e+03
1.064100000000000e-07	7.66141992020e-01	5.535694028424000e+02
9.969000000000000e-08	1.30262991097e+00	6.286598968340400e+03
9.720999999999999e-08	4.23925472239e+00	1.349867409658800e+03
9.452000000000000e-08	2.69957062864e+00	2.427286039740000e+02
8.577000000000001e-08	5.64475868067e+00	9.517184062506000e+02
7.576000000000000e-08	5.30062664886e+00	2.352866153771800e+03
6.385000000000001e-08	2.65033984967e+00	9.437762934887000e+03
6.101000000000000e-08	4.66632584188e+00	4.690479836358600e+03

Table B.2.: Second summand of heliocentric latitude (VSOP87D)

L3		
a_k	b_k	c_k
5.291887000000000e-04	0.00000000000e+00	0.000000000000000e+00
table B.3 to be continued ...		

L3		
a_k	b_k	c_k
8.719837000000000e-05	1.07209665242e+00	6.283075849991400e+03
3.091250000000000e-06	8.67288188320e-01	1.256615169998280e+04
2.733900000000000e-07	5.29787169100e-02	3.523118349000000e+00
1.633400000000000e-07	5.18826691036e+00	2.629831979980000e+01
1.575200000000000e-07	3.68457889430e+00	1.554203994342000e+02
9.541000000000001e-08	7.57422976750e-01	1.884922754997420e+04
8.937000000000000e-08	2.05705419118e+00	7.771377146812050e+04
6.952000000000000e-08	8.26733054100e-01	7.755226113240000e+02
5.064000000000000e-08	4.66284525271e+00	1.577343542447800e+03
4.061000000000000e-08	1.03057162962e+00	7.113547000800000e+00
3.810000000000000e-08	3.44050803490e+00	5.573142801433100e+03
3.463000000000000e-08	5.14074632811e+00	7.962980068163999e+02
3.169000000000000e-08	6.05291851171e+00	5.507553238667400e+03
3.020000000000000e-08	1.19246506441e+00	2.427286039740000e+02
2.886000000000000e-08	6.11652627155e+00	5.296909650946000e+02
2.714000000000000e-08	3.06378810250e-01	3.981490034082000e+02
2.538000000000000e-08	2.27992810679e+00	5.535694028424000e+02
2.371000000000000e-08	4.38118838167e+00	5.223693919802200e+03
2.079000000000000e-08	3.75435330484e+00	9.803210682000000e-01

Table B.3.: Third summand of heliocentric latitude (VSOP87D)

L4		
a_k	b_k	c_k
2.892260000000000e-06	5.84384198723e+00	6.283075849991400e+03
3.495500000000000e-07	0.00000000000e+00	0.000000000000000e+00
1.681900000000000e-07	5.48766912348e+00	1.256615169998280e+04
2.962000000000000e-08	5.19577265202e+00	1.554203994342000e+02
1.288000000000000e-08	4.72200252235e+00	3.523118349000000e+00
7.140000000000000e-09	5.30045809128e+00	1.884922754997420e+04
6.350000000000000e-09	5.96925937141e+00	2.427286039740000e+02

Table B.4.: Fourth summand of heliocentric latitude (VSOP87D)

L5		
a_k	b_k	c_k
1.140840000000000e-06	3.14159265359e+00	0.000000000000000e+00
table B.5 to be continued ...		

L5		
a_k	b_k	c_k
7.717000000000000e-08	4.13446589358e+00	6.283075849991400e+03
7.650000000000001e-09	3.83803776214e+00	1.256615169998280e+04

Table B.5.: Fifth summand of heliocentric latitude (VSOP87D)

L6		
a_k	b_k	c_k
8.780000000000000e-09	3.14159265359e+00	0.000000000000000e+00

Table B.6.: Sixth summand of heliocentric latitude (VSOP87D)

B1		
a_k	b_k	c_k
2.796200000000000e-06	3.19870156017e+00	8.433466158130829e+04
1.016430000000000e-06	5.42248619256e+00	5.507553238667400e+03
8.044500000000000e-07	3.88013204458e+00	5.223693919802200e+03
4.380600000000000e-07	3.70444689758e+00	2.352866153771800e+03
3.193300000000000e-07	4.00026369781e+00	1.577343542447800e+03

Table B.7.: First summand of heliocentric longitude (VSOP87D)

B2		
a_k	b_k	c_k
9.029999999999999e-08	3.89729061890e+00	5.507553238667400e+03
6.177000000000000e-08	1.73038850355e+00	5.223693919802200e+03

Table B.8.: Second summand of heliocentric longitude (VSOP87D)

R1		
a_k	b_k	c_k
1.000139887990000e+00	0.00000000000e+00	0.000000000000000e+00
1.670699626000000e-02	3.09846350771e+00	6.283075849991400e+03
1.395602300000000e-04	3.05524609620e+00	1.256615169998280e+04
3.083720000000000e-05	5.19846674381e+00	7.771377146812050e+04
table B.9 to be continued ...		

R1		
a_k	b_k	c_k
1.628461000000000e-05	1.17387749012e+00	5.753384884896800e+03
1.575568000000000e-05	2.84685245825e+00	7.860419392439200e+03
9.247990000000000e-06	5.45292234084e+00	1.150676976979360e+04
5.424440000000000e-06	4.56409149777e+00	3.930209696219600e+03
4.721100000000000e-06	3.66100022149e+00	5.884926846583200e+03
3.459830000000000e-06	9.63686176870e-01	5.507553238667400e+03
3.287800000000000e-06	5.89983646482e+00	5.223693919802200e+03
3.067840000000000e-06	2.98671395120e-01	5.573142801433100e+03
2.431890000000000e-06	4.27349536153e+00	1.179062908865880e+04
2.118290000000000e-06	5.84714540314e+00	1.577343542447800e+03
1.857520000000000e-06	5.02194447178e+00	1.097707880469900e+04
1.748440000000000e-06	3.01193636534e+00	1.884922754997420e+04
1.098350000000000e-06	5.05510636285e+00	5.486777843175000e+03
9.831599999999999e-07	8.86813112770e-01	6.069776754553400e+03
8.649900000000000e-07	5.68959778254e+00	1.572083878487840e+04
8.582500000000000e-07	1.27083733351e+00	1.610006857376741e+05
6.490300000000000e-07	2.72506137870e-01	1.726015465469040e+04
6.291600000000000e-07	9.21771088320e-01	5.296909650946000e+02
5.705600000000000e-07	2.01374292014e+00	8.399684731811189e+04
5.573600000000000e-07	5.24159798933e+00	7.143069561812909e+04
4.938400000000000e-07	3.24501240359e+00	2.544314419883400e+03
4.696300000000000e-07	2.57805070386e+00	7.755226113240000e+02
4.466100000000000e-07	5.53715807302e+00	9.437762934887000e+03
4.251500000000000e-07	6.01110242003e+00	6.275962302990600e+03
3.896800000000000e-07	5.36071738169e+00	4.694002954707600e+03
3.824500000000000e-07	2.39255343974e+00	8.827390269874801e+03
3.749000000000000e-07	8.29529223320e-01	1.965104848109800e+04
3.695700000000000e-07	4.90107591914e+00	1.213955350910680e+04
3.566000000000000e-07	1.67468058995e+00	1.203646073488820e+04
3.453700000000000e-07	1.84270693282e+00	2.942463423291600e+03
3.319300000000000e-07	2.43703000980e-01	7.084896781115200e+03
3.192100000000000e-07	1.83682297810e-01	5.088628839766800e+03
3.184600000000000e-07	1.77775642085e+00	3.981490034082000e+02
2.846400000000000e-07	1.21344868176e+00	6.286598968340400e+03
2.779300000000000e-07	1.89934330904e+00	6.279552731642400e+03

table B.9 to be continued ...

R1		
a_k	b_k	c_k
2.627500000000000e-07	4.58896850401e+00	1.044738783960440e+04

Table B.9.: First summand of distance (VSOP87D)

R2		
a_k	b_k	c_k
1.030186080000000e-03	1.10748969588e+00	6.283075849991400e+03
1.721238000000000e-05	1.06442301418e+00	1.256615169998280e+04
7.022150000000000e-06	3.14159265359e+00	0.000000000000000e+00
3.234600000000000e-07	1.02169059149e+00	1.884922754997420e+04
3.079900000000000e-07	2.84353804832e+00	5.507553238667400e+03
2.497100000000000e-07	1.31906709482e+00	5.223693919802200e+03
1.848500000000000e-07	1.42429748614e+00	1.577343542447800e+03
1.007800000000000e-07	5.91378194648e+00	1.097707880469900e+04
8.654000000000001e-08	1.42046854427e+00	6.275962302990600e+03
8.634000000000000e-08	2.71461506020e-01	5.486777843175000e+03

Table B.10.: Second summand of distance (VSOP87D)

R3		
a_k	b_k	c_k
4.359385000000000e-05	5.78455133738e+00	6.283075849991400e+03
1.236330000000000e-06	5.57934722157e+00	1.256615169998280e+04
1.234100000000000e-07	3.14159265359e+00	0.000000000000000e+00
8.792000000000000e-08	3.62777733395e+00	7.771377146812050e+04
5.689000000000000e-08	1.86958905084e+00	5.573142801433100e+03
3.301000000000000e-08	5.47027913302e+00	1.884922754997420e+04

Table B.11.: Third summand of distance (VSOP87D)

R4		
a_k	b_k	c_k
1.445950000000000e-06	4.27319435148e+00	6.283075849991400e+03
6.729000000000000e-08	3.91697608662e+00	1.256615169998280e+04

Table B.12.: Fourth summand of distance (VSOP87D)

160

R5		
a_k	b_k	c_k
3.858000000000000e-08	2.56384387339e+00	6.283075849991400e+03

Table B.13.: Fifth summand of distance (VSOP87D)

Table for calculating the periodic terms of nutation in longitude (ΔL) and obliquity (Δi).

Argument					ΔL		ΔL	
multiples of					sine arguments		cosine arguments	
D	M	M'	F	Ω	a_k	$b_k t$	c_k	$d_k t$
0	0	0	0	1	-171996.0	-174.2	92025.0	8.9
0	0	2	-2	2	-13187.0	-1.6	5736.0	-3.1
0	0	2	0	2	-2274.0	-0.2	977.0	-0.5
0	0	0	0	2	2062.0	0.2	-895.0	0.5
0	-1	0	0	0	-1426.0	3.4	54.0	-0.1
1	0	0	0	0	712.0	0.1	-7.0	0.0
0	1	2	-2	2	-517.0	1.2	224.0	-0.6
0	0	2	0	1	-386.0	-0.4	200.0	0.0
1	0	2	0	2	-301.0	0.0	129.0	-0.1
0	-1	2	-2	2	217.0	-0.5	-95.0	0.3
-1	0	0	2	0	158.0	0.0	-1.0	0.0
0	0	2	-2	1	129.0	0.1	-70.0	0.0
-1	0	2	0	2	123.0	0.0	-53.0	0.0
1	0	0	0	1	63.0	0.1	-33.0	0.0
0	0	0	2	0	63.0	0.0	-2.0	0.0
-1	0	2	2	2	-59.0	0.0	26.0	0.0
-1	0	0	0	1	-58.0	-0.1	32.0	0.0
1	0	2	0	1	-51.0	0.0	27.0	0.0
-2	0	0	2	0	-48.0	0.0	1.0	0.0
-2	0	2	0	1	46.0	0.0	-24.0	0.0
0	0	2	2	2	-38.0	0.0	16.0	0.0
2	0	2	0	2	-31.0	0.0	13.0	0.0
2	0	0	0	0	29.0	0.0	-1.0	0.0
1	0	2	-2	2	29.0	0.0	-12.0	0.0
0	0	2	0	0	26.0	0.0	-1.0	0.0
0	0	2	-2	0	-22.0	0.0	0.0	0.0
-1	0	2	0	1	21.0	0.0	-10.0	0.0
0	2	0	0	0	17.0	-0.1	0.0	0.0
0	2	2	-2	2	-16.0	0.1	7.0	0.0
-1	0	0	2	1	16.0	0.0	-8.0	0.0
0	1	0	0	1	-15.0	0.0	9.0	0.0
to be continued ...								

Argument					ΔL		ΔL	
multiples of					sine arguments		cosine arguments	
D	M	M'	F	Ω	a_k	$b_k t$	c_k	$d_k t$
1	0	0	-2	1	-13.0	0.0	7.0	0.0
0	-1	0	0	1	-12.0	0.0	6.0	0.0
2	0	-2	0	0	11.0	0.0	0.0	0.0
-1	0	2	2	1	-10.0	0.0	5.0	0.0
1	0	2	2	2	-8.0	0.0	3.0	0.0
0	-1	2	0	2	-7.0	0.0	3.0	0.0
0	0	2	2	1	-7.0	0.0	3.0	0.0
1	1	0	-2	0	-7.0	0.0	0.0	0.0
0	1	2	0	2	7.0	0.0	-3.0	0.0
-2	0	0	2	1	-6.0	0.0	3.0	0.0
0	0	0	2	1	-6.0	0.0	3.0	0.0
2	0	2	-2	2	6.0	0.0	-3.0	0.0
1	0	0	2	0	6.0	0.0	0.0	0.0
1	0	2	-2	1	6.0	0.0	-3.0	0.0
0	0	0	-2	1	-5.0	0.0	3.0	0.0
0	-1	2	-2	1	-5.0	0.0	3.0	0.0
2	0	2	0	1	-5.0	0.0	3.0	0.0
1	-1	0	0	0	5.0	0.0	0.0	0.0
1	0	0	-1	0	-4.0	0.0	0.0	0.0
0	0	0	1	0	-4.0	0.0	0.0	0.0
0	1	0	-2	0	-4.0	0.0	0.0	0.0
1	0	-2	0	0	4.0	0.0	0.0	0.0
2	0	0	-2	1	4.0	0.0	-2.0	0.0
0	1	2	-2	1	4.0	0.0	-2.0	0.0
1	1	0	0	0	-3.0	0.0	0.0	0.0
1	-1	0	-1	0	-3.0	0.0	0.0	0.0
-1	-1	2	2	2	-3.0	0.0	1.0	0.0
0	-1	2	2	2	-3.0	0.0	1.0	0.0
1	-1	2	0	2	-3.0	0.0	1.0	0.0
3	0	2	0	2	-3.0	0.0	1.0	0.0
-2	0	2	0	2	-3.0	0.0	1.0	0.0
1	0	2	0	0	3.0	0.0	0.0	0.0
-1	0	2	4	2	-2.0	0.0	1.0	0.0
1	0	0	0	2	-2.0	0.0	1.0	0.0
to be continued ...								

Argument					ΔL		ΔL	
multiples of					sine arguments		cosine arguments	
D	M	M'	F	Ω	a_k	$b_k t$	c_k	$d_k t$
-1	0	2	-2	1	-2.0	0.0	1.0	0.0
0	-2	2	-2	1	-2.0	0.0	1.0	0.0
-2	0	0	0	1	-2.0	0.0	1.0	0.0
2	0	0	0	1	2.0	0.0	-1.0	0.0
3	0	0	0	0	2.0	0.0	0.0	0.0
1	1	2	0	2	2.0	0.0	-1.0	0.0
0	0	2	1	2	2.0	0.0	-1.0	0.0
1	0	0	2	1	-1.0	0.0	0.0	0.0
1	0	2	2	1	-1.0	0.0	1.0	0.0
1	1	0	-2	1	-1.0	0.0	0.0	0.0
0	1	0	2	0	-1.0	0.0	0.0	0.0
0	1	2	-2	0	-1.0	0.0	0.0	0.0
0	1	-2	2	0	-1.0	0.0	0.0	0.0
1	0	-2	2	0	-1.0	0.0	0.0	0.0
1	0	-2	-2	0	-1.0	0.0	0.0	0.0
1	0	2	-2	0	-1.0	0.0	0.0	0.0
1	0	0	-4	0	-1.0	0.0	0.0	0.0
2	0	0	-4	0	-1.0	0.0	0.0	0.0
0	0	2	4	2	-1.0	0.0	0.0	0.0
0	0	2	-1	2	-1.0	0.0	0.0	0.0
-2	0	2	4	2	-1.0	0.0	1.0	0.0
2	0	2	2	2	-1.0	0.0	0.0	0.0
0	-1	2	0	1	-1.0	0.0	0.0	0.0
0	0	-2	0	1	-1.0	0.0	0.0	0.0
0	0	4	-2	2	1.0	0.0	0.0	0.0
0	1	0	0	2	1.0	0.0	0.0	0.0
1	1	2	-2	2	1.0	0.0	-1.0	0.0
3	0	2	-2	2	1.0	0.0	0.0	0.0
-2	0	2	2	2	1.0	0.0	-1.0	0.0
-1	0	0	0	2	1.0	0.0	-1.0	0.0
0	0	-2	2	1	1.0	0.0	0.0	0.0
0	1	2	0	1	1.0	0.0	0.0	0.0
-1	0	4	0	2	1.0	0.0	0.0	0.0
2	1	0	-2	0	1.0	0.0	0.0	0.0
to be continued ...								

| Argument | | | | | ΔL | | ΔL | |
| multiples of | | | | | sine arguments | | cosine arguments | |
D	M	M'	F	Ω	a_k	$b_k t$	c_k	$d_k t$
2	0	0	2	0	1.0	0.0	0.0	0.0
2	0	2	-2	1	1.0	0.0	-1.0	0.0
2	0	-2	0	1	1.0	0.0	0.0	0.0
1	-1	0	-2	0	1.0	0.0	0.0	0.0
-1	0	0	1	1	1.0	0.0	0.0	0.0
-1	-1	0	2	1	1.0	0.0	0.0	0.0
0	1	0	1	0	1.0	0.0	0.0	0.0

Table B.14.: periodic terms of nutation in longitude (ΔL) and obliquity (Δi)

Bibliography

Allen, S. J. and Vincent, R. A. (1995): *Gravity wave activity in the lower atmosphere: Seasonal and latitudinal variations*. J. Geophys. Res., **100**, 1327–1350. 76, 82

Andrews, D. G., Holton, J. R. and Leovy, C. B. (1987): *Middle atmospheric dynamics*. Academic Press. 76, 77

Asselin, R. (1972): *Frequency filter for time integrations*. Mon. Wea. Rev., **100**, 487–490. 28

Baines, P. G. and Palmer, T. N. (1990): *Rationale for a new physically-based parameterization of subgridscale orographic effects*. Technical Memorandum 169, ECMWF, Reading, UK. 85

Beheng, K. D. (1994): *A parameterization of warm cloud microphysical conversion processes*. Atmos. Res., **33**, 193 – 206. 70

Berger, A. (1976): *Obliquity and precession for the last 5,000,000 years*. Astronomy and Astrophysics, **51**, 127–135. 145

Berger, A. (1978): *Long-term variations of daily insolation and quaternary climatic changes*. J. Atmos. Sci., **35**, 2362–2367. 150

Bigg, E. K. (1953): *The supercooling of water*. Proc. Roy. Soc., **66**, 688–694. 69

Blackadar, A. K. (1962): *The vertical distribution of wind and turbulent exchange in a neutral atmosphere*. J. Geophys. Res., **67**, 3095–3102. 51

Boucher, O. and Pham, M. (2002): *History of sulfate aerosol radiative forcings*. Geophys. Res. Lett., **29, no. 9**, 22–25. 120

Bourke, W. (1972): *An efficient one level primitive-equation spectral model*. Mon. Wea. Rev., **100**, 683–689. 14

Bourke, W. (1974): *A multi-level spectral model: Formulation and hemispheric integrations*. Mon. Wea. Rev., **102**, 688–701. 18

Brandt, R., Warren, S. G., Worby, A. P. and Grenfell, T. C. (2005): *Surface albedo of the Antarctic sea ice zone*. J. Clim., **18**, 3606–3622. 99, 100

Brasseur, G. P., Orlando, J. J. and Tyndall, G. S. (1999): *Atmospheric Chemistry and Climate Change*. Oxford University Press, New York, Oxford. 114

Brasseur, G. P. and Solomon, S. (2005): *Aeronomy of the Middle Atmosphere*. Springer, Dordrect, The Netherlands. 89

Bretagnon, P. (1982): *Theory for the motion of all the planets - the VSOP 82 solution*. Astronomy and Astrophysics, **114**, 278–288. 146

Bretagnon, P. and Francou, G. (1988): *Planetary theories in rectangular and spherical variables - VSOP 87 solutions.* Astronomy and Astrophysics, **202**, 309–315. 144

Brinkop, S. and Roeckner, E. (1995): *Sensitivity of a general circulation model to parameterizations of cloud-turbulence interactions in the atmospheric boundary layer.* Tellus, **47A**, 197–220. 49

Burridge, D. M. and Haseler, J. (1977): *A model for medium range weather forecasting - Adiabatic formulation.* Technical Report 4, ECMWF, Reading, UK. 25

Charnock, M. (1955): *Wind stress on a water surface.* Quart. J. Roy. Meteor. Soc., **81**, 639–640. 54

Cionni, I. et al. (2011): *Ozone database in support of CMIP5 simulations: results and corresponding radiative forcing.* Atmos. Chem. Phys., **11, no. 21**, 11267–11292. 114, 115

Croll, J. (1867a): *On the change in the obliquity of the eliptic, its influence on the climate of the polar regions and on the level of the sea.* Philosophical Magazine, **33**, 426–445. 144

Croll, J. (1867b): *On the excentricity of the earth's orbit, and its physical relations to the glacial epoch.* Philosophical Magazine, **33**, 119–131. 144

Crowell, J. C. and North, G. R. (1991): *Palaeoclimatology.* No. 18 in Oxford Monographs on Geology and Geophysics. Oxford University Press, New York. 146

Deardorff, J. (1974): *Three-dimensional numerical study of the height and mean structure of a heated planetary boundary layer.* Bound.-Layer Meteor., **7**, 81–106. 64

Dewan, E. M. and Good, R. E. (1986): *Saturation and the universal spectrum for vertical profiles of horizontal scalar winds in the atmosphere.* J. Geophys. Res., **91**, 2742–2748. 76

Dickinson, R. E., Henderson-Sellers, A., Kennedy, P. J. and Wilson, M. F. (1986): *Biosphere Atmosphere Transfer Scheme (BATS) for the NCAR Community Climate Model.* NCAR/TN-275+STR 69 pp., Natl. Cent. for Atmos. Res., Boulder, Colo. 98, 99

Eckermann, S. D., Hirota, I. and Hocking, W. K. (1994): *Gravity wave and equatorial morphology of the stratosphere derived from long-term rocket sounding.* Quart. J. Roy. Meteor. Soc., **112**, 149–186. 76

Eliasen, E., Machenhauer, B. and Rasmussen, E. (1970): *On a numerical method for integration of the hydrodynamical equations with a spectral representation of the horizontal fields.* Tech. Rep. 2, Institute of Theoretical Meteorology, University of Copenhagen. 12, 19

Eyring, V. et al. (2010): *Sensitivity of 21st century stratospheric ozone to greenhouse gas scenarios.* Geophys. Res. Letters, **37**, DOI:10.1029/2010GL044443. 115

Fetterer, F. and Untersteiner, N. (1998): *Observations of melt ponds on Arctic sea ice.* J. Geophys. Res., **103, no. C11**, 24821–24835. 100

Fritsch, J. M. and Chapell, C. G. (1980): *Numerical prediction of convectively driven mesoscale pressure systems, Part I: Convective parameterization.* J. Atmos. Sci., **37**, 1722–1733. 62

Fritts, D. C. (1984): *Gravity wave saturation in the middle atmosphere: A review of theory and observations.* Rev. Geophys. Space Sci., **22**, 275–308. 76

Fritts, D. C. (1989): *A review of gravity wave saturation processes, effects, and variability in the middle atmosphere.* Pure Appl. Geophys., **130**, 343–371. 76

Fritts, D. C. and Nastrom, G. D. (1992): *Sources of mesoscale variability of gravity waves. Part II: Frontal, convective and jet stream excitation.* J. Atmos. Sci., **49**, 111–127. 82

Fritz, S. (1954): *Scattering of solar energy by "large" drops.* J. Meteor., **11**, 291–300. 43

Fröhlich, C. and Lean, J. (2004): *Solar radiative output and its variability: Evidence and mechanisms.* Astron. Astrophys. Rev., **12**, 273–320. 110

Geleyn, J. F. and Hollingsworth, A. (1979): *An economical analytical method for the computation of the interaction between scattering and line absorption of radiation.* Beitr. Phys. Atm., **52**, 1–16. 46

Giorgetta, M. et al. (2006): *Climatology and forcing of the quasi-biennial oscillation in the maecham5 model.* J. Climate, **19**, 3882–3901. 76

Girard, C. and Jarraud, M. (1982): *Short and medium range forecast differences between a spectral and a grid-point model: An extensive quasi-operational comparison.* Technical Report 32, ECMWF, Reading, UK. 12

Goodess, C. M., Palutikof, J. P. and Davies, T. D. (1992): *The nature and causes of climate change.* Belhaven Press, London. 145

Gunn, K. L. S. and Marshall, J. S. (1958): *The distribution with size of aggregate snowflakes.* Journal of Meteorology, **15**, 452–461. 71

Hamilton, K. (1991): *Climatological statistics of stratospheric inertia-gravity waves deduced from historical rocketsonde wind and temperature data.* J. Geophys. Res., **96**, 20831–20839. 76

Herzog, M. and Graf, H.-F. (2010): *Applying the three–dimensional model ATHAM to volcanic plumes: Dynamic of large co–ignimbrite eruptions and associated injection heights for volcanic gases.* Geophys. Res. Lett., **37**, doi:10.1029/2010GL044986. 129

Heymsfield, A. J. and Donner, L. J. (1990): *A scheme for parameterizing ice-cloud water content in general cirulation models.* J. Atmos. Sci., **47**, 1865–1877. 68, 74

Hines, C. O. (1991a): *The saturation of gravity waves in the middle atmosphere. Part I: Critique of linear-instability theory.* J. Atmos. Sci., **48**, 1348–1359. 76, 81

Hines, C. O. (1991b): *The saturation of gravity waves in the middle atmosphere. Part II: Development of Doppler-spread theory.* J. Atmos. Sci., **48**, 1360–1379. 76, 80

Hines, C. O. (1991c): *The saturation of gravity waves in the middle atmosphere. Part III: Formation of the turbopause and of turbulent layers beneath it.* J. Atmos. Sci., **48**, 1380–1385. 76

Hines, C. O. (1993): *The saturation of gravity waves in the middle atmosphere. Part IV: Cutoff of the incident wave spectrum..* J. Atmos. Sci., **50**, 3045–3060. 76, 79, 80

Hines, C. O. (1997a): *Doppler spread parameterization of gravity wave momentum deposition in the middle atmosphere. Part I: Basic formulation.* J. Atmos. Solar Terr. Phys., **59**, 371–386. 76, 79, 80, 83

Hines, C. O. (1997b): *Doppler spread parameterization of gravity wave momentum deposition in the middle atmosphere. Part II: Broad and quasi monochromatic spectra and implementation.* J. Atmos. Solar Terr. Phys., **59**, 387–400. 76

Hirota, I. (1984): *Climatology of gravity waves in the middle atmosphere.* J. Atm. Terr. Phys., **46**, 767–773. 76

Holben, B. et al. (1998): *AERONET — A federated instrument network and data archive for aerosol characterization.* Remote sensing of environment, **66, no. 1**, 1–16. 117

Hoskins, B. J. and Simmons, A. J. (1975): *A multi-layer spectral model and the semi-implicit method.* Quart. J. Roy. Meteor. Soc., **101**, 637–655. 18

Hurrell, J. et al. (2008): *A new sea surface temperature and sea ice boundary dataset for the community atmosphere model.* J. Climate, **21**, 5145–5153. 130

Iacono, M. et al. (2008): *Radiative forcing by long-lived greenhouse gases: Calculations with the aer radiative transfer models.* J. Geophys. Res., **113**. 9, 41

ICAO (1964): *Manual of the ICAO Standard Atmosphere.* U.S. Government Printing Office, Washington, D.C. 27

Jakob, C. and Klein, S. A. (1999): *A scheme for parameterizing ice-cloud water content in general cirulation models.* J. Atmos. Sci., **47**, 1865–1877. 73

Jarraud, M., Girard, C. and Cubasch, U. (1981): *Comparison of medium-range forecasts made with the models using spectral or finite-difference techniques in the horizontal.* Technical Report 23, ECMWF, Reading, UK. 12

Jarraud, M., Girard, C. and Geleyn, J.-F. (1982): *Note on a possible linearization of the vorticity equation in a primitive equations spectral model.* In: *Research Activities in Atmospheric and Oceanic Modelling*, no. 3 in Working Group on Numerical Experimentation, pp. 4.2–4.4, Geneva. WMO. 12

Jeuken, A. et al. (1996): *On the potential of assimilating meteorological analyses in a global climate model for the purpose of model validation.* **101, no. D12**, 16939–16950. 35

Joseph, J. H., Wiscombe, W. J. and Weinman, J. A. (1976): *The delta-eddington approximation for radiative flux transfer.* J. Atmos. Sci., **33**, 2452–2459. 43

Kasahara, A. (1974): *Various vertical coordinate systems used for numerical weather prediction.* Mon. Wea. Rev., **102**, 509–522. 12

Kessler, E. (1969): *On the distribution and continuity of water substance in atmospheric circulation.* Met. Mon. American Meteorological Society, **32**. Boston, Mass. 74

Kinne, S. (2012): *Aerosol optical properties.* in preparation. 118

Kinne, S. et al. (2006): *An AeroCom initial assessment – optical properties in aerosol component modules of global models.* Atmos. Chem. Phys., **6, no. 7**, 1815–1837. 117

Krishnamurti, T. et al. (1991): *Physical initialization for numerical weather prediction over the tropics.* Tellus, **43AB**, 53–81. 33

Krylov, V. I. (1962): *Approximate calculation of integrals.* Macmillan, York. 19

Laskar, J., F. J. and Boudin, F. (1993): *Orbital, precessional, and insolation quantities for the earth from -20 myr to +10 myr*. Astronomy and Astrophysics, **270**, 522–533. 144, 148

Lean, J. (2000): *Evolution of the sun's spectral irradiance since the maunder minimum*. Geophys. Res. Lett., **27**, 2425–2428. 110

Levkov, L., Rockel, B., Kapitza, H. and Raschke, E. (1992): *3d mesoscale numerical studies of cirrus and stratus clouds by their time and space evolution*. Beitr. Phys. Atmos., **65**, 35–58. 69, 70, 71, 72

Lin, S. J. and Rood, R. B. (1996): *Multidimensional flux form semi-Lagrangian transport*. Mon. Wea. Rev., **124**, 2046–2068. 12, 36, 37

Lin, Y.-L., Farley, R. D. and Orville, H. D. (1983): *Bulk parameterization of the snow field in a cloud model*. Journal of Climate and Applied Meteorology, **22**, 1065–1092. 71

Lindzen, R. S. (1981): *Turbulence and stress due to gravity wave and tidal breakdown*. J. Geophys. Res., **86**, 9707–9714. 80, 87

Lohmann, U. and Roeckner, E. (1996): *Design and performance of a new cloud microphysics scheme developed for the ECHAM4 general circulation model*. Clim. Dyn., **12**, 557–572. 65

Lott, F. (1999): *Alleviation of stationary biases in a GCM through a mountain drag parameterization scheme and a simple representation of mountain lift forces*. Mon. Wea. Rev., **127**, 788–801. 85, 86, 107

Lott, F. and Miller, M. J. (1997): *A new-subgrid-scale orographic drag parameterization: Its formulation and testing*. Quart. J. Roy. Meteor. Soc., **123**, 101–127. 85, 86

Louis, J. F. (1979): *A parametric model of vertical eddy fluxes in the atmosphere*. Bound.-Layer Meteor., **17**, 187–202. 54

Lüthje, M., Feltham, D. L., Taylor, P. D. and Worster, M. G. (2006): *Modelling the summertime evolution of sea-ice melt ponds*. J. Geophys. Res., **111**, C02001, doi:10.1029/2004JC002818. 102, 103

Machenhauer, B. and Rasmussen, E. (1972): *On the integration of the spectral hydrodynamical equations by a transform method*. Tech. Rep. 4, Institute of Theoretical Meteorology, University of Copenhagen. 12, 19

Mailhot, J. and Benoit, R. (1982): *A finite-element model of the atmospheric boundary layer suitable for use with numerical weather prediction models*. J. Atmos. Sci., **39**, 2249–2266. 53

Manzini, E. et al. (2006): *The influence of sea surface temperatures on the northern winter stratosphere: Ensemble simulations with the maecham5 model*. J. Climate, **19**, 3863–3881. 76

Manzini, E. and McFarlane, N. A. (1998): *The effect of varying the source spectrum of a gravity wave parameterization in a middle atmosphere general circulation model*. J. Geophys. Res., **103**, 31523–31539. 76

Manzini, E., McFarlane, N. A. and McLandress, C. (1997): *Impact of the Doppler spread parameterization on the simulation of the middle atmosphere circulation using the MA/ECHAM4 general circulation model*. J. Geophys. Res., **102**, 25751–25762. 76

Marshall, J. S. and Palmer, W. M. (1948): *The distribution of raindrops with size*. Journal of Meteorology, **5**, 165–166. 71

Meador, W. and Weaver, W. (1980): *Two-stream approximations to radiative transfer in planetary atmospheres: A unified description of existing methods and a new improvement*. J. Atm. Sci., **37**, 630–643. 44

Meeus, J. (1998): *Astronomical Algorithms*. Willmann-Bell, Richmond, 2nd edn.. 145, 151

Meinshausen, M. et al. (2011): *The rcp greenhouse gas concentrations and their extensions from 1765 to 2300*. Clim. Change, **109**, 213–241. 113

Mellor, G. L. and Yamada, T. (1974): *A hierarchy of turbulence closure models for planetary boundary layers*. J. Atm. Sci., **31**, 1791–1806. 49

Mellor, G. L. and Yamada, T. (1982): *Development of a turbulence closure model for geophysical fluid problems*. Rev. Geophys. Space Phys., **20**, 851–875. 52

Milankovitch, M. M. (1941): *Canon of Insolation and the Ice Age Problem*. Kñiglich Serbische Academie, Belgrade. English translation by the Israel Program for Scientific Translations, United States Department of Commerce and the National Science Foundation, Washington D.C. 144, 150

Miller, M. J., Palmer, T. N. and Swinbank, R. (1989): *Parameterization and influence of subgrid scale orography in general circulation and numerical weather prediction models*. Meteor. Atmos. Phys., **40**, 84–109. 85

Mlawer, E. J. et al. (1997): *Radiative transfer for inhomogeneous atmospheres: RRTM, a validated correlated-k model for the longwave*. J. Geophys. Res., **102**, 16663–16682. 41

Morassutti, M. P. and LeDrew, E. F. (1996): *Albedo and depth of melt ponds on sea ice*. Int. J. Climatol., **16**, 817–838. 101, 104

Moss, R. et al. (2010): *The next generation of scenarios for climate change research and assessment*. Nature, **463, no. 7282**, 747–756. 117, 121

Murakami, M. (1990): *Numerical modeling of dynamical and microphysical evolution of an isolated convective cloud - the 19 July 1981 CCOPE cloud*. Journal of the Meteorological Society of Japan, **68**, 107–128. 69, 70

Nilsson, B. (1979): *Meteorological infuence on aerosol extinction in the 0.2–40-µm wavelength range*. Applied Optics, **18, no. 20**, 3457–3473. 6, 119

Nordeng, T. E. (1994): *Extended versions of the convective parameterization scheme at ECMWF and their impact on the mean and transient activity of the model in the tropics*. Technical Memorandum 206, ECMWF, Reading, UK. 60, 62, 63

Oreopoulos, L. and Barker, H. W. (1999): *Accounting or subgrid-scale cloud variability in a multi-layer 1d solar radiative transfer algorithm*. Q.J.R. Meteorol. Soc., **125**, 301–330. 44, 45

Orszag, S. A. (1970): *Transform method for calculation of vector coupled sums*. J. Atmos. Sci., **27**, 890–895. 12

Palmer, T. N., Shutts, G. J. and Swinbank, R. (1986): *Alleviation of systematic weasterly bias in general circulation and numerical weather prediction models through an orographic gravity wave drag parameterization*. Quart. J. Roy. Meteor. Soc., **112**, 2056–2066. 85, 87

Paltridge, G. W. and Platt, C. M. R. (1976): *Radiative Processes in Meteorology and Climatology*. No. 5 in Developments in Atmospheric Science. Elsevier, Amsterdam. 45

Pedersen, C. A., Roeckner, E., Lüthje, M. and Winther, J.-G. (2009): *A new sea ice albedo scheme including melt ponds for ECHAM5 general circulation model*. J. Geophys. Res., **114**, D08101, doi:10.1029/2008JD010440. 98, 102

Pedersen, C. A. and Winther, J.-G. (2005): *Intercomparison and validation of snow albedo parameterisation schemes in climate models*. Clim. Dyn., **25**, 351–362. 98

Perovich, D. K. and Tucker III, W. B. (1997): *Arctic sea-ice conditions and the distribution of solar radiation during summer*. Ann. Glaciol., **25**, 445–450. 100

Perovich, D. K., TuckerIII, W. B. and Ligett, K. A. (2002): *Aerial observations of the evolution of ice surface conditions during summer*. J. Geophys. Res., **107, no. C10**, 8048, doi:10.1029/2000JC000449. 99

Phillips, N. A. (1957): *A coordinate system having some special advantages for numerical forecasting*. Journal of Meteorology, **14**, 184–185. 12

Pincus, R., Barker, H. W. and Morcrette, J.-J. (2003): *A fast, flexible, approximate technique for computing radiative transfer in inhomogeneous cloud fields*. J. Geophys. Res., **108**, 4376. 47

Pincus, R. and Stevens, B. (2013): *Paths to accuracy for radiation parameterizations in atmospheric models*. J. Adv. Model. Earth Syst., **5**, 225–223. 41, 48

Podgorny, I. A. and Grenfell, T. C. (1996): *Partitioning of solar energy in melt ponds from measurements of pond albedo and depth*. J. Geophys Res., **101, no. C10**, 22737–22748. 100

Potter, B. E. (1991): *Improvements to a commonly used cloud microphysical bulk parameterization*. J. Appl. Meteorol., **30**, 1040–1042. 71

Pruppacher, H. R. and Klett, J. D. (1978): *Microphysics of Clouds and Precipitation*. D. Reidel Publishing Company, Amsterdam. 69

Raddatz, T. J. et al. (2007): *Will the tropical land biosphere dominate the climate-carbon cycle feedback during the twenty-first century?*. Clim. Dyn., **29**, 565–574. 9, 90, 105, 131

Riahi, K. et al. (2011): *Rcp 8.5 a scenario of comparatively high greenhouse gas emissions*. Clim. Change, **109**, 33–57. 113

Robert, A. J. (1981): *A stable numerical integration scheme for the primitive meteorological equations*. Atmos. Ocean, **19**, 35–46. 28

Robert, A. J. (1982): *A semi-Lagrangian and semi-implicit numerical integration scheme for the primitive meteorological equations*. J. Met. Soc. Japan, **60**, 319–325. 28

Robert, A. J., Henderson, J. and Turnbull, C. (1972): *An implicit time integration scheme for baroclinic models in the atmosphere.* Mon. Wea. Rev., **100**, 329–335. 12, 28

Roeckner, E. et al. (2003): *The atmospheric general circulation model ECHAM5. Part I: Model Description.* Report 349, Max-Planck-Institut für Meteorologie, Hamburg. 9, 64, 65

Roeckner, E. et al. (2006): *Sensitivity of simulated climate to horizontal and vertical resolution in the echam5 atmosphere model.* J. Climate, **19**, 3771–3791. 9

Roeckner, E. et al. (2011): *Historical and future anthropogenic emission pathways derived from coupled climate-carbon cycle simulations.* Climatic Change, **105**, 91–108. 9

Roeckner, E., Mauritsen, T., Esch, M. and Brokopf, R. (2012): *Impact of melt ponds on arctic sea ice in past and future climates as simulated by mpi–esm.* J. Adv. Model. Earth Syst., **4**, M00A02, doi:10.1029/2012MS000157. 104

Roesch, A. C. (2000): *Assessment of the land surface scheme in climate models with focus on surface albedo and snow cover.* Ph.D. thesis, ETH Zurich, Zurich, Switzerland. 98, 99

Rotstayn, L. D. (1997): *A physically based scheme for the treatment of stratiform precipitation in large-scale models. I: Description and evaluation of the microphysical processes.* Quart. J. Roy. Meteor. Soc., **123**, 1227–1282. 68, 72

Schramm, J. L., Holland, M. M., Curry, J. A. and Ebert, E. E. (1997): *Modeling the thermodynamics of a sea-ice thickness distribution: 1. Sensitivity to ice thickness resolution.* J. Geophys. Res., **102, no. C10**, 23079–23091. 100

Seidelmann, P. K. (1982): *1980 IAU theory of nutation: The final report of the IAU working group on nutation.* Celestial Mechanics, **27**, 79–106. 149

Simmons, A. J. and Burridge, D. M. (1981): *An energy and angular-momentum conserving vertical finite difference scheme and hybrid vertical coordinates.* Mon. Wea. Rev., **109**, 758–766. 12, 21, 25, 30

Simmons, A. J. and Chen, J. (1991): *The calculation of geopotential and pressure-gradient in the ecmwf atmospheric model: Influence on the simulation of the polar atmosphere and on temperature analyses.* Quart. J. Roy. Meteor. Soc., **117**, 29–58. 27

Simmons, A. J., Hoskins, B. J. and Burridge, D. M. (1978): *Stability of the semi-implicit time scheme.* Mon. Wea. Rev., **106**, 405–412. 30

Simmons, A. J. and Strüfing, R. (1981): *An energy and angular-momentum conserving finite difference scheme, hybrid coordinates and medium-range weather prediction.* Technical Report 28, ECMWF, Reading, UK. 12, 21, 25, 26, 30

Simpson, J. and Wiggert, V. (1969): *Models of precipitating cumulus towers.* Mon. Wea. Rev., **97**, 471–489. 61

Smith, S. A., Fritts, D. C. and VanZandt, T. E. (1987): *Evidence for a saturated spectrum of atmospheric gravity waves.* J. Atmos. Sci., **44**, 1404–1410. 76

Sokolik, I., Toon, O. and Bergstrom, R. (1998): *Modeling the radiative characteristics of airborne mineral aerosols at infrared wavelengths.* J. Geophys. Res., **103**, 8813–8826. 6, 119

Sparks, R. et al. (1997): *Volcanic Plumes*. John Wiley & Sons, Inc., New York. 129

Stenchikov, G. et al. (2004): *Arctic oscillation response to the 1991 Pinatubo eruption in the SKYHI general circulation model with a realistic quasi–biennial oscillation*. J. Geophys. Res., **109**, doi:10.1029/2003JD003699. 126

Stenchikov, G. et al. (2009): *Volcanic signals in oceans*. J. Geophys. Res., **114**, doi:10.1029/2008JD011673. 126

Stenchikov, G. L. et al. (1998): *Radiative forcing from the 1991 Mount Pinatubo volcanic eruption*. J. Geophys. Res., **103, no. D12**, 13,837–13,857. 126

Stier, P. et al. (2005): *The aerosol–climate model ECHAM5–HAM*. Atmos. Chem. Phys., **5**, 1125–1156. 121

Sundqvist, H., Berge, E. and Kristjansson, J. (1989): *Condensation and cloud parameterization studies with a mesoscale numerical weather prediction model*. Mon. Wea. Rev., **117**, 1641–1657. 65, 66

Thomas, M. et al. (2009a): *Simulation of the climate impact of Mt. Pinatubo eruption using ECHAM5 — Part 1: Sensitivity to the modes of atmospheric circulation and boundary conditions*. Atmos. Chem. Phys., **9**, 757–769. 126

Thomas, M. et al. (2009b): *Simulation of the climate impact of Mt. Pinatubo eruption using ECHAM5 — Part 1: Sensitivity to the phase of the QBO and ENSO*. Atmos. Chem. Phys., **9**, 3001–3009. 126

Thomson, A. et al. (2011): *Rcp4.5: a pathway for stabilization of radiative forcing by 2100*. Clim. Change, **109**, 77–94. 113

Tiedtke, M. (1989): *A comprehensive mass flux scheme for cumulus parameterization in large-scale models*. Mon. Wea. Rev., **117**, 1779–1800. 60, 107

Tiedtke, M. (1993): *Representation of clouds in large-scale models*. Mon. Wea. Rev., **121**, 3040–3061. 73

Timmreck, C. et al. (2009): *Limited temperature response to the very large AD 1258 volcanic eruption*. Geophys. Res. Lett., **36**, doi:10.1029/2009GL040083. 129

Tompkins, A. (2002): *A prognostic parameterization for the subgrid-scale variability of water vapor and clouds in large-scale models and its use to diagnose cloud cover*. J. Atmos. Sci., **59**, 1917–1942. 65

Tschudi, M. A., Curry, J. A. and Maslanik, J. A. (2001): *Airborne observations of summertime surface features and their effect on surface albedo during FIRE/SHEBA*. J. Geophys. Res., **106, no. D14**, 15335–15344. 99

Turner, J. S. (1963): *The motion of buoyant elements in turbulent surroundings*. J. Fluid Mech., **16**, 1–16. 60

van Vuuren, D. et al. (2011): *Rcp2.6: exploring the possibility to keep global mean temperature increase below 2°Cc*. Clim. Change, **109**, 95–116. 113

Vincent, R. A., Allen, S. J. and Eckermann, S. D. (1997): *Gravity wave processes and their parameterization in global climate models*. In: *Gravity wave parameters in the lower stratosphere*, edited by Hamilton, K., NATO ASI Series I, pp. 7–25. Springer. 82

Xu, K. M. and Krueger, S. K. (1991): *Evaluation of cloudiness parameterizations using a cumulus ensemble model.* Mon. Wea. Rev., **119**, 342–367. 67

Yang, Z. L., Dickinson, R. E., Robock, A. and Vinnikov, K. Y. (1997): *Validation of the snow submodel of the biosphere-atmosphere transfer scheme with Russian snow cover and meteorological observational data.* J. Clim., **10**, 353–373. 99

Zdunkowski, W. G., Welch, R. M. and Korb, G. J. (1980): *An investigation of the structure of typical two-stream methods for the calculation of solar fluxes and heating rates in clouds.* Beitr. Phys. Atmos., **53**, 147–166. 44